ISBN 978-82-471-1581-7 (printed ver.)
ISBN 978-82-471-1582-4 (electronic ver.)
ISSN 1503-8181

Knut Arild Maråk

Doctoral Thesis

Doctoral theses at NTNU, 2009:100

Knut Arild Maråk

Condensation Heat Transfer and Pressure Drop for Methane and Binary Methane Fluids in Small Channels

NTNU
Norwegian University of
Science and Technology

Doctoral theses at NTNU, 2009:100

NTNU
Norwegian University of
Science and Technology
Thesis for the degree of
philosophiae doctor
Faculty of Engineering Science & Technology
Department of Energy and Process Engineering

NTNU
Norwegian University of
Science and Technology

Knut Arild Maråk

Condensation Heat Transfer and Pressure Drop for Methane and Binary Methane Fluids in Small Channels

Thesis for the degree of philosophiae doctor

Trondheim, June 2009

Norwegian University of
Science and Technology
Faculty of Engineering Science & Technology
Department of Energy and Process Engineering

NTNU
Norwegian University of
Science and Technology

NTNU
Norwegian University of Science and Technology

Thesis for the degree of philosophiae doctor

Faculty of Engineering Science & Technology
Department of Energy and Process Engineering

ISBN 978-82-471-1581-7 (printed ver.)
ISBN 978-82-471-1582-4 (electronic ver.)
ISSN 1503-8181

Doctoral Theses at NTNU, 2009:100

Printed by Tapir Uttrykk

Knut Arild Maråk

Condensation Heat Transfer and Pressure Drop for Methane and Binary Methane Fluids in Small Channels

Doctoral thesis
for the degree of philosophiae doctor

Trondheim, June 2009

Norwegian University of Science and Technology
Faculty of Engineering Science & Technology
Department of Energy and Process Engineering

NTNU

Norwegian University of Science and Technology

Doctoral thesis
for the degree of philosophiae doctor

Faculty of Engineering Science & Technology
Department of Energy and Process Engineering

ISBN 978-82-471-1581-7 (printed version)
ISBN 978-82-471-1582-4 (electronic version)

Doctoral theses at NTNU, 2009:100

Printed by Tapir-trykk

Abstract

A conventional heat exchanger consists of fluid channels with diameter larger than approximately 3 mm. Here, the phenomena around heat transfer and pressure drop are more or less well understood and can be well predicted. Newer and more compact heat exchangers use channels with smaller diameter which gives multiple advantages; they occupy less volume, are lighter, may be modular and can be faster and cheaper to produce. However, it is uncertain whether the phenomena affecting heat transfer and pressure drop are the same as in the larger channels. Clarifying this with respect to possible usage in the LNG-industry has been the main purpose of this work.

An experimental set-up designed by Dr. Steffen Grohmann has been used in these investigations. A total of 749 measurements in tubes with diameter 1 mm, 0.5 mm and 0.25 mm have been done. Both single and two-phase flow measurements of pure methane, methane/ethane- and methane/nitrogen-mixtures have been carried out. The measurements were done over a broad range with respect to pressure, vapour fraction, mass flux and heat flux. Also the pressure drop was measured.

The conclusion is that the models concerning heat transfer and pressure drop in conventional channels also can be used in tubes with diameter 1 mm and 0.5 mm. The results from the 0.25 mm tube are burdened with too high uncertainty to be used in the conclusion. The results can also be relevant for non-circular diameters in microscale, e.g. for plate-fin heat exchangers.

Samandrag

Konvensjonelle varmevekslarar nyttar kanalar med diameter ned til omlag 3 mm. I desse er fenomena kring varmeovergang og trykktap i stor grad kjende. Nyare og meir kompakte varmevekslarar har kanalar med mindre diameter som inneber ei rekkje fordelar; dei tek mindre plass, er lettare og kan vere raskare og billigare å produsere. Det herskar imidlertid uvisse om fenomena kring varmeovergang og trykktap er dei same som i konvensjonelle kanalar. Å få dette avklart i høve til mogleg bruk i LNG-industrien har vore hovudføremålet med arbeidet.

Eit eksperimentelt oppsett designa av Steffen Grohmann vart brukt i undersøkjingane. Tilsaman 749 målingar i røyr med diameter 1 mm, 0.5 mm og 0.25 mm vart utført. Både einfase kjøling og kondensasjon av metan og blandingar av metan/etan og metan/nitrogen vart gjort. Målingane varierte over eit stort område med omsyn til trykk, dampfraksjon, massefluks og varmefluks. Også trykkfall gjennom røyra vart målt.

Resultata viser at varmeovergang i einfase veske kan forutseiast med eksisterande modellar i 1 mm og 0.5 mm røyra. Trykkfallsmålingane for 1 mm røyret er som forventa utifrå konvensjonelle modellar. For 0.5 mm-røyret er trykkfallet høgare enn forventa. For 0.25-mm røyret er uvissa for stor til at resultata kan brukast i ein konklusjon.

For kondensering av rein metan kan varmeovergangen i 1 mm-røyret forutseiast med konvensjonelle modellar. I 0.5 mm røyret er varmeovergangen høgare enn berekna. For kondensering av binære blandingar kan varmeovergangen bereknast med konvensjonelle modellar for både 1 mm og 0.5 mm røyret.

For tofasemålingar i 1 mm-røyret er den gjennomsnittlege uvissa for varmeovergang rundt 10 % og hovudsakleg knytt til temperatursensorane. For 0.5 mm røyret er uvissa for kondensering av rein metan litt over 20 %, medan den er rundt 10 % for kondensering av binærblandingane. For 0.5 mm-røyet og særskilt for 0.25 mm-røyret er massestraumsmålaren ei mykje viktigare kjelde til uvisse.

Den større uvissa for målingane av Methane-100 er hovudargumentet for å trekkje desse i tvil i høve til målingane av binærblandingane. Konklusjonen er derfor at røyr med diameter 1 mm og 0.5 mm ikkje skil seg frå konvensjonelle røyr med omsyn til varmeovergang.

For friksjonstrykktap i tofasestrømning kan denne forutsjåast med god presisjon med eksisterande modellar både for 1 mm og 0.5 mm røyret.

Sjølv om målingane er gjort i runde røyr, kan resultata også vere relevante for andre røyrgeometriar med tilsvarande hydraulisk diameter.

Acknowledgements

Firstly, thanks to my family who gave me the opportunity to pursue a PhD. On the academic level, I wish to thank my supervisors for guiding me in the work:

- Dr. Arne Olav Fredheim, NTNU/StatoilHydro
- Dr. Jostein Pettersen, NTNU/StatoilHydro
- Dr. Armin Hafner, SINTEF Energy Research.

I also like to thanks Helge Johansen, SINTEF Energy Research for working for me on the test setup, Steffen Grohmann for designing the test rig and giving me a flying start, Roger Khalil for setting up and showing me how to operate a gas chromatograph, Erling Næss for fruitful discussions when no explanations of the results could be found and to Mona Mølnvik, SINTEF Energy Research for funding when new gadgets were needed.

This thesis would not have been possible without the research collaboration between Norwegian University of Science and Technology (NTNU), SINTEF Energy Research and StatoilHydro. From NTNU, this particularly involves the Department of Energy and Process Engineering.

I would also like to thank my PhD-colleagues. I would particularly mention the people with whom I shared office during most of these three and a half years; Konrad Eichhorn, Audun Aspelund, Lars Nord, Torleif Weydahl and Liang Wang. They provided a good and motivating working atmosphere. Thanks also to Torgeir Skiple, Michael Drescher and Gunnar Lohse for interesting conversations in the lab.

Contents

Nomenclature

Br	Brinkman number, see page 68	-
c_p	Specific heat capacity	J/kgK
d	Diameter	m
e	Enthalpy	J/kg
$Eö$	Eötwös number, see page 16	-
f	Friction factor	-
Fr	Froude number, see page 201	-
g	Gravitational constant, see page 16	m/s^2
h	Heat transfer coefficient	W/m^2K
J	Dimensionless velocity	-
j	Superficial velocity	m/s
k	Thermal conductivity	W/mK
L^+	Reduced length	-
G	Mass flux	kg/m^2s
$\dot{n}$	Molar condensation flux	mol/m^2s
Nu	Nusselt number, see page 4	-
p	Pressure	Pa or bar
p_r	Reduced pressure (p/p_crit)	-
Pr	Prandtl number, see page 5	-

$\mathrm{d}p/\mathrm{d}z$	Pressure drop	Pa/m
q''	Heat flux	$\mathrm{W/m^2}$
Re	Reynolds number, see page 4	-
ΔT_{gl}	Temperature glide in binary mixture	K
T	Temperature	°C
$\overline{u}$	Average velocity in the tube direction	m/s
We	Weber number, see page 201	-
$\tilde{x}$	Molar concentration in the liquid phase	-
x	Vapour fraction	kg/kg
X_{tt}	Martinelli-parameter	-
$\tilde{y}$	Molar concentration in the vapour phase	-

Greek Symbols

Δ	Difference, uncertainty	
δ	Film thickness, uncertainty	m
ϵ	Average roughness height	m
ε	Void fraction	-
μ	Viscosity	Pa s
Φ	Two-phase multiplier	-
ρ	Density	$\mathrm{kg/m^3}$
σ	Surface tension, standard deviation	N/m
τ	Shear tension	Pa

Subscripts

1ph	single phase
2ph	two phase
an	annular

crit	critical
eq	equivalent, equilibrium
eth	ethane
f	frictional
h	hydraulic, homogeneous
i	interface
l	liquid phase
lo	flow as liquid only
m	middle
mc	Multi component
met	methane
sat	saturation condition
sc	Single component
v	vapour phase
vo	flow as vapour only
w	wall
x	local

Test Facility

$A_{\mathrm{C,HS}}$	Cross-sectional area of copper rod	m^2
A_{c}	Cross-sectional area, see page 51	m^2
A_{w}	Wetted surface of the test section	m^2
$d_{w,c,h}$	Diameters, see page 51	m
$\overline{h}$	Average heat transfer coefficient, see page 42	$\mathrm{W/m^2K}$
I_{PH}	Current through pre-heaters	A
k_{Cu}	Thermal conductivity of copper	W/mK

L	Length of the test section	m
L_{HS}	Length between $T_{\mathrm{HS},1}$ and $T_{\mathrm{HS},2}$ along the copper rod	m
$\dot{m}$	Mass flow	kg/s
P	Perimeter, see page 51	m
p_{m}	Pressure in the middle of the test section	bar
$\dot{Q}_{\mathrm{HB}}$	Heat balance over the test section, see page 43	W
$\dot{Q}_{\mathrm{HS}}$	Heat added to heat sink heater	W
$\dot{Q}_{\mathrm{IHX}}$	Heat transferred in the internal heat exchanger	W
$\dot{Q}_{\mathrm{PH}}$	Effect added to the pre-heaters	W
$\dot{Q}_{\mathrm{TS}}$	Heat flowing down the rod from the test section	W
$\Delta T_{\mathrm{m,w}}$	Temperature difference, see page 42	K
T_{b}	Temperature measured close to the tube wall	°C
$T_{\mathrm{HS},1}$	Temperature on the top of the copper rod	°C
$T_{\mathrm{HS},2}$	Temperature at the bottom of the copper rod	°C
T_{in}	Temperature measured at the inlet of the test section	°C
T_{out}	Temperature measured at the outlet of the test section	°C
$T_{\mathrm{TI,out}}$	Temperature at the outlet of the thermal interface	°C
U_{PH}	Voltage across pre-heater cartridge	V

Nobody trusts the model except the author.
Everybody trusts the experiments except the author.

— *unknown*

Chapter 1

Introduction

This thesis presents measurements of heat transfer coefficients in small tubes at low temperatures, both for cooling of single phase flow and condensation of two-phase flow. The main purpose of the results is to create a basis for designing a new type of heat exchanger for natural gas liquefaction.

Liquefied natural gas (LNG) consists predominantly of methane with smaller amounts of typically ethane, propane, butane and nitrogen. It is stored and transported at its boiling point at approximately -162 °C at atmospheric pressure. Due to the much larger density in liquid form, large amounts of natural gas can then be transported by ship over vast distances. The LNG carriers can take up to 250 000 m^3, which corresponds to approx. 150 million standard cubic meter of natural gas.

Liquefaction plants are located near gas fields and at the sea. The largest importer of LNG is by far Japan, and the biggest producer is Qatar. A modern production line (called train) produces from 4 to 8 MTPA (Million Tons Per Annum) and there are usually economy of scale effects. Liquefying the gas requires huge refrigeration duties, and most new facilities use two or three refrigeration cycles. The precooling, liquefaction and subcooling of the natural gas take place in two or three heat exchangers. Different designs exists, but the spiral wound heat exchanger has a predominant position as the main heat exchanger. It is developed specifically for the LNG-industry and has been used for over 30 years.

The Statoil/Linde-alliance developed the Mixed Fluid Cascade process (MFC), which is shown in Figure 1.1. It consists of three mixed refrigerant cooling cycles and three heat exchangers. The first heat exchanger is a plate/fin type and precools the natural gas down to approximately -55 °C. It is then condensed in a spiral wound heat exchanger, thereafter it is subcooled in a second spiral wound heat exchanger. The same heat exchangers also

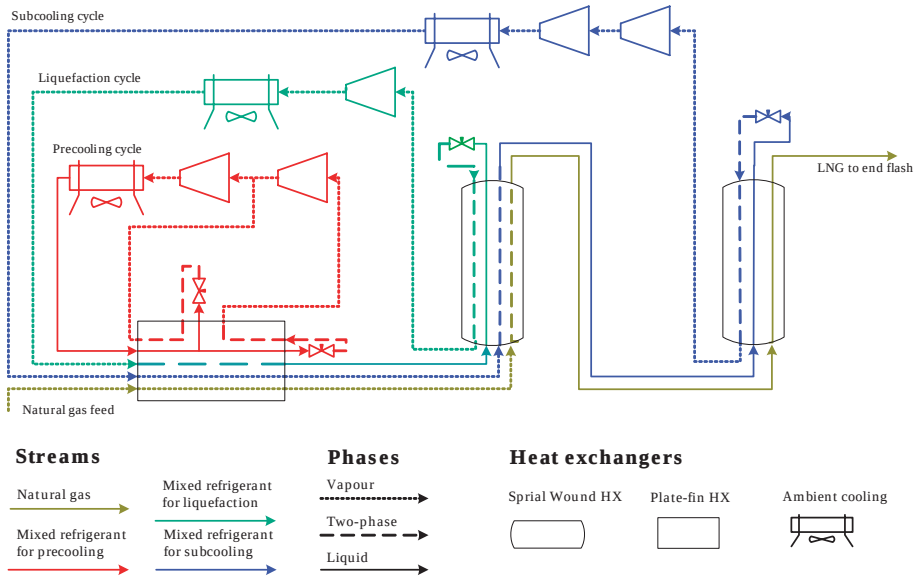

Figure 1.1: The MFC-process from Statoil/Linde.

cool the refrigerants, which are expanded and/or throttled after each heat exchanger to provide refrigeration.

The spiral would heat exchanger is a proven technology, and it is known to be robust and can handle small temperature differences between the warm and cold side. However, it must be produced by hand and it therefore has a long and expensive production time.

There has been an interest in developing a new type of heat exchanger, an exchanger that is cheaper, smaller, modular, less expensive and has shorter production time. Focus has been drawn to using smaller hydraulic diameters with diameters ranging down to approx. 0.1 mm and a research initiative has among other things substantiated in this thesis.

Early investigations of heat transfer in small geometries pointed towards increased heat transfer mechanisms compared to conventional diameters. However, the increased understanding in the most recent years indicate that there are no new mechanisms occurring. Yet, the research on condensation in small channels is still limited and not many investigations have been done, certainly not on low temperature binary component condensation.

In addition to being a tool for designing a new generation of heat exchangers, the results from this work can also be a contribution to the understanding of small scale flow and heat transfer.

Chapter 2

Theoretical background

2.1 Introduction to small diameter channels

Heat transfer and fluid flow in small channels is a relatively new scientific area, but it is already applied in many engineering devices. One of the most used is the cooling of microprocessors, where continuously smaller chips produce ever larger heat fluxes. More compact heat exchangers in air conditions units and in car radiators is another application where more compact equipment is desired.

Various definitions of the difference between microchannels, minichannels and conventional channels exists in the literature. Kandlikar et al. [36] suggests the following segmentation:

Name	Hydraulic Diameter d_h
Conventional Channels	$d_\mathrm{h} > 3$ mm
Minichannels	3 mm $> d_\mathrm{h} > 200$ µm
Microchannels	200 µm $> d_\mathrm{h} > 10$ µm
Transitional Channels	10 µm $> d_\mathrm{h} > 0.1$ µm
Molecular Nanochannels	0.1 µm $> d_\mathrm{h}$

Table 2.1: Tube classification as suggested by Kandlikar et al. [36]

The separation at 200 µm is based on the rarefaction effects for gases. Absence of stratified flow pattern in two-phase flow can be another criteria. The significance of tube orientation a third.

Small uncertainties of a measurement may be very relevant to the final conclusion at this scale. For instance, as the pressure drop is proportional to the inverse of the square diameter, a small uncertainty in the diameter measurement make out a large uncertainty for the pressure drop estima-

tion. Similar effect may occur to e.g. flow rate measurements and heat flux measurements and may be of such scale that the total uncertainty of the experiments is too large to draw any clear conclusion. According to Kandlikar et al. [35], this can explain the discrepancies in the literature reported for the earlier studies of fluid flow and heat transfer in small channels. Morini [51] argues that effects that are neglected in conventional diameters can be relevant in small channels, typically axial conduction and viscous dissipation effects.

2.2 Flow and heat transfer in conventional channels

The use of the terms conventional channels, minichannels or microchannels is used as suggested in Table 2.1.

The heat transfer coefficient h is the ratio of heat transferred per area (heat flux q") to a temperature difference ΔT between the bulk fluid and the tube wall:

$$h = \frac{q''}{\Delta T} \tag{2.1}$$

This is analogous to electricity, where the heat flux can be seen as the current, the temperature difference is the voltage difference and h is the capacitance. The temperature difference is the driving force in heat transfer.

For single phase flow, the numerical value of h can be expressed by the Nusselt-number as in Equation 2.2. Here, k is the conductivity of the fluid and d_h is the hydraulic diameter. The Nusselt number Nu can be interpreted as a dimensionless capacitance between the wetted surface and the flow, and there exists many equations to predict it.

$$h = \frac{Nu \cdot k}{d} \tag{2.2}$$

2.2.1 Heat transfer in single phase in conventional channels

The Reynolds number is an important number when discussing fluid flow and heat transfer. The Reynolds number Re is dimensionless and can be seen as the ratio between inertia and viscous forces in a fluid flow. It is expressed by

$$Re = \frac{d\overline{u}\rho}{\mu} = \frac{Gd}{\mu} \tag{2.3}$$

For $Re < 2300$ the flow is said to be laminar and viscous forces are dominant. The flow is very stable and equations for heat transfer, velocity profile and thermal boundary layer can be found analytically. For circular tubes and for constant tube wall temperature in fully developed laminar flow, the Nusselt number is constant and has the value $Nu = 3.66$.

For higher Reynolds numbers, turbulence will occur as flow fluctuations and the flow is much more complex. For $Re > 10000$, the flow is said to be fully turbulent. Between the fully laminar and the fully turbulent flow, for $2300 < Re < 10000$, lies the transition area [33].

For flow with $Re > 2300$ the Nusselt number is empirically found to be a function of the Reynolds number and the Prandtl number. The Prandtl number Pr is a thermal property of the fluid and is independent of the behaviour of the flow. It expresses the ratio of momentum diffusivity to thermal diffusivity:

$$Pr = \frac{c_{\mathrm{p}}\mu}{k} \tag{2.4}$$

Correlations for single-phase heat transfer in conventional channels have been established by authors like Dittus-Boelter as introduced by McAdams [47] and Petukhov [57]. The first-mentioned of these is rather simple and given in Equation 2.5 for cooling[1]:

$$Nu = 0.023 Re^{0.8} Pr^{0.3} \tag{2.5}$$

Gnielinski [29] used the work by Petukhov [57] and extended his correlation into the transition area using data from a number of publications. Gnielinski's equation is more precise than Equation 2.5 and is regarded as the most used correlation for single phase heat transfer:

$$Nu = \frac{(f/8)\,(Re - 1000)\,Pr}{1 + 12.7\,(f/8)^{0.5}\left(Pr^{2/3} - 1\right)} \tag{2.6}$$

where the friction factor f for smooth tubes was set to

$$f = (1.82 \cdot Log_{10}(Re) - 1.64)^{-2} \tag{2.7}$$

This equation is valid for $2300 < Re < 10^6$ and Prandtl number from 0.6 to 10^5.

For short tubes, the undeveloped temperature profile in the entry region can have an effect on the heat transfer. The term $1 + (d/L)^{2/3}$ is often

[1] Although Equation 2.5 usually is referred to as the Dittus-Boelter equation, the original equation for cooling is $Nu = 0.0265 Re^{0.8} Pr^{0.3}$ as discussed by Winterton [72].

multiplied with Equation 2.6 to take this into account assuming fully developed velocity profile, but undeveloped thermal profile at the entrance [31]. Due to the temperature profile from bulk towards the tube wall, the term $\left(\frac{\mu}{\mu_w}\right)^{0.25}$ corrects for changing temperature-dependent fluid properties for cooling [38].

A tube-average heat transfer coefficient prediction with the Gnielinski-correlation is then given by

$$\overline{Nu} = \frac{(f/8)\,(Re - 1000)\,Pr}{1 + 12.7\,(f/8)^{0.5}\left(Pr^{2/3} - 1\right)}\left[1 + (d/L)^{2/3}\right]\left(\frac{\mu}{\mu_w}\right)^{0.25} \tag{2.8}$$

2.2.2 Two phase flow in conventional channels

For two-phase flow, the situation is a lot more complex as the behaviour of the liquid/vapour interface is highly complicated.

For convective condensing flow in a vertical tube with saturated vapour inlet ($x = 1$), the first liquid condensate is formed as a film at the tube wall as shown in Figure 2.1. As more vapour is condensed, the film thickness δ increases. If the flow velocity would have been zero, the condensation process would have been gravity controlled and followed Nusselt film theory. For a downwards directed flow, the influence of the shear tension τ at the liquid/vapour interface comes in addition to the influence of gravity when it comes to the behaviour of the liquid film. At a certain film thickness, the flow goes from the annular pattern into slug/plug and eventually into bubble and liquid flow where $x = 0$.

For convective condensation in a horizontal tube (shown in Figure 2.2), the first liquid condensate is formed as a thin film on the tube wall as for vertical flow. However, due to gravity, the film tends to drain down the tube wall and accumulation in the lower part of the tube. This flow pattern is called stratified flow.

For moderate to high vapour velocities, the stratified flow very often takes an annular shape like in vertical tubes. When shear forces due to the vapour velocity are large compared to gravity, the tube orientation is unimportant and the gravity can be neglected. The flow is then symmetric around the tube circumference.

The two most important parameters deciding the flow pattern in a conventional channel is the mass flux and the vapour fraction. The relation between the mass flux and the vapour fraction have led to the development of flow maps, where the different flow types can be found. A flow map for R-134a can be seen in Figure 2.7.

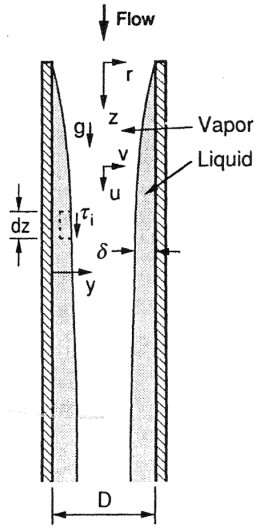

Figure 2.1: Example of film condensation in a vertical tube. Illustration from Carey [7].

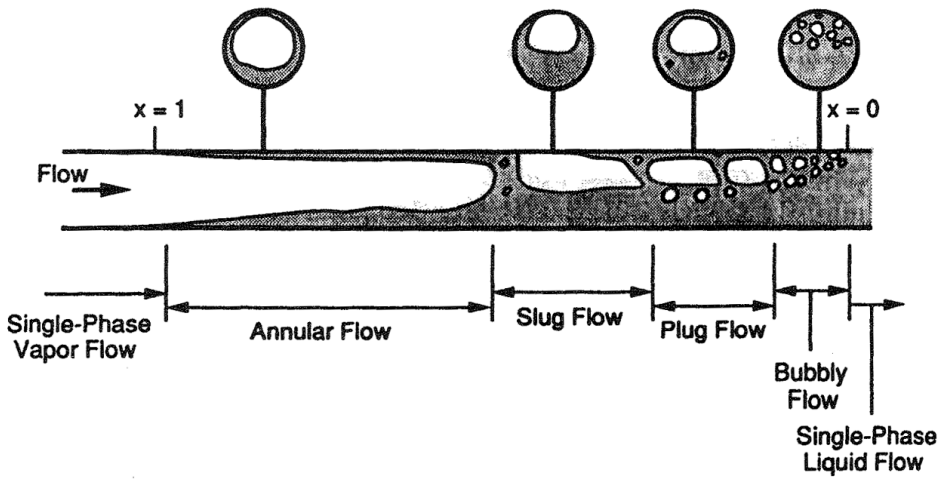

Figure 2.2: Example of flow types as a function of vapour fraction in a horizontal tube. Illustration from Carey [7].

2.2.3 Two phase heat transfer in conventional channels

Heat transfer in two-phase flow is closely linked to the complexity of the flow patterns. For adiabatic flow of a pure fluid, the liquid/vapour interface is in equilibrium. Adding or removing heat from the fluid shifts the equilibrium and a net mass flow occurs from vapour to liquid or from liquid to vapour respectively. The vapourisation or condensation at the liquid/vapour interface occurs instantly with negligible "resistance".

Because of this and excluding effects such as nucleate boiling, the overall heat transfer is limited by how efficient heat is transferred between the tube wall and the liquid/vapour interface. Depending on the flow type, the liquid/vapour interface appears in the form of the surface of bubbles or droplets, or for an annular flow as the surface of the liquid film. These effects are illustrated in Figure 2.3 for three flow types:

If the flow is annular and the liquid film is perfectly laminar, the heat transfer rate is determined by the conductivity of the liquid film. However, the film is often affected by the higher velocity of the vapour flow and turbulence occurs in the liquid layer. Then, mixing of the fluid helps transfer heat in the liquid film and the heat transfer increases. For high vapour velocities, the mixing effects at the liquid/vapour interface are high and the ripples on the film can cause a large interface surface and droplets from the liquid can be entrained in the vapour core.

For a bubbly flow, the vapour and liquid tends to have more or less the same velocity and hence mixing of the liquid is limited. The distance in the liquid between the tube wall and the liquid/vapour interface is long and the surface of the liquid/vapour interface is also small. This yields a low heat transfer coefficient. When the bubbles grow bigger, the distance between the interface and the tube wall decreases and more mixing in the liquid occurs.

For slug/plug flow, the surface of the liquid/vapour interface is large and the phases are continuously well mixed. Combined, this leads to a high heat transfer coefficient.

To summarise, the convection condensation heat transfer coefficient in two-phase flow is mainly dependent on these effects:

- Liquid thermal properties, often expressed through the Prandtl number Pr

- Liquid layer mixing effects, often expressed through the Reynolds number Re of the liquid and/or the vapour phase

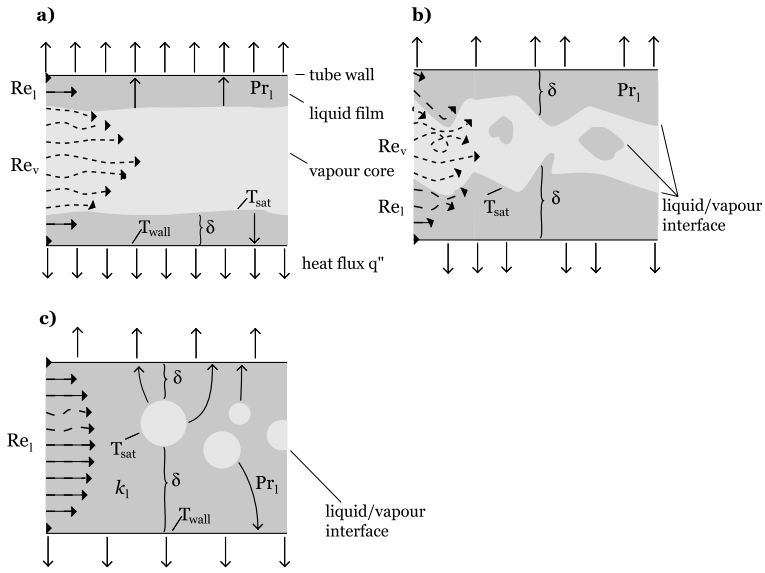

Figure 2.3: Principle phenomena of condensation heat transfer in tube flow. a) Annular flow b) Slug flow and c) Bubble flow.

- Distance between tube wall and liquid/vapour interface, often expressed by the liquid layer thickness δ

- Area of the liquid/vapour interface

Based on these effects, many authors have tried to predict the heat transfer coefficient for two-phase convective condensation. For annular flow, some correlations use boundary layer analysis (e.g. Traviss [69]), while others use a two-phase multiplier for calculating an equivalent *Re*-number for use in a single-phase correlation (e.g. Akers [3] and Shah [62]). A third way to model the phenomenon is by using approaches based on shear forces at the liquid/vapour interface (e.g. Carpenter and Colburn (1951) and improvements by Chen et al. [15]). The models that require the shear stress τ usually requires a pressure drop model. Recent models are based on flow patterns as exemplified by the work from Thome et al. [68].

Carey [7] gives an excellent review of existing correlations for condensation in tubes. The most important ones are mentioned here and more can be found in the appendix.

Akers' correlation (1959)

Akers et al. [3] developed a correlation for condensation in horizontal tubes based on their data for R-12 and propane. The correlation assumes annular flow and that the flow is vapour shear dominated. It defines an equivalent all liquid mass velocity G_{eq} that has the same wall shear stress as the actual two-phase flow. This is defined as

$$G_{\mathrm{eq}} = G\left[(1-x) + x\left(\frac{\rho_{\mathrm{l}}}{\rho_{\mathrm{v}}}\right)^{0.5}\right] \tag{2.9}$$

where ρ_{l} and ρ_{v} is the liquid and vapour density respectively.

Assuming Reynolds analogy, the heat transfer coefficient for this equivalent all liquid flow should be the same as the annular film condensing flow.

$$h = \frac{Nu \cdot k_{\mathrm{l}}}{d} = 0.0265 Re_{\mathrm{eq}}^{0.8} Pr_{\mathrm{l}}^{1/3} \frac{k_{\mathrm{l}}}{d} \tag{2.10}$$

for $Re_{\mathrm{eq}} > 50000$ where

$$Re_{\mathrm{eq}} = \frac{G_{\mathrm{eq}} d_{\mathrm{h}}}{\mu_{\mathrm{l}}} \tag{2.11}$$

The Nusselt number is very similar to the Dittus-Boelter equation given in Equation 2.5 using a modified Reynolds number Re_{eq}. This model is simple and has no new empirically determined constants and it is based only on two fluids.

Shah's correlation (1979)

One of the best known correlations for condensation inside circular tubes is presented by Shah [62]. He used results from many refrigerants condensing in horizontal, vertical and inclined pipes with diameters from 7 to 40 mm. The fluids were condensed at reduced pressure ranging from 0.002 to 0.44, at saturation temperatures from 21 °C to 310 °C and at a wide range of mass fluxes, vapour fraction and heat fluxes. A total of 474 data points from 21 independent studies were used.

His correlation states that

$$h = h_{\mathrm{l}}\left[(1-x)^{0.8} + \frac{3.8 x^{0.76} (1-x)^{0.04}}{p_r^{0.38}}\right] \tag{2.12}$$

where p_r is the reduced pressure and h_{l} is the heat transfer coefficient assuming all mass flowing as liquid. This model is a two-phase multiplier approach. h_{l} is based on the Dittus-Boelter equation and it is strictly empirical.

Thome's correlation (2003)

Thome et al. [68] developed a correlation for condensation in horizontal tubes. The correlation is based on a physically based approach of heat transfer in different flow patterns (annular, intermittent, stratified and mist flow), where a new void fraction model is used to determine the flow pattern. The correlations contains only three parameters which have been determined from a database of 15 different fluids at different vapour fraction, in tubes with diameter ranging from 3.1 to 21.4 mm, mass flux from 22 to 1022 kg/m^{2}s and reduced pressure from 0.02 to 0.8.

For annular, intermittent or mist flow, the following correlation is suggested:

$$h = cRe_{\mathrm{l}}^{n} Pr_{\mathrm{l}}^{m} \frac{k_{\mathrm{l}}}{\delta} f_{\mathrm{i}} \tag{2.13}$$

where f_{i} is a roughness factor between the liquid/vapour interface and c, m and n are the three empirically determined coefficients where best fit values were found to be $c = 0.003$, $m = 0.5$ and $n = 0.74$.

The correlation is based on convection heat transfer for single phase flow, and the similarity is obvious when Equation 2.2 and 2.5 are compared to the correlation. The only difference is that the diameter is replaced by the liquid layer thickness δ and the introduction of a interface roughness factor f_{i} taking increased surface area for heat exchange into account. An overview how to find the film thickness and the interfacial roughness factor is found in Appendix B.1.3.

Summary

Several correlation for condensation in conventional channels heat transfer exist. Many of them are developed by using measurement data within certain pressures, for only a few fluids and for certain tube diameters. These may not be reliable outside their parameter range. Some are purely empirical, while others are based on analytic models.

A persuasive correlation should be based on a physical model, reflecting the mechanisms and phenomenons occurring in the flow. A low number of empirically determined constants is a good indication that the physics involved is captured by the model. Further, the tuning of the parameters in the model should be based on experimental data from a wide range for substances, pressures, vapour fraction, mass and heat fluxes. Only in that way can the different effects be intercepted and an overall general correlation developed. In that respect, the model from Thome et al. [68] appears to be the most convincing.

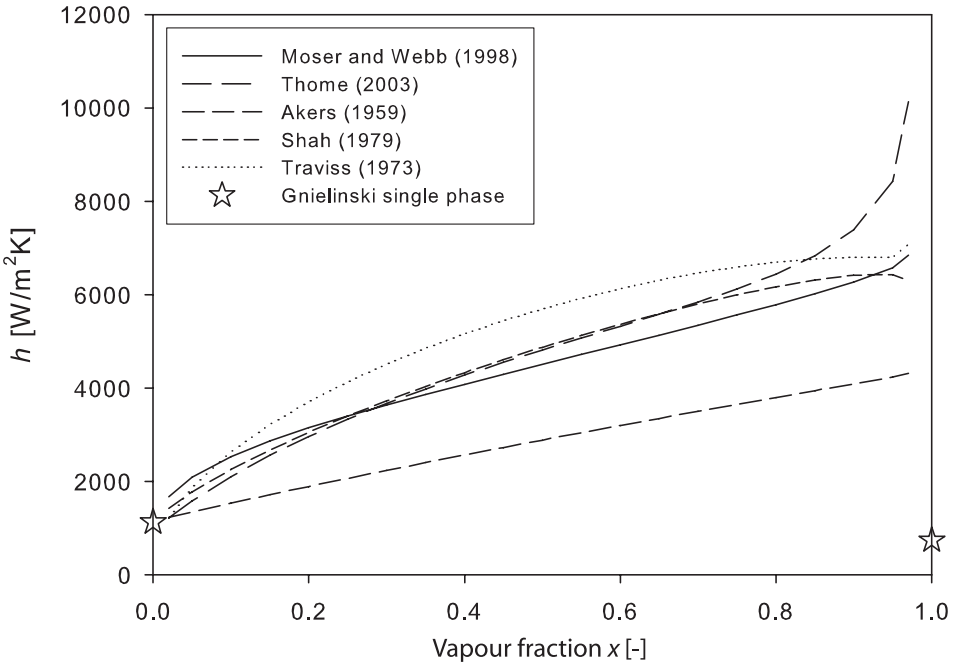

Figure 2.4: Heat transfer models for condensation of R-22. $G = 500$ kg/m^{2}s, $p = 10$ bar, $d = 10$ mm. The stars indicate the single phase values.

A comparison of the different correlations is done in Figure 2.4 for R-22, for which all correlations are reported to be valid. It is evident that the different correlation give different results. From $x \approx 0.1$, the correlations vary with a factor two where the correlation from Akers [3] deviates from the others. The trend of the correlations is roughly the same up to $x \approx 0.7$ above which the trend both is declining and increasing heat transfer coefficient.

A reliable correlation should also yield a physically reasonable overlap between single phase flow for $x \to 0$ and $x \to 1$. The heat transfer coefficient results using the Gnielinski-correlation (Equation 2.6) for liquid and vapour respectively is also shown in Figure 2.4. The trend fits well for liquid fluid flow, but not at all for gas flow.

2.3 Flow and heat transfer in minichannels

2.3.1 Heat Transfer in Single Phase in Minichannels

Morini [50] gives a review of recent work done on single phase heat transfer in microchannels. He reports that some authors have measured higher Nusselt numbers than predicted by the conventional correlation, while others have measured lower Nusselt numbers.

The work of Adams (1998)

Adams et al. [1] performed an experimental investigation of heat transfer behaviour of water in minichannels with diameter ranging from 0.76 mm to 1.09 mm. They found that the measured Nusselt number was higher than predicted by Gnielinski's correlation, and that it increased with decreasing tube diameter and increasing Reynolds-number. Including data from Yu et al. [74], they suggested a correction factor based on a threshold diameter and the Reynolds number to fit the Gnielinski-equation to their the experimental data.

Grohmann's work (2004)

Grohmann [30] measured single and two-phase argon flowing in tubes with diameters of 250 µm and 500 µm, and found higher heat transfer coefficients than predicted by the conventional correlations. He explained this increase by the larger inner surface of the tubes due to roughness and wrinkles. With this effect taken into consideration, the heat transfer coefficient followed the conventional Gnielinski correlation.

The work of Lelea (2004)

Lelea et al. [42] measured the heat transfer to laminar liquid water in stainless tubes of diameter of 0.1, 0.3 and 0.5 mm. The experimental results, including the entrance effects, followed the conventional theories (Shah and London (1978)).

Results from Agostini (2004)

Agostini et al. [2] investigated the friction factor and heat transfer for R-134a in rectangular minichannels in extruded aluminium. Hydraulic diameter was 1.17 mm and 0.77 mm. Their data for heat transfer coefficient fitted well with the Gnielinski-correlation [29].

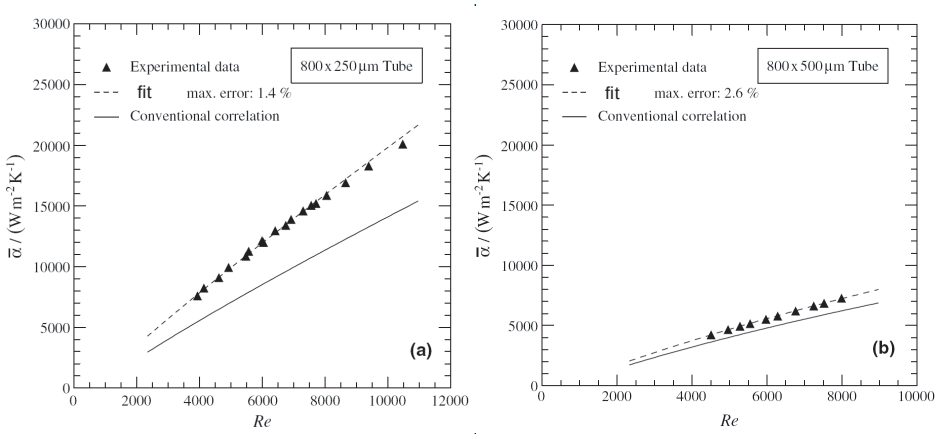

Figure 2.5: Single phase liquid heat transfer coefficient measured by Grohmann [30]. Conventional correlations is Gnielinski.

Work done by Celata (2006)

Work done by Celata [13] on steel and glass tubes with a diameter from 0.12 mm to 0.5 mm shows that in turbulent flow, the experimental Nusselt number showed no appreciable difference to the corresponding values obtained from the classical Gnielinski correlation in Equation 2.6.

Summary of Kandlikar and co-workers (2006)

Kandlikar et al. [35] summarise the latest work on heat transfer for single phase laminar flow, and state that it is expected to follow the analytical solution for conventional tubes. They explain the large scatter reported by many authors due to difficulties encountered in making accurate local heat flux and temperature measurements. The trend is an increasing Nusselt number with increasing Reynolds number also in the laminar area. Due to the relatively short length of microtubes used in experimental work, the entrance effects cannot be neglected. This effect becomes more significant at higher Reynolds number, which in parts can explain the trend of increasing Nusselt number.

Morini (2006)

Morini [51] argues that scaling effects such as thermal entry length, viscous heating and axial conduction along the tube wall may explain the discrepancies around the experimental results for microchannels.

Qi et al. (2007)

Qi et al. [58] investigated pressure drop and turbulent liquid heat transfer in four tubes with diameters ranging from 1.931 mm to 0.531 mm. They used a microscope and a surface profiler to find the surface roughness.

They found higher heat transfer coefficients than predicted by the Gnielinski-correlation, particularly for the smallest diameter. They explained this by the increased surface roughness, which was more pronounced for the smaller tubes. They then used the friction factor from Colebrook (Equation 2.41), which takes the surface roughness into account. Doing this, the experimental results fitted well with the predicted using the modified Gnielinski-correlation.

Summary

Despite different authors reporting higher heat transfer coefficients for single phase flow in small tubes, evidence point towards the conclusion that it follows the correlations for conventional tubes. Both Grohmann [30] and Qi et al. [58] explained the higher heat transfer coefficient with the effects from increased surface roughness.

The most recent scientific papers report that single phase flow heat transfer in mini- and microchannels is not fundamentally different from conventional tube single phase flow if scaling effects and measurement uncertainty is taken into account [49]. Not including scaling effects such as thermal entry length, viscous heating and axial conduction may also explain the varying results reported by some authors.

2.3.2 Two Phase Flow in Minichannels

Reviewing recent literature, it can be stated that flow regimes in tubes strongly influence the heat- and mass transfer behaviour, and any sound predictions of condensation heat transfer in minichannels should be based on analysis of flow patterns.

Several studies have been made on two-phase flow in minichannels, of which some are discussed below. Different authors have given different criteria for when flow characteristics in a mini- or microchannel occur.

One way of defining a microscale flow is where surface forces are much stronger that gravitational forces so that the tube orientation has a negligible effect on flow patterns. The ratio between surface tension forces and gravity forces increases with decreasing diameter, for which Brauner and Moalem-Maron [6] developed a criterion using the Eötwös-number:

$$\text{Eö} = \frac{(2\pi)^2 \sigma}{(\rho_\text{l} - \rho_\text{v}) d^2 g} > 1 \tag{2.14}$$

For values of Eö > 1, surface tension is more dominant that gravity forces. From this is it evident that different fluids in the same tube will result in different Eö-numbers. Therefore it can be argued that the definitions in Table 2.1 should be based on flow pattern behaviour and not on absolute diameter. From this reasoning, Kew and Cornwell [39] gives another criterion which classifies a threshold diameter d_th under which conventional laws are not suitable to predict flow boiling coefficients or flow patterns:

$$d_\text{th} = \sqrt{\frac{4\sigma}{g\,(\rho_\text{l} - \rho_\text{v})}} \tag{2.15}$$

The criteria from Brauner and Moalem-Maron, Kew and Cornwell and a criterion suggested by Triplett et al. [70] (not mentioned here) are very similar.

Coleman and Garimella (1999)

Coleman and Garimella [22] observed flow patterns in tubes with diameter from 1.3 to 5.50 mm, using air-water at adiabatic conditions. They used both circular and square minichannels, and found that the hydraulic diameter had a substantial effect on flow patterns and transitions, while the tube shape (circular or rectangular) was of secondary importance.

They observed four major flow regimes; annular, wavy annular (gravity-influenced annular flow and with waves), intermittent (slug, plug) and dispersed (bubble). Stratified smooth flow was not observed for any of the tubes tested.

Garimella (2002)

Garimella et al. [28] investigated pressure drop for intermittent flow of R-134a in circular tubes with diameters from 0.5 mm to 4.91 mm. They also gave a criteria for the transition from intermittent to annular flow,

$$x = \frac{a}{G + b} \tag{2.16}$$

where

$$a = 69.5673 + 22.595 \cdot e^{0.2586 \cdot d_\text{h}} \tag{2.17}$$

$$b = -59.9899 + 176.8137 \cdot e^{0.3826 \cdot d_\text{h}} \tag{2.18}$$

The work of Niño (2002)

Niño [55] recognized the difficulty of determining the flow pattern by introducing a probabilistic flow map based on the likelihood of the occurrence of four flow patterns. He used experimental results for R-134a, R-410A and air-water. For each vapour fraction and mass flux, he developed likelihood functions for the occurrence of these flow patterns:

- Liquid only flow
- Intermittent flow, shifting flow condition for low x which is not annular
- Annular flow
- Vapour only flow

In this way, the transition between the main flow patterns is continuous, and pure liquid and vapour flow represent the end conditions with probability equal to 1 for vapour fraction $x = 0$ and $x = 1$ respectively.

The work of Pettersen (2002)

Pettersen [56] investigated flow patterns, flow boiling heat transfer and pressure drop of CO_2 in horizontal minichannels with diameter $d = 0.81$ mm. He found that two-phase flow regimes could not be predicted using existing models and generalized flow charts. The observed patterns were dominated by intermittent and annular flow. Stratified flow was not observed.

The work of Kim (2003)

Annular, slug and bubbly flow was observed by Kim et al. [40] during condensation of R-134a at 40 °C in a horizontal, circular tube of diameter 0.75 mm. Mass flux ranged between $100 < G < 600$ kg/m^{2}s and stratified flow did not occur for any of the flow conditions. Transition from slug to annular flow occurred between $x = 0.3$ and 0.4 at $G = 100$ kg/m^{2}s and at $x = 0.1$ at $G = 600$ kg/m^{2}s.

Yun and Kim (2004)

Yun and Kim [75] suggested a criterion for the transition between intermittent (or slug) flow and annular flow in narrow channels for CO_2:

$$We_{\mathrm{gs}} = \frac{\rho_{\mathrm{v}} j_{\mathrm{v}}^2 d_{\mathrm{h}}}{\sigma} \approx 20 \tag{2.19}$$

where

$$j_v = \frac{Gx}{\rho_v} \tag{2.20}$$

Revellin's work (2007)

Revellin and Thome [59] and [60] studied two-phase flow patterns for R-134a and R-245fa in 0.51 mm and 0.79 mm horizontal glass tubes at saturation temperatures between 26 °C and 35 °C. Four flow patterns were detected:

- Bubbly flow, at low vapour fraction and mass flux. The bubbles are much smaller than the tube diameter.
- Slug flow, where bigger bubbles with diameter near the tube diameter and length from one tube diameter up to many tube diameters. They are separated by liquid slugs.
- Semi-annular flow, which is a mixtures of churning slugs breaking down and annular flow.
- Annular flow, where there is a liquid film at the tube wall and a vapour core with a higher velocity. The liquid surface can be wavy or smooth.

The flow patterns can be seen for R-245fa in Figure 2.6 and in the flow map of R-134a in Figure 2.7. The two-phase flow pattern transitions observed for R-134a did not agree well with a conventional tube flow map (Kattan et al. [37]) for refrigerants nor with a microscale map for air-water flow (Triplett et al. [70]). However, the criterion given in Equation 2.16 by Garimella et al. [28] give a good indication for R-134a.

He also stated that even though there is no stratified flow at these diameters, buoyancy is noticeable at diameters larger than 0.5 mm. For elongated bubble flow (e.g. Figure 2.6c) in larger tubes, the liquid layer below the bubble is thicker than above the bubble.

Revellin and Thome also developed objective criteria for the transition between the different flow patterns, based on an optical measurement method and parameters like the bubble frequency, bubble length and percentage of surviving small bubbles.

Cheng's work on CO_2

Cheng et al. [16] worked on CO_2 flow in horizontal channels where 0.8 mm $< d <$ 10 mm and used the following criterion between intermittent and

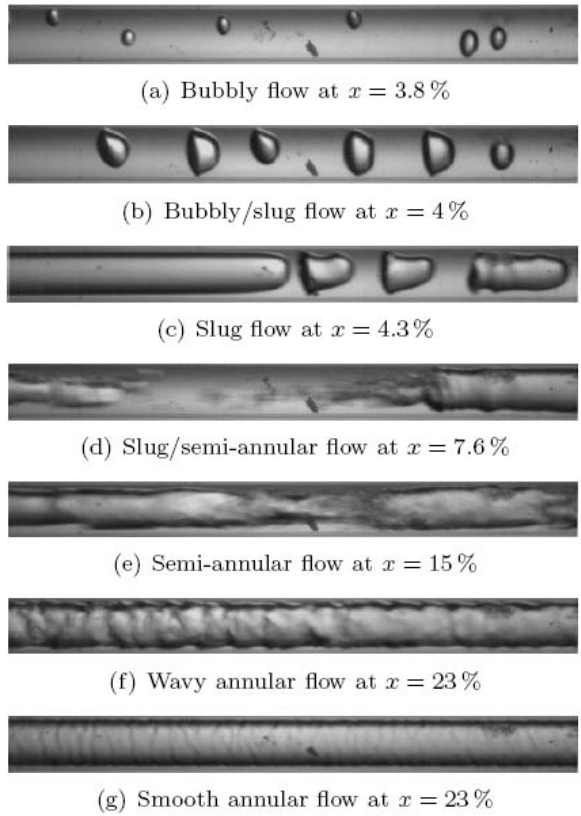

(a) Bubbly flow at $x = 3.8\,\%$

(b) Bubbly/slug flow at $x = 4\,\%$

(c) Slug flow at $x = 4.3\,\%$

(d) Slug/semi-annular flow at $x = 7.6\,\%$

(e) Semi-annular flow at $x = 15\,\%$

(f) Wavy annular flow at $x = 23\,\%$

(g) Smooth annular flow at $x = 23\,\%$

Figure 2.6: The four flow patterns found by Revellin et al. [59] for R-245fa include a,c,e and f/g, while transition flows include b and d. In this case, $G = 500$ kg/m^{2}s, $T_{\text{sat}} = 35\,^{\circ}$C and $d = 0.509$ mm.

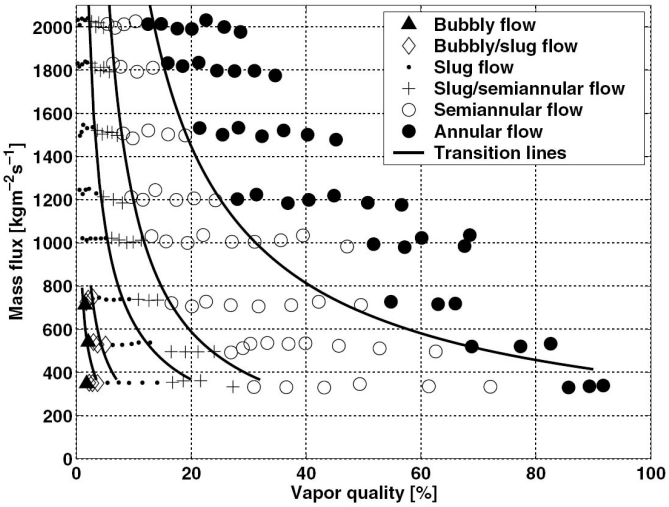

Figure 2.7: Flowmap for R-134a taken from Revellin and Thome [60]. $d = 0.5$ mm, $T_{\text{sat}} = 35\,^{\circ}\text{C}$.

annular flow:

$$x_{\text{IA}} = \left[1.8^{1/0.875}\left(\frac{\rho_{\text{v}}}{\rho_{\text{l}}}\right)^{1/1.75}\left(\frac{\mu_{\text{l}}}{\mu_{\text{v}}}\right)^{-1/7} + 1\right]^{-1} \tag{2.21}$$

where a flow where $x > x_{\text{IA}}$ is in the annular regime. This criteria is independent of mass flux and will appear as a vertical line in a diagram like in Figure 2.7. It is developed for CO_2 so its application for other fluids should be done with care.

Flow patterns for methane

A brief comparison of dimensionless numbers relevant for flow maps is given in Table 2.2. The fluids shown are popular refrigerants and the fluids used in this work. See Table 6.1 for an explanation of the fluid names.

Methane is characterised by lower viscosity and lower density than the other refrigerants mentioned. This makes the We, Re and partly the We_{gs}-number for the methane-based fluids much higher than for the other fluids. For Methane-100, the We_{gs}-number increases for increasing pressure while it decreases for Ethane-10 and Ethane-27. This could also have to do with the shift in equilibrium concentration. This criterion suggests that for Methane-100, annular flow is the dominant flow regime.

In contrast to the We_{gs}-number, the values of x_{IA} do not indicate that there is a large difference between the fluids. The criterion also indicates

				G [kg/m^{2}s]		280	490		
Fluid	p_{crit}	p_{r}	T_{sat}	x_{IA}	Eö	We_{gs}	We_{gs}	We	Re_{lo}
R-134a	40.6	0.2	32	0.10	25.3	11	34	845	2738
		0.5	68	0.16	12.6	10	31	778	4469
R-245fa	36.5	0.2	77	0.10	26.5	10	32	788	2247
		0.5	117	0.16	13.0	10	30	738	3775
CO_2	73.8	0.2	-29	0.10	41.2	8	24	592	3032
		0.5	-2	0.16	20.6	7	22	555	5123
Methane-100*	46.0	0.2	-126	0.10	65.4	39	118	2934	8333
		0.5	-104	0.16	31.2	39	118	2952	12657
		0.9	-86	0.25	5.7	167	511	12763	19873
Ethane-10*	57.3	0.1	-133	0.07	166.1	23	71	1775	5502
		0.5	-92	0.17	124.6	8	23	583	11279
		0.8	-75	0.23	96.9	8	23	578	15716
Ethane-27*	65.7	0.1	-125	0.07	121.5	28	86	2140	4326
		0.5	-76	0.17	74.8	11	33	820	9096
		0.7	-61	0.21	60.8	11	33	818	11681
Nitrogen-10*	48.1	0.2	-132	0.11	62.4	29	91	2254	7696
		0.5	-110	0.17	30.4	31	93	2344	11875
		0.8	-96	0.23	11.8	63	193	4829	16627

Table 2.2: Different properties for refrigerants at different pressure. d = 1 mm and x = 0.2. *Compositions listed in Table 6.1 and calculated at equilibrium. T_{sat} in Celsius and pressure in bara.

that intermittent flow is more dominant at higher pressure. This makes sense as the vapour density increases for higher pressure, reducing the vapour velocity and shear required to sustain an annular flow.

According to Brauner and Moalem-Maron [6], an Eötwös number larger than unity states that the surface tension forces dominate over the gravitational forces. This is indeed true for the methane fluids. Strong surface forces suggests that higher vapour velocity and hence a higher mass flux is required for entrainment to occur.

Another criterion for annular flow is presented by Cavallini et al. in Equation 2.25. All the flow situations for the methane-based fluids in Table 2.2 are in the annular regime according to this criterion. For $p_{\text{r}} = 0.5$ for R-134a, R-245fa and CO_2, the superficial gas velocity is below 2.5.

The thermophysical properties vary greatly for the methane fluids. Also, the flow pattern criteria are party contradictory, although annular flow seems to be more dominant for the methane-based fluids than for the other

fluids in Table 2.2. Flow observations are necessary to develop a flow map for methane.

Summary

Flow maps of R-134a (reported by Cavalini et al. [11] and Revellin and Thome [60]) and R-245fa (Revellin [60]) are available in the literature. Stratified flow is essentially absent in small channels. This has been shown by e.g. Triplett et al. [70], Pettersen [56] and Revellin and Thome [60].

In a review article, Thome [67] states that bubbly, elongated bubble (also called intermittent or slug flow), annular and mist flows and flows with partial dry out are sufficient to capture most of the physics involved in two-phase flow in microscale. Criteria have been suggested for the transition between the different flow regimes.

2.3.3 Condensation in two-phase flow in minichannels

Yang and Webb (1996)

Yang and Webb [73] measured heat transfer in single- and two-phase flow of R-12 at 65 °C in rectangular plain and microfin tubes with $d_h = 2.64$ mm and 1.56 mm respectively. The mass flux varied from 400-1400 kg/m^2s, vapour fraction from 0.12 to 0.97 and heat flux from 4-12 kW/m^2. The experiments were carried out using a flat, extruded aluminium tube with four flow channels.

For single phase liquid, they observed good agreement with the Petukhov-correlation for both geometries. For condensation they observed improved heat transfer with increasing mass flux and vapour fraction for both tubes. The measurements were compared to the correlations from both Shah [62] and Akers [3], and matched the Akers-correlation well at low mass flux. At higher mass flux, Akers' correlation over predicts the data by 10-20%.

They also observed improved heat transfer coefficient with increasing heat flux in the order of $h \propto q''^{0.2}$, and commented that similar dependency also was observed by Akers [3] and other authors. They explained this by the momentum contribution analysed by Soliman et al. [65].

Wang's work (2002)

Wang et al. [71] developed heat transfer correlation for condensation in rectangular minitubes based on experiments on R-134a in a multiport aluminium condenser with 1.46 mm hydraulic diameter. The correlation for annular flow predicts 72.5% of their experimental values within ±10 %,

while similar accuracy was achieved by another correlation for stratified flow. They used the Froude number as a criterion to determine the flow type. However, the developed correlation does not fit well with experimental data from other authors.

The work by Shin and Kim (2005)

Shin and Kim [63] measured condensation of R-134a in circular and rectangular tubes with hydraulic diameters ranging from 0.49 mm to 0.97 mm. They investigated the effects of heat flux, vapour fraction, mass flux, diameter and channel geometry on the Nusselt number.

In their work, Shin and Kim refers to the Nusselt number for two phase flow heat transfer. This is unusual as the conductivity is not the same in the vapour and liquid phase. It appears that they have applied Equation 2.2 with the conductivity for the liquid phase when calculating the Nusselt number from the measured heat transfer coefficient.

They found that the Nusselt number was independent of heat flux, and that the heat transfer improved with increasing vapour fraction and increasing mass flux. The Nusselt number for the circular channels showed a higher sensitivity to increased mass flux compared to the rectangular channels. This can be seen in Figure 2.8.

The Nusselt number clearly increased with smaller diameters. The experimental data fit well with many conventional channel correlations at high mass flux, but bad at mass flux below 200 kg/m^{2}s.

Bandhauer and co-workers (2005)

Bandhauer et al. [4] noted that the flow pattern in a large majority of their observations were overlaps between annular flow and the two other flow types observed, i.e. mist flow and intermittent. Therefore, they developed their new model for heat transfer based on annular flow. The fluid was R-134a which was measured in three circular tube of diameter $0.5 < d_{\mathrm{h}} < 1.5$ mm over mass flux range $150 < G < 750$ kg/m^{2}s.

They compared their measurements with the predictions from the different types of correlations mentioned in Chapter 2.2.2, and decided to develop their correlation based on a shear-driven model similar to the model by Traviss et al. [69] and Moser et al. [52]. However, these authors' correlations does not predict Bandhauer et al.'s data very well. Based on work by Garimella et al. [27], Bandhauer et al. explained these deviations by stating that the pressure drop model used by Traviss et al. [69] and Moser et al. [52] are not applicable to minichannels. Instead, they developed their

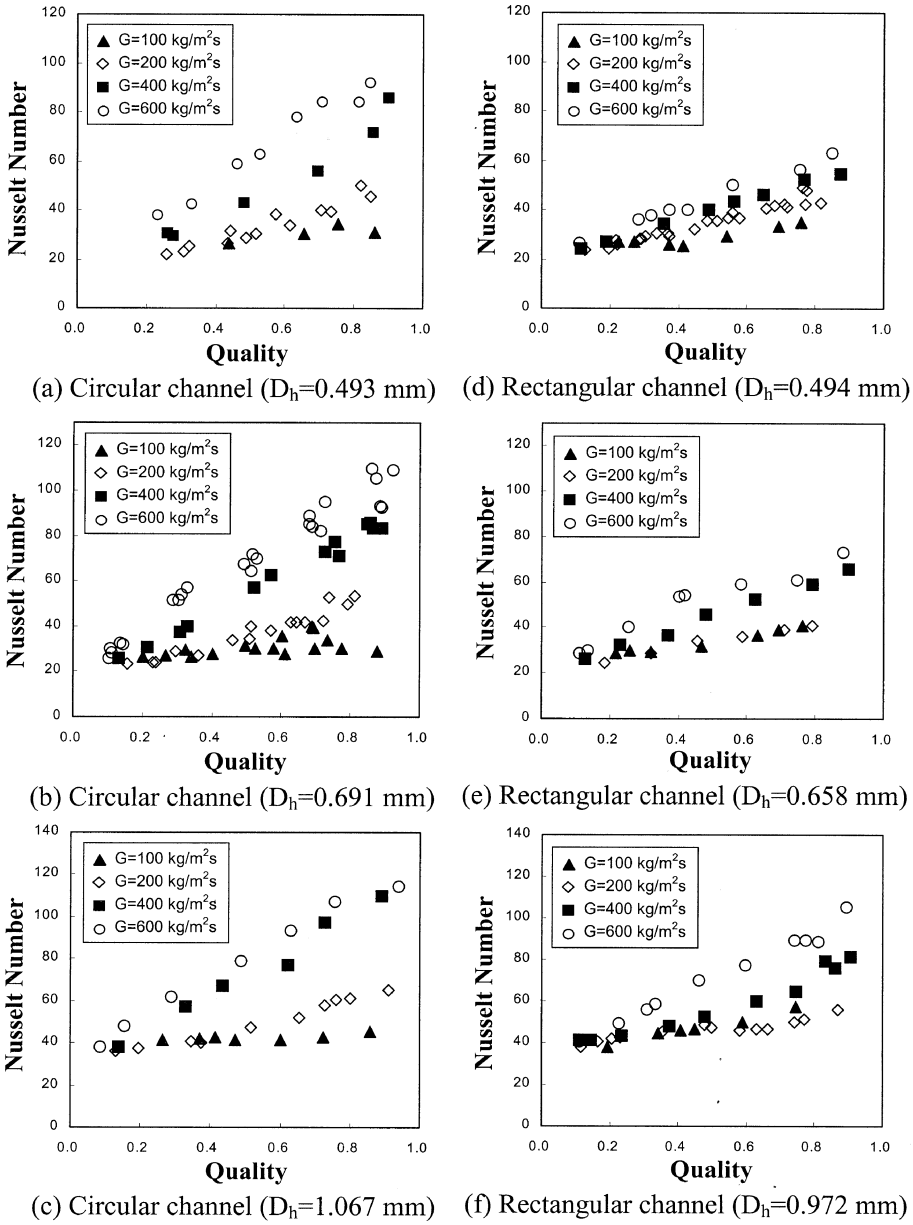

Figure 2.8: Nusselt number for condensation of R-134a as a function of mass flux, vapour fraction, hydraulic diameter and tube geometry as found by Shin and Kim [63]

model based on pressure drop model from Garimella et al. [27] (Presented in Chapter B.3.2).

$$h = \frac{q''}{T_{\mathrm{sat}} - T_{\mathrm{w}}} = \frac{\rho_{\mathrm{l}} c_{\mathrm{p,l}} u^*}{T^+} \tag{2.22}$$

where for $Re_{\mathrm{l}} < 2100$:

$$T^+ = 5Pr_{\mathrm{l}} + 5ln\left[Pr_{\mathrm{l}}\left(\frac{\delta^+}{5} - 1\right) + 1\right] \tag{2.23}$$

and for $Re_{\mathrm{l}} > 2100$:

$$T^+ = 5Pr_{\mathrm{l}} + 5ln\left(5Pr_{\mathrm{l}} + 1\right) + \int_{30}^{\delta^+} \frac{dy^+}{\left(\frac{1}{Pr_{\mathrm{l}}} - 1\right) + \frac{y^+}{5}\left(1 - \frac{y^+}{R^+}\right)} \tag{2.24}$$

u^* is a friction velocity given by $\sqrt{\tau_{\mathrm{i}}/\rho_{\mathrm{l}}}$. The model predicts 86% of the results within ±20%. This model is similar to the model used by Cavallini [10].

Work done by Cavallini and co-workers (2005/2006)

From the work from Wang et al. [71] and Pettersen [56] for R-134a and CO_2 respectively, Cavallini argued that annular flow always occurs for dimensionless gas velocity $J_{\mathrm{v}} > 2.5$, where J_{v} is defined by Equation 2.25:

$$J_{\mathrm{v}} = \frac{x \cdot G}{\left[g d_{\mathrm{h}} \rho_{\mathrm{v}} (\rho_{\mathrm{l}} - \rho_{\mathrm{v}})\right]^{0.5}} \tag{2.25}$$

Cavallini et al. [10] and [11] developed a model for condensation in minichannels, based on the theoretical work by Kosky and Staub [41]. For annular flow, the heat transfer coefficient is related to the frictional pressure drop at the liquid/vapour interface. The method can be divided into three parts:

1. Find the entrainment factor, i.e. an expression for the extent of entrainment of liquid by the annular gas core.

2. Find the frictional pressure gradient

3. Apply the Kosty and Staub-model [41] for heat transfer coefficient with the entrainment and frictional pressure drop gradient.

The entrainment factor E is found by Equation 2.26 which fits well with observations of R-113 and air/water flow in conventional channels:

$$E = 0.015 + 0.44\mathrm{Log}\left[\frac{\rho_{\mathrm{gc}}}{\rho_{\mathrm{l}}}\frac{\mu_{\mathrm{l}}\dot{j}_{\mathrm{v}}}{\sigma}10^4\right] \tag{2.26}$$

and

$$\rho_{\mathrm{gc}} = \rho_g\left(1 + (1-x)\,E/x\right) \tag{2.27}$$

The friction pressure gradient $(\mathrm{d}p/\mathrm{d}z)_f$ is taken by a correlation previously developed by Cavallini presented on page 203. If available, frictional pressure drop measurements could be used instead.

Finally, the entrainment factor E and the pressure drop gradient $(\mathrm{d}p/\mathrm{d}z)_{\mathrm{f}}$ are inserted into the following equations for the heat transfer coefficient:

$$h = h_{\mathrm{an}} = \frac{\rho_{\mathrm{l}} c_{\mathrm{p,l}}(\tau/\rho_{\mathrm{l}})^{0.5}}{T^+} \tag{2.28}$$

where

$$\tau = (\frac{\mathrm{d}p}{\mathrm{d}z})_{\mathrm{f}}\frac{d_{\mathrm{h}}}{4} \tag{2.29}$$

and T^+ is a dimensionless temperature containing the Pr and Re-number and is found in the paper from Cavallini et al. [10].

Summary

It is clear that there is no reliable general model for the prediction of condensation heat transfer coefficients in mini- and microchannels.

Some authors (Yang and Webb [73] and Shin and Kim [63]) observed a weak dependence between heat flux and condensation heat transfer, in the order of $h \propto q''^{0.2}$. This contradicts the understanding of condensation in conventional channels, which is heat flux independent. This would mean that condensation is phenomenological different in microscale. Other authors have found that the heat transfer coefficient is independent from heat flux also in microscale.

The model from Bandhauer [4] is based on R-134a only and should therefore be used with care for other fluids. Due to the small scale of experimental set-ups, getting reliable measurements within acceptable error margin seems to be challenging.

2.4 Heat transfer in binary mixtures

Intuitively, single phase heat transfer for binary mixtures should not be physically different from single component heat transfer as long as the physical properties are evaluated at the mixture composition.

2.4.1 Phase change behaviour of binary mixtures

The condensation behaviour of mixtures is more complex than single component condensation. The condensation can take place at gliding temperature and mass transfer effects can be involved.

Mixtures containing two components are called binary mixtures, while mixtures with more than two components are called multi component mixtures. A component A, which in pure form has a lower saturation temperature than a pure component B at the same pressure, is said to be more volatile than component B.

A mixture is called zeotropic if the concentration in the liquid and the vapour phase are never equal at the same temperature. This means that the mixture has different boiling and condensation temperatures at any concentration.

A diagram showing the equilibrium state of a binary mixture of methane and ethane is shown in Figure 2.9. Methane is here the most volatile component with lowest saturation temperature. The dew point and bubble point temperatures for pure methane and pure ethane are the end points on the curves. As the pure substance saturation temperature changes with pressure, so does the shape and size of the two phase area. The temperature glide is reduced when the pressure is increased.

2.4.2 In-tube condensation principles of binary mixtures

In a condensing flow of a binary mixture, the less volatile component is more disposed to condense on the liquid film than the more volatile component. This leads to an enrichment of the more volatile component in the vapour at the liquid/vapour interface, which lowers the dew point temperature at the interface. The concentration difference leads to transport of the least volatile component from the vapour bulk to the interface. Mass transfer also occurs back from the liquid film. A concentration profile appears from the vapour core to the liquid/vapour interface. The mixing due to turbulence and diffusion in the vapour phase, along with the rate of condensation, determines the shape of these profiles as well as the saturation temperature

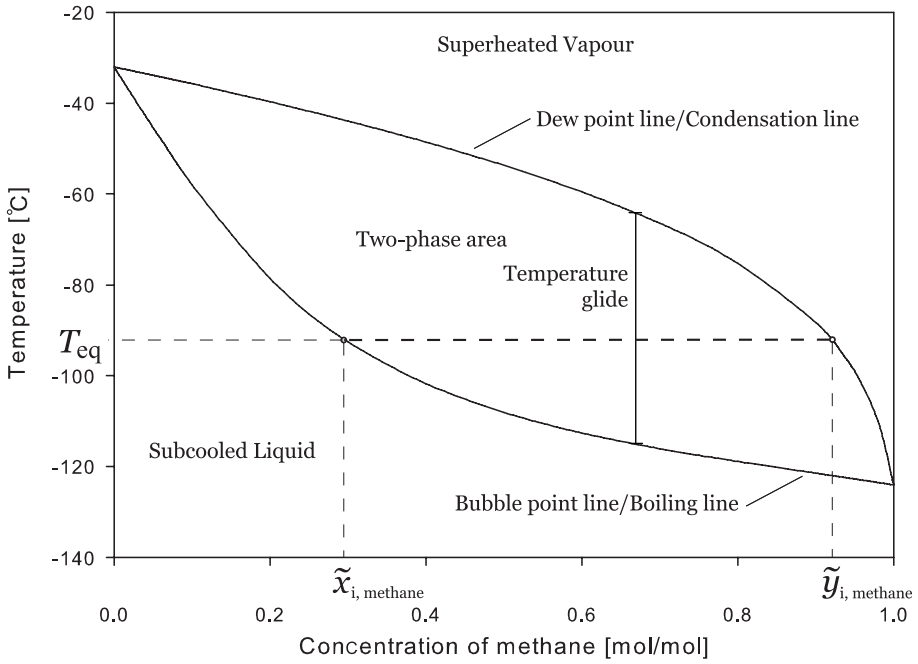

Figure 2.9: Equilibrium phase diagram for methane and ethane at 10 bar.

at the interface. An example of such a temperature profile is shown in Figure 2.10.

As argued in Equation 2.1, the driving force in heat transfer is the temperature difference $T_{\mathrm{v,bulk}} - T_{\mathrm{w}}$. The heat from the condensation process is lead through the liquid film by convection and conduction. For single component condensation, $T_{\mathrm{sat}} = T_{\mathrm{v,bulk}}$ and the resistance is limited to the liquid film. The transferred heat in single component condensation can be expressed as the driving potential divided on the resistance:

$$q''_{\mathrm{sc}} = \frac{T_{\mathrm{v,bulk}} - T_{\mathrm{w}}}{R} = \frac{T_{\mathrm{sat}} - T_{\mathrm{w}}}{R_{\mathrm{l}}} \tag{2.30}$$

where the resistance R is the inverse of the heat transfer coefficient.

For binary or multi component condensation, the temperature at the liquid/vapour interface T_{i} is usually lower than $T_{\mathrm{v,bulk}}$ due to the enrichment of the more volatile component at the interface. T_{i} is determined by the composition at the interface. If T_{i} is known, the heat transfer coefficient can be calculated as for single component condensation; then, $T_{\mathrm{sat}} = T_{\mathrm{i}}$ and the fluid properties of the liquid film is used to calculate R_{l}.

However, the composition at the interface and hence T_{i} can be difficult

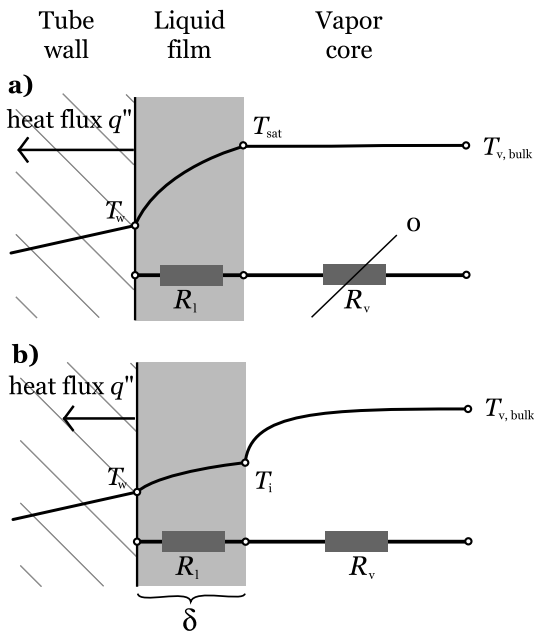

Figure 2.10: Principles of a) pure component condensation and b) mixure condensation.

to determine as diffusion and mixing effects influence on the interface concentration. Alternatively, the mass transfer effects in the vapour phase can be expressed as a resistance R_v. This depends on the difference between $T_\mathrm{v,bulk}$ and T_i, i.e. on the heat flux q'' itself. The advantage of this approach is that T_i is not required. These two approaches are expressed in Equation 2.31 and illustrated in Figure 2.10.

$$q''_\mathrm{mc} = \frac{T_\mathrm{v,bulk} - T_\mathrm{w}}{R} = \frac{T_\mathrm{i} - T_\mathrm{w}}{R_\mathrm{l}} = \frac{T_\mathrm{v,bulk} - T_\mathrm{w}}{R_\mathrm{l} + R_\mathrm{v}} \tag{2.31}$$

Assuming that both components are condensable, the influence of the heat flux q'' can be explained by defining two extreme situations:

Condensation at equilibrium occurs when $q'' \to 0$, which means that the condensation mass flux $\dot{n} \to 0$. It means that there are no concentration gradients in the phases and the temperature in the vapour is the same as in the liquid film. The concentrations of the vapour and liquid phases can be read out directly from diagrams like in Figure 2.9 as $T_\mathrm{v,bulk} = T_\mathrm{i} = T_\mathrm{w}$.

Total condensation can be assumed for very high heat fluxes $q'' \to \infty$

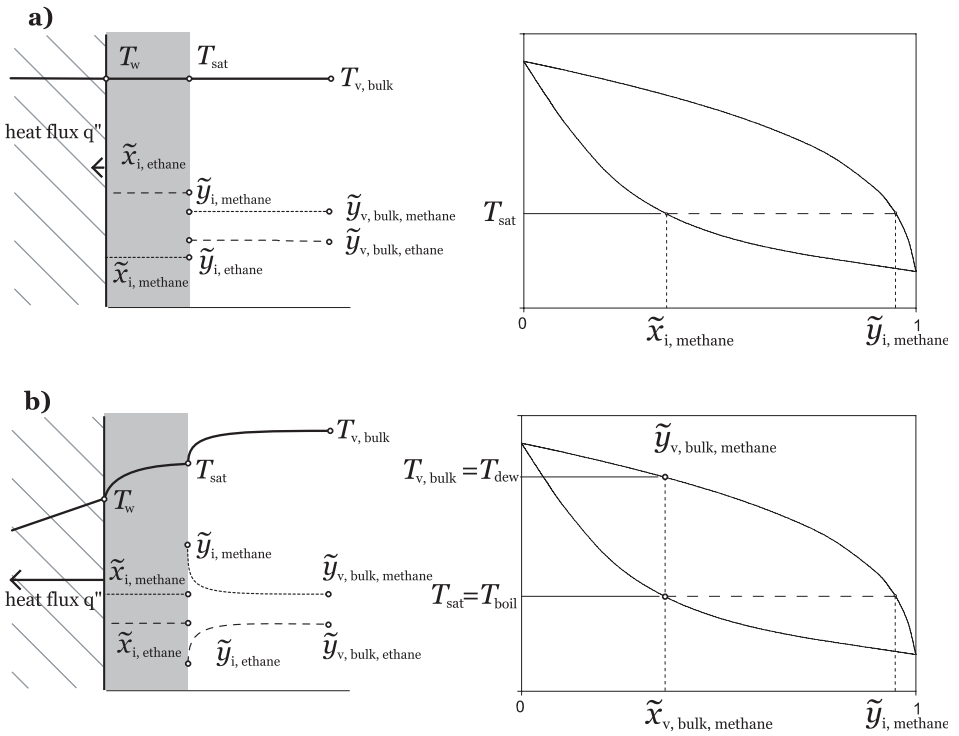

Figure 2.11: Condensation in equilibrium and total condensation

which means that $\dot{n} \to \infty$. The vapour condenses like a single component vapour, i.e. the temperature at the liquid/vapour interface has dropped to the boiling temperature and the most volatile component condenses just as the least volatile component. For this reason, the bulk concentration in the vapour phase equals the liquid concentration.

These two cases are illustrated in Figure 2.11 a) and b). In a real condensation process, obviously $0 < q'' < \infty$ and the situation lies somewhere case a) and b).

Regardless of the assumption, one of the effects occurring when condensing multi component vapour is that the average temperature will decrease with decreasing vapour fraction. This means that also sensible heat must be removed from both vapour and liquid during the condensation process. Although the sensible heat generally is small compared to the latent heat, the cooling of the vapour represents a resistance as the heat transfer coefficient between the vapour phase and the liquid/vapour interface is low.

2.4.3 Intube condensation models of binary mixtures

Two types of heat transfer models exists for condensation of multi component fluids. The Silver [64], Bell and Ghaly [5] model approach assumes condensation in equilibrium; it assumes that the liquid layer resistance is as for pure component condensation, but it adds a single phase heat transfer resistance for the gas phase. This is based on the cooling of the vapour from inlet bulk temperature to the interface temperature. The mass transfer resistance during condensation they argued, is proportional to the heat transfer resistance in the vapour phase. This model is based on heat transfer resistance alone.

The other type of model is referred to as the Colburn and Drew [19] model. They introduced a one-dimension transport model taking the concentration gradient close to the vapour/liquid interface into account. The latter is a more physically realistic model, but a lot more complex as it takes mass transfer effects into account. Then, the diffusion coefficients between each component are needed. Particularly for multi component mixtures, this approach therefore becomes very complex. It is however particularly useful when not all of the gases in the mixture are condensable.

Equilibrium approach model from Del Col et al. (2005)

Del Col et al. [23] developed a heat transfer coefficient correlation for zeotropic mixtures in tubes based on the Silver-Bell-Ghaly approach. A derivation of the basis for this approach is found in Chapter B.2 in the Appendix. From there, Equation B.2.5 can be written as

$$h_{\mathrm{mc}} = \frac{1}{1/h_{\mathrm{sc}} + R_{\mathrm{mc}}} \tag{2.32}$$

where R_{mc} reflects the necessary cooling of the multi component vapour. The single component condensation model h_{sc} is taken from Thome, El Hajal and Cavallini [68] described in Chapter 2.2.3 using physical properties for the mixture and assuming equilibrium between the phases.

The ratio $q''_{\mathrm{v}}/q''_{\mathrm{mc}}$ from Equation B.2.5 is approximated by the ratio $xc_{\mathrm{p,v}}(\mathrm{d}T/\mathrm{d}e)$, which is further approximated by $xc_{\mathrm{p,v}}(\Delta T_{\mathrm{gl}}/\Delta e_{\mathrm{m}})$. Here, $T_{\mathrm{gl}}/\Delta e_{\mathrm{m}}$ is the temperature glide of the mixture divided on the heat of evaporation at the given pressure. This is valid if the slope $\mathrm{d}T/\mathrm{d}e$ remains constant for $0 < x < 1$ (such a curve can be found in Figure 5.50).

$$R_{\mathrm{mc}} = xc_{\mathrm{p,v}} \frac{\Delta T_{\mathrm{gl}}}{\Delta e_{\mathrm{m}}} \frac{1}{h_{\mathrm{conv,v}}} \tag{2.33}$$

The sensible heat from the vapour core is transferred into the liquid film by single phase forced convection which can be expressed by the Dittus-Boelter-equation:

$$h_{\mathrm{conv,v}} = 0.023 Re_{\mathrm{v}}^{0.8} Pr_{\mathrm{v}}^{0.33} \frac{k_{\mathrm{v}}}{d} f_{\mathrm{i}} \tag{2.34}$$

The Reynolds number for the vapour phase Re_{v} is calculated using vapour phase properties. The vapour velocity u_{v} is calculated from Equation B.1.8:

$$Re_{\mathrm{v}} = \frac{\rho_{\mathrm{v}} u_{\mathrm{v}} d}{\mu_{\mathrm{v}}} \tag{2.35}$$

The concentration of the liquid and vapour phase is assumed to be at equilibrium, which means that their concentrations $\tilde{x}$ and $\tilde{y}$ respectively can be found from an equilibrium diagram as in Figure 2.9. The equilibrium temperature is assumed to the be average bulk vapour temperature. As in the pure fluid model, the parameter f_{i} takes into account the increased surface area due to film surface roughness and is found in Equation B.1.7.

Del Col et al. [23] found good agreement between the experimental data and their model. Notice in Equation 2.34 that the diameter is used as the distance the heat must be transferred across. A more physically correct distance would be $d-2\delta$. This was noted by Neeraas [54] who used a similar approach and included a modification factor from Sardesai et al. [61] to fit his experimental data. Also Neeraas found good agreement between his experimental data and the model approach by Silver-Bell-Ghaly. Both the work from Del Col et al. and Neeraas were done in conventional channels.

2.5 Frictional Pressure drop models

The frictional pressure drop reflects the shear tension at the interface between tube wall and the fluid flow. When working with frictional pressure drop, it is often convenient to work with the Moody or Darcy friction factor f, which is a dimensionless parameter defined as

$$f \equiv \frac{-\left(\mathrm{d}p/\mathrm{d}z\right)_{\mathrm{f}} \cdot d \cdot 2}{\rho u_m^2} = \frac{-\left(\mathrm{d}p/\mathrm{d}z\right)_{\mathrm{f}} \cdot d \cdot 2 \cdot \rho}{G^2} \tag{2.36}$$

The frictional pressure drop can then be written as:

$$-\left(\frac{\mathrm{d}p}{\mathrm{d}z}\right)_{\mathrm{f}} = f \frac{\rho u_{\mathrm{m}}^2}{d \cdot 2} = f \frac{G^2}{d \cdot 2 \cdot \rho} \tag{2.37}$$

The friction factor is generally more decisive for the pressure drop than for the heat transfer. This can be seen when comparing Equation 2.6 and 2.37; the pressure drop is proportional to the friction factor while it is partially cancelled out in the denominator for the heat transfer expression.

2.5.1 Single Phase flow

For single phase laminar flow, it can be shown that

$$f = \frac{64}{Re} \tag{2.38}$$

For turbulent single phase flow, no analytic solution is available and one must rely on empirically developed friction factors. For a smooth tube, there are many friction factor correlations available. Incopera and DeWitt [33] gives the following friction factors:

$$f = 0.316Re^{-0.25} \qquad \text{for } Re < 20000 \tag{2.39}$$

and

$$f = 0.184Re^{-0.2} \qquad \text{for } Re > 20000 \tag{2.40}$$

For rough tubes, the friction factor will increase with increased roughness and can be found in e.g. a Moody-diagram [33]. The Colebrook-equation [20] can also be used to find the friction factor:

$$\frac{1}{\sqrt{f}} = -2.0 \ \mathrm{Log}_{10}\left(\frac{\epsilon/d}{3.7} + \frac{2.51}{Re\sqrt{f}}\right) \tag{2.41}$$

Here, ϵ/d is called the relative roughness and it is a ratio of the average roughness height divided on the diameter. For the transition between laminar and turbulent flow ($2300 < Re < 10000$), there exists a transition regime where the friction factor leaves the laminar characteristics and align to the turbulent characteristics at a higher Reynolds-number. The prediction of the behaviour in this regime is difficult.

A wide range of publications verify single phase pressure drop and its relationship to the relative roughness in conventional tubes. Two publications on pressure drop in mini- and microchannels:

The work of Judy (2002)

Judy et al. [34] investigated frictional pressure drop for liquid laminar flow in microchannels with diameter 15-150 µm. They used water, methanol and isopropanol and the Reynolds number ranged from 8-2300. Distinguishable deviation from Equation 2.38 was not observed for any channel cross-section, diameter, material or fluid explored.

Work from Qi et al. (2007)

Qi et al. [58] investigated pressure drop and heat transfer for liquid nitrogen in four channels with diameter ranging from 0.531 mm to 1.931 mm and Reynolds numbers from 10 000 - 90 000. They measured the surface roughness by using a surface profiler. The Colebrook-correlation could capture the effect of the surface roughness well for all but the 0.531 mm tube. They concluded that roughness effect on this small scale is not completely understood.

2.5.2 Two-phase flow

As for heat transfer, two-phase flow pressure drop models can comprise of a two-phase multiplier multiplied with a equivalent single phase pressure drop expression on the form

$$\left(\frac{\mathrm{d}p}{\mathrm{d}z}\right)_{\mathrm{f,2ph}} = \Phi^2 \left(\frac{\mathrm{d}p}{\mathrm{d}z}\right)_{\mathrm{f,1ph}} \tag{2.42}$$

The two-phase flow multiplier is often based on vapour fraction x, void fraction ε, density and viscosity ratios of liquid and vapour, and it usually includes some parameters found by regression of experimental data. It is often written squared, without that having any physical meaning.

Classic pressure drop correlations for conventional tubes include the work by Lockhart and Martinelli in 1949 [44], Chisholm [18] from 1973 and Friedel's work from 1979/1980 [26]. Pressure drop models used in this thesis is found in Appendix B.3 and presented in Figure 2.12 for a given flow situation. Unlike the condensation models shown in Figure 2.4, all the pressure drop models converge to the single phase values. This is because they are based on two phase flow multipliers which encompass also the cases where $x = 0$ and $x = 1$. Some of the multipliers are multiplied with the vapour-only pressure drop while others with the liquid-only pressure drop.

The models from Cavallini et al. [11], Müller-Steinhagen and Heck [53] and Friedel [25] show roughly the same trend. The model from Cavallini et al. [11] is based on minichannels measurements, as are the models from Niño [55] and Garimella et al. [27]. The two latter show a different behaviour.

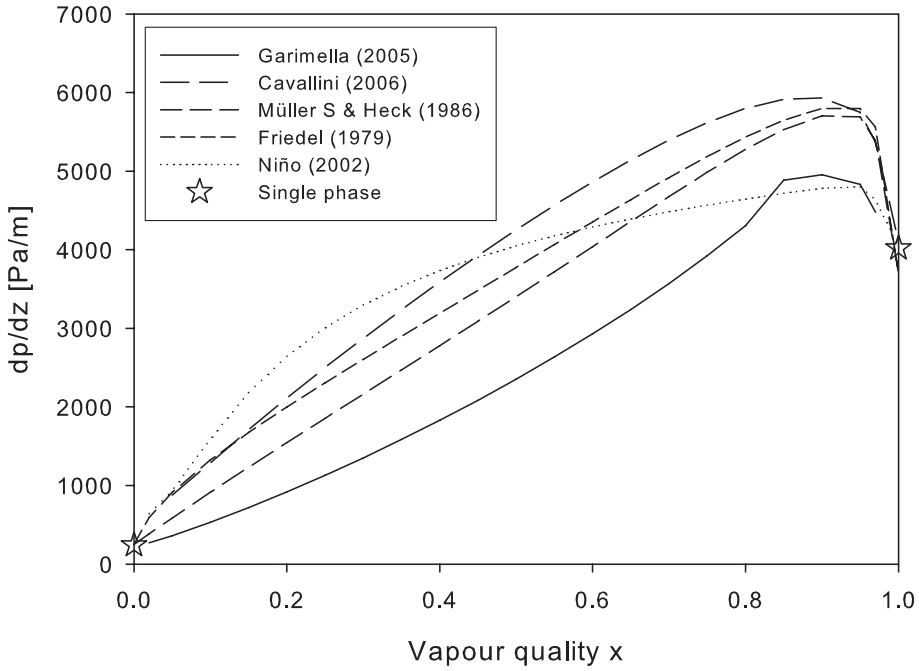

Figure 2.12: Pressure drop models for flow of R-22. $G = 500$ kg/m^{2}s, $p = 10$ bar, $d = 10$ mm. The stars indicates the single phase values using saturated liquid and vapour respectively with Equation 2.37.

Chapter 3

Experimental set-up

3.1 Test facility

The test setup was designed by Dr. Steffen Grohmann [30] and minor modifications have been carried out by the author.

3.1.1 Features

The experimental setup is designed to measure both single and two phase heat transfer (cooling and condensing) and pressure drop in small channels with $d \leq 2$ mm. Its temperature range is approx. -230 °C to -50 °C and the maximum pressure is 70 bar, which means that a wide range of fluids and fluid mixtures can be used.

The maximum flow rate is $\dot{m} = 2.5 \cdot 10^{-3}$ kg/s, which corresponds to $G = 800$ kg/m^{2}s for a 2 mm tube. The uncertainty of the current mass flow meter limits the smallest tube size to approx. 0.25 mm for practical purposes. With modifications of the setup, it is also possible to measure flow boiling heat transfer.

3.1.2 Mechanical design

Referring to Figure 3.1 and 3.2, the experimental setup consists of a warm and a cold part, where the cold part, holding the test section, is contained inside a vacuum chamber. The working fluid is circulated through both parts and undergoes a number of phase changes. The cooling is provided by a Stirling cryocooler which cools the whole cold part of the setup, i.e. everything inside the vacuum chamber. The circulation in the system is provided by a compressor (between point 1 and 2). The gas is then cooled by a water cooler (between point 2 and 3). From point 3, the gas goes through an oil

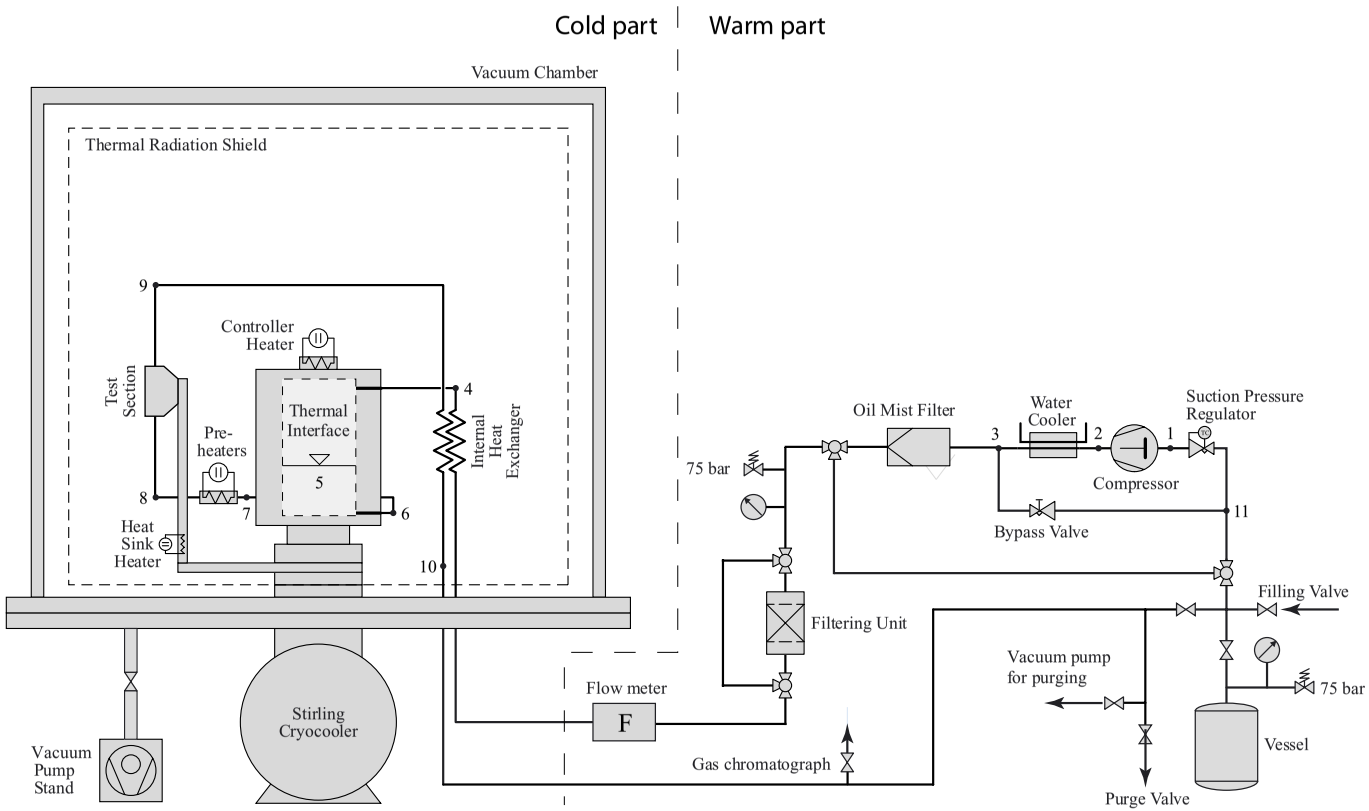

Figure 3.1: Schematic overview of the test setup. Illustration by Steffen Grohmann.

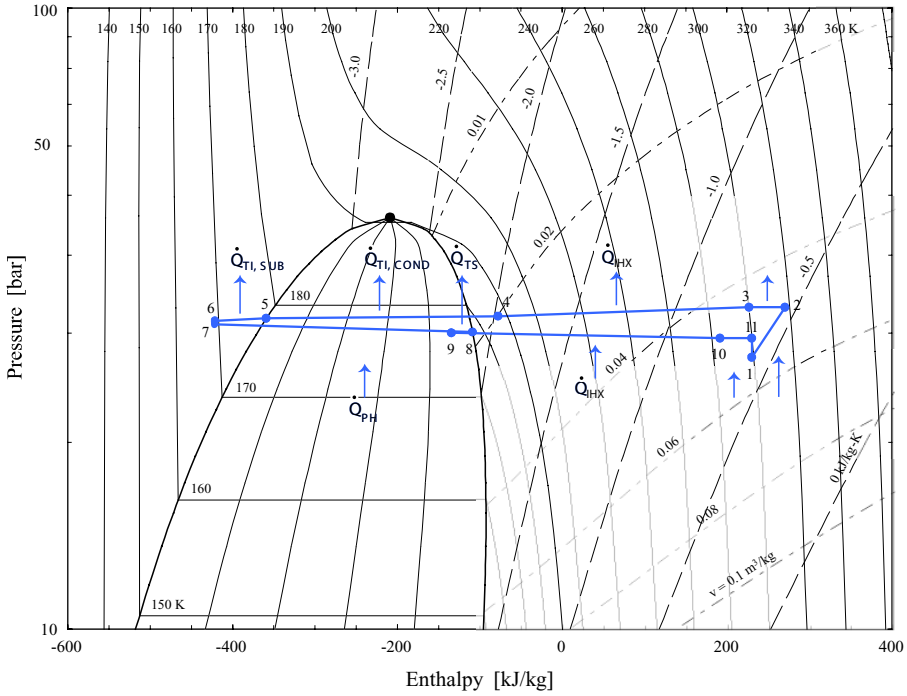

Figure 3.2: Pressure-enthalpy diagram for methane in the test rig cycle. Illustration by Steffen Grohmann.

separator, followed by an oil and particle filter and a flow meter. Inside the vacuum chamber, the gas is first cooled in the internal heat exchanger (point 4), after which it is condensed and sub-cooled in the thermal interface (point 5). This is a copper vessel containing an amount of liquid during operation, and the pressure/temperature in the system can be controlled by adding power to the controller heater.

The fluid then enters the pre-heater (point 7 to 8), which for two phase measurements controls the vapour fraction of the fluid. Then the fluid enters the test tube (point 8 and 9), and the enthalpy removed from the fluid can be controlled by applying power to the heater $\dot{Q}_{\mathrm{HS}}$. After that, the test fluid passes through the internal heat exchanger again in order to cool the incoming fluid (point 9 to 10). A suction pressure regulator helps control the flow rate (point 11 to point 1).

$\dot{Q}_{\mathrm{IHX}}$ denotes the heat transferred in the internal heat exchanger (point 9 to 10 and point 3 to 4 in Figure 3.2) while the remaining enthalpy before the compressor is added to the test fluid by the surroundings (point 10 to 11). The pressure difference before the compressor is regulated by a suction

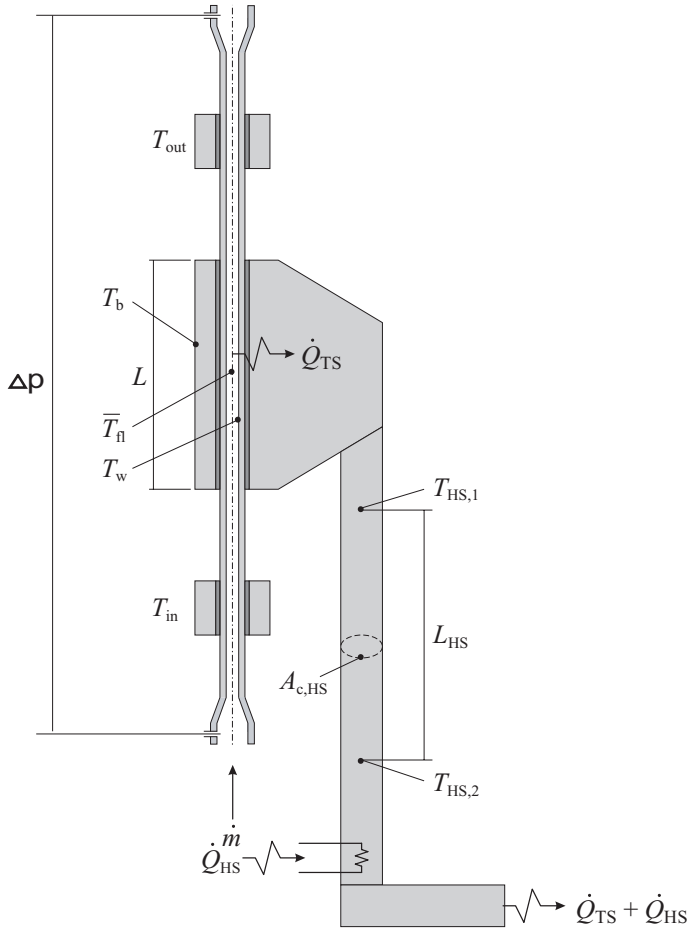

Figure 3.3: Details of the test section. Illustration by Steffen Grohmann.

pressure regulator (point 11 to 1).

Also referring to Figures 3.3 and 3.4, the test tube is a stainless steel tube soldered on the inside of a oxygen free copper block, which again is connected to a copper rod. The rod works as a measurement device for determining the heat $\dot{Q}_{TS}$ transferred from the fluid in Figure 3.3. The part of the test tube located within the copper block has a length $L = 5$ cm and is from now on referred to as the test section. It is preceded by a 20 cm adiabatic section, which means that temperature differences within the fluid can be assumed to be annihilated.

The temperature sensors T_{in} and T_{out} are inserted into two small copper blocks which are soft soldered on each side of the test section. The sensor

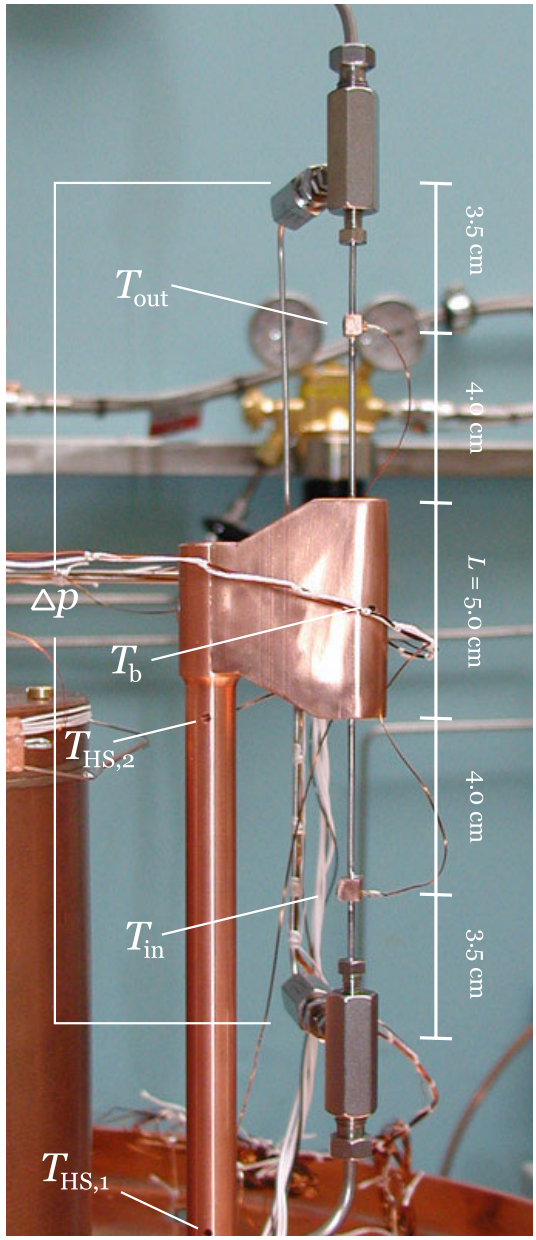

Figure 3.4: Photography of the test section.

T_{b} is inserted into the copper block close to the test tube, while $T_{\mathrm{HS},1}$ and $T_{\mathrm{HS},2}$ are inserted into the copper rod and are used to measure $\dot{Q}_{\mathrm{TS}}$.

The vacuum chamber is a stainless steel tank and measurements are carried out at a pressure of approx. 10^{-5} mbar. Vacuum is needed to remove measurement errors due to natural convection of air inside the chamber, and also to avoid freezing of water vapour from the air on the cold parts.

A circular copper plate is connected to the cryocooler and placed between the test section and the cryocooler inside the vacuum chamber. Another thin copper plate is bent in a circle and screwed onto the circular copper plate with a top lid, completely surrounding the cold part as a shield. In this way, the shield is cooled down to a temperature around the temperature of the test fluid and shields the cold part from radiation from the inside of the vacuum chamber, which is at ambient temperature.

3.1.3 Temperature measurement

The heat transfer coefficient $\overline{h}$ is a relation between the heat flux and the mean temperature difference between the fluid flow and the tube wall and is expressed by

$$\overline{h} = \frac{\dot{Q}_{\mathrm{TS}}}{A_{\mathrm{w}} \cdot \Delta T_{\mathrm{m,w}}} \tag{3.1}$$

where $\overline{h}$ is the mean heat transfer coefficient over the tube length, $\dot{Q}_{\mathrm{TS}}$ is the heat load from the test section, A_{w} is the area of the wetted surface inside the tube, and $\Delta T_{\mathrm{m,w}}$ is the mean temperature difference.

$\Delta T_{\mathrm{m,w}}$ is for single phase given by the logarithmic mean temperature difference

$$\Delta T_{\mathrm{m,w}} = \frac{T_{\mathrm{in}} - T_{\mathrm{out}}}{ln\left(\frac{T_{\mathrm{in}} - T_{\mathrm{w}}}{T_{\mathrm{out}} - T_{\mathrm{w}}}\right)} \tag{3.2}$$

and for two phase flow by

$$\Delta T_{\mathrm{m,w}} = \frac{T_{\mathrm{in}} + T_{\mathrm{out}}}{2} - T_{\mathrm{w}}. \tag{3.3}$$

This assumes that the specific heat value of the fluid c_p is constant through the test section, something that can be assumed for small temperature differences between the inlet T_{in} and outlet T_{out} bulk temperatures. Equations 3.2 and 3.3 are also only valid as long as the wall temperature is constant in the flow-direction along the flow channel, something that can be assumed in this case due to the high conductivity of the copper.

Finding the average heat transfer coefficient at the wetted surface $\overline{h}$ requires the surface temperature T_{w}. As this is very difficult to measure

without interrupting the flow, it is calculated from the measured T_b by a thermal resistance model between the location of the sensor T_b and the tube wall.

As the test facility is mainly designed to do tests on two phase flow, the heat transferred from the fluid $\dot{Q}_\mathrm{TS}$ measured by a heat flux measurement concept shown in Equation 3.4 and in Figure 3.3. By measuring the temperature difference between $T_\mathrm{HS,1}$ and $T_\mathrm{HS,2}$, and by knowing the length L_HS, the area $A_\mathrm{C,HS}$ and the thermal conductivity k_Cu of the copper, $\dot{Q}_\mathrm{TS}$ can be found as

$$\dot{Q}_\mathrm{TS} = \frac{k_{Cu}}{L_\mathrm{HS}} \cdot A_\mathrm{C,HS} \cdot (T_\mathrm{HS,1} - T_\mathrm{HS,2}) \cdot C_1 + C_2. \tag{3.4}$$

Fitting the coefficients C_1 and C_2 is done by comparing $\dot{Q}_\mathrm{TS}$ to the heat balance $\dot{Q}_\mathrm{HB}$ across the test section over a series of measurements of single phase flow at different values of $\dot{m}$ and q''.

$$\dot{Q}_\mathrm{HB} = \dot{m} \cdot c_p \left(T_\mathrm{in} - T_\mathrm{out}\right) \tag{3.5}$$

$\dot{Q}_\mathrm{TS}$ can be varied by adjusting the voltage to the heater yielding $\dot{Q}_\mathrm{HS}$, as shown in Figure 3.3 and Figure 3.15. This will reduce the temperature difference between $T_\mathrm{HS,1}$ and $T_\mathrm{HS,2}$ and hence reduce $\dot{Q}_\mathrm{TS}$. Some details of the test section details are found in Table 3.1.

The pressure drop Δp is measured across the test tube and is illustrated in Figure 3.3 and in Figure 3.7.

All the fluid properties are evaluated at the average pressure and temperature through the test section, i.e. for viscosity $\mu = \mu(T_\mathrm{m}, p_\mathrm{m})$ where $T_\mathrm{m} = \frac{T_\mathrm{in}+T_\mathrm{out}}{2}$. The pressure in the middle of the test section p_m was found by the measured p_PH and substracting the estimated pressure drop from the pre-heater to the middle of the test section. The fluid properties were found by REFPROP [43].

Calculating T_w from T_b

A finite element model was constructed in Comsol Multiphysics to simulate the difference between the wall temperature T_w from T_b. The resistance between the tube wall and the location of T_b comprise of conduction in the copper, soldering and the tube wall. The resistance should be constant and independent of the flow inside the tube. To investigate the resistance, a number of positive heat fluxes were imposed on the tube wall, and equivalently negative heat fluxes where the heat is lead into the copper rod.

Category	Design Parameter	Symbol	Value
Geometry	Test section length	L	50 mm
	Heat sink rod diameter	d_{HS}	0.012 m
	Distance between $T_{\mathrm{HS},1}$ and $T_{\mathrm{HS},2}$	L_{HS}	120 mm
Nominal operating conditions	Heat flux	q''	12.0 kW/m^2
	Heat load for the 1 mm tube	$\dot{Q}_{\mathrm{TS}}$	1.88 W
	Mean temp. difference	$\Delta T_{\mathrm{m,w}}$	Approx. 1-3 K

Table 3.1: Properties of the test section

Due to the high conductivity of the copper, almost all of the resistance is connected to the soldering and the tube wall, which consists of soldering tin and Type 316 stainless steel respectively. This can be seen in Figure 3.5 for the 0.5 mm tube.

The resistance across the soldering is difficult to estimate, but assuming a worst case scenario where half of the tube circumference is connected to the copper block, Figure 3.6 still shows that the temperature is evenly distributed on the inner tube wall.

Based on simulations with different heat fluxes, the difference between T_{w} and T_{b} was found on the form

$$T_{\mathrm{w}} = T_{\mathrm{b}} + c \cdot \dot{Q}_{\mathrm{TS}} \tag{3.6}$$

where c is a constant expressing the resistance and has the unit K/W. The different values of c is found in Table 3.2. A solder covering most of the tube outer circumference was chosen for the simulations, however the vast majority of the resistance is in the tube wall due to its low thermal conductivity.

3.1.4 Pressure drop measurements

The pressure drop measurements takes place across a 20 cm long section of the test tube as shown in Figure 3.4. The measured pressure drop can be divided into following parts:

$$\Delta p_{\mathrm{measured}} = \Delta p_{\mathrm{f}} + \Delta p_{\Delta x} + \Delta p_{\mathrm{static}} + \Delta p_{\mathrm{entrance/exit}} \tag{3.7}$$

Frictional pressure drop

Δp_{f} is the pressure drop due to shear tensions between the fluid flow and the wall, and also across the liquid/vapour interface.

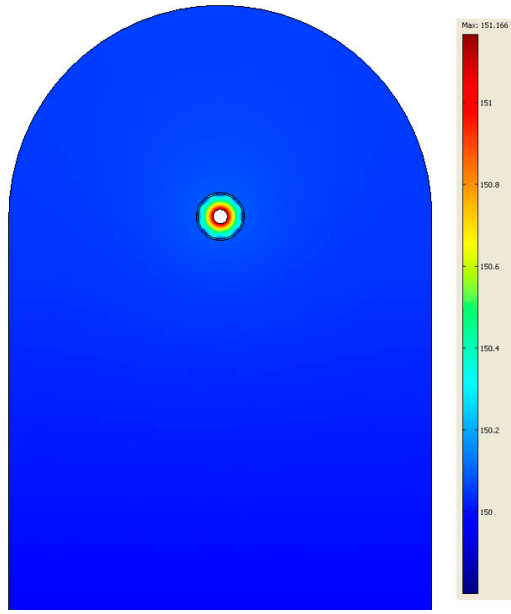

Figure 3.5: The temperature profile in the test section seen from above for the 0.5 mm tube.

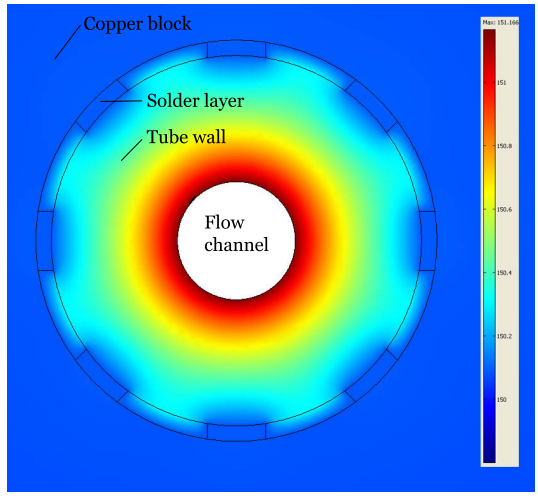

Figure 3.6: The temperature profile in the test section in detail for the 0.5 mm tube.

Pressure drop due to momentum change

$\Delta p_{\Delta x}$ is the pressure change in diabatic two phase flow due to acceleration or deceleration due to changing average density from the change in vapour fraction. For condensation this factor gives a pressure recovery as some of the vapour is decelerated when condensed into the liquid film. For adiabatic flow $\Delta p_{\Delta x} = 0$. The contribution from $\Delta p_{\Delta x}$ is usually small. Garimella et al. [28] used a model from Carey [7] to calculate the momentum pressure drop for two phase flow as:

$$\Delta p_{\Delta x} = G^2 \left(\left[\frac{x^2}{\rho_v \varepsilon} + \frac{(1-x)^2}{\rho_l (1-\varepsilon)} \right]_{x=x_{out}} - \left[\frac{x^2}{\rho_v \varepsilon} + \frac{(1-x)^2}{\rho_l (1-\varepsilon)} \right]_{x=x_{in}} \right) \tag{3.8}$$

For single phase flow $\Delta p_{\Delta x}$ is practically zero except for single phase flow near the critical and pseudo-critical point where $\partial \rho / \partial T$ can be large and $\Delta p_{\Delta x}$ can make out a small contribution.

Static pressure drop

Δp_{static} is the pressure change due to hydrostatic pressure difference as there is a vertical fluid column between the entrance and exit pressure outlets. For horizontal tubes, this factor equals zero, but for inclined tubes it must be taken into account. It can make out an important contribution, particular for liquid flow where the density is high.

$$\Delta p_{\text{static}} = gL\overline{\rho} \tag{3.9}$$

where $\overline{\rho} = \rho_{\text{l}}(1-\varepsilon) + \rho_{\text{v}}\varepsilon$

Entrance/exit header pressure drop

$\Delta p_{\text{entrance/exit}}$ takes possible pressure drop from entrance and exit geometry of the tube into account. Going from a wider tube to a narrower tube accelerates the fluid causing pressure loss. This pressure loss can for single phase flow to some extent be recovered at the expansion at the other end.

For two phase flow, the situation is quite different. According to VDI Wärmeatlas, the energy used to accelerate the flow at the contraction is not regained at the expansion in the same way as for single phase flow, and irreversible pressure losses occur.

The fitting used for the pressure difference measurement outlet at the entrance of the test tube is seen in Figure 3.7. The fitting at the exit of the test tube is equivalent. At the entrance, the pressure drop occurs along

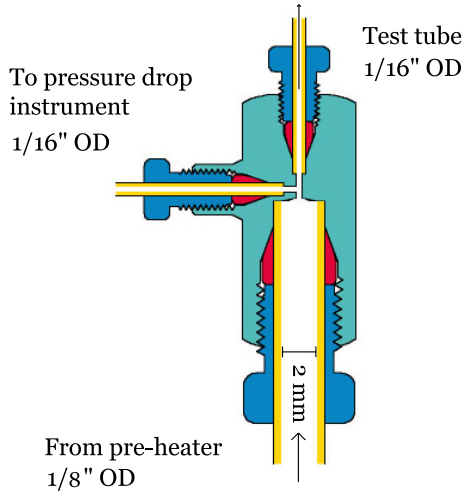

Figure 3.7: Design of the pressure difference outlet for the highest pressure part of the test tube. Drawing from Vici.

a length of the test tube, and not only at the contraction. For the fitting after the test section, the sudden expansion into the 1/8" mm tube happens *after* the outlet to the pressure drop instrument. This indicates that only parts of the inlet pressure drop should be taken into account.

Equations for calculating the entrance and exit pressure drop due to geometry changes can be found in Chapter B.3.3. As it is difficult to determine to what extent the actual entrance/exit pressure drop is included in the measured $\Delta p_{\text{measured}}$, it is decided to set $\Delta p_{\text{entrance/exit}} = 0$ for all pressure drop measurements.

3.2 Choice of tube diameter

The choice of correct diameter is crucial to getting reliable results at this small scale, this applies particularly for pressure drop considerations. Grohmann [30] found that his single phase heat transfer measurements followed the conventional correlations if the increased surface area due to the roughness was taken into account. Qi et al. [58] came to the same conclusion when they used the measured friction factor instead of the smooth tube friction factor.

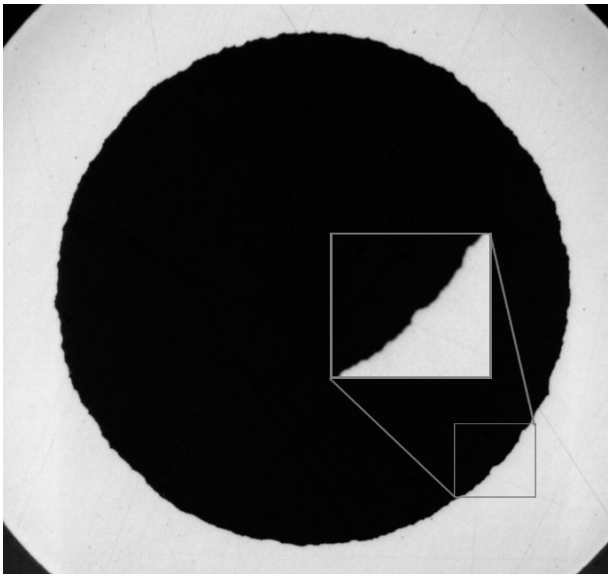

Figure 3.8: Microscope photo of the 1 mm test tube used for determining d_{w}, d_c and d_h.

3.2.1 Optical photographs of the tubes

Figures 3.8 - 3.10 show optical photographs obtained from an optical microscope of the three tubes in question.

From the magnification window in Figure 3.8 it is clear that the 1 mm tube is not smooth. The imperfections are most likely an effect of the production technique of the tubes.

For the 0.5 mm tube in Figure 3.9, this effect is more pronounced, and very clear for the 0.25 mm tube in Figure 3.10. The inside of this tube is far from smooth, nevertheless circular.

The roughness in the tube stirs up sublayers close to the tube wall, increasing heat transfer and pressure drop. The roughness also creates a larger wetted wall surface, increasing the heat transfer area. There are more ways to implement the effects of tube wall irregularities on the pressure drop and heat transfer, two of them presented in chapter 3.2.2 and 3.2.3 respectively:

3.2.2 Friction factor from surface roughness

Due to the imperfections/roughness at the tube wall, flow and heat transfer effects deviating from that occurring close to a smooth wall are likely to oc-

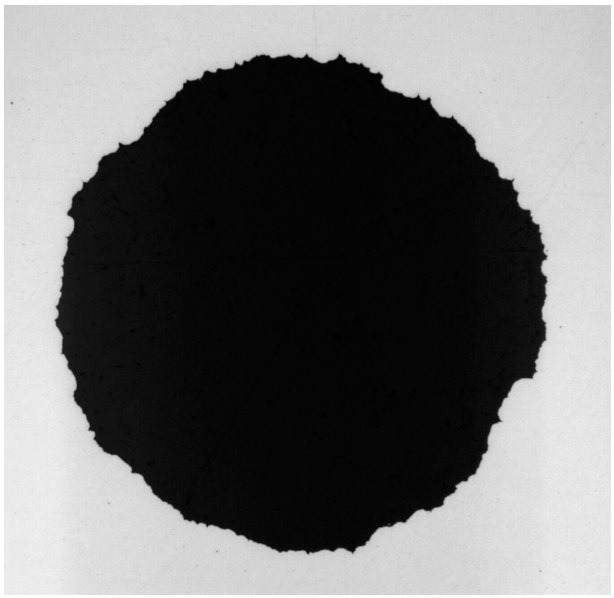

Figure 3.9: Microscope photo of the 0.5 mm test tube. The magnification is twice as large as for Figure 3.8.

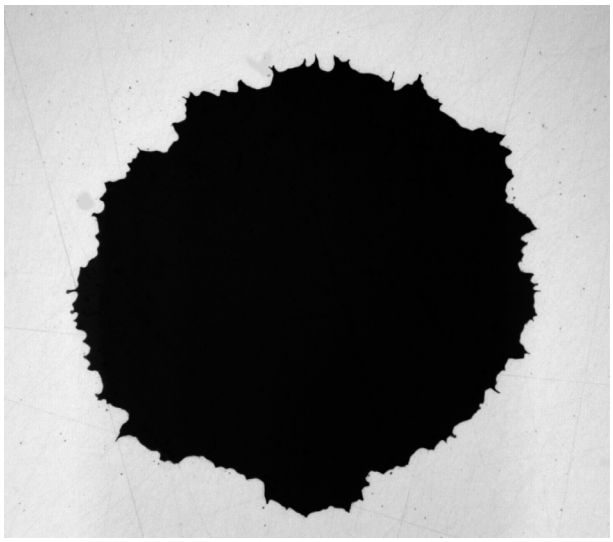

Figure 3.10: Microscope photo of the 0.25 mm test tube. The magnification is four times as large as for Figure 3.8.

cur. Also, velocity and temperature profiles will not develop equally around the tube wall due to the imperfections, and this effect increases for smaller tube diameters for a given roughness height. These effects are captured by the friction factor for large tubes, which is often included in equations for heat transfer and pressure drop. The friction factor for a smooth tube can be found from e.g. Equation 2.7.

For a rough tube, the friction factor is usually obtained from models based on relative roughness ($=\epsilon/d$). Such a friction factor can be found e.g. from a Moody-diagram [48] or from the equation by Colebrook [20]. In this work, the friction factor was found from the Colebrook-equation. Using the photographs presented in Figures 3.8 - 3.10, 10 or more diameters were measured and their average deviation from the average diameter $\overline{d}$ represented the average roughness height $\overline{\epsilon}$. Figure 3.11 and Equation 3.10 show this, and the resulting relative roughness values are listed in Table 3.2.

$$\overline{d} = \frac{1}{n}\sum_{i=1}^{n} d_{\mathrm{i}} \qquad \overline{\epsilon} = \frac{1}{n}\sum_{i=1}^{n} |d_{\mathrm{i}} - \overline{d}| \tag{3.10}$$

As the tubes used in this work are drawn during production, it is possible that the roughness is observed differently in a cross-sectional photo compared to a photo across the length of the tube. This means that the surface structure could resemble grooves in the axial direction of the tube, i.e. mostly parallel to the flow direction. This is obviously a different type of roughness as they differ from the randomly scattered surface irregularities found in conventional tubes on which the many friction factor correlations are based. The roughness measured based on the cross-sectional photos in Figures 3.8 to 3.10 may not be representative.

3.2.3 Equivalent smooth diameters

Different diameters for an equivalent smooth tube can be defined as done in Equation 3.11. Further calculations of flow properties can be done with these equivalent diameters.

From Figure 3.10, it is obvious that the perimeter is larger than what a smooth tube with the same nominal diameter would represent. This causes a larger surface for heat transfer. This effect is largest of the smallest tube.

Three smooth tube equivalent diameters were defined, based upon the diameter calculated from the perimeter P, the cross-sectional area A_{c} and the definition of the hydraulic diameter. The values of P and A_{c} were found by 6 optical photographs of each of the test tubes analyzed by a morphology

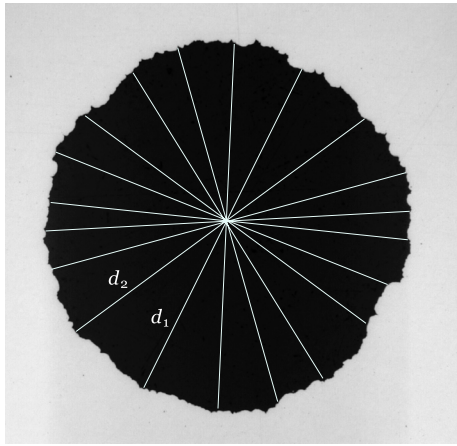

Figure 3.11: 10 diameters measured to find the relative roughness, here the 0.5 mm test tube.

software.

$$d_{\mathrm{w}} = \frac{P}{\pi}, \qquad d_{\mathrm{c}} = \sqrt{\frac{4A_{\mathrm{c}}}{\pi}}, \qquad d_{\mathrm{h}} = \frac{4A_c}{P} = \frac{d_c^2}{d_{\mathrm{w}}} \tag{3.11}$$

The diameter d_{c} reflects the physical cross sectional area of the tube. The diameter based on the perimeter of the tube, d_{w}, reflects the wetted surface. The hydraulic diameter d_{h} is a combination of the two, often used as an equivalent diameter for non-circular geometries.

Table 3.2 shows the obtained diameters and Figure 3.12 illustrates the difference between the diameters for the 0.5 mm tube. The diameter d_{w} based on the perimeter is much larger than the diameter based on the cross-sectional area d_{c}. This causes the hydraulic diameter d_{h} to be smaller than either of d_{c} or d_{w}.

3.2.4 Choice of diameters for flow properties

In this work, the results are presented and compared to correlations using the friction factor-based method described in chapter 3.2.2. The reason for this is that it is believed that the disturbance of the sublayers by the roughness are of a crucial importance, and that the smooth equivalent diameter can not capture this effect.

When it comes to an applicable diameter for the flow properties, the choice of diameter needs to be discussed. In the literature, the hydraulic diameter is very often the preferred diameter used when working with non-

Tube name	1.0 mm	0.5 mm	0.25 mm
ID (nominal)	0.04”	0.02”	0.01”
	1.02 mm	0.51 mm	0.25 mm
OD (nominal)	1/16” (1.59 mm)		
d_w [µm]	1159.5	650.4	369.6
d_c [µm]	1039.3	555.6	274.4
d_h [µm]	931.4	474.6	203.8
σ_{d_w}	2.5 %	3.0 %	8.5 %
σ_{d_c}	0.1 %	1.2 %	1.5 %
$\overline{\epsilon}/\overline{d}$ [-]	0.0024	0.0123	0.0425
d_w/d_c	1.115	1.171	1.347
c (Eq. 3.6)	0.155	0.39	0.45

Table 3.2: Properties of the different tubes tested.

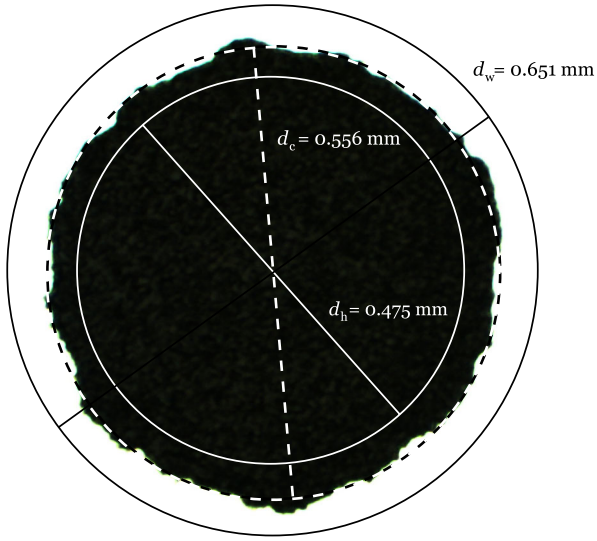

Figure 3.12: Comparison of the three diameters obtained for the 0.5 mm tube compared to a photo of the tube.

circular geometries. However, comparing the diameters listed in Table 3.2 and taking a look at Figure 3.12, it is a legitimate question to ask if the hydraulic diameter d_h represents the physical reality of the tubes in question. d_c appears to be much closer to the physical reality than d_h. Therefore, d_c is chosen as the diameter for the flow and heat transfer properties.

The mass flux calculated from the measurements is therefore found as

$$G = \frac{\dot{m}}{(d_\mathrm{c}/2)^2\pi} \tag{3.12}$$

and the heat transfer area as

$$A_\mathrm{w} = d_\mathrm{c}\pi L \tag{3.13}$$

Combining the transfer coefficient definition in Equation 3.1 and the wetted area in Equation 3.13, the diameter is cancelled out. This means that it is irrelevant which diameter is chosen for A_w and the Nusselt-number, as long as it is the same.

$$\overline{Nu} = \frac{\overline{h}d_\mathrm{c}}{k} = \frac{\dot{Q}_{TS}}{\pi L \Delta T_\mathrm{m,w} k} \tag{3.14}$$

For two phase flow, the Nusselt number is not employed and the choice of diameter is relevant. The Reynolds-number is expressed as in Equation 3.15.

$$Re = \frac{d_\mathrm{c}G}{\mu} \tag{3.15}$$

and the heat flux q'' is found as:

$$q'' = \frac{\dot{Q}_\mathrm{TS}}{A_\mathrm{w}} \tag{3.16}$$

3.3 Thermal and mechanical design

3.3.1 Cryocooler

The cryogenic temperature was provided by a Stirling Cryocooler of type CPC-1. It was originally used to liquefy air at ambient pressure, so its cold head had to be modified. A vacuum-tight flexible flange connection was mounted and a plain copper surface for fitting the thermal interface. It can be seen in Figure 3.13.

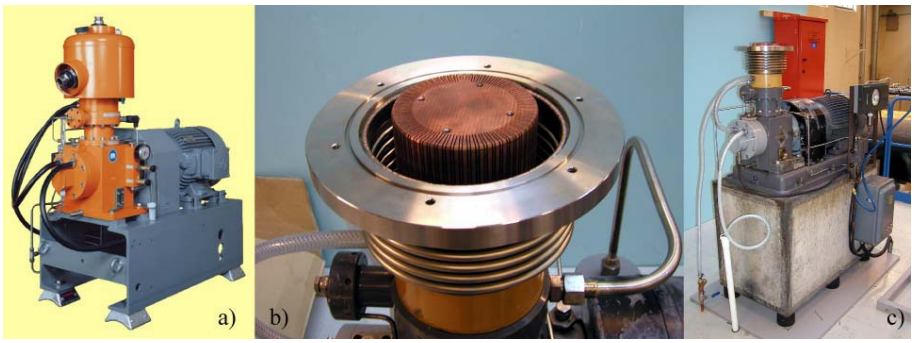

Figure 3.13: Modification of the Stirling Cryocooler. Photos (b) and (c) by Steffen Grohmann

3.3.2 Vacuum

Two vacuum systems are used; one for evacuating the circuit tubing after it has been opened or when changing working fluids (not show or described here) and one for the vacuum tank to ensure no convection effects in the cold part.

The vacuum in the vacuum tank is provided by a Leybold PT 301 Dry pump stand. This is an oil-free pump stand, which consists of a diaphragm pump in the first stage and a turbomolecular pump in the second stage. When evacuating the vacuum tank, the first stage takes the pressure down to approx. 2-3 mbar. After a careful start-up of the second stage, the pressure is normally stabilised in the order of 10^{-5} mbar. The vacuum pressure goes slightly down when the system is cooled down.

A burst disk is installed as a safety precaution in case of fluid circuit rupture within the vacuum tank. Should this occur, up to 400 g of methane would enter the vacuum tank and exert a pressure of approx. 3 bar. In this case, the burst disk bursts would burst at 1 bar overpressure to prevent damage to the vacuum pump.

3.3.3 Design of the cold part of the test facility

Thermal interface

The thermal interface connects the cryocooler to the fluid circuit. It is hollow, where the top part condenses the incoming fluid and the bottom part sub-cools the fluid. The hollow space in the thermal interface works as a buffer for changing flow-rates and temperature/pressure. The design of the thermal interface is shown in Figure 3.14. The overall heat balance

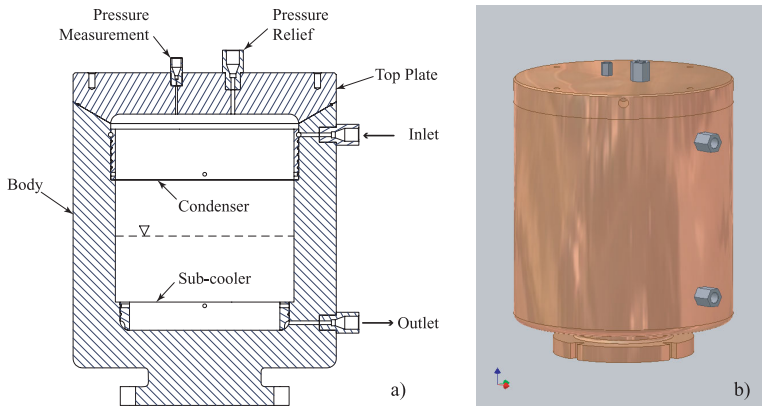

Figure 3.14: Design of the thermal interface. Illustration by Steffen Grohmann.

in the system is given by

$$\dot{Q}_0 = \dot{Q}_{\mathrm{CH}} + \dot{Q}_{\mathrm{C}} + \dot{Q}_{\mathrm{SC}} + \dot{Q}_{\mathrm{PH}} + \dot{Q}_{\mathrm{TS}} + \dot{Q}_{\mathrm{HS}} + \dot{Q}_{\mathrm{RS}} \tag{3.17}$$

$\dot{Q}_0$ is the cooling provided by the cryocooler, $\dot{Q}_{\mathrm{CH}}$ is the heat from the controller heater, $\dot{Q}_{\mathrm{C}}$ is the heat from condensation, $\dot{Q}_{\mathrm{SC}}$ is the heat from the sub-cooling, $\dot{Q}_{\mathrm{PH}}$ is part of the heat from the pre-heaters, $\dot{Q}_{\mathrm{TS}}$ is the heat from the test section, $\dot{Q}_{\mathrm{HS}}$ is the heat from the heat sink heaters and $\dot{Q}_{\mathrm{RS}}$ is heat from the radiation shield. This can be seen in Figure 3.15.

The controller heater $\dot{Q}_{\mathrm{CH}}$ is used to control the saturation pressure in the thermal interface, $\dot{Q}_{\mathrm{PH}}$ determines the vapour fraction of the fluid entering the test section and the heat sink heater $\dot{Q}_{\mathrm{HS}}$ sets the heat from the test section by determining the temperature difference along the copper rod.

The thermal interface is made out of oxygen-free copper (OFC) and has a mass of approx. 15 kg. As the other parts in the fluid circuit, it is designed for a maximum operating pressure of 70 bar. The inner volume is approx. 0.75 l. The components of the thermal interface were connected by vacuum bracing at temperatures of ca 820 °C. This made the copper parts fully annealed. The production of the thermal interface was done by *Institut für Luft- und Kältetechnik GmbH* Dresden, Germany.

Internal heat exchanger

The internal heat exchanger connects the warm part with the cold part of the circuit. It takes heat from the incoming fluid by heating the outgoing

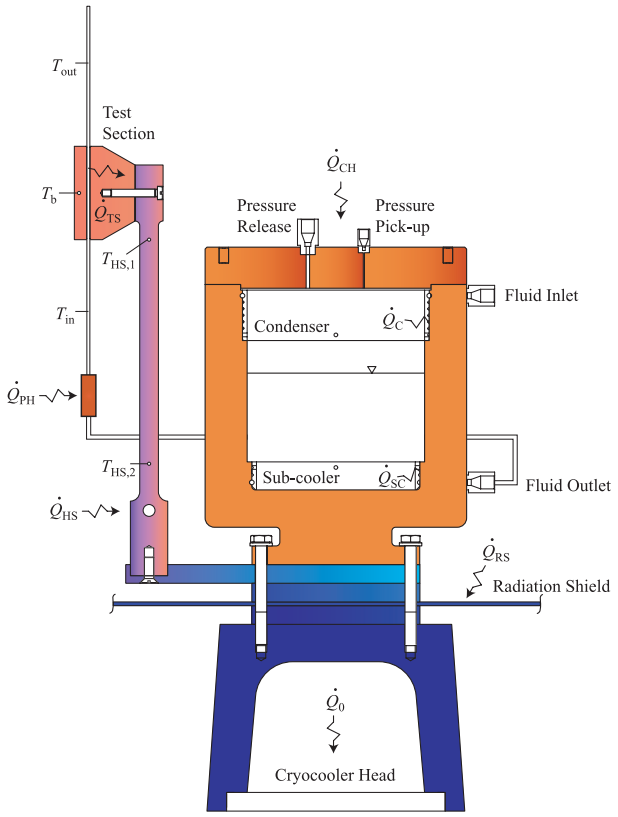

Figure 3.15: Illustration of the cryogenic interface, the lower plate of the radiation shield and the test section. Illustration by Steffen Grohmann.

fluid, as shown in Figure 3.2 denoted $\dot{Q}_{IHX}$. It consists of two concentric tubes (OD 1/8" inner tube and OD 6 mm outer tube) and has a length of 1 m. The tubes are wound up to a coil having a diameter of approx. 15 cm as shown in Figure 3.16.

Pre-heaters

The two pre-heaters heat the sub-cooled fluid from the thermal interface to the desired vapour fraction or superheat before it enters the test section. Careful design is necessary to ensure that enough heat is transferred to the fluid by convection and nucleate boiling without the risk of thermal runaway.

The pre-heater consists of two parts. The first part (main pre-heater) has approx. 25 cm of tubing which is wounded up in a spiral surrounded by a copper cylinder, as illustrated in Figure 3.17. In one end of the cylinder,

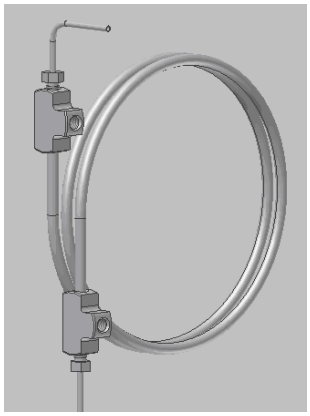

Figure 3.16: Illustration of the internal heat exchanger. Illustration by Steffen Grohmann.

a heater cartridge 50 Ω is installed to provide heat to the fluid. In the opposite end of the cylinder, a temperature sensor is installed in order to monitor the temperature in the copper with respect to thermal runaway.

The main pre-heater is followed by the auxiliary pre-heater, which task is to provide the last heating of the fluid. It consists of a 10 cm long copper cylinder block which surrounds a 10 cm straight section of the tube. A heater cartridge of 20 Ω and a temperature sensor is also installed in the auxiliary pre-heater. The design criteria was that it should provide a smaller heat flux than the main pre-heater, in order to avoid burn-out and thermal runaway for high vapour qualities. The resistors in the two pre-heaters are connected in series to one power supply, so the power from the auxiliary pre-heater makes out approx. 27 % of the total pre-heater power.

The auxiliary pre-heater is succeeded by a 20 cm adiabatic 1/8" DO and 1/12" ID tubing before the entrance to the test tube. A drawing of the connection between the 1/8" tubing and the test tube is found in Figure 3.7.

The vapour fraction x for single component fluids is usually defined as the ratio of vapour gas mass flow to the total mass flow. Alternatively for pure fluids, it can be found as the enthalpy ratio:

$$x = \frac{e_{\mathrm{x}} - e_{\mathrm{l,sat}}}{e_{\mathrm{v,sat}} - e_{\mathrm{l,sat}}} \left[\frac{\mathrm{J/kg}}{\mathrm{J/kg}}\right] \tag{3.18}$$

where e_{x} is the enthalpy at the state where x is to be found and $e_{\mathrm{l,sat}}$ and $e_{\mathrm{v,sat}}$ is the enthalpy at saturated liquid and vapour at p_{m} respectively. For the test section, the average enthalpy value is obtained from REFPROP

[43] as

$$\overline{e_{\mathrm{x}}} = \mathrm{Enthalpy}(T_{\mathrm{TI,out}}, p_{\mathrm{m}}) + \frac{\dot{Q}_{\mathrm{PH}}}{\dot{m}} \tag{3.19}$$

where $T_{\mathrm{TI,out}}$ is the temperature at the outlet of the thermal interface. $\dot{Q}_{\mathrm{PH}}$ is the power added to the pre-heater and is found as the voltage across the cartridge multiplied with the current.

$$\dot{Q}_{\mathrm{PH}} = U_{\mathrm{PH}} \cdot I_{\mathrm{TS}} \tag{3.20}$$

For a binary or multicomponent fluids, finding the vapour fraction is more complex as the concentration in the phases changes. Therefore, the vapour fraction is determined by the REFPROP-function Quality() which can take enthalpy and pressure as input variables:

$$\overline{x} = \mathrm{Quality}(\overline{e_{\mathrm{x}}}, p_{\mathrm{m}}) \tag{3.21}$$

This function returns the vapour fraction as $\mathrm{kg_v/kg_{v+l}}$ and is used for pure component fluids and for binary fluids.

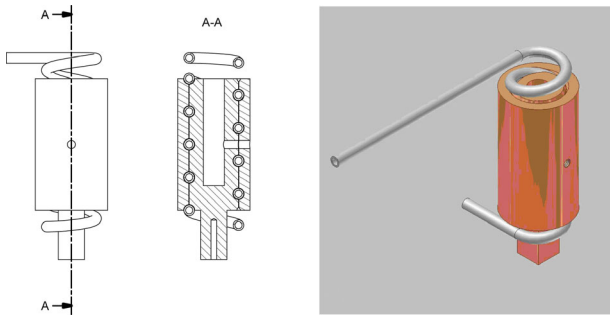

Figure 3.17: Illustration of the main pre-heater. Illustration by Steffen Grohmann.

3.3.4 Design of the warm part of the test facility

Compressor

The compressor unit provides the circulation in the fluid circuit. The compressor is an open-type CO_2-compressor from *Obrist Engineering* operating at room temperatures up to a pressure of 70 bar.

Referring to Figure 3.1 and 3.2, a water cooler cools the gas out of the compressor, and a bypass valve is used to roughly control the flow in the

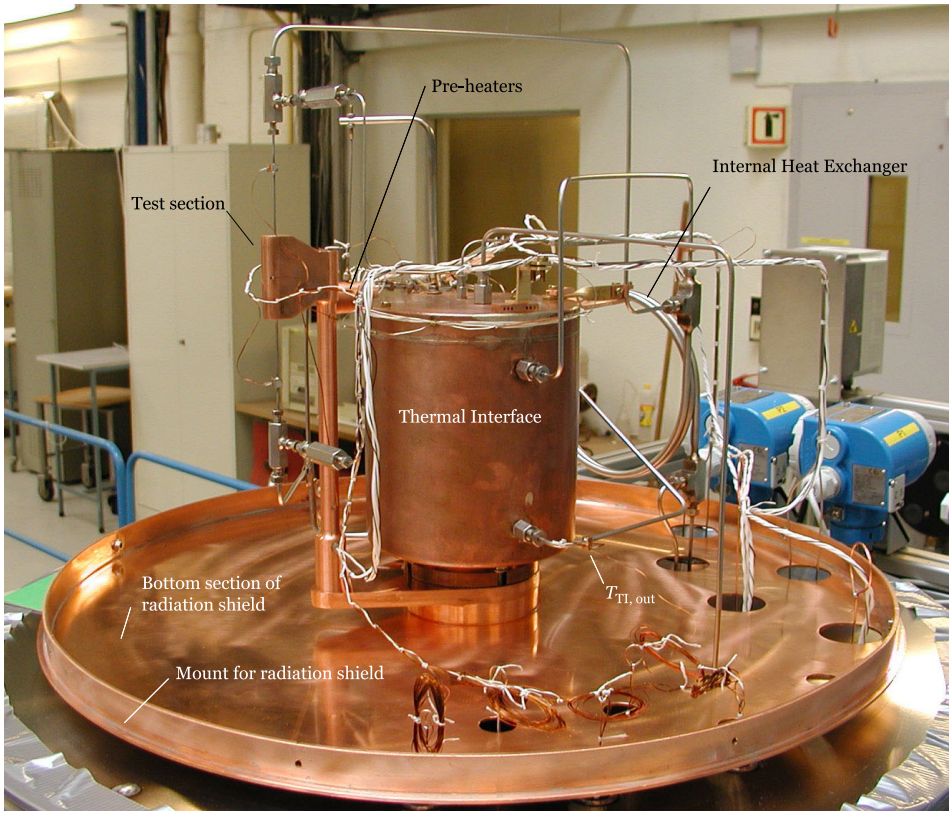

Figure 3.18: Photography of the cold part of the experimental setup

circuit. An oil cyclone separates most of the oil from the gas and leads the oil back to the compressor. Two filters in series after the oil separator purifies the gas of oil droplets and heavy hydrocarbons (active carbon). The filtering units can be bypassed during purging and maintenance.

Gas handling system

Referring to Figure 3.1, two expansion vessels are mounted on the warm side of the facility to contain the fluid when it is at ambient temperature. The two vessels have a total volume of approx. 6 l.

Three safety valves are installed in the fluid circuit; one on top of the thermal interface, one after the compressor and one to the main circuit. They are all adjusted to burst at 75 bar to prevent overpressure.

3.4 Instrumentation

The instruments used in the test facility is listed in Table 3.3.

Function	Manufacturer	Model
Temperatur Controller	LakeShore	LakeShore 340
Power supply for controller heater	Xantrex	XFR-300-4
Power supply for pre-heater	Xantrex	XFR-300-4-GPIB
Power supply for heat sink heater	Xantrex	XDL56-4PHV
Flow meter	Bronkhorst	M54-CO-AGD-22-VC

Table 3.3: Instruments used on the test rig.

3.4.1 Temperature control

The LakeShore 340 temperature controller is equipped with two temperature sensor channels as default, which can be used for controlling two independent control loops though a PID regulator. Only one of these is in use in this setup, where it controls the temperature in the thermal interface.

In the top of the thermal interface, 4 heater cartridges of type LakeShore HTR-25-100 with 25 Ω resistance are installed and connected in series. Together they have a rated capacity of 400 W and they can safely generate more, assuming good thermal contact between them and the copper. A temperature sensor T_{CH} is mounted on top of the thermal interface and its temperature is compared to the setpoint temperature in the regulation loop.

The power output from LakeShore controller is limited to 100 W. As the maximum power requirement for controlling the temperature in the thermal interface was approx. 400 W, a booster power supply of type Xantrex XFR-300-4 was connected. The power supply reads the voltage over a resistance connected to the power output of the temperature controller (in the range of 0-10 V), and sets a voltage across the heater cartridges accordingly.

It was further necessary to install a signal conditioner of type M-System M3LU between the temperature controller and the power supply, as the inlet fuse in the power supply for some reason kept burning out.

An extension card of type 3468 Eight Channel Input Option Card was installed in the LakeShore controller so that a total of 10 temperature sensors were installed. The temperature sensors in use are listed in Table 3.4. They are all platinum sensors from LakeShore. The models marked * were delivered with a calibration certificate and curves, but they still failed to show the same temperature when submerged in liquid nitrogen. As their main purpose is to measure temperature difference, they were calibrated to each other using both single and two phase measurement techniques. The absolute accuracy from this type of calibration is estimated to ±0.08 K. The other sensors have an accuracy of ±1.2 K.

Name	Model	Location	Uncertainty $\sigma_{\text{inst}} + \sigma_{\text{cal}}$ [K]
T_{CH}	PT-103	Controller heater sensor	1.2
T_{PH1}	PT-103	Main pre-heater sensor	1.2
T_{PH2}	PT-103	Aux. pre-heater sensor	1.2
$T_{\text{PH1,in}}$	PT-103	Main pre-heater, in	1.2
$T_{\text{HS,1}}$	PT-111*	Heat sink, lower	0.08
$T_{\text{HS,2}}$	PT-111*	Heat sink, upper	0.08
T_{in}	PT-111*	Test section, in	0.08
T_{b}	PT-111*	Test section sensor	0.2**
T_{out}	PT-111*	Test section, out	0.08
$T_{\text{TI,out}}$	PT-111	Thermal interface, out	1.2

Table 3.4: Temperature sensors installed. *Calibration certificate from producer. **See Chapter 5.2 for explanation of deviation uncertainty.

All temperature sensors are used in four-lead measurement mode, being equipped with AWG 36 low-conductivity phosphor-bronze wire. The sensors are heat-sinked to the heat shield in the vacuum chamber to avoid errors due to heat leaking to the sensors by conduction from outside the vacuum chamber.

Data is communicated from the LakeShore temperature controller to the PC through a GPIB-interface.

The temperature in the main and the auxiliary pre-heater was regulated manually by constantly observing its value, and then controlling the heat load to the pre-heaters $\dot{Q}_{\mathrm{PH}}$. At high vapour qualities, the temperature must be controlled carefully, as there is a chance for burnout and thermal runaway. The amount of heat from the test section $\dot{Q}_{\mathrm{TS}}$ was controlled by setting the voltage across the heater cartridge inserted in the bottom of the copper rod holding the test section.

3.4.2 Flow

A flow meter from Bronkhorst was used to measure the flow rate entering the cold part of the test facility. It uses the Coriolis principle for measuring and was calibrated before the experiments. Vibrations from the cryocooler inflicted on the measurements made by the flow meter, and it was therefore necessary to install the flow meter on a concrete block next to the test facility.

The flow rate was controlled manually by three mechanisms:

- Speed of compressor
- Bypass rate after compressor
- Compressor suction pressure

The speed of the compressor had a lower limit of 600 rpm, and was usually fixed at this speed. A bypass tube controlled by a needle valve was used to roughly set the flow rate in the circuit. However, the flow rate started oscillating when the needle valve was almost closed. Therefore, the flow rate was usually set by controlling the suction pressure to the compressor. As the compressor has a constant swept volume per second at a given speed, the mass flow can be controlled by changing the suction pressure.

3.4.3 Pressure

The pressure in the system was determined through the temperature level regulated by the controller heater $\dot{Q}_{\mathrm{CH}}$. As the circuit in the test facility is of constant volume, the temperature level determines the saturation pressure and the amount of liquid in the thermal interface. The pressure could also be controlled by the amount of fluid filled into the circuit. An upper limit of 75 bar existed due to safety reasons.

The pressure was measured by two pressure transducers of type PMP731, and by a pressure difference transducer PMD75, all three from Endress + Hauser. Data are communicated though analogue outputs (4-20 mA). One of the pressure transducers was connected to the top of the thermal interface, while the other one measuring p_{PH} was placed just before the main pre-heater. Details about the pressure difference measurement mounting can be found in Figure 3.7.

3.4.4 Data acquisition

The instruments in the experimental set-up are controlled as shown in Figure 3.19. Two of the power supplies and the temperature controller communicate directly with the PC through a GPIB interface. The third power supply is directly connected to the temperature controller, as this power supply works as a booster for the temperature controller.

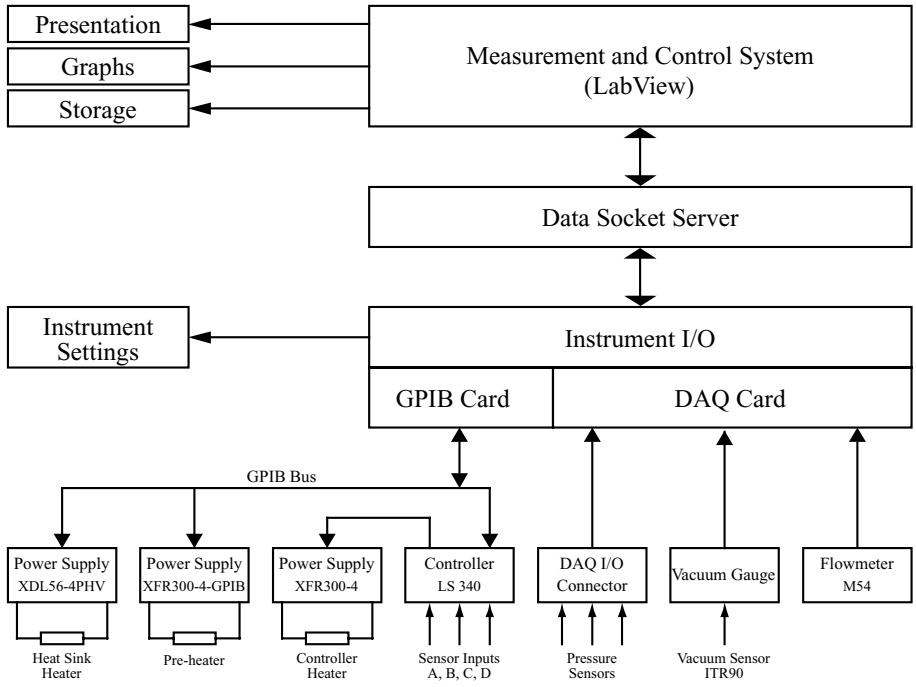

Figure 3.19: Data Acquisition System. Illustration by Steffen Grohmann.

The signal from the pressure sensors and the flow meter are analog signals. The calibration made of the flow meter and pressure sensors takes place in the Instrument I/O-application, which is a CVI-software.

The measurement and control system chosen is LabView 7.1. A user interface of the test rig with the various sensors and controls were used for operating the test facility. For various reasons, it was chosen to use a data socket server for the communication between LabView and the CVI-software. A screen shot of the LabView operating panel is shown in Figure 3.20.

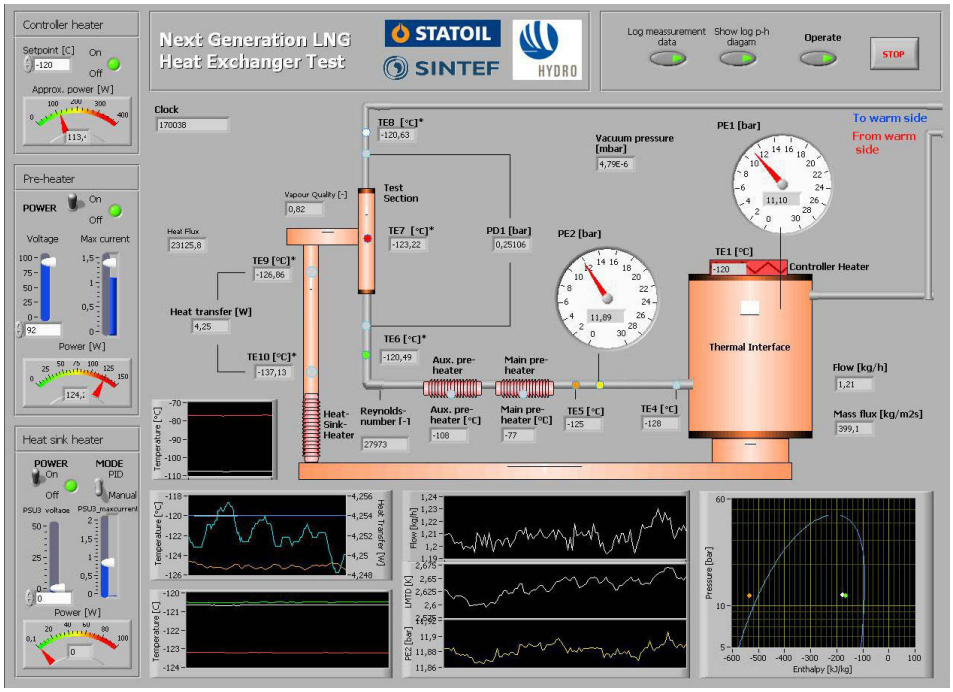

Figure 3.20: Screen shot of the LabView operation panel.

3.5 Error management

3.5.1 Error analysis

Each measurement point $x_{i,m}$ of a total j quantities was recorded over a period of 5 minutes, during which the facility was stable. In this period, data was recorded every 5 seconds and the $n = 60$ measurements makes out the sample mean value defined as $\bar{x}_i$ in Equation 3.22.

$$\bar{x}_i = \frac{1}{n} \sum_{m=1}^{n} x_{i,m} \tag{3.22}$$

The sample mean $\bar{x_i}$ is the best estimate for the actual quantity x_i, but this quantity has an uncertainty of Δx_i consisting of multiple parts. The standard deviation $\sigma_{\bar{x_i}}$ of a single measurement $x_{i,m}$ is calculated from Equation 3.23.

$$\sigma_{x_i} = \sqrt{\frac{1}{n-1}\sum_{m=1}^{n}\left(x_{i,m} - \bar{x}_i\right)^2} \tag{3.23}$$

This value is further used to find the standard deviation of the sample mean, expressed in Equation 3.24.

$$\sigma_{\bar{x_i}} = \frac{\sigma_{x_i}}{\sqrt{n}} \tag{3.24}$$

This expresses the uncertainty of $\bar{x_i}$ caused by the random fluctuations naturally occurring everywhere in nature and in all experiments.

Further, there is an error margin of the quantity caused by the uncertainties in the instruments used to measure its value. This include repeatability and stability in sensors, expressed by a deviation σ_{inst}, and possibly a calibration causing an uncertainty σ_{cal}. The error $\delta\bar{x_i}$ of a measured quantity $\bar{x_i}$ is expressed as the sum of squares of these errors as shown in Equation 3.25.

$$\delta\bar{x_i} = \sqrt{\sigma_{\bar{x_i}}^2 + \sigma_{\text{inst}}^2 + \sigma_{\text{cal}}^2} \tag{3.25}$$

As measurement values are used to calculate other values through functions $\bar{y} = f(\bar{x_1}, \bar{x_2}, \cdots, \bar{x_j})$, error is propagated from the measured values to the function value. The influence of the errors from the different values $\bar{x_i}$ on a functional value $\bar{y}$ is determined by finding the sensitivity $\partial\bar{y}/\partial\bar{x_i}$ of the measured value $\bar{x_i}$ on $\bar{y}$, and multiply it by its error δx_i. The summation of the different errors is done according to Equation 3.26.

$$\delta\bar{y} = \sqrt{\left(\frac{\partial\bar{y}}{\partial\bar{x_1}}\delta\bar{x_1}\right)^2 + \left(\frac{\partial\bar{y}}{\partial\bar{x_2}}\delta\bar{x_2}\right)^2 + \cdots + \left(\frac{\partial\bar{y}}{\partial\bar{x_j}}\delta\bar{x_j}\right)^2} \tag{3.26}$$

Uncertainty in correlation values

The horizontal uncertainty bars in the figures presented in Chapter 5 are caused by uncertainties in e.g. the measured mass flow $\dot{m}$ and the determination of d_{c}. The uncertainty of the mass flow $\delta\dot{m}$ influences the mass flux G and the vapour fraction x, yielding the uncertainties δG and δx respectively. The uncertainty of d_{c} also influence the uncertainty of the mass flux and the vapour fraction, as well as shear tensions, film thicknesses and

Reynolds numbers in the correlations. Due to the complexity of the different correlations, this is implemented in a different form than in Equation 3.26.

The different correlations depend on different parameters like mass flux G, diameter d, vapour fraction x and different fluid properties:

$$\mathrm{HTC_{calc}} = \mathrm{HTC_{calc}}(G, d, x, \mu_\mathrm{l}, \mu_\mathrm{v}, \rho_\mathrm{l}, \rho_\mathrm{v}, \sigma) \tag{3.27}$$

and the error caused by the different parameters is found in the following way, here for mass flux G:

$$\frac{\partial \mathrm{HTC_{calc}}}{\partial G} = \mathrm{HTC_{calc}}(G + \delta G, d, x, ...) - \mathrm{HTC_{calc}}(G, d, x, ...) \tag{3.28}$$

The total uncertainty of the correlation value is then found as

$$\delta \mathrm{HTC_{calc}} = \sqrt{\left(\frac{\partial \mathrm{HTC_{calc}}}{\partial G} \cdot \delta G\right)^2 + ... + \left(\frac{\partial \mathrm{HTC_{calc}}}{\partial x} \cdot \delta x\right)^2} \tag{3.29}$$

The standard deviation of the diameter d_c is shown in Table 3.2. The systematic uncertainty of determining d_c due to uncertainties in the microscope, the aperture setting and impurities in the tube samples is difficult to determine. Therefore, as its size is unknown, the uncertainty of the diameter is not included in Equation 3.29 as the only known size $\delta d_\mathrm{c} = \sigma_{d_\mathrm{c}}$ is small. This is a hidden factor that can make out a contribution.

The fluid properties like density ρ, viscosity μ and surface tension σ are determined by the pressure and temperature. Due to their moderate sensitivity to changes in temperature and pressure compared to the uncertainty level of temperature and pressure, their contribution to $\delta \mathrm{HTC_{calc}}$ in Equation 3.29 is considered negligible outside the area around the critical point and therefore left out.

3.5.2 Quantification of uncertainty

Table 3.5 shows the quantifiable uncertainties.

3.5.3 Other sources of uncertainty

Other errors are here listed in order to qualitatively say something about the reliability of the results from the test setup.

Instrument	Uncertainty	Unit
Flow meter	$\sigma_{\text{inst}} = 1\ \% + 0.05$ zero stability $\sigma_{\text{cal}} = 0.044$	kg/h
Pressure gauge	$\sigma_{\text{inst}} = 0.4\ \%$ $\sigma_{\text{cal}} = 0.1\ \%$	bar
Pressure difference gauge	$\sigma_{\text{inst}} = 0.33\ \%$ $\sigma_{\text{cal}} = 0.1\ \%$	bar
Temperature sensors	See Table 3.4	
Tube diameter	See Table 3.2	

Table 3.5: Quantification of errors

Thermal radiation shield

No temperature sensors are mounted on the temperature shield, but due to the use of high conductivity copper and the heat sink, it can be assumed that the temperature difference between the radiation shield and the test section is small. The temperature difference between the thermal interface and the test setup is also small.

For different fluids and pressure levels in the circuit, the temperature level of the cold part will vary. The temperature in the radiation shield is linked to this temperature level as it is thermally connected between the cold part of the setup and the cryo generator. At realistic temperature differences at different operation conditions, it has been estimated that an amount of max. 0.1 W net can be radiated to or from the copper rod where the sensors $T_{\text{HS},1}$ and $T_{\text{HS},1}$ are mounted. Therefore, the copper rod is covered with insulating foil to reduce this problem and this uncertainty is not included in the uncertainty calculations. The foil is not shown in Figure 3.18.

Bars for suspension and stabilisation

In order to suspend the pre-heaters and the general tubing in the cold part of the circuit, and number of bars where mounted to the top of the thermal interface and to the various tubes. It was also necessary to stabilise the circuit elements from vibrations caused by the cryo generator, as this is a reciprocating machine. These bars will always cause a heat leakage if there is a temperature difference between the thermal interface and the element being stabilised.

Three bars were identified that could influence the experiments; two bars suspending each of the pre-heaters, and a bar to suspend the tube

between the auxiliary pre-heater and the test section. All will reduce the actual enthalpy being added to the fluid by the pre-heaters compared with the power added to the pre-heaters by the power supplies. As these bars are made of thin low conductivity stainless steel tubes, the heat transfer from the circuit to the thermal interfaced was estimated to be in the order of 0.05 W. As the magnitude of the heat added to the pre-heaters is 10-150 W, this error is considered negligible for the experimental results.

Viscous heating

Morini [51] argues that viscous heating can explain some of the discrepancies among researchers for the Nusselt-number in microchannels. A correction factor to take viscous heating into account is given by Morini [51] in Equation 3.30:

$$Nu_\infty = \frac{Nu_0}{1 + \sigma Br} \tag{3.30}$$

where Nu_0 is a Nusselt number where $Br = 0$, Br is the Brinkman number defined by Equation 3.31 and σ is here a geometry and heating factor with the value $\sigma = 48\pi/11$.

$$Br = \frac{\mu u_\mathrm{l}^2}{k_\mathrm{l}(T_\mathrm{bulk} - T_\mathrm{w})} \tag{3.31}$$

The correction factor for the test facility is in the order of 10^{-5} K for the 1 mm tube and 10^{-4} K for the 250 µm tube. Hence, the error is too small to have practical influence for the results and will therefore not be accounted for. The diameter of the tubes in this work is simply too large.

Axial conduction

Axial conduction is heat transfer in the tube wall in the axial direction. It is predominant at low Re-numbers and occurs due to large temperature differences in the fluid. The fluid temperature has influence on the tube temperature, and heat will flow along the tube in axial direction as a result of this.

Chiou [17] gives a criteria for which the effects of axial conduction effects are not negligible, given as the value of M in Equation 3.32. Also Hetsroni et al. [32] and Maranzana et al. [46] did work on this subject.

$$M = \left(\frac{k_\mathrm{tube}}{k_f}\right)\left(\frac{d_o^2 - d_i^2}{d_i L}\right)\frac{1}{RePr} \tag{3.32}$$

If $M > 10^{-2}$, axial conduction has a significant effect. For the test facility, values are below this critical value and axial conduction effects will therefore not be taken into account.

Thermal entry length

Entrance length effects results in an increased heat transfer coefficient due to the not fully developed thermal layer in the entrance region of a tube. The undeveloped thermal boundary layer here is thinner than the developed, and there is therefore a larger temperature gradient across this layer, leading to a better local heat transfer in the entrance. This will cause an increase in the average heat transfer coefficient. The velocity profile however is regarded as fully developed.

Especially for short tubes and laminar flow, the measured average heat transfer coefficient can deviate from the heat transfer coefficient at fully developed conditions. A much used inequality, for which fulfilment the entrance length effect can be neglected for turbulent flow is given by e.g. Kays and Crawford [38] and [35].

$$\frac{Re \cdot Pr \cdot d}{L} < 20 \tag{3.33}$$

This inequality is not fulfilled for many operation situations for the test facility, and the thermal entrance length effect must therefore be accounted for. This applies for single phase flow where the correction factor is included in Equation 2.8.

Thermal entry length in two phase flow

For two phase flow, thermal entry length effects are not mentioned in the literature. In annular flow, one could imagine that the same principle as in Equation 3.33 applies, but now based on the film thickness δ instead of the diameter. Equation 3.33 is first written based on the tube radius, and then replacing the radius with the film thickness δ, as this is as far as the thermal boundary layer in the liquid must develop:

$$\frac{Re \cdot Pr \cdot 2r}{L} < 20 \Rightarrow \frac{Re_{\text{film}} \cdot Pr_{\text{film}} \cdot \delta}{L} < 10 \tag{3.34}$$

For Methane-100 in the 0.5 mm tube, the equation is fulfilled for 16% of the measurements, which means that thermal entry length effects can be neglected for most of the 0.5 mm tube measurements. The film is simply too thin.

Checking for thermal entry length effects using Equation 3.34 assumes that the same thermal mechanisms apply in the liquid film as for fluids in single phase flow. This is already the presumption in the condensation heat transfer coefficient from Thome [68], shown in Equation 2.13. This should indicate that for turbulent film, the thermal entry length effects could be accounted for on the same form as for single phase flow. In the case of Thome's correlation, this would look like

$$h = cRe_{\mathrm{l}}^{n} Pr_{\mathrm{l}}^{m} \frac{k_{\mathrm{l}}}{\delta} f_{\mathrm{i}} \left[1 + \left(\frac{2\delta}{L} \right)^{2/3} \right] \tag{3.35}$$

The correction is small for high x where the liquid film thinkness δ is small, but larger for low x. For the 1 mm tube with Methane-100, the improvement using Equation 3.35 predicts an average 3.3% larger heat transfer coefficient. The increase is small as the thermal boundary layer in the liquid thin film develops rather quickly through the test section.

Chapter 4

Experimental Program

4.1 Measurement parameters

The parameters to be investigated are listed in Table 4.1.

The nominal operating conditions of the test rig are based on current LNG heat exchanger design with $q'' = 12\ 000$ W/m^2 and $G = 400$ kg/m^{2}s. The heat flux and mass flux were mostly varied within twice and half of the nominal conditions but experiments outside this band were also carried out. The vapour fraction is a very important parameter and was varied at least three times during each measurement series. The behaviour at different pressure levels influence the surface tension and the density of the phases.

A design process of a heat exchanger involves the balancing between heat transfer at the cost of pressure drop and surface area. A broad investigation of the relevant parameters related to heat transfer and pressure drop is therefore important.

4.2 Test fluids

As can be seen in Table 4.1, three binary fluids with methane as the main component were chosen in addition to pure methane. The number in their name refers to their percentage to methane on a molar basis, e.g. Ethane-10 has 10% ethane and 90% methane. Pure nitrogen was used for some single phase measurements.

Methane-100 Firstly, pure methane is chosen as it is the main component in natural gas. The results from pure methane establish the reference basis for the rest of the fluids, and it can be compared to heat transfer and pressure drop correlations developed for other pure substances.

Parameter	Min - Max (single phase)	Min - Max (two-phase)
Mass flux G [kg/m^{2}s]	270 - 4 200	140 - 1370
Vapour fraction x [-]	-	0.12 - 0.87
Heat Flux q'' [kW/m^2]	4.0 - 41	7.2 - 50
Pressure p [bar]	7 - 60	7 - 41
	Number of variations	Variation values
Tube diameter	3	0.25 mm 0.5 mm 1.0 mm
Fluid composition*	5	Methane-100 Ethane-27 Ethane-10 Nitrogen-10 Nitrogen-100

Table 4.1: Parameter variation and names of fluids. *Fluid compositions are found in Table 6.1.

Ethane-27 This mixture clarify the effects when a component which is less volatile is mixed with methane.

Ethane-10 This mixture is not very far from a typical natural gas composition liquefied in an actual LNG-plant, as ethane and heavier components can make out approx. 10% of the composition.

Nitrogen-10 As opposed to ethane, nitrogen is a more volatile component than methane and the condensation process and mass transfer effects are different from the Ethane-10 mixture.

Nitrogen-100 Some tests of single phase nitrogen at both liquid and supercritical conditions were done.

All the binary fluids are zeotropic. As will be discussed in Chapter 6.3, the composition of the fluid circulated was slightly different from the composition filled into the fluid circuit. Therefore, the fluids are named according to the actual circulated composition, and not according to their certified composition.

4.3 Measurement program

First, measurements were done on cooled single phase liquid flow. The single phase heat transfer data have a value of its own and are also used to calibrate the set-up. In order to capture different effects, these include measurements at different pressure, mass flux and heat flux on each tube and on most of the fluids.

For two-phase flow, the vapour fraction is an additional variable. Within the same pressure, most measurement series have been taken with constant heat flux or constant mass flux with varying vapour fraction. Some series have been recorded with constant mass flux and vapour fraction, with varying heat flux.

The number of measurements conducted are listed in Table 5.1 and all the 749 measurement values are listed in Appendix A. The test period lasted from August 2007 to September 2008.

Chapter 5

Experimental results and discussion

The most important presumptions in the evaluation of the results are:

- Based on the discussion in Chapter 3.2, d_c is used as the diameter in the calculations for each tube. However, the tubes are named after their nominal diameter for easy reference. A complete overview of the actual diameters can be found in Table 3.2.
- For pressure drop comparison with correlations, the friction factor f is calculated from the Colebrook-equation. A comparison using the friction factor in a smooth tube is also done. If the smooth tube friction factor is not specified in the correlation, the friction factor $f = 0.316Re^{-0.25}$ is used for $Re > 3000$ and $f = 64/Re$ for $Re < 3000$.
- All results are presented at average values. The test section is short and the difference in vapour fraction is small. Therefore the average values should be close to the local values, i.e. $h \approx \overline{h}$, $x \approx \overline{x}$ and $p \approx \overline{p}$.
- The pressure is always presented as the absolute pressure.
- Inlet effects caused by the undeveloped temperature profile are not taken into account for laminar flow except in Figure 5.4. They are taken into account for turbulent flow in the models predicting the measured heat transfer (Equation 2.6). Inlet effects for two phase flow are discussed in Chapter 3.5.3.
- For the single phase flow, the heat transfer is expressed by the Nusselt number. For two phase flow, the heat transfer coefficient (denoted HTC or h) is used.

5.1 Overview of measurements

The total number of measurements is shown in Table 5.1, where the number of single phase measurements are shown in parenthesis. For overview, Figures C.4 to C.1 in Appendix C show the measurements in pressure-enthalpy diagrams and in mass flux-vapour fraction diagrams for all fluids.

Fluid/Tube name	1 mm	0.5 mm	0.25 mm	Total
Methane-100	135 (104)	42 (26)	12 (11)	189 (141)
Ethane-27	104 (23)	25 (18)	4	133 (41)
Ethane-10	94	21	5 (26)	120 (26)
Nitrogen-10	62 (10)			62 (10)
Nitrogen-100	(18)	(9)		(27)
Total	395 (155)	88 (53)	21 (37)	504 (245)

Table 5.1: Number of measurements for each fluid and tube. Single phase measurements in parenthesis.

5.2 Single phase flow verification

Figure 5.1 shows the values of $\dot{Q}_{\mathrm{TS}}$ and $\dot{Q}_{\mathrm{HB}}$ for all the single phase flow measurements, i.e. over a wide range of pressure, fluids, flow rates for all three tubes. They show that the sensors $T_{\mathrm{HS},1}$, $T_{\mathrm{HS},2}$, T_{in} and T_{out} are correctly calibrated and that the measuring concept behind $\dot{Q}_{\mathrm{TS}}$ in Equation 3.4 is appropriate. The data in Figure 5.1 corresponds to a maximum heat flux of 25.4, 27.3 and 76.2 kW/m^2 for the 1, 0.5 and 0.25 mm tubes respectively.

The two deviating measurements for Ethane-10 in the 0.25 mm tube marked (a) were taken at very low mass flow rate, and hence their value of $\dot{Q}_{\mathrm{HB}}$ has a large uncertainty. The cause for the deviating measurements for Ethane-27 marked (b) for the 1 mm tube is unknown.

The calibration of T_{b} was done by a number of adiabatic measurements, both in single phase and two phase flow. T_{b} should be the same as the value of both T_{in} and T_{out} for adiabatic single phase flow, and equal to the average of T_{in} and T_{out} for adiabatic two-phase flow. However, a discrepancy of approx. 0.1 K was observed between T_{b} for single and two-phase flow. This can be caused by a small heat flux in the copper block as there is a drop in saturation temperature along the 5 cm long test section for two phase flow. Nevertheless, this represents an additional uncertainty, and the original uncertainty of T_{b} of 0.08 K is therefore changed to 0.2 K in Table

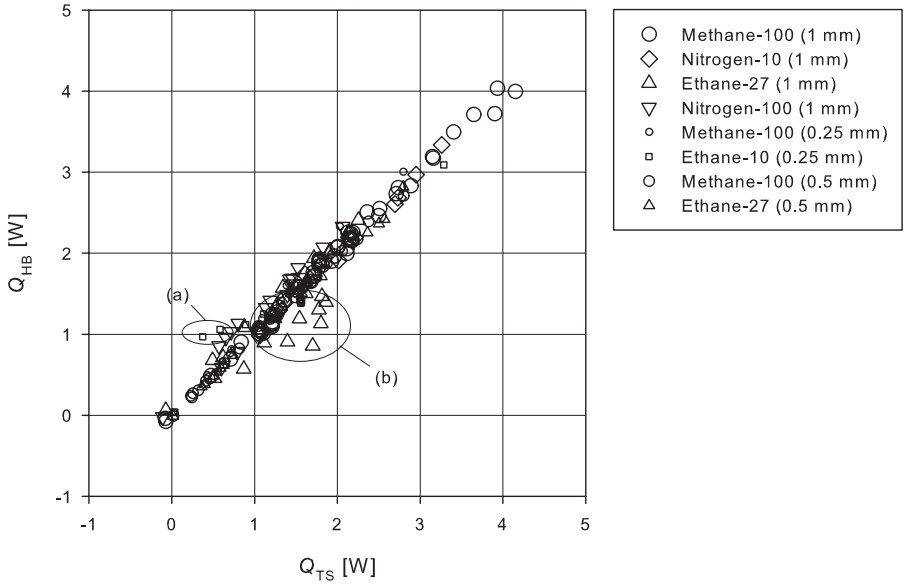

Figure 5.1: Heat balance for the fluids in the three tubes.

3.4. This is a conservative approach which yields a higher uncertainty of all the presented measurements.

A criterion for determining if heating by viscous dissipation is relevant is found in Celata et al. [14], where the uncertainty of the temperature sensors, 0.08 K, was chosen as the characteristic temperature. The temperature rise even for the 0.25 mm tube was below the measurement uncertainty of the sensors. Hence, heating by viscous dissipation can be neglected.

5.2.1 Single phase heat transfer - laminar to turbulent flow

Figures 5.2 and 5.3 show the heat transfer characteristics in the transition area from laminar to turbulent flow in the 0.5 mm and 0.25 mm tube, respectively. For the 0.5 mm tube, the Reynolds number for the transition point is not obvious. The transition is more visible in the 0.25 mm tube, where it appears at Reynolds number around 2000. The value of $Re \approx 2300$ is often used as the transition Reynolds number in conventional tubes. In reality, the transition area ranges from Re $\approx$ 2000 to Re $\approx$ 10000. The uncertainty of G is large at these small flow rates, which is reflected in the uncertainty of the Re-number.

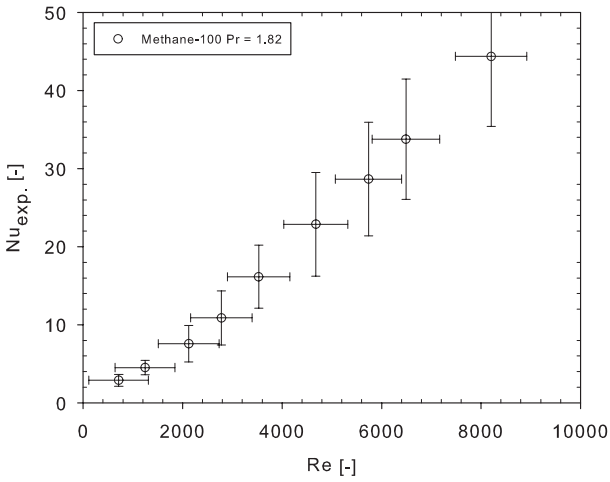

Figure 5.2: Experimentally obtained heat transfer in laminar/turbulent flow for Methane-100 in the 0.5 mm tube.

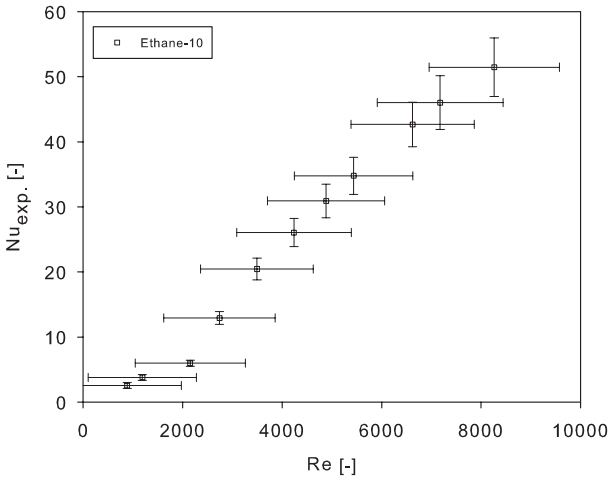

Figure 5.3: Experimentally obtained heat transfer in laminar/turbulent flow for Ethane-10 in the 0.25 mm tube.

As the thermal boundary layer starts developing at the entrance of the test section, the initial thermal boundary layer is thin and the local Nusselt number Nu_x high. As the boundary layer develops, the Nusselt number is reduced and reaches the asymptotic value of $Nu_\infty = 3.66$ for constant wall temperature conditions if the tube is long enough. The average Nusselt number Nu_m through a section with developing boundary layer can be written

$$Nu_m = \frac{1}{L^+} \int_0^{L^+} Nu_x(L^+)\, dL^+ \tag{5.1}$$

where L^+ is a reduced length which in this case is written as:

$$L^+ = \frac{2L}{d_c Re Pr} \tag{5.2}$$

as found in Kays and Crawford [38]. Analytical values of Nu_x can be found from boundary layer analysis and by using Equation 5.1, values for Nu_m can be found as a function of L^+. These values are plotted in Figure 5.4 and apply for laminar flow in a smooth tube.

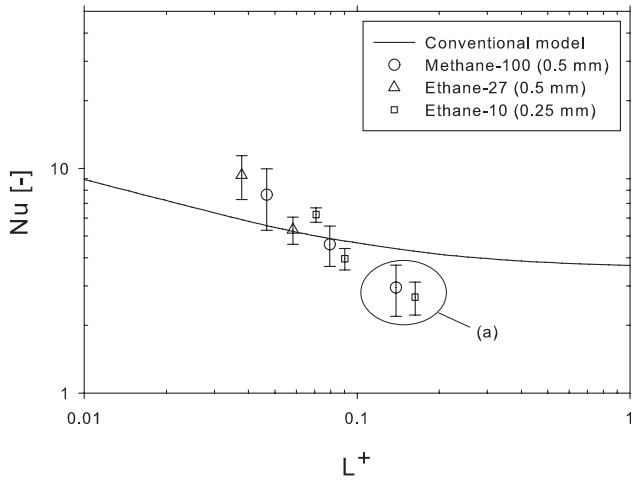

Figure 5.4: Experimentally obtained heat transfer for $Re < 2300$ compared to Equation 5.1. (a) shows measurements with Nusselt number below 3.0.

The agreement between the experimental Nusselt numbers and the predicted is not good. The results where the measured Nusselt numbers are larger than predicted can be explained by enhanced heat transfer due to the surface roughness. The experimental Nusselt numbers that are below the

predicted, and particularly the one below the asymptotic value 3.66 must be explained by incorrect calculation of the Nusselt number. A Nusselt number below 3.66 could indicate conduction (no flow) instead of convection, which also might be the case; The uncertainty of G is 123 % for the 0.25 mm measurement and 84 % for the 0.5 mm tube encircled in (a). Obviously, the test set-up is not designed for such low flow measurements and the validity of the results can be questioned.

5.2.2 Single phase heat transfer - turbulent flow

In the turbulent flow results presented in Figures 5.5 to 5.7, the Dittus-Boelter equation is shown for comparison. It applies for smooth tubes, for $Re > 10000$, does not take inlet effects into account and is plotted for a constant Prandtl-number. It is therefore for illustration purposes only as it is simple to implement. Further comparison with the much more acknowledged Gnielinski model is done in Chapter 5.2.2.

Figure 5.5 shows most of the single phase measurements for the 1 mm tube. The large scatter for the supercritical measurements can be due to the fact that the fluid properties are very temperature sensitive around the critical point. This gives a large variation in the heat transfer properties of the flow.

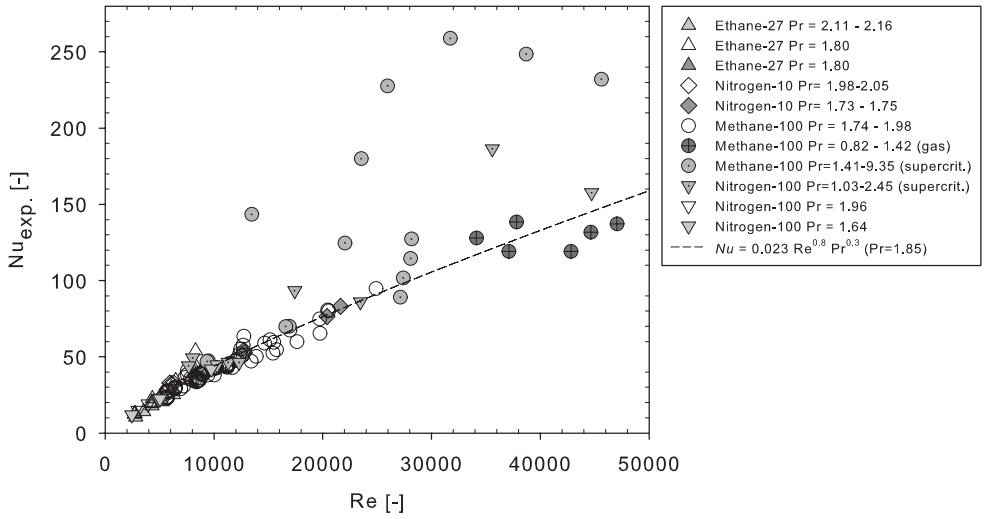

Figure 5.5: Nusselt number versus Reynolds number for single phase flow of all fluids in the 1.0 mm tube

The seven gas phase measurements included also show a good agreement with the liquid flow measurements for Methane-100. The supercritical measurements of Nitrogen-100 show less scatter. They are conducted at pressure close to twice the critical pressure for nitrogen where the fluid properties are less temperature sensitive.

As the relative roughness for the 1 mm tube is small, the good agreement between measurement data and the Dittus-Boelter-equation indicates that the data are well predicted. A more detailed view of these measurements

with uncertainties can be found in Figure 5.9.

For the single flow results for the 0.5 mm tube shown in Figure 5.6, the Methane-100 measurements show a lower Nusselt-number than the other fluids. The reason for this could be related to the prediction of thermophysical properties of the fluid or to the mass flow uncertainty. Most of the measurements show a higher Nusselt-number than predicted by the Dittus-Boelter-equation, which is no surprise as the surface roughness breaks up the laminar sub layers and leads to larger heat transfer. This is particularly valid for high Reynolds-numbers. A comparison with the Gnielinski-equation taking the roughness into account in presented in Figure 5.10. All the results for the 0.5 mm tube are in the liquid phase.

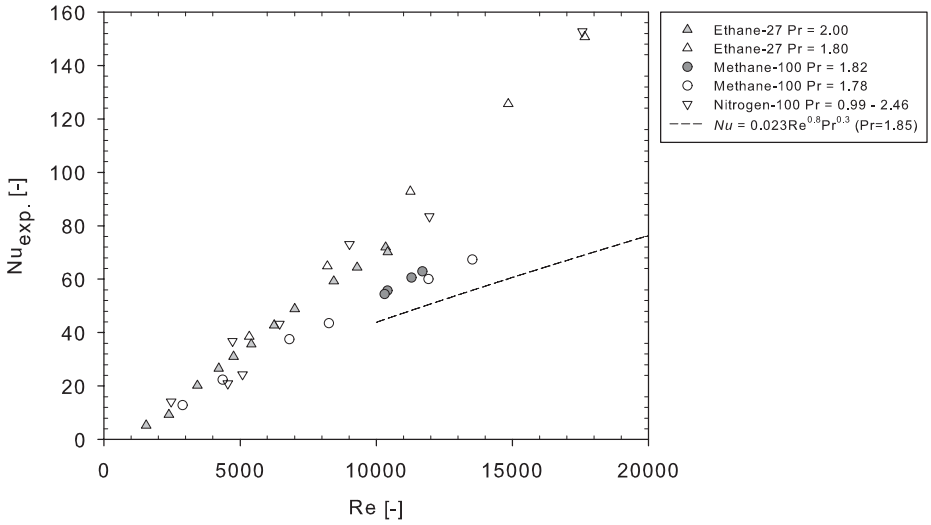

Figure 5.6: Nusselt number versus Reynolds number for single phase flow of all fluids in the 0.5 mm tube (Not including the results shown in Figure 5.2.)

For the 0.25 mm tube in Figure 5.7, the differences between the fluids are not large and the measured Nusselt-numbers are also higher than what the Dittus-Boelter-equation predicts. The relative roughness is higher for the 0.25 mm tube than for the 0.5 mm tube and therefore the Nusselt-numbers are higher when comparing to the plots of the Dittus-Boelter-equation.

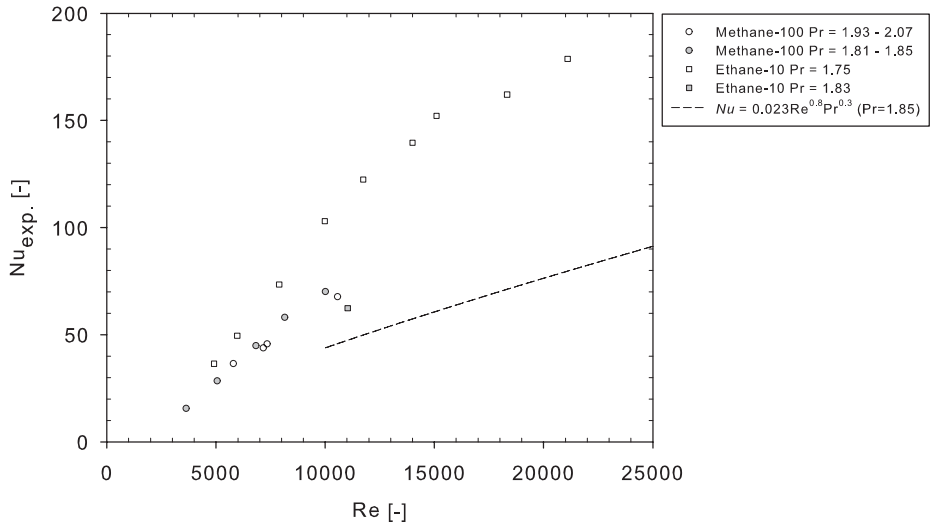

Figure 5.7: Nusselt number versus Reynolds number for single phase flow of all fluids in the 0.25 mm tube (Not including the results shown in Figure 5.3).

Figure 5.8 shows measured Nusselt-number for the 1 mm tube for different heat flux q'' using the Reynolds number as parameter. The maximum increase from the lower to the highest Nusselt number within the series is 5.5 %, which is well within the uncertainty of the Nusselt-number. The uncertainty increases for lower heat flux as the difference between T_w and the average fluid temperature decreases. The uncertainty is also larger for higher Reynolds number as the heat transfer is higher and thus the temperature difference is lower for a given heat flux.

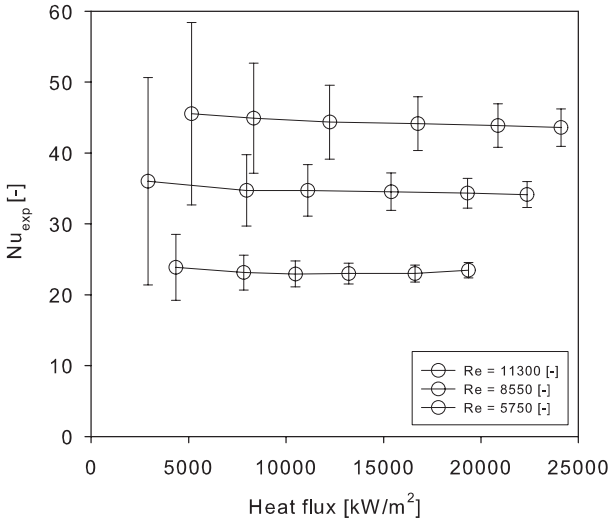

Figure 5.8: Experimentally obtained heat transfer for different heat flux using the Reynolds number as parameter in the 1 mm tube. Pr = 1.83-1.86.

For turbulent flow, Figures 5.9 to 5.11 shows the experimental heat transfer coefficient compared to the calculated Nusselt number from the Gnielinski-equation [29] using the Colebrook friction factor. The Methane-100 measurements were performed with pressure ranging from 7.5 to 52 bar, hence also in the supercritical area. The Nitrogen-100 measurements are all done at approx. 60 bar. The heat flux varied from 4000 to 41000 W/m^{2}K and mass flux varied from 270 to 4200 kg/m^{2}s.

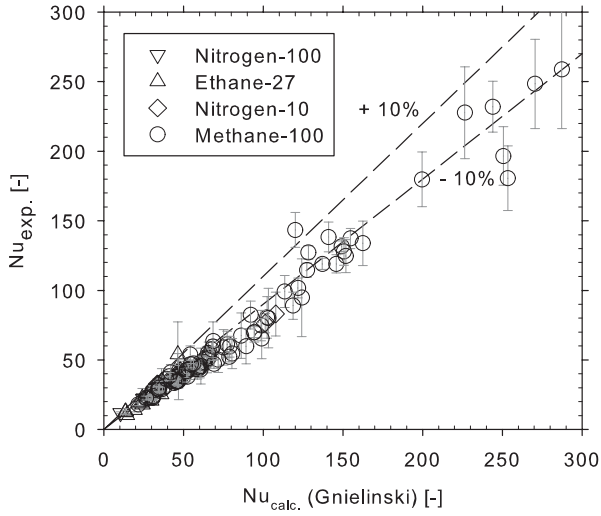

Figure 5.9: Calculated and experimentally obtained heat transfer in turbulent flow for all fluids in the 1.0 mm tube.

For the 1 mm tube, only the uncertainty for the experimental Nusselt number is shown as the uncertainty in the calculated Nusselt number generally is small due to the small uncertainty in the mass flow at these flow rates. For the Methane-100 measurements for the 1 mm tube, the measurements in the gas phase and super critical phase represent the results with the highest Nusselt-number in Figure 5.9.

Table 5.2 summarises the single phase heat transfer results, and the results are also compared with the Gnielinski-correlation using the friction factor for a smooth tube.

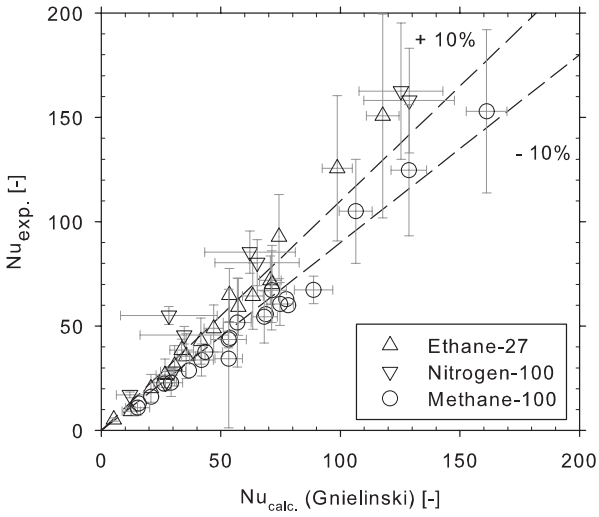

Figure 5.10: Calculated and experimentally obtained heat transfer in turbulent flow for all fluids in the 0.5 mm tube.

On average for all the fluids using $f_{\text{Colebrook}}$, the measured Nusselt-number for the 1 mm tube is lower than predicted and as predicted for the 0.5 mm tube. The average measured Nusselt-number is also lower than predicted for the 0.25 mm tube. Using the friction factor for a smooth tube under predicts the Nusselt number for the 0.5 mm and 0.25 mm tubes. This indicates that a suitable roughness is lower than the measured roughness.

The Methane-100 measurements seem to be lower than expected while the ethane-mixture experiments yield a higher Nusselt number. The reason for this is unknown but can be related to property calculations.

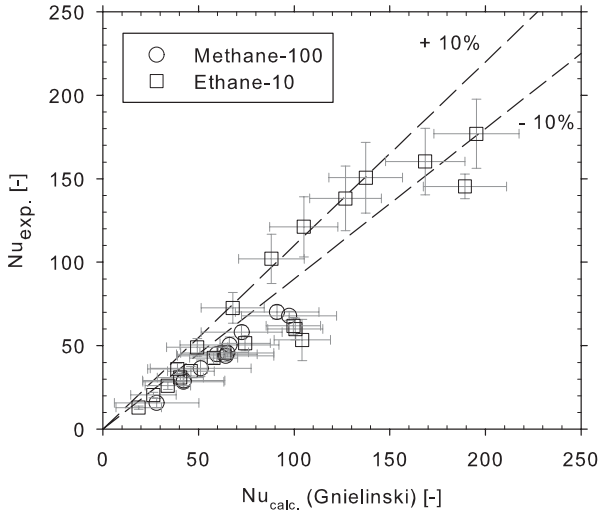

Figure 5.11: Calculated and experimentally obtained heat transfer in turbulent flow for all fluids in the 0.25 mm tube.

Correlation / Tube		Gnielinski [29] and $f_{\text{Colebrook}}$	Gnielinski [29] and f_{smooth}
1 mm	Average deviation	1.21	1.11
	Within 0.8 and 1.2	49 %	75 %
0.5 mm	Average deviation	1.05	0.81
	Within 0.8 and 1.2	52 %	50 %
0.25 mm	Average deviation	1.31	0.73
	Within 0.8 and 1.2	28 %	38 %

Table 5.2: Heat transfer results for single phase flow. Average deviation refers to the average value of Nu_{calc} / Nu_{exp}.

5.2.3 Liquid phase pressure drop

Figure 5.12 shows the frictional pressure drop plotted against the mass flux for Methane-100. The measurements correspond to the results for Methane-100 presented in Figures 5.5 - 5.7. The pressure drop dependence on the mass flux can for each tube be fitted well to an equation on the form $y = ax^b$ and the values of a and b are shown. The agreement is good.

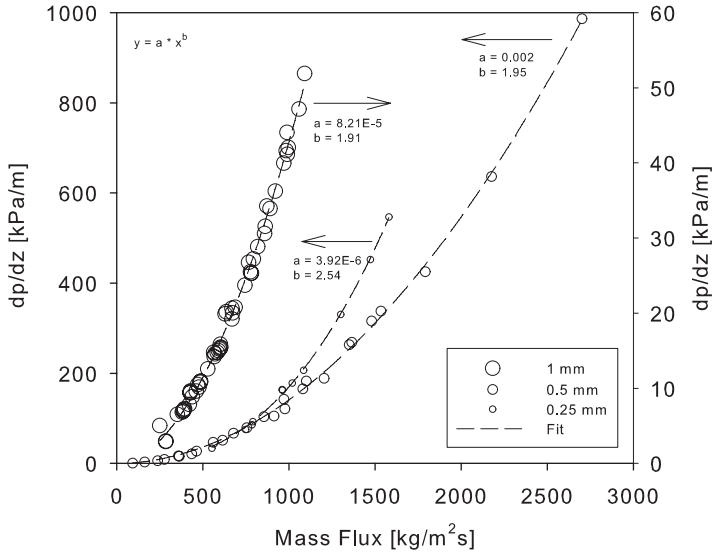

Figure 5.12: Pressure drop versus mass flux for Methane-100 for all tubes. Only subcritical liquid measurements included for the 1 mm tube.

Figure 5.13 shows the friction factor obtained from Equation 2.36 as a function of the Reynolds-number. The measurement points are the same as presented in Figure 5.12 in addition to some binary fluid measurements. The friction factor predicted by the Colebrook-equation based on the relative roughness for each tube is shown. Also shown is the turbulent friction factor for a smooth tube and the friction factor for laminar flow.

The results for the 1 mm tube is in good agreement with the Colebrook friction factor. This is not the case for the 0.5 mm and 0.25 mm tubes, where the friction factor is mostly higher than predicted for the 0.5 mm tube and lower for the 0.25 mm tube.

For the 0.5 mm tube, the friction factor is constant and seemingly independent of the Reynolds-number for $Re > 10000$ and approximately 30 % higher than predicted by the Colebrook-equation. For $Re < 10000$, the

friction factor decreases towards the values for laminar flow. This is an indication that the flow is not fully turbulent in this area. For the lowest Reynolds numbers, the pressure drop is very low and the resulting uncertainty of the friction factor is high. The measurement series for Methane-100 and Ethane-27 are consistent except for the few measurement points at $Re > 15000$.

It seems that the Methane-100 measurements in the 0.25 mm tube all are in the transition regime between laminar and turbulent flow. The results for Ethane-10 series span from the transition area and into the turbulent area. However, there is a systematic difference between the friction factor in the transition regime between Methane-100 and Ethane-10.

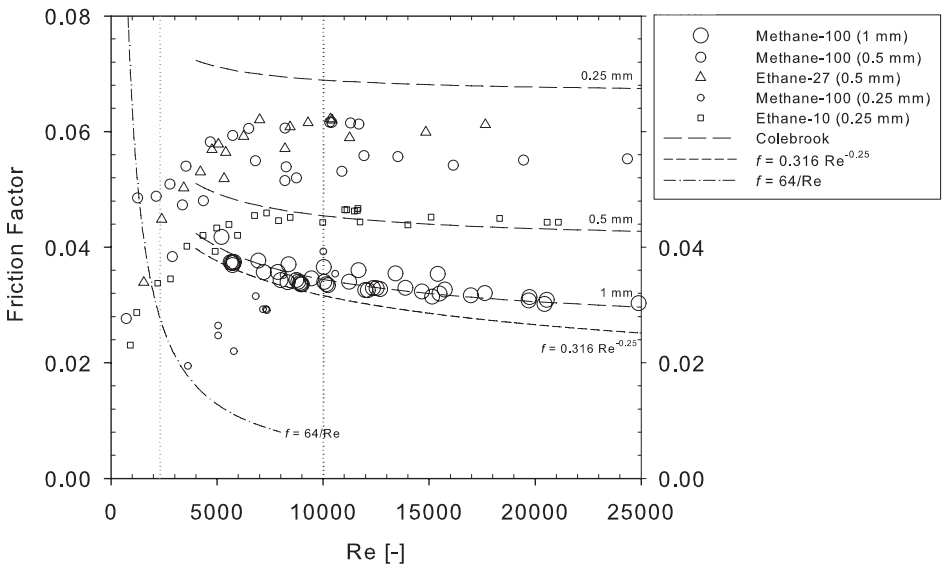

Figure 5.13: Measured friction factor as a function of Reynolds number for Methane-100 for all tubes. Only subcritical liquid measurements included.

There is an inconsistency between the results from the 0.5 mm and 0.25 mm tubes compared to the relative roughness given in Table 3.2, where the experimentally obtained friction factor for the 0.5 mm tube is larger than for the 0.25 mm tube.

Discussion

The agreement between the measured pressure drop and the predicted pressure drop from Equation 2.37 and the Colebrook-equation is shown in Table 5.5 for all the tubes and fluids. As also shown in Figure 5.14, the pressure drop measurements for the 1 mm tube fits well with the expected based on the friction factor from the Colebrook-equation while this is not the case for the 0.5 mm and 0.25 mm results.

As for the heat transfer measurements, the uncertainty of the mass flow illustrated by the error bars can explain the deviation for the 0.25 mm tube. For the lowest pressure drop measurement for the 0.25 mm tube, a mass flow of 0.07 kg/h was circulated, which yields an uncertainty of ±0.051 kg/h (see Table 3.5). Obviously, this leads to very broad error bars.

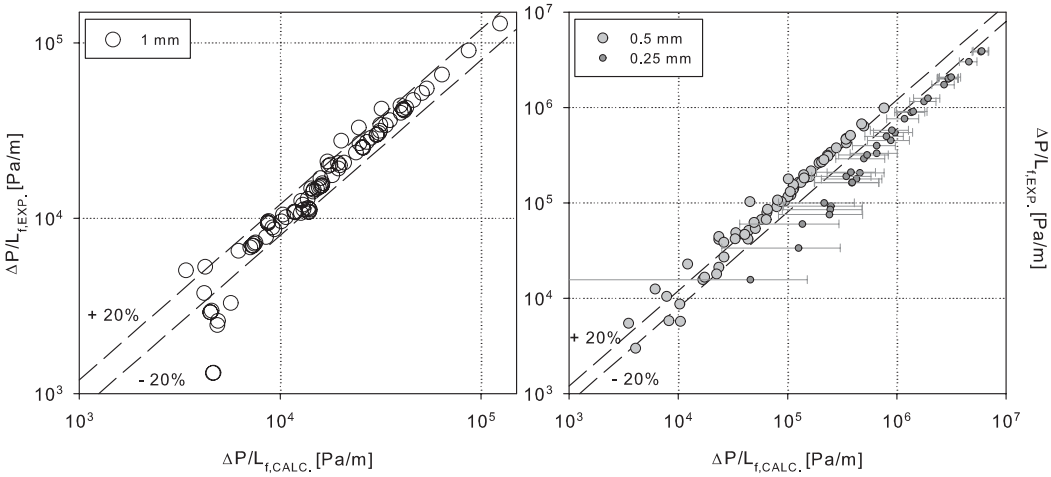

Figure 5.14: Calculated and experimentally obtained pressure drop for single phase flow for all fluids in all tubes $f_{\text{Colebrook}}$.

The evaluated uncertainty for the measured friction factor is almost exclusively dependent on the uncertainty of the mass flux. This is because the full uncertainty of d_c is not known and the uncertainty of ρ is small. The uncertainty of the Reynolds number in Figure 5.2 and 5.3 is closely linked to the uncertainty of G. As a result, the uncertainty of the friction factor in Figure 5.13 is 50 % or higher in the 0.25 mm tube and 18 % or higher in the 0.5 mm tube. This can explain the difference between the Methane-100 and Ethane-10 series in the 0.25 mm tube and also compared to the friction factor for the 0.5 mm tube. More emphasis should therefore be put to the

0.5 mm friction factor results than on the 0.25 mm results.

Another explanation could be that the Colebrook friction factor in Equation 2.41 is unsuited to represent the surface effects at this scale. A comparison is therefore made where the smooth tube friction factor is employed. The results are presented in Table 5.5. The predicted pressure drop in the 1 mm tube is more or less unchanged, while the 0.5 mm measurements are under predicted. The 0.25 mm measurements now fit better with the prediction, but are generally under predicted for high pressured drop and over predicted for low pressure drop.

5.2.4 Summary

Most of the results presented in Figures 5.1 to 5.14 are within the error margin compared to the values obtained from the established theory. Some results are outside a ± 10 % band, but some scatter must be expected.

It can not be argued that single phase heat transfer and pressure drop in small channels differ phenomenologically from larger tubes. Though it is unclear if the friction factor using the relative roughness can express the tube wall conditions in a satisfactory way. The high uncertainty of the mass flow meter makes the results from 0.25 mm unfit for a conclusion.

5.3 Two phase flow results

5.3.1 Introduction

For many measurement series with constant parameters, such as mass flux, heat flux, pressure or vapour fraction, it could be difficult to preserve the exact same values throughout the series. Where there has been a variation, this is mentioned in the figure caption. These variation are normally not important for the comparison. Where it is relevant, it is mentioned in the legend.

The vapour fraction does in some figures extend the usual range of $0 \leq x \leq 1$ on the abscissa, which does not give any physical meaning when the vapour fraction is defined as the vapour flow rate divided on the total flow rate. Alternatively, it can be defined as the enthalpy faction as in Equation 3.18, which for a pure component equals the vapour fraction. In this way it can be used to correctly place the corresponding liquid and gas phase measurements alongside the two phase measurements.

For most series, three graphs are presented. The upper shows the heat transfer coefficient as a function of either the vapour fraction or heat flux. The second graph shows the uncertainty for the heat transfer coefficient. For the 0.5 and 0.25 mm tubes, also uncertainty in the vapour fraction is included. This is small and may be neglected for the 1 mm tube.

The third graph shows comparison with a heat transfer model. For the 1 mm Methane-100 measurements, the experimental data are compared to the model from Thome et al. [68] as this is the model with the most extensive physical basis. This model however did not give a good agreement for the 0.5 and 0.25 mm tubes, therefore these results are compared with the model from Cavallini et al. [11]. The binary heat transfer results are all compared to the multi component model (Equation 2.32) using Cavallini et al. [11] as the single component model. This is discussed in Chapter 5.3.8.

5.3.2 Condensation heat transfer - Methane-100

Results for the 1 mm tube

Figure 5.15 shows the heat transfer coefficient as a function of vapour fraction x with mass flux as a parameter. The pressure and heat flux is kept constant. The heat transfer coefficient increases with increasing mass flux and increasing vapour fraction. Three corresponding single phase measurements are also included in order to show the transition between single and two phase heat transfer.

The uncertainty increases with increasing heat transfer coefficient but never exceeds 13 %. As $\dot{Q}_{\mathrm{TS}}$ is kept constant and h increases for increasing vapour fraction, the difference $\Delta T_{\mathrm{w,m}}$ is reduced. The closer the wall temperature is to the bulk temperature, the larger the uncertainty is. The uncertainty of $\dot{Q}_{\mathrm{TS}}$ also increases for reduced heat flux due to the reduction in temperature difference between $T_{\mathrm{HS},1} - T_{\mathrm{HS},2}$ in Equation 3.4. However, the contribution from $\Delta T_{\mathrm{w,m}}$ is dominating.

The experimental values are higher than predicted by the model from Thome et al. [68] and the deviation is increasing for reduced vapour fraction.

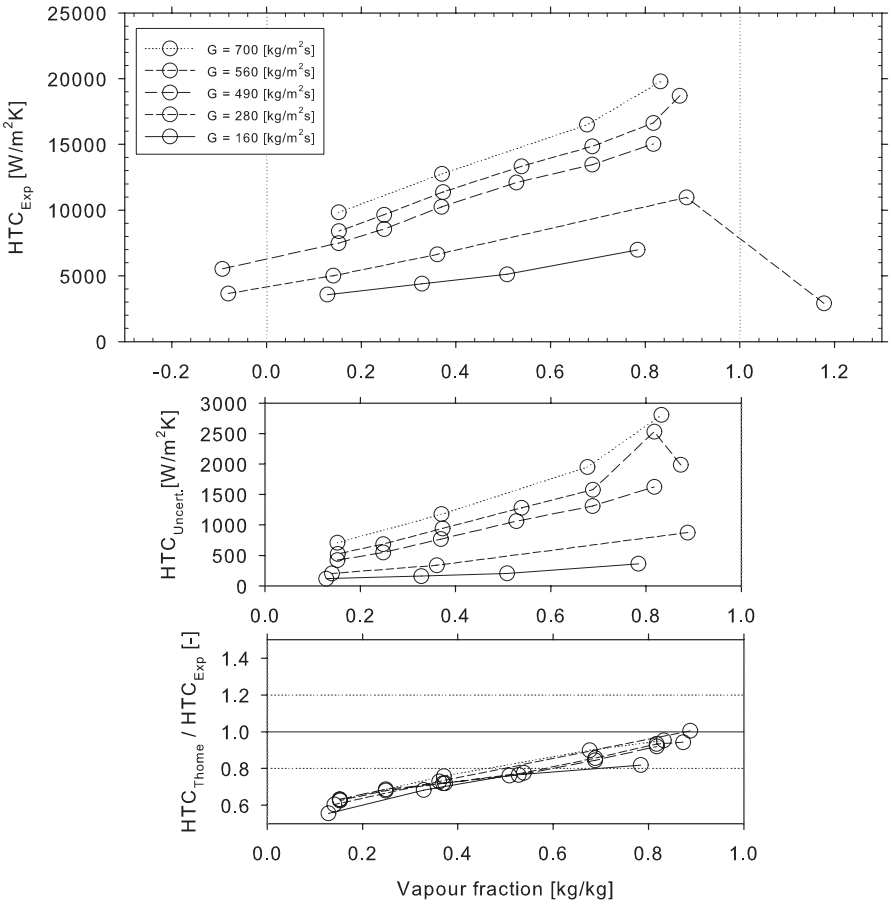

Figure 5.15: Heat transfer coefficient for Methane-100 in the 1 mm tube with mass flux as parameter. $q'' \approx 26.3$ kW/m^2, pressure $25.6 < p < 26.8$ bar.

Figure 5.16 shows the influence of vapour fraction x on the heat transfer coefficient with heat flux q'' as a parameter. The heat transfer coefficient is independent of the heat flux for single component condensation, which is in agreement with the models. This is also an important validation of the test facility, as results are consistent for different operating conditions. As can be read of from Figure 5.16, the uncertainty approaches approx. 35 % for the lowest heat flux.

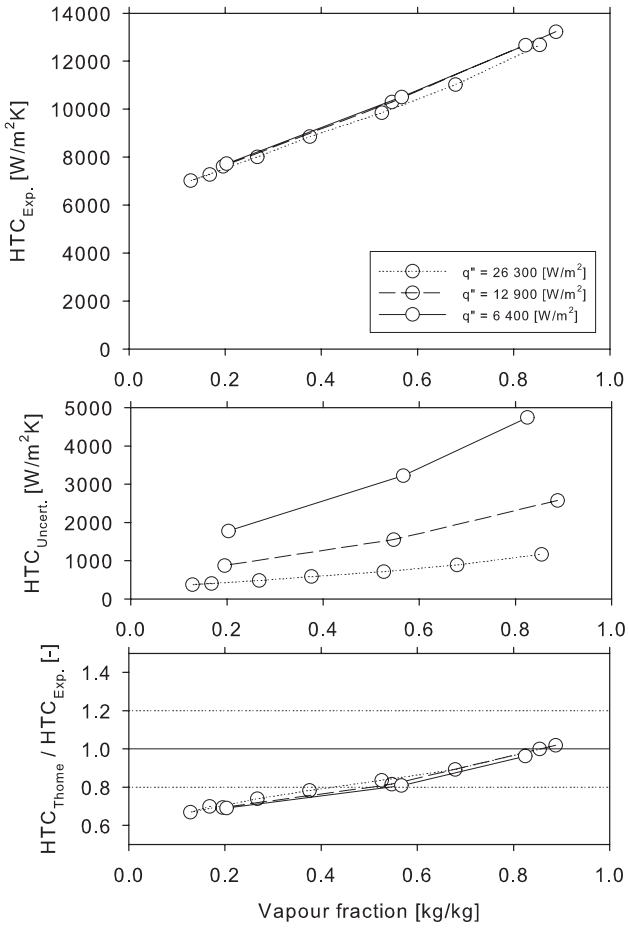

Figure 5.16: Heat transfer coefficient for Methane-100 in the 1 mm tube with heat flux as parameter. Constant mass flux $G \approx 490$ kg/m^{2}s, pressure $p \approx 35.7$ bar.

The figures 5.17 and 5.18 show the influence of pressure for two mass fluxes where also corresponding single phase measurements are included. At high pressure, the density difference between liquid and vapour is reduced, viscosity is reduced, specific heat is increased and the surface tension approaches zero when approaching the critical pressure. A small difference between the vapour and liquid phase densities usually leads to a lower slip ratio (ratio between the vapour velocity and the liquid velocity). This usually leads to lower shear stress between vapour and liquid and lower heat transfer coefficient. Though for high pressures, the Prandtl number increases and this counteracts the effects from the reduced shear stress.

This effect is evident in the case for $G = 280$ kg/m^{2}s where the heat transfer coefficient decreases for higher pressure except for the case for 41.6 bar which shows a heat transfer coefficient slightly higher than at 35.3 bar. The situation is the same where $G = 490$ kg/m^{2}s, but the difference between 35 bar and 41 bar is larger.

The increase at $p \approx 41$ bar is anticipated in the model from Thome et al. [68] where $G = 280$ kg/m^{2}s, as the model deviation is roughly the same for $p = 6.7$ bar and $p = 41.6$ bar. For $G = 490$ kg/m^{2}s, the model does not capture this effect that well. In Figure 5.18, the series at $p = 12.8$ bar stands out as it has a much lower heat transfer coefficient compared to the other series.

Spite a lower slip ratio, the model from Thome et al. [68] predicts an increase in the heat transfer coefficient from $p = 36$ bar to $p = 41$ bar. At pressures close the critical pressure (41 bar corresponds to $p_r = 0.89$), the liquid Prandtl-number more than doubles compared to $p = 26$ bar and the viscosity is reduced. The latter leads to an increase in the liquid Reynolds number. These two effects appear to outweigh the effect from the decrease in velocity.

The corresponding single phase flow measurements show a good agreement with the two-phase flow measurements. The single phase heat transfer coefficient is generally higher for high pressures as the liquid density near saturation decreases and the velocity increases. For $-0.3 < x < 0.6$ there appears to be a smooth transition between the measurements. However for $0.8 < x < 1.2$, there is a abrupt difference between two phase and single phase heat transfer and the x which gives the maximum heat transfer can not be located. The flow was unstable for $x > 0.85$ and therefore no measurements were recorded in this area. The instability is probably caused by unstable boiling in the pre-heaters.

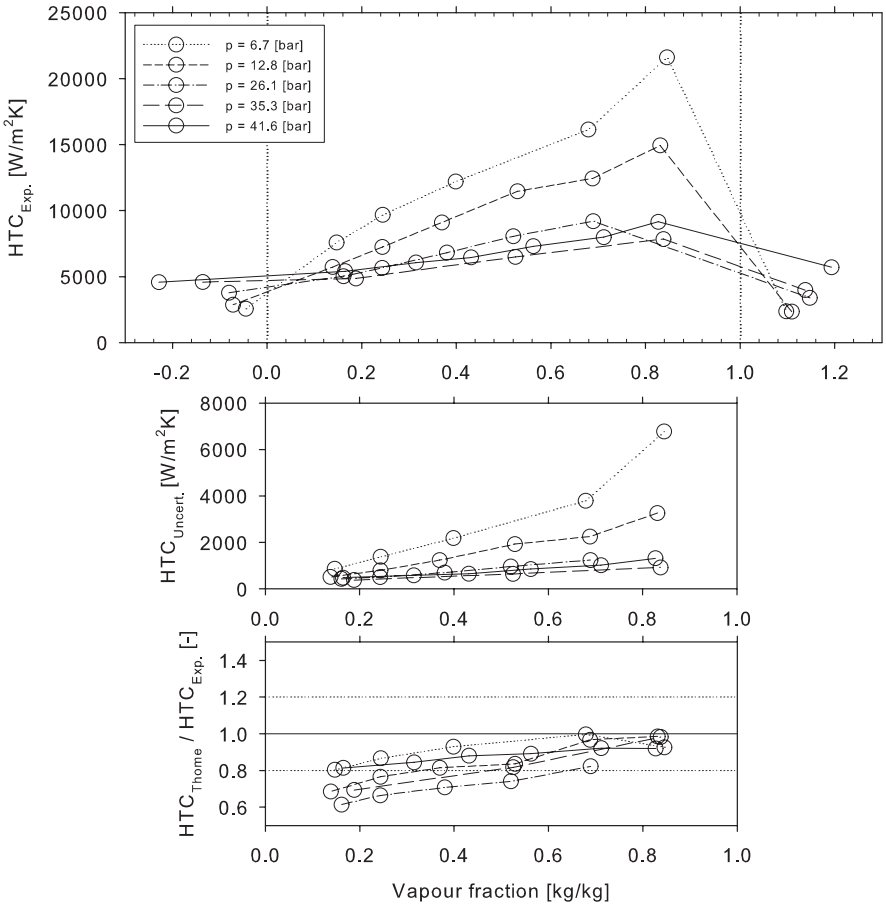

Figure 5.17: Heat transfer coefficient for Methane-100 in the 1 mm tube with pressure as parameter. Constant mass flux $G \approx 280$ kg/m^{2}s and 12.0 $< q'' <$ 13.1 kW/m^2.

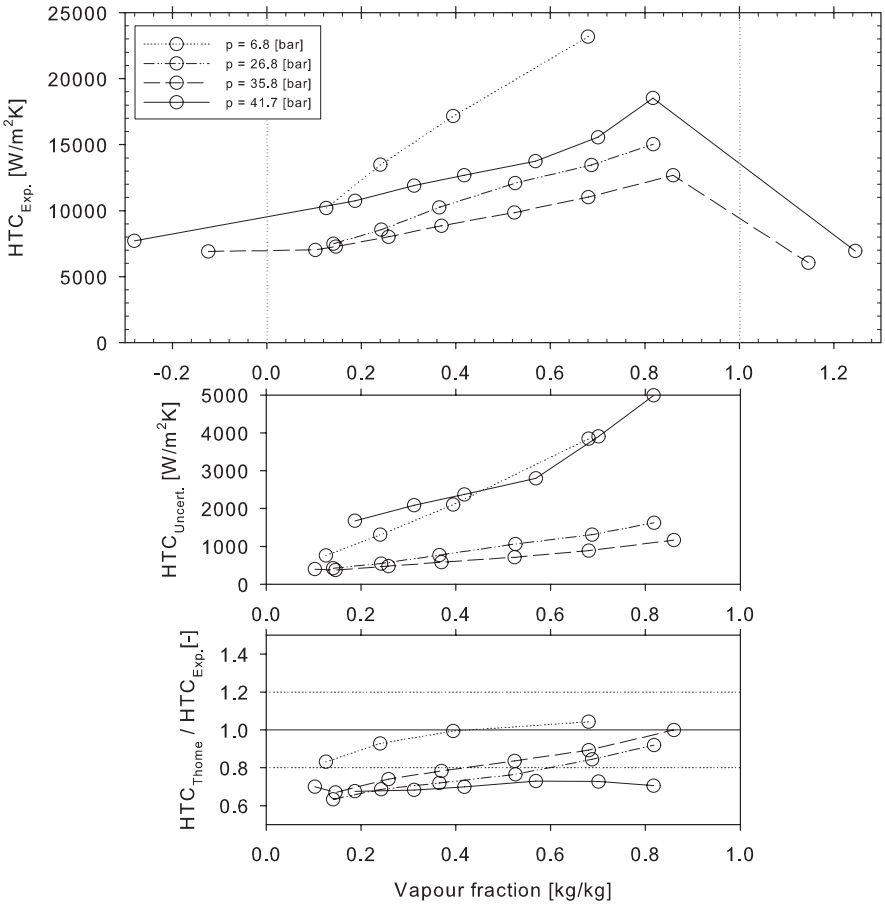

Figure 5.18: Heat transfer coefficient for Methane-100 in the 1 mm tube with pressure as parameter. Constant mass flux $G \approx 490$ kg/m^{2}s, $q'' \approx 26.4$ kW/m^2 for $p \leq 35.8$ bar, $q'' = 12.7$ kW/m^2 for $p = 41.7$ bar.

Figure 5.19 also shows that the two series taken at equal mass flux and pressure are independent of heat flux. The deviation from the model from Thome et al. [68] is not large.

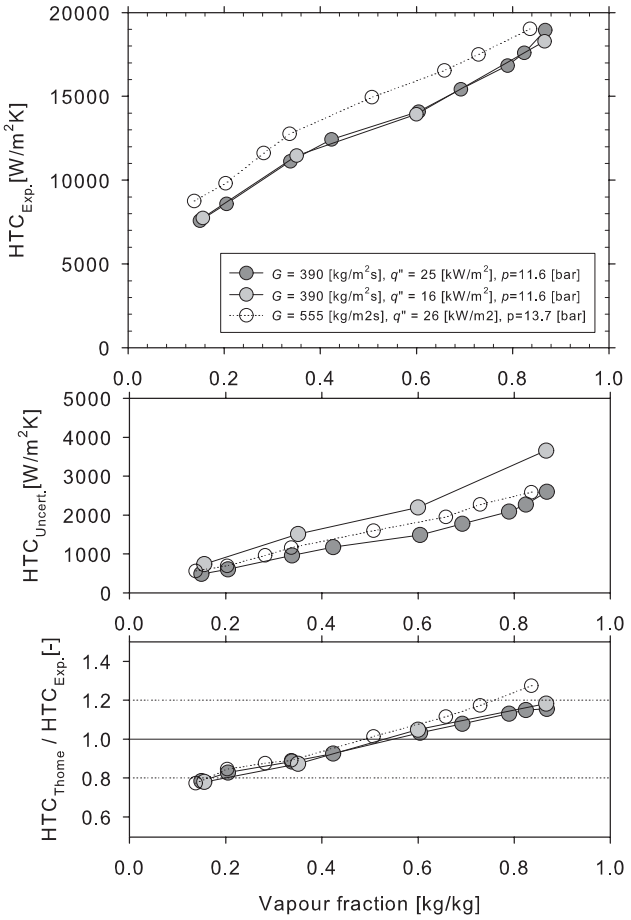

Figure 5.19: Heat transfer coefficient for Methane-100 in the 1 mm tube.

From the previous figures, it appears that the agreement between the experimental results and the model from Thome et al. [68] depends on the vapour fraction. The model under predicts the results at the most for low vapour fraction.

Results from the 0.5 mm tube

For the 0.5 mm tube, the heat transfer coefficient increases for higher mass flux, as can be seen in Figure 5.20. The uncertainty for the series where $x = 0.65$ and $G = 1360$ kg/m^{2}s is $\pm 26\,400$ W/m^{2}K, which corresponds to approx. ± 35 %. For $x = 0.16$ in the same series, the uncertainty equals 3100 W/m^{2}K which corresponds to approx. ± 12 %. The pressure drop for the measurements can be found in Figure 5.57.

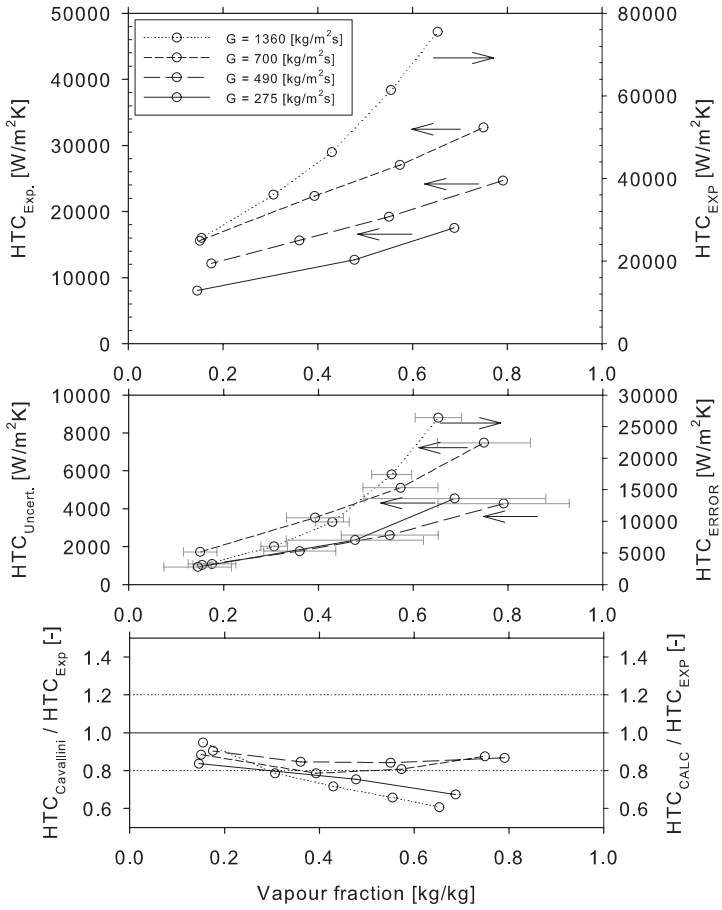

Figure 5.20: Heat transfer coefficient for Methane-100 in the 0.5 mm tube with mass flux as parameter. $12.3 < q'' < 38.7$ kW/m^2, $24.3 < p < 26$ bar.

As mentioned, the Cavallini et al. [11] model was used as a comparison to the 0.5 mm and 0.25 mm tube results as the agreement was much better

than with the model form Thome et al. [68]. The data for the 0.5 mm and 0.25 mm tube show a satisfactory agreement at low vapour fraction while the model under predicts the data for high and low pressure for high vapour fraction.

In the figures 5.21 and 5.22, the heat transfer coefficient is shown with pressure as the parameter. As mentioned, lower pressure tends to increase heat transfer coefficient but is usually not a model parameter itself. The lower pressure levels yields the highest heat transfer coefficient for both the case where $G = 280$ kg/m^{2}s and $G = 490$ kg/m^{2}s with one exception. The exception is the series where $p \approx 41$ bar in Figure 5.22 which shows a very high heat transfer coefficient with a very large increase at $x = 0.57$. Not much emphasise should be placed on this measurement point, but the other points for lower vapour fraction are considered reliable and they are all above the lower pressure series. The same trend but less distinct is found for lower mass flux in Figure 5.21.

The same was found for the 1 mm tube in Figure 5.18 and 5.17 where the effect also is stronger for higher mass flux. Unfortunately, no measurements at $p \approx 41$ bar were done in the 0.25 mm tube.

From Figures 5.18, 5.21 and 5.22, it appears that the model from Cavallini et al. [11] is pressure dependent as the low pressure results are over predicted and the high pressure results are under predicted. This effect could be directly linked to the pressure drop model used in the heat transfer model. This can be seen in Figure 5.64, where the pressure drop is over predicted at low pressure and under predicted at high pressure. Correspondingly, a dependence on the vapour fraction was not observed for the pressure drop comparison, so the increasing deviation with vapour fraction can not be explained by deviations in the pressure drop model.

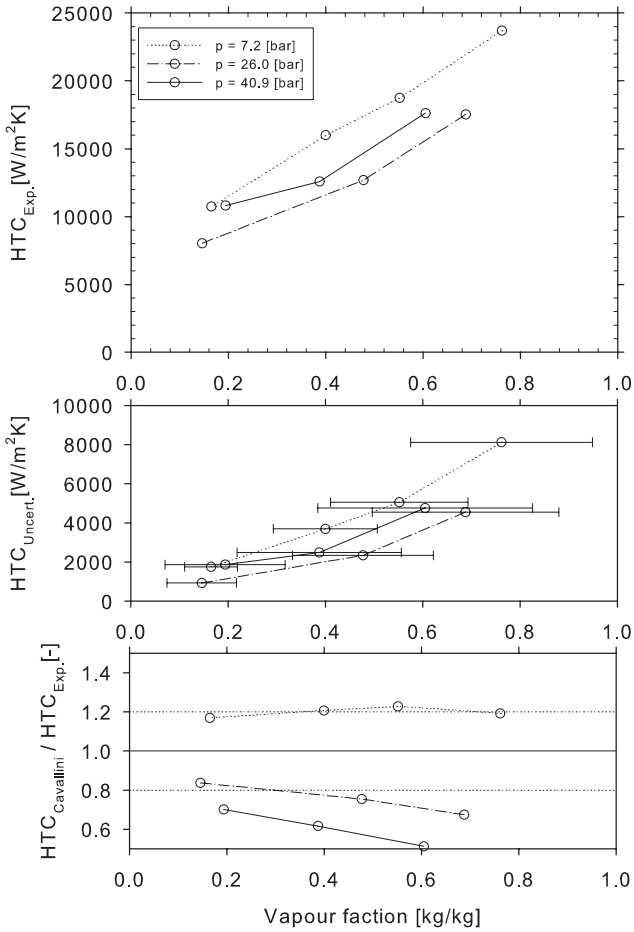

Figure 5.21: Heat transfer coefficient for Methane-100 in the 0.5 mm tube with pressure as parameter. $11.7 < q'' < 13.6$ kW/m^2, $274 < G < 298$ kg/m^{2}s.

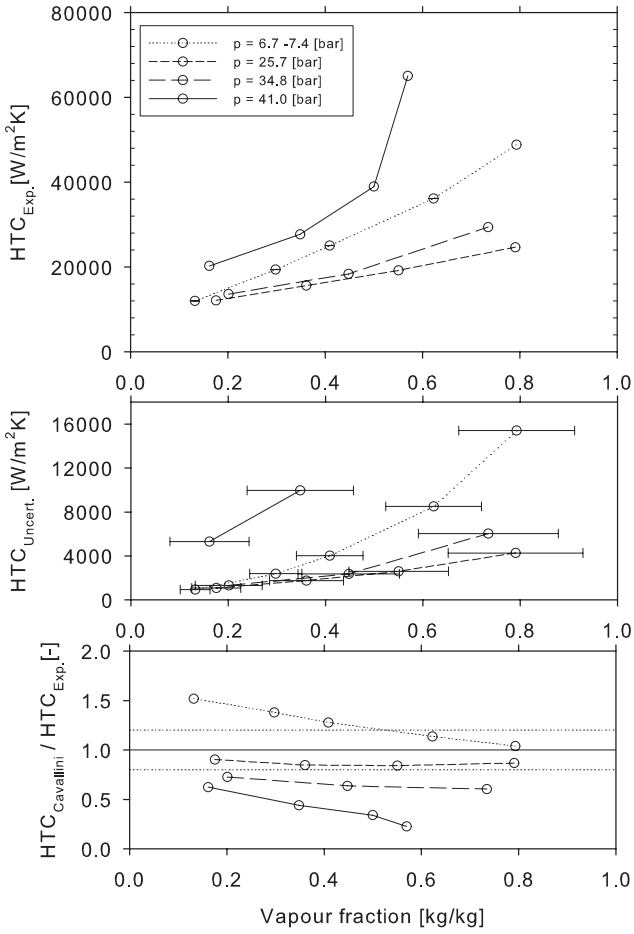

Figure 5.22: Heat transfer coefficient for Methane-100 in the 0.5 mm tube with pressure as parameter. $13.4 < q'' < 29.2$ kW/m^2, $482 < G < 509$ kg/m^{2}s.

Results from the 0.25 mm tube

Figure 5.23 shows the heat transfer coefficient with pressure level as parameter for the 0.25 mm tube. Unfortunately, the test run at 7 bar was not regarded as reliable due to stability problems and very high pressure drop. As for the 1 mm and 0.5 mm tubes, the heat transfer coefficient appears to be lower where $p \approx 35$ bar than where $p \approx 26$ bar. The large uncertainty makes it difficult to say anything conclusive.

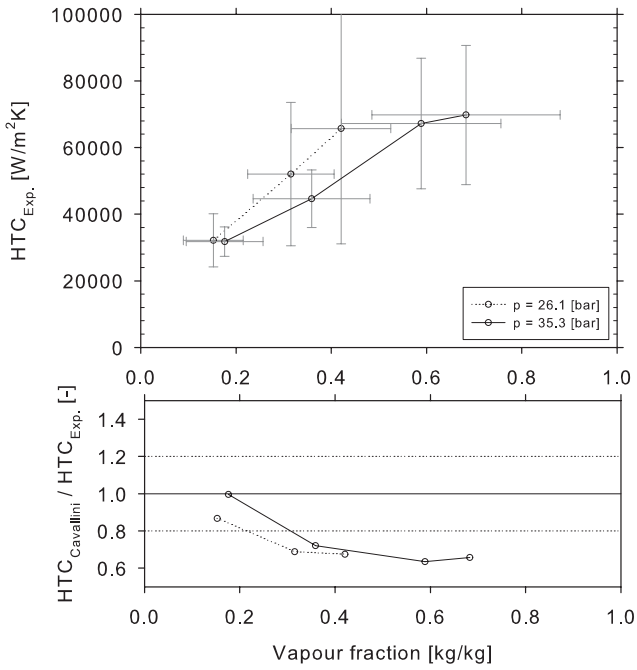

Figure 5.23: Heat transfer coefficient for Methane-100 in the 0.25 mm tube with pressure as parameter. $36.1 < q'' < 62.1$ kW/m^2, $1114 < G < 1367$ kg/m^{2}s.

Figure 5.24 shows the difference between measurement series for the 0.25 mm tube when heat flux is varied. However the heat transfer coefficient is not expected to be the same as there is a small difference in mass flux between the series. The uncertainty of the measurement point where $q'' = 60.0$ kW/m^2 and $x = 0.58$ is approx. $\pm 12\,700$ W/m^{2}K which corresponds to ± 18 %. The uncertainty of the determination of the vapour fraction is ± 0.13 for the same point.

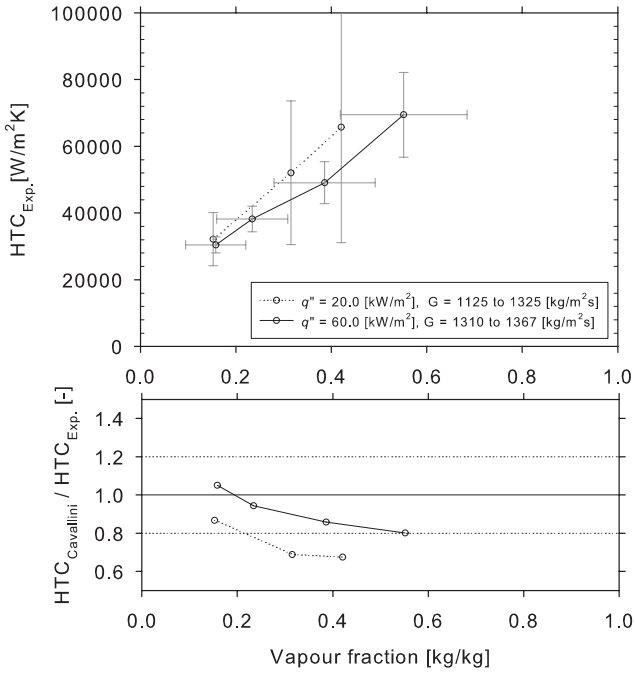

Figure 5.24: Heat transfer coefficient dependence on heat flux for Methane-100 in the 0.25 mm tube. $1125 < G < 1367$ kg/m^{2}s, $23.7 < p < 25.1$ bar.

5.3.3 Comparison with models

A further comparison with other correlations is done in Figures 5.25 and 5.26. If a wall friction factor is required in the correlation, the Colebrook friction factor is used instead of the smooth tube friction factor. The average deviation for each correlation and the percentage of data results within ± 20 % of the different correlations is shown in Table 5.3.

Thome et al. (2003)

For most of the Methane-100 results in the 1 mm tube, the model from Thome et al. [68] seems to under predict the results for low vapour fraction and predict the results better for middle and higher vapour fraction. Figure 5.25 shows that the deviation from the results in the 0.5 mm and 0.25 mm tubes are more or less independent of the vapour fraction.

The model from Thome assumes annular flow. This is also the assumption in the tubes investigated based on the discussion in Chapter 2.3.2. Entrainment or mist flow or other flow pattern related phenomenon could occur in the 1 mm tube, causing the dependence of the vapour fraction. It could also be related to the layer thickness δ, as this is an important parameter in Equation 2.13. As no flow observations were done, such ideas will remain speculations.

The parameters in Equation 2.13 which gives the best fit to the experimental results from the 1 mm tube have the values $a = 0.000831$, $b = 0.82$ and $c = 0.87$. Then, 68.2 % of the measurements fit within ±20 % of the predicted values. With these values however, the model clearly under predicts the results from the 0.5 mm and 0.25 mm tubes.

This correlation was developed for horizontal tubes where $d \geq 3.1$ mm, but annular flow should be no different in vertical flow. Attempts were made to fit the parameters c, n and m to all of the experimental results, but a good agreement satisfying all the tube diameters could not be found.

Cavallini et al. (2006)

Cavallini et al. [11] developed the correlation presented in Chapter 2.3.3, which is developed specifically for mini- and microchannels. The experimental heat transfer is an average of 20 % lower than predicted for the 1 mm tube and 51 % of the experimental data satisfy $0.8 \leq \mathrm{HTC_{Model}} \ / \ \mathrm{HTC_{Exp.}} \leq 1.2$. The prediction of the 0.5 mm and 0.25 mm tube results is fairly good. In fact, for both the 0.5 and 0.25 mm tube, almost all the results with their uncertainties (shown in Figures 5.28 and 5.29) are within ±20 % of the predicted data.

Shah (1979)

The correlation from Shah [62] presented in Figure 5.25 does not match the experimental results very well for the 1 mm tube, but match very well for the 0.5 mm and 0.25 mm tubes. There, over 80 % of the experimental data are within ±20 %. This correlation is a two-phase multiplier method, developed

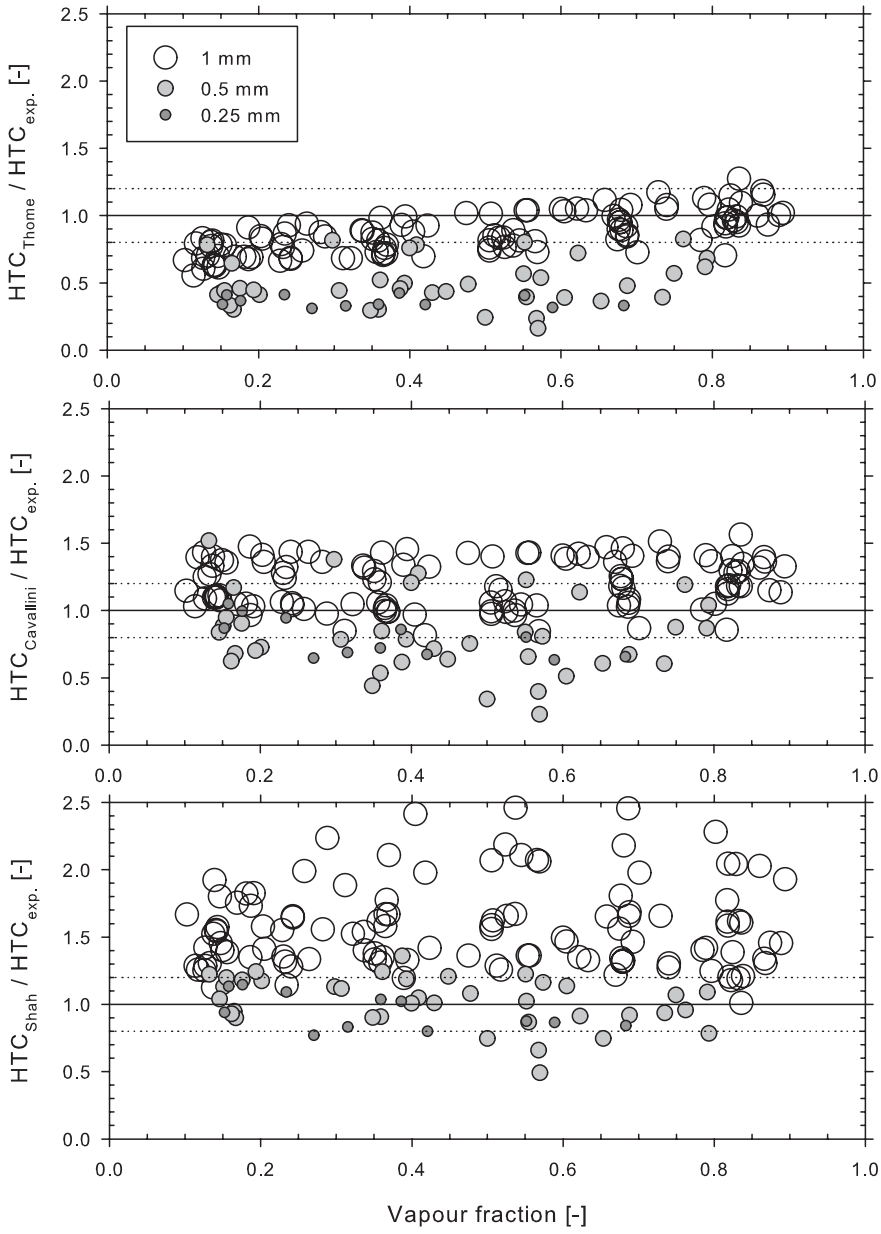

Figure 5.25: Calculated compared to experimentally obtained heat transfer results for Methane-100 in all tubes.

from 10 fluids, both horizontal and vertical tubes, diameters ranging from 7 mm to 40 mm and over a wide range of vapour fraction, mass flux and heat flux. This gives the correlation credibility for conventional channels. However, the bad agreement with the 1 mm tube results questions its applicability even though the agreement is good for the 0.5 mm and 0.25 tubes. The correlation is independent from the surface roughness conditions.

Akers (1959)

The Akers [3] correlation gives the best prediction for the 1 mm tube, but completely fails to predict the 0.5 mm and 0.25 mm data as none of the experimental results are within ±20 %. This is seen in Figure 5.26.

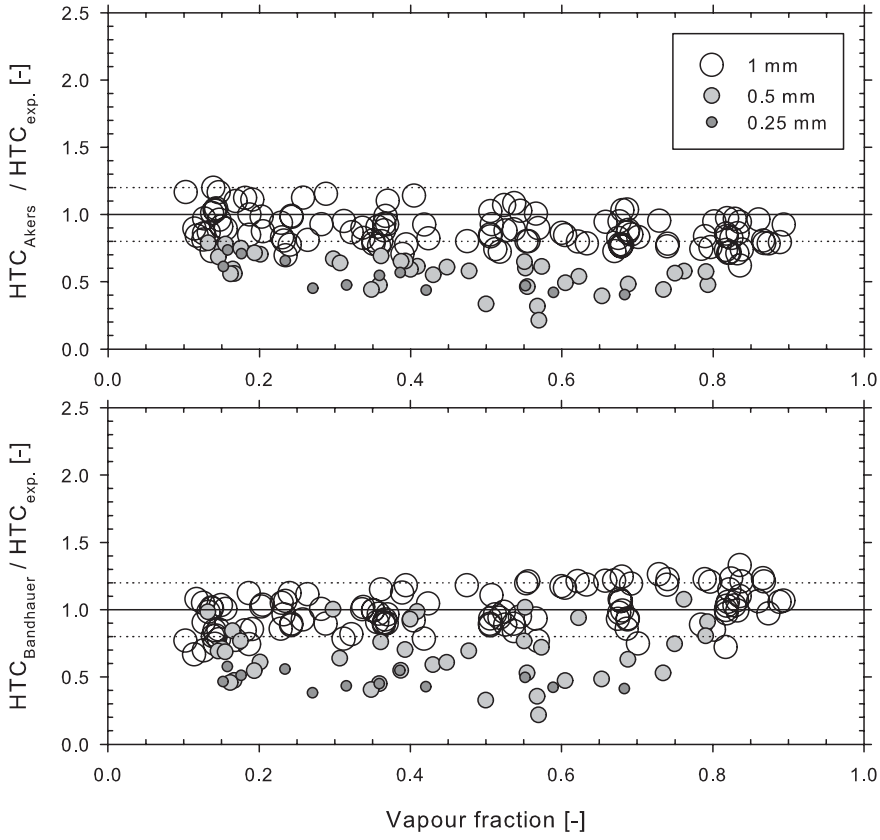

Figure 5.26: Calculated compared to experimentally obtained heat transfer results for Methane-100 in all tubes.

Bandhauer et al. (2005)

The correlation from Bandhauer et al. [4] was developed for R-134a and uses the Garimella et al. [27] pressure model to predict the interface shear τ_i between the liquid and vapour phases. As it will be shown later in Figure 5.61 and in Table 5.5, the agreement with the experimental pressure drop results and this correlation is not good. Therefore, the actual measured pressure drop is used in the Bandhauer-correlation where the shear at the interface is found from

$$\tau_\mathrm{i} = \frac{\mathrm{d}p}{\mathrm{d}z}\frac{d_\mathrm{i}}{4} \tag{5.3}$$

where $d_\mathrm{i} = d_\mathrm{c} - 2\delta$. The length scale used in the Bandhauer-correlation was set to the length of the test section $L = 5$ cm.

The agreement with the 1 mm experiments is quite good, where 77.0 % of the measurements satisfy $0.8 \leq \mathrm{HTC_{Bandhauer}} \,/\, \mathrm{HTC_{Exp.}} \leq 1.2$. For the 0.5 mm and 0.25 mm tube, the model under predicts the heat transfer coefficient and there is a large scatter.

It was noted in Chapter 2.3.3 that the Bandhauer et al. [4] correlation is similar to the correlation from Cavallini et al. [11], except for a different pressure gradient calculation, different dimensionless layer thickness calculation and the absence of an entrainment factor. A very important difference is also that the Bandhauer-model was based on R-134a measurements only. The Cavallini-correlation predicts the heat transfer in the two smallest tubes better than the Bandhauer-correlation.

Summary

All the models, except the model from Shah [62], shows satisfactory or good agreement for the 1 mm data. The Bandhauer et al. [4] model has the best agreement.

For the 0.5 mm tube, only the model from Shah [62] agrees well with the results. All the other models under predict the results considerably.

For the 0.25 mm tube, the number of experimental data is limited. The experimental window was limited due to high uncertainty at low flow rates, and high pressure drop at higher mass flow rates. However, the reliable experimentally obtained heat transfer coefficients are far higher than the predicted by the correlations from Thome et al. [68], Akers et al. [3] and Bandhauer et al. [4]. On the other side, the correlation from Cavallini et al. [11] and particularly the correlation from Shah [62] seems to predict the experimental data well.

Correlation/Tube		Thome et al. [68]	Cavallini et al. [11]	Shah [62]	Akers [3]	Bandhauer et al. [4]
1 mm	Average deviation	0.87	1.20	1.58	0.89	1.00
	Within 0.8 and 1.2	64 %	51 %	5 %	75 %	77 %
0.5 mm	Average deviation	0.50	0.82	1.02	0.57	0.67
	Within 0.8 and 1.2	8 %	34 %	71 %	0 %	26 %
0.25 mm	Average deviation	0.36	0.79	0.95	0.54	0.47
	Within 0.8 and 1.2	0 %	50 %	83 %	0 %	0 %

Table 5.3: Results for single component condensation of Methane-100. Average deviation refers to the average value of $\mathrm{HTC_{Model}}$ / $\mathrm{HTC_{Exp.}}$.

In the results from all heat transfer models presented in Figure 5.25 and 5.26, the results from the 1 mm tube are systematically predicted higher than the results from the 0.5 and 0.25 mm tubes. The 0.5 mm and 0.25 mm tubes results seem to be on the same average level. This is an indication that either some systematically reoccurring parameter related to the diameter is wrong or that there is some phenomenological threshold between 1 mm and 0.5/0.25 mm.

In Equation 3.13 the characteristic diameter for the surface area A_w was set by using the cross-sectional based diameter d_c. The diameter based on the perimeter d_w is a more physically based diameter for A_w. By changing Equation 3.13 to $A_\mathrm{w} = d_\mathrm{w}\pi L$, the measured heat transfer coefficient is changed accordingly. A comparison between the heat transfer coefficient based on d_w is shown in Figure 5.27 for the Cavallini et al. [11] and the Thome et al. [68] correlation. As the measured heat transfer coefficient now is reduced, the values in Figure 5.27 are shifted to higher values. The 0.25 mm values are shifted more as the $d_\mathrm{w}/d_\mathrm{w}$-ratio is higher for the smaller tubes (seen in Table 3.2). As a result, many of the 0.5 mm and most of the 0.25 mm predictions from the Cavallini et al. [11]-model are within ±20% for the measured. However, most of the 1 mm tube measurements are now over predicted. The same applies for the comparison with the Thome et al. [68]-model, however the 0.5 mm and 0.25 mm measurements are still under predicted.

The single phase flow measurements presented in Figure 5.9 to 5.11

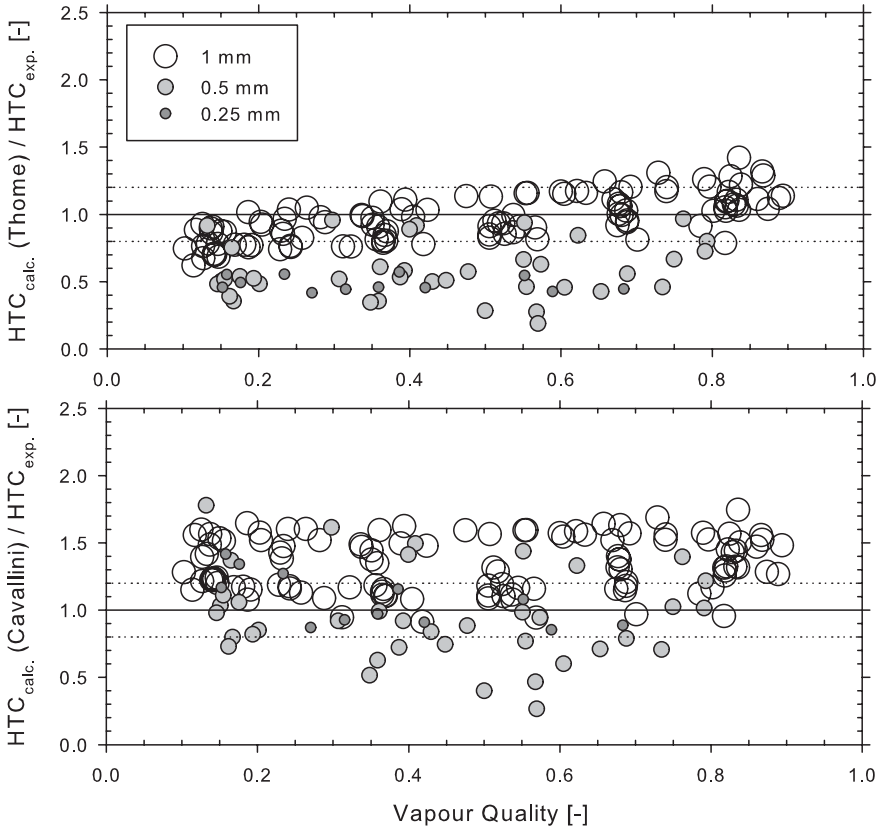

Figure 5.27: Calculated compared to experimentally obtained heat transfer results for Methane-100 in all tubes using d_w in Equation 3.13.

showed that the heat transfer results agree fairly well with the prediction in all three tubes. The seeming inconsistency between the 1 mm tube and 0.5/0.25 mm tubes for condensation heat transfer could therefore be related to the be liquid/vapour flow behaviour.

The difference in heat transfer could also be explained by the higher measurement uncertainty for the 0.5 mm and 0.25 mm tubes. This is shown for the Cavallini et al. [11]-model in Figure 5.28 and in Figure 5.29. In fact, many of the 0.5 mm and most of the 0.25 mm results are not far from the predicted considering their uncertainties.

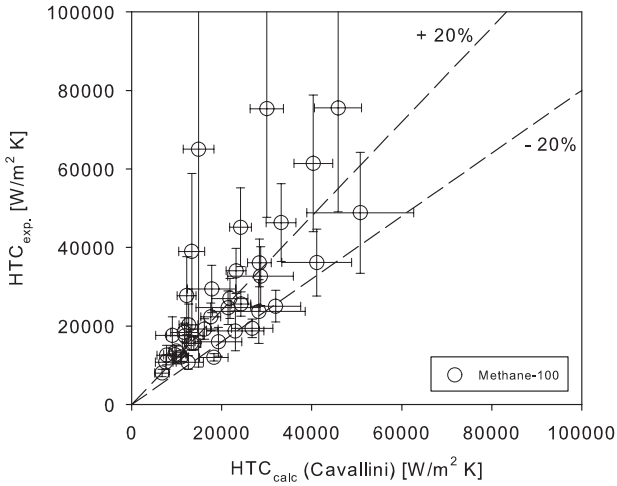

Figure 5.28: Experimentally obtained heat transfer results for Methane-100 in the 0.5 mm tube compared to the correlation from Cavallini et al. [11].

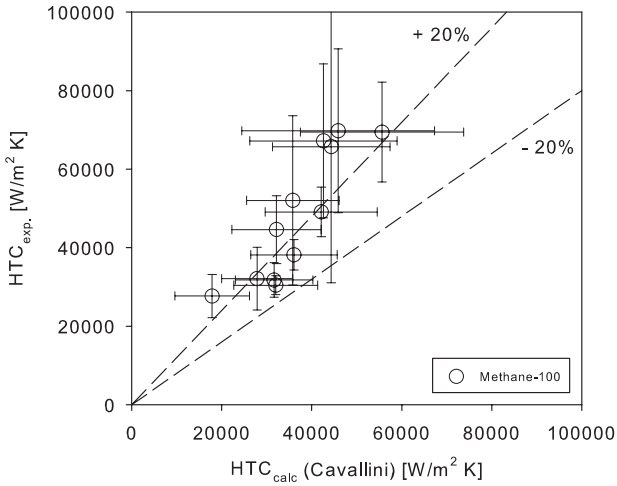

Figure 5.29: Experimentally obtained heat transfer results for Methane-100 in the 0.25 mm tube compared to the correlation from Cavallini et al. [11].

5.3.4 Condensation heat transfer - Ethane-10

1.0 mm tube

In Figure 5.30, it is difficult to see a dependence on heat flux although the smallest heat flux series shows a slightly higher heat transfer coefficient. Heat transfer results under similar conditions for Methane-100 was presented in Figure 5.16 where the heat transfer coefficient is clearly higher. However, a direct comparison must be done with care as the molecular weight difference between methane and ethane results in a lower fluid velocity for Ethane-10 when the mass flux is equal. Some of the thermophysical properties are also different.

The uncertainty is higher for lower heat fluxes for the same reasons as for single component condensation. However for binary mixtures, the saturation temperature is reduced through the test section due to the change in vapour fraction. This causes a larger difference between T_{w} and $T_{\mathrm{v,bulk}}$. This leads to a lower uncertainty compared to single component condensation as can be seen when comparing Figure 5.16 and 5.30.

The experimental data are compared to the multi component condensation model h_{mc} given in Equation 2.32, using the single component heat transfer model h_{sc} from Cavallini et al. [11]. The agreement between experimental results and the model is good.

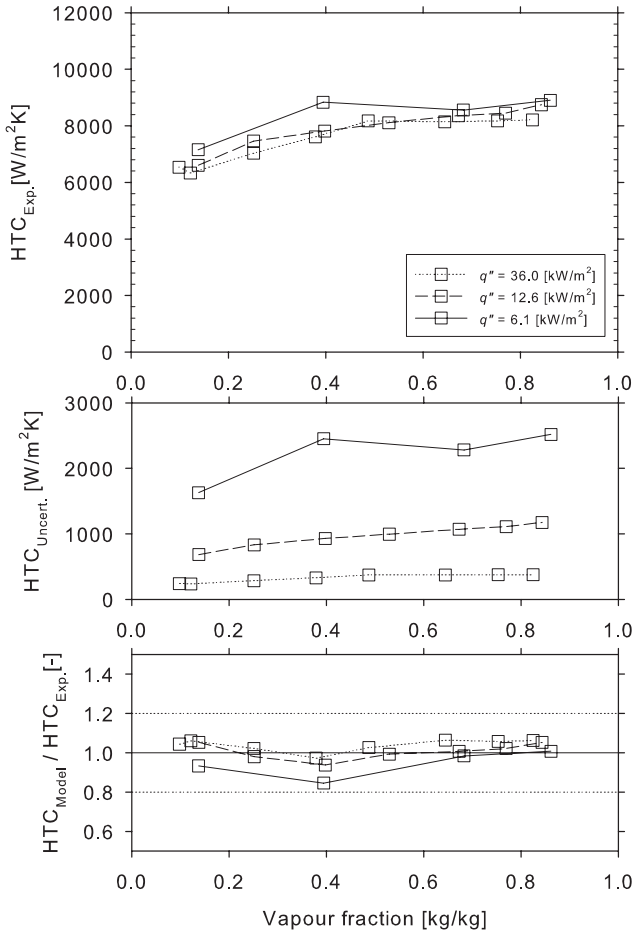

Figure 5.30: Heat transfer coefficient for Ethane-10 in the 1.0 mm tube with heat flux as parameter. $35.5 < p < 36.2$ bar, $482 < G < 503$ kW/m^2.

Figures 5.31 and 5.32 show the heat transfer coefficient with pressure as parameter for two different mass fluxes in the 1 mm tube. Higher heat transfer coefficient for lower pressure is seen, which is believed to be caused by higher shear due to the higher vapour velocity at low pressure. This is seen also for Methane-100. Unlike for Methane-100, the heat transfer coefficient is lowest for the highest pressure level.

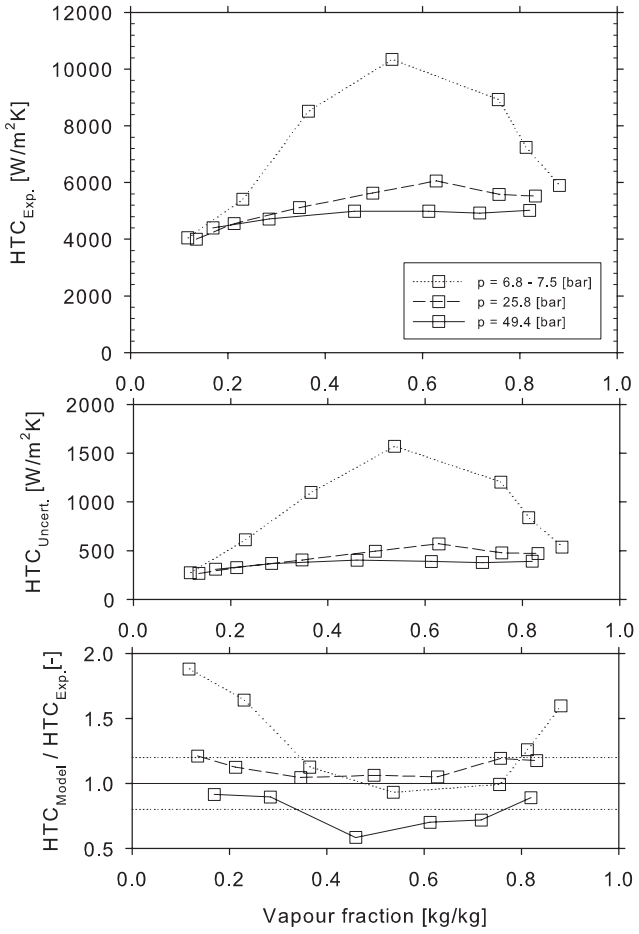

Figure 5.31: Heat transfer coefficient for Ethane-10 in the 1.0 mm tube with pressure as parameter. $274 < G < 285$ kg/m^{2}s, $12.1 < q'' < 13.1$ kW/m^2.

The behaviour of the lowest pressure series is interesting as there is a decrease in the heat transfer coefficient at low and high vapour fractions compared to Methane-100. Similar observations is made for other measure-

ments and the cause of the drop in heat transfer coefficient is therefore discussed in Section 5.3.7 on page 134. The series in grey at $p = 25.8$ bar in Figure 5.32 is shown as a comparison at higher heat flux. It shows the same trend as the series at low pressure but at a much smaller magnitude. It is also given in Figure 5.34.

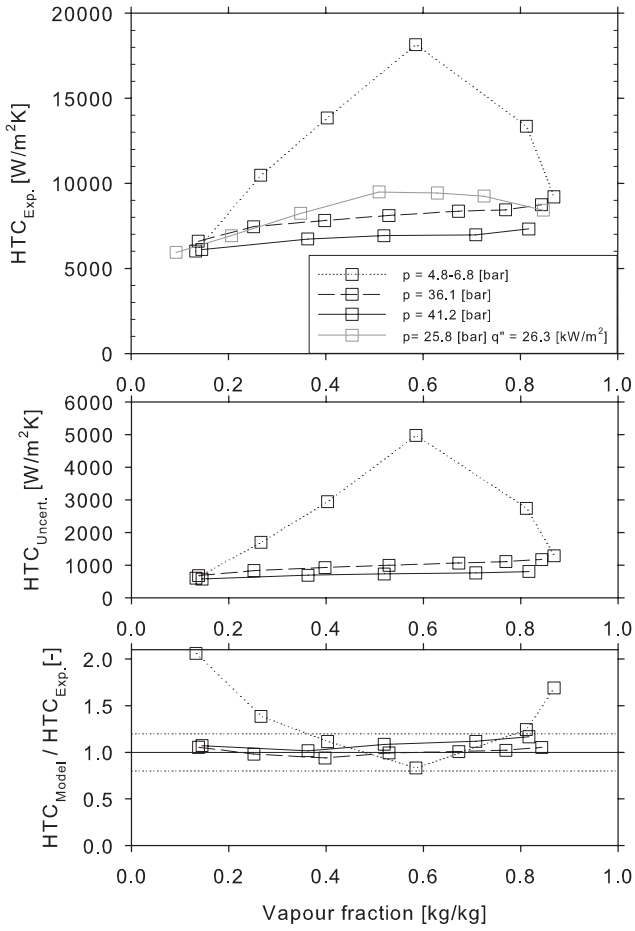

Figure 5.32: Heat transfer coefficient for Ethane-10 in the 1.0 mm tube with pressure as parameter. $485 < G < 499$ kg/m^{2}s, $12.3 < q'' < 12.9$ kW/m^2.

As seen also in Figure 5.33, the heat transfer coefficient does not vary much as a function of the vapour fraction at high pressure. This is in contrast to the measurement of Methane-100 when regarding the series at $p = 41.6$ and 41.7 bar in Figure 5.17 and 5.18 respectively.

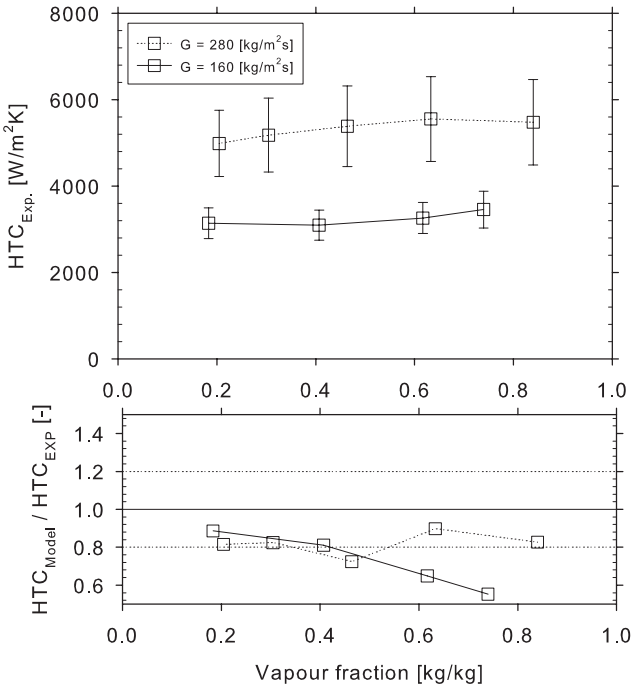

Figure 5.33: Heat transfer coefficient for Ethane-10 in the 1.0 mm tube with mass flux as parameter. $48.6 < p < 49.2$ bar ($p_r = 0.85$), $6.0 < q'' < 6.5$ kW/m^2.

At lower pressure as shown in Figure 5.34 (26 bar), the heat transfer coefficient dependence on vapour fraction is clear; a maximum at $x \approx 0.6$. This was also indicated in Figure 5.31 but there for a lower mass flux.

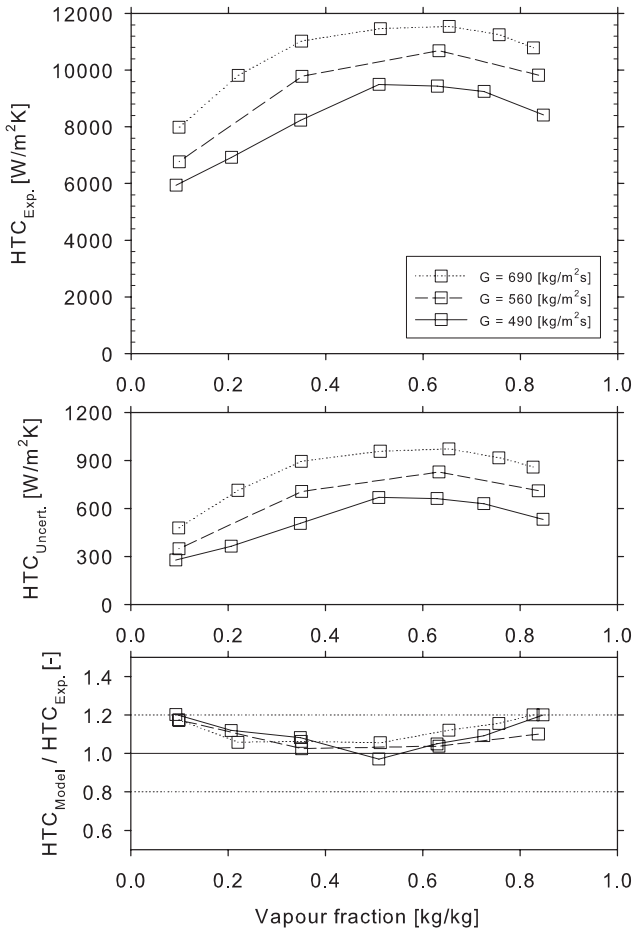

Figure 5.34: Heat transfer coefficient for Ethane-10 in the 1.0 mm tube with mass flux as parameter. $25.2 < p < 25.8$ bar, $26.0 < q'' < 26.5$ kW/m^2.

0.5 mm tube

The model compared with the measurements for the 0.5 mm tube is the same as for the 1 mm tube; Equation 2.32 using Cavallini et al.-model for h_{sc}.

Figure 5.35 shows that the heat transfer coefficient is higher for lower heat flux for the 0.5 mm tube. The corresponding measurements in the 1 mm tube is shown in Figure 5.30 where the difference was not clear. For the 0.5 mm tube, the predicted values are roughly the same for both series, which leads to a good agreement with the measurement series where $q'' = 36.0$ kW/m^2, while the series where $q'' = 12.3$ kW/m^2 is under predicted.

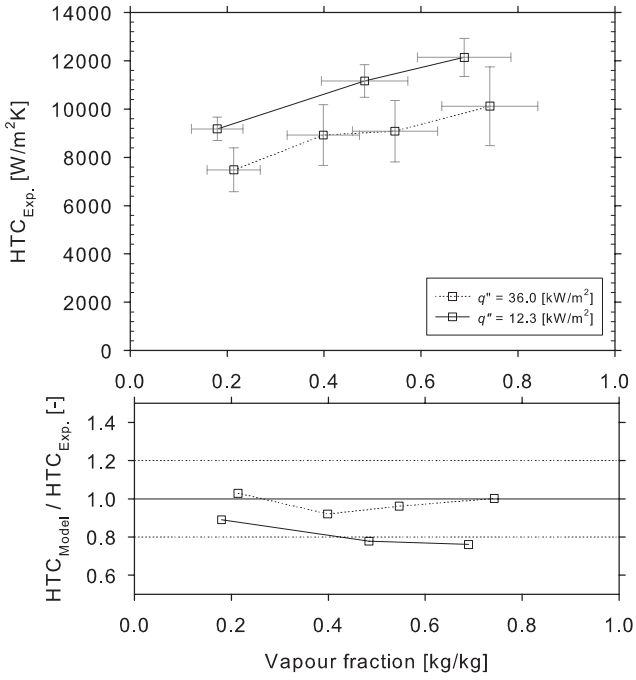

Figure 5.35: Heat transfer coefficient for Ethane-10 in the 0.5 mm tube with heat flux as parameter. $36.3 < p < 36.8$ bar, $470 < G < 508$ kg/m^{2}s.

Figure 5.36 shows that a higher mass flux leads to a higher heat transfer coefficient also for the 0.5 mm tube. This figure corresponds to the results shown in Figure 5.34 for the 1 mm tube. The trend with a maximum heat transfer coefficient at $x \approx 0.6$ is indicated also in the 0.5 mm tube, all though no measurements for $x > 0.73$ were recorded. Note that the heat flux is different for the series where $G = 280$ kg/m^{2}s.

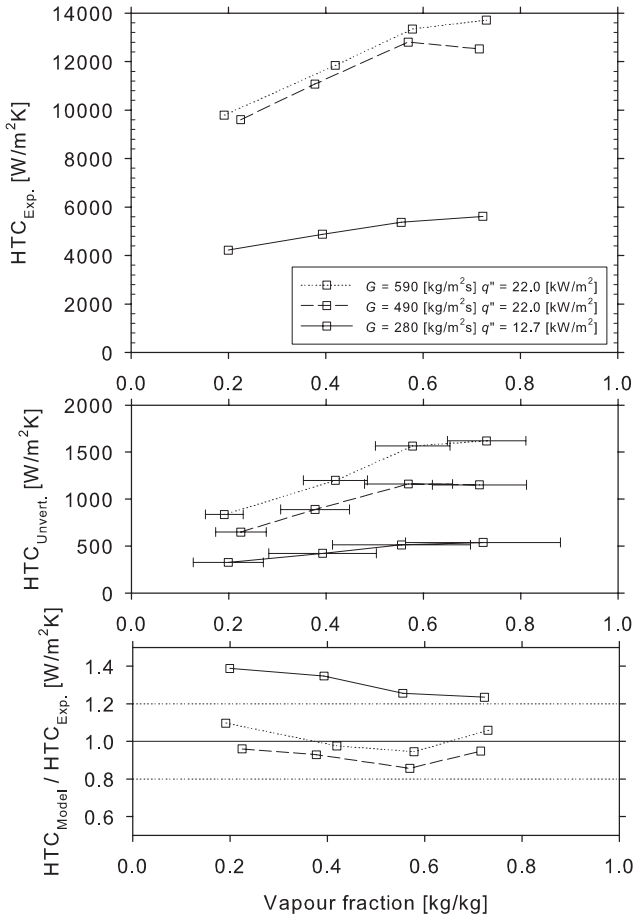

Figure 5.36: Heat transfer coefficient dependence on mass flux for Ethane-10 in the 0.5 mm tube. $25.7 < p < 26.5$ bar.

0.25 mm tube

The number of experiments regarded as reliable in the 0.25 mm tube is limited, so only five measurement points are presented for condensing Ethane-10 in the 0.25 mm tube. Figure 5.37 shows that the heat transfer coefficient is rather independent from the vapour fraction, except for a small increase at $x = 0.71$. The measured values are much higher than predicted.

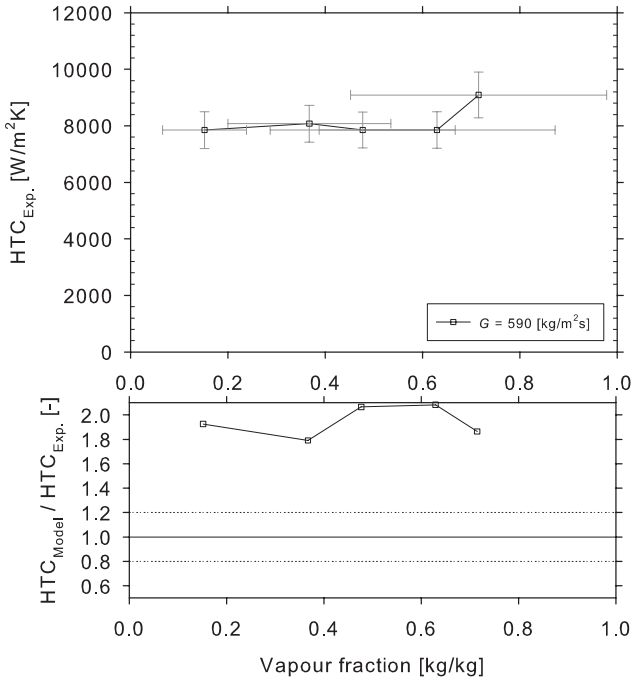

Figure 5.37: Heat transfer coefficient for Ethane-10 in the 0.25 mm tube. $25.7 < p < 25.8$ bar, $21.7 < q'' < 22.6$ kW/m^2.

5.3.5 Condensation heat transfer - Ethane-27

1.0 mm tube

The mass flux dependence on the heat transfer coefficient for Ethane-27 is shown in Figure 5.38 for the 1 mm tube. There is an increase for increasing mass flux which is in agreement with the corresponding Ethane-10 results in Figure 5.34.

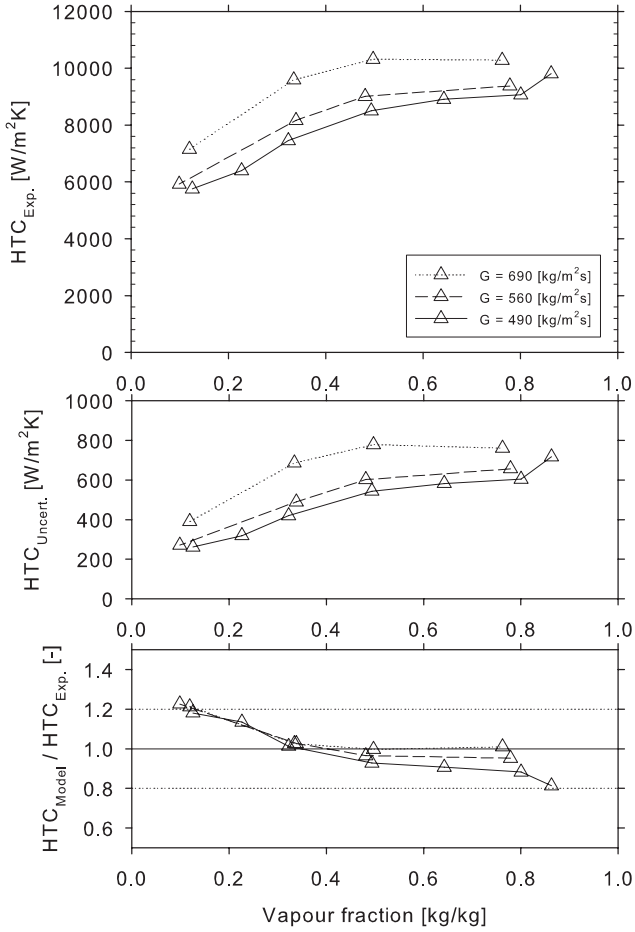

Figure 5.38: Heat transfer coefficient dependence for Ethane-27 in the 1.0 mm tube with mass flux as parameter. $25.6 \leq p \leq 26.3$ bar, $26.0 < q'' < 26.9$ kW/m^2.

There is also an increase in the heat transfer coefficient for increasing

vapour fraction up to $x \approx 0.5$, after which the heat transfer coefficient is rather constant. This is in contrast to the Ethane-10 observations in Figure 5.34 where a decrease for $x > 0.5$ is observed.

The sudden increase in the heat transfer coefficient for $x > 0.8$ for the 490 kg/m^{2}s case can be explained by natural scatter in the experimental results. No other explanation is found.

The behaviour of the high pressure series in Figure 5.39 are comparable with the high pressure series for Ethane-10 in Figure 5.32. However, the low pressure series behaves somewhat different where the heat transfer coefficient is rather constant for $x > 0.4$. An explanation for this is given in Chapter 5.3.7. The series at $p = 26$ bar is taken from Figure 5.38. It is taken at a higher heat flux but still illustrates the transition from low to high pressure.

For $x < 0.2$, the low pressure series show a low heat transfer coefficient both for Ethane-27 and Ethane-10. While the other observations could be rather well predicted by the correlation, the two measurement points at $0.22 \leq x$ for the low pressure series are substantially over predicted in Figure 5.39. The most plausible explanation to this is that the flow pattern is intermittent and gives a lower heat transfer coefficient. However, judging from the values of We_{gs} in Table 2.2 for low pressure, the values are well above ≈ 20 which Yun and Kim [75] suggested as the transition values between intermittent and annular flow for CO_2. Obviously, as there are no visual observations of the flow pattern, intermittent flow can not be ruled out and it is also the most probable explanation.

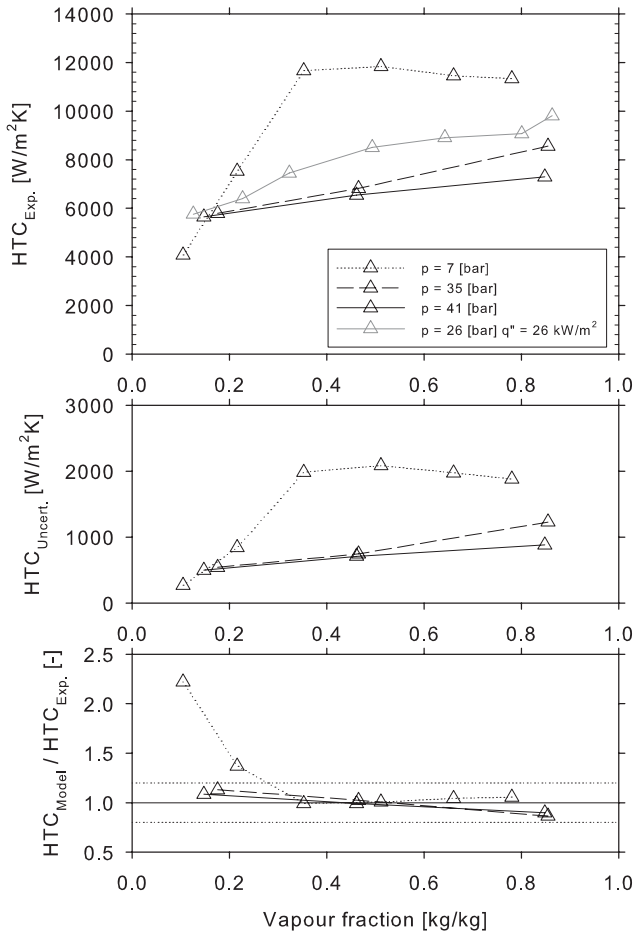

Figure 5.39: Heat transfer coefficient dependence on vapour fraction for Ethane-27 in the 1.0 mm tube with pressure as parameter. $487 < G < 496$ kg/m^{2}s, $11.7 < q'' < 13.3$ kW/m^2.

When comparing Figure 5.40 (where $G = 280$ kg/m^{2}s) with Figure 5.39 (where $G = 490$ kg/m^{2}s), the same trend with regards to the constant heat transfer coefficient for $x > 0.4$ was observed.

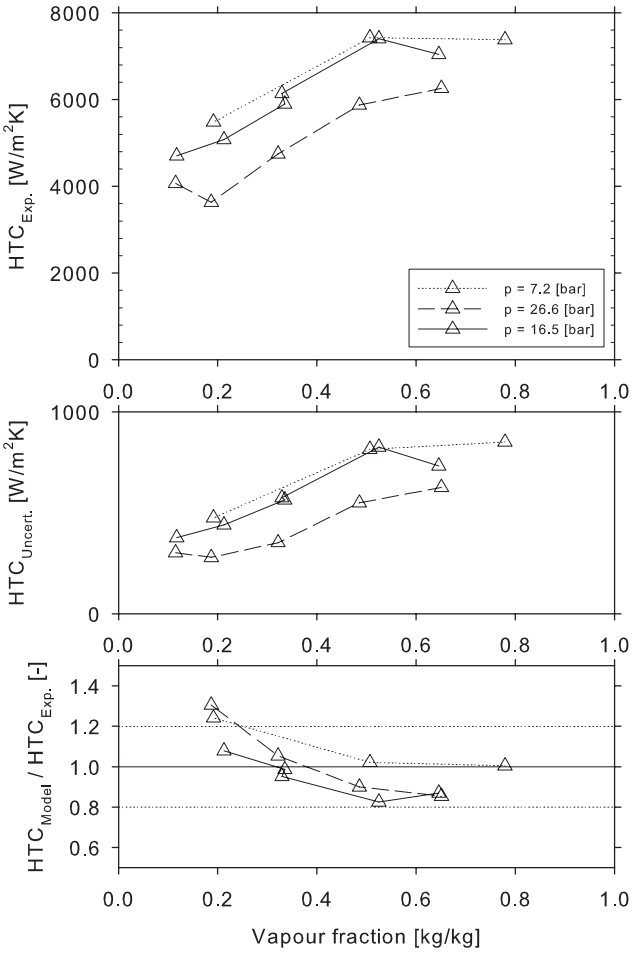

Figure 5.40: Heat transfer coefficient dependence on pressure for Ethane-27 in the 1.0 mm tube. $272 < G < 285$ kg/m^{2}s, $10.1 < q'' < 13.2$ kW/m^2.

As was shown for Methane-100 in Figure 5.64, the predicted pressure drop is larger than the measured and this difference decreases for increasing vapour fraction. This explains partly why $\mathrm{HTC_{Model}/HTC_{Exp.}}$ decreases for increasing vapour fraction for Ethane-27. This is also very easy to see in Figure 5.41 and 5.43. A similar behaviour was not seen for Ethane-10.

Figure 5.41 shows that the heat transfer coefficient is slightly increase by reduced heat flux. It is also shown that the difference is small for $q'' > 10\ 000\ \mathrm{W/m^2}$ and more rapidly increasing for $q'' < 10\ 000\ \mathrm{W/m^2}$. Also the uncertainty for the measurements are shown, which show that no certain conclusions can be drawn for low heat fluxes.

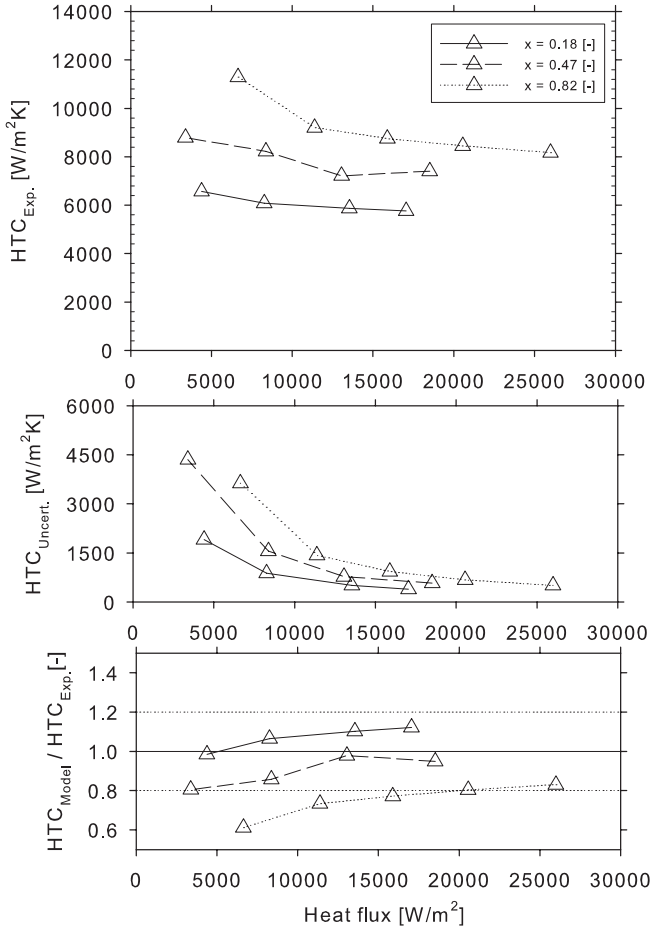

Figure 5.41: Heat transfer coefficient dependence on heat flux for Ethane-27 in the 1.0 mm tube. $12.4 < p < 13.1$ bar, $278 < G < 283\ \mathrm{kg/m^2s}$.

The high uncertainty is caused by the uncertainty of ΔT (Equation 3.3) where the difference between T_w and the average of T_in and T_out is small (As an example: $\Delta T = 0.39\ ^\circ\mathrm{C}$ for the measurement point where $x = 0.47$ and $q'' = 3390\ \mathrm{W/m^2}$). There is also an uncertainty in the determination of

$\dot{Q}_{\mathrm{TS}}$, where $\dot{Q}_{\mathrm{TS}} = 0.55$ W for the mentioned measurement point. However, this contribution is small compared to the uncertainty of ΔT. This can be seen when comparing the measurement point with lowest value of q'' for the series where $x = 0.82$ and $x = 0.18$ respectively: The value of q'' is lower for the $x = 0.18$ measurement point, yet the uncertainty is larger of the point with lowest q'' for the $x = 0.82$ series.

Figure 5.42, in contrast to Figure 5.41, shows a lower heat transfer coefficient for lower heat flux. The mass flux is lower and the pressure higher than in Figure 5.41, but this does not explain the opposite trend.

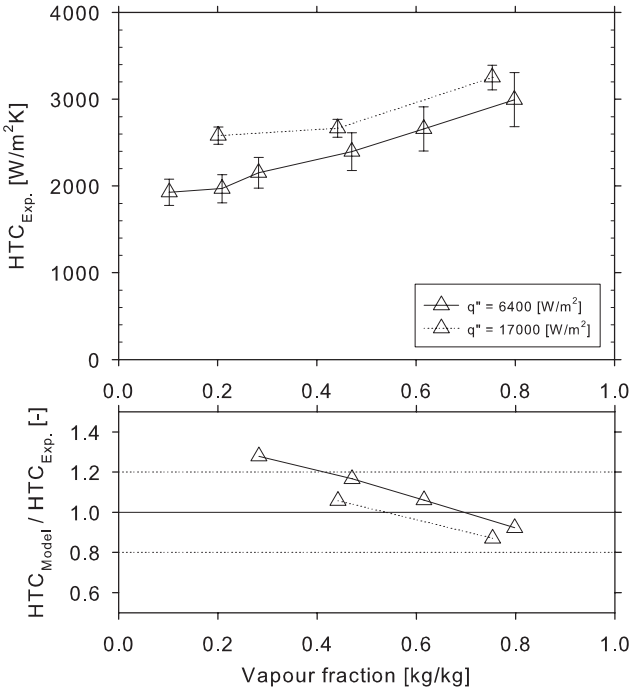

Figure 5.42: Heat transfer coefficient for Ethane-27 in the 1.0 mm tube with heat flux as parameter. $34.9 < p < 36.2$ bar, $140 < G < 149$ kg/m^{2}s.

0.5 mm tube

Figure 5.43 shows the heat transfer coefficient with the heat flux along the x-axis and vapour fraction as parameter for the 0.5 mm tube. The two lower vapour fraction series appear to be in contrast with the previously mentioned results with decreasing heat transfer coefficient for lower heat flux. However the uncertainty for the measurements at low heat flux is considerable. As A_w for the 0.5 mm tube is just approximately half of the value for the 1 mm tube, the uncertainty of $\dot{Q}_{TS}$ is more important than in the 1 mm tube.

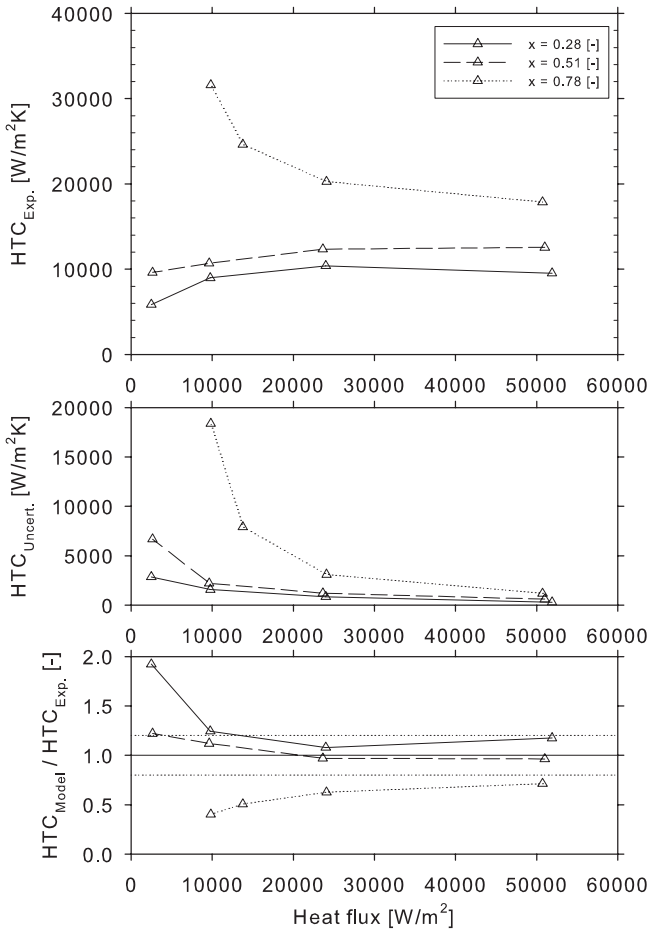

Figure 5.43: Heat transfer coefficient dependence on heat flux for Ethane-27 in the 0.5 mm tube. $9.6 < p < 9.7$ bar, $512 < G < 536$ W/m^{2}s.

From Figure 5.44 it is obvious that the heat transfer coefficient increases for increasing mass flux and vapour fraction also for the 0.5 mm tube. This is more evident for Ethane-27 compared to Ethane-10 in the same tube as seen in Figure 5.36.

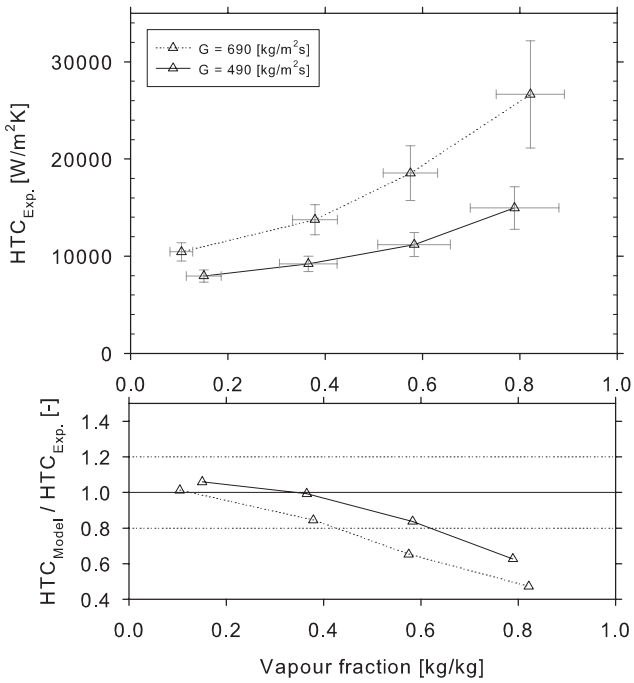

Figure 5.44: Heat transfer coefficient for Ethane-27 in the 0.5 mm tube with mass flux as parameter. $25.8 < p < 26.6$ bar, $19.2 < q'' < 23.1$ kW/m^2.

0.25 mm tube

As for Ethane-10, the number of measurements of Ethane-27 in the 0.25 mm tube is limited. The increase in heat transfer coefficient with increasing vapour fraction is evident from Figure 5.45, and much more distinct than from the Ethane-10 measurement. The two measurements at $0.55 \leq x$ appear to be not far from the predicted values.

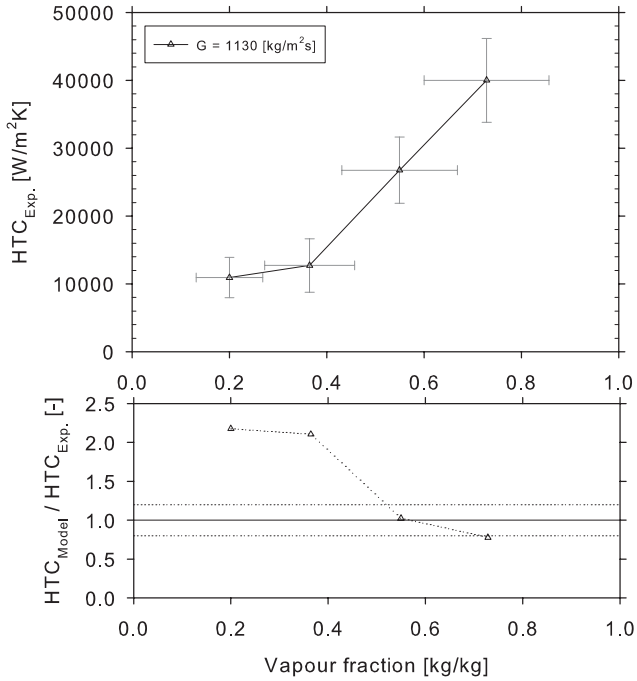

Figure 5.45: Heat transfer coefficient for Ethane-27 in the 0.25 mm tube. $24.1 < p < 25.6$ bar, $28.0 < q'' < 35.2$ kW/m^2.

5.3.6 Condensation heat transfer - Nitrogen-10

1.0 mm tube

The heat transfer coefficient as a function of the heat flux for Nitrogen-10 for the 1 mm tube is plotted in Figure 5.46. It shows a similar characteristic as for Ethane-27 in Figure 5.41 and the uncertainty is again high for low heat flux.

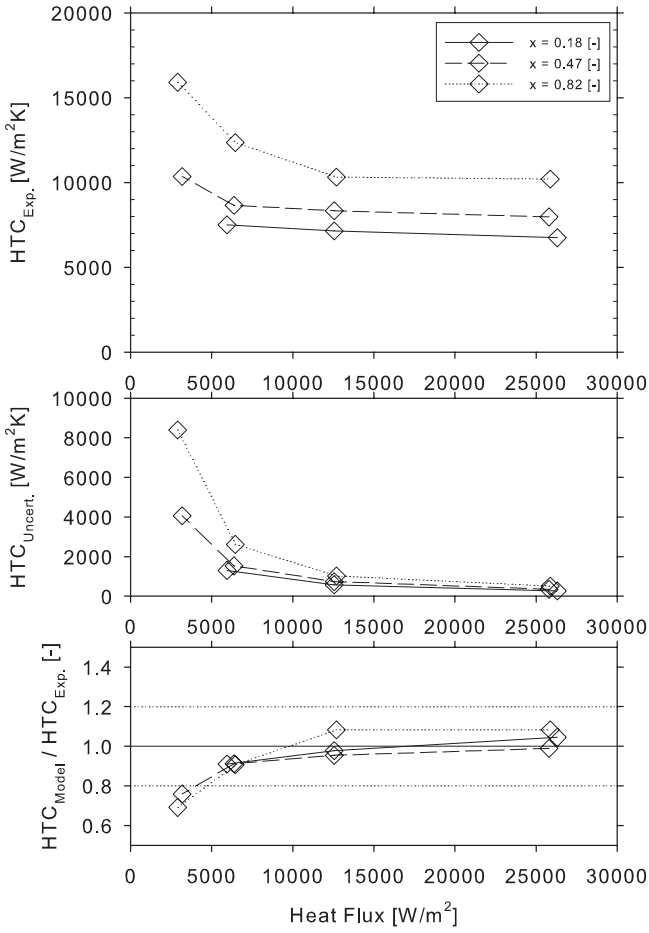

Figure 5.46: Heat transfer for Nitrogen-10 as a function of heat flux in the 1 mm tube. $36.2 < p < 36.5$ bar, $484 < G < 495$ kg/m^{2}s.

In Figure 5.47, the heat transfer coefficient increases with increasing mass flux, and there is no flattening or reduction at $x > 0.5$ as for Ethane-27 and Ethane-10 respectively. From Table 2.2 the values of $We_{\mathrm{gs}} >> 20$ even for $G = 280$ kg/m^{2}s, which indicates that the flow is always in the annular flow regime for all mass fluxes in Figure 5.47.

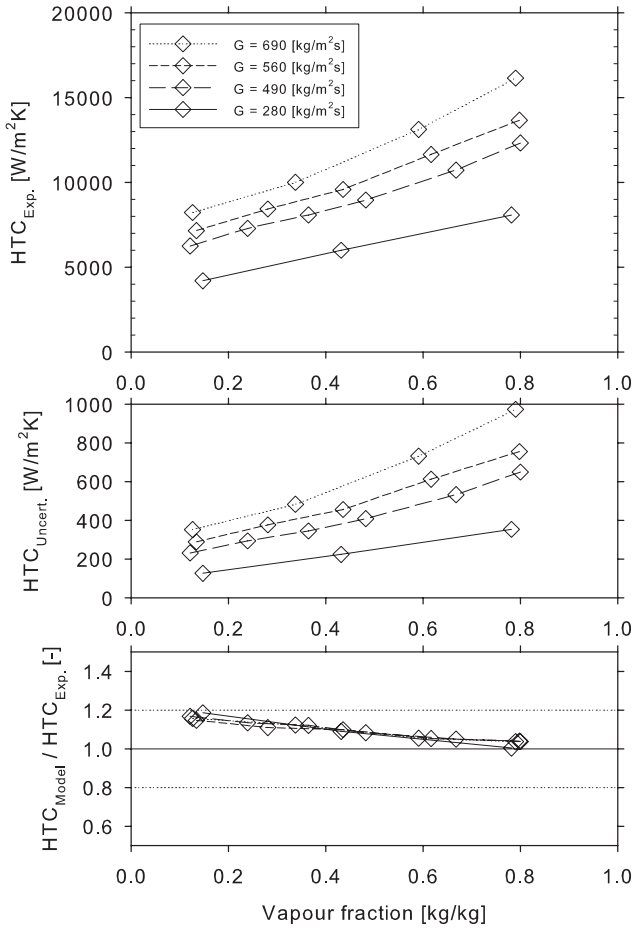

Figure 5.47: Heat transfer coefficient Nitrogen-10 in the 1.0 mm tube with mass flux as parameter. $25.6 < p < 26.3$ bar, $26.0 < q'' < 26.9$ kW/m^2.

For low pressure at $G = 490$ kg/m^{2}s in Figure 5.48, the heat transfer coefficient also increases for increasing vapour fraction. This is also clear for $p = 36$ bar and $p = 42$ bar, but the difference in the heat transfer coefficient for these two series is small. This is similar to the observations of Methane-100 but not for Ethane-10 and Ethane-27.

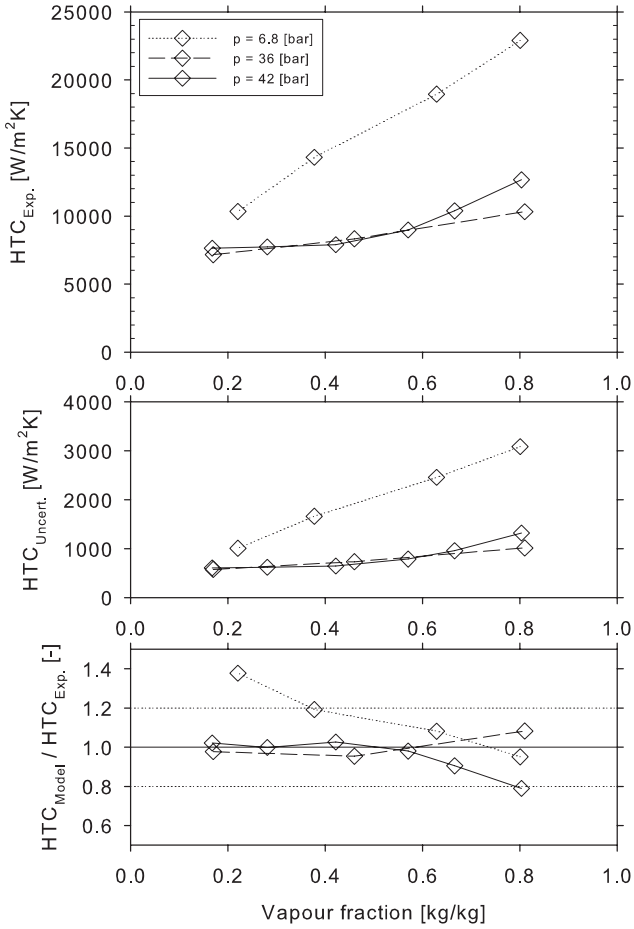

Figure 5.48: Heat transfer coefficient for Nitrogen-10 in the 1.0 mm tube with pressure as parameter. $484 < G < 499$ kg/m^{2}s, $12.5 < q'' < 14.0$ kW/m^2.

For $G = 280$ kg/m^{2}s in Figure 5.49, the trend is the same as for $G = 490$ kg/m^{2}s. Also for Methane-100 the trend was the same for $G = 280$ and 490 kg/m^{2}s. Note that the series at $p = 41.4$ bar is at a different mass flux and therefore yields a lower heat transfer coefficient.

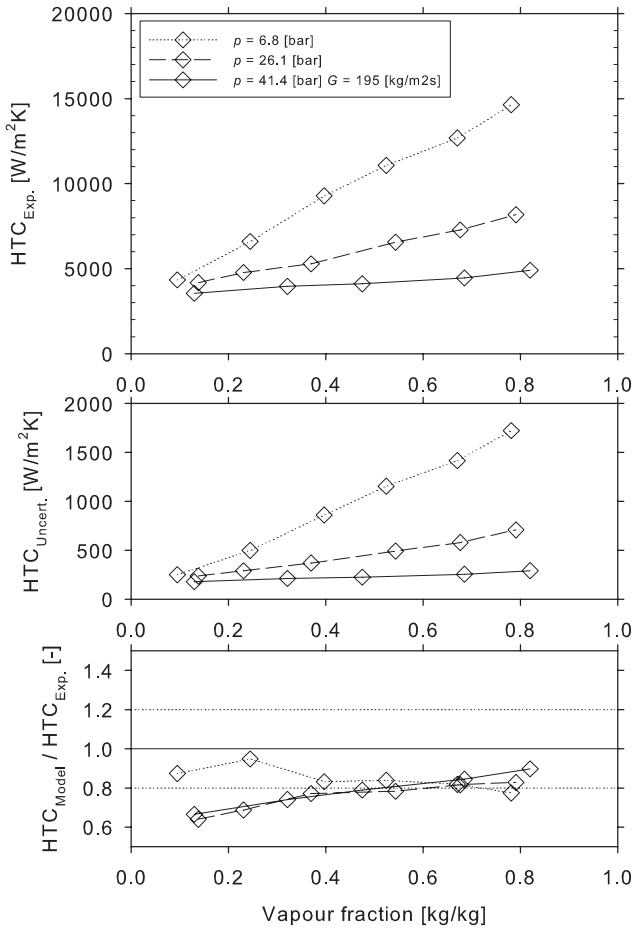

Figure 5.49: Heat transfer coefficient for Nitrogen-10 in the 1.0 mm tube with pressure as parameter. $275 < G < 283$ kg/m^{2}s, $12.0 < q'' < 12.9$ kW/m^2.

5.3.7 Effects from temperature glide

Effect on experimental results

For condensation of Methane-100 at low pressure, the heat transfer coefficient keeps increasing for increasing vapour fraction. For Ethane-10 and Ethane-27 at similar conditions, this is only seen over a range of vapour fraction: in Figure 5.32 for Ethane-10, the heat transfer coefficient is reduced for approximately $x > 0.8$. In Figure 5.31 for Ethane-27, it does not increase for $x > 0.4$.

A possible explanation for this is that the equilibrium temperature is very sensitive to changes in vapour fraction at low pressure. Figure 5.50 shows the equilibrium temperature for different pressures for the binary fluids as a function of the vapour fraction $T_{\mathrm{eq}}(x)$ (black lines).

As the enthalpy is not proportional to the vapour fraction for binary mixtures, the enthalpy curves at the corresponding temperature is plotted along the second x-axis $T_{\mathrm{eq}}(e)$ (gray lines). The slope of these curves at a given point equals $\mathrm{d}T/\mathrm{d}x$ and $\mathrm{d}T/\mathrm{d}e$ respectively.

It is assumed that the equilibrium temperature equals the interface temperature. For the 6 bar series for Ethane-10, $\mathrm{d}T/\mathrm{d}e$ is much higher for approximately $0.8 < x$ than for $0.8 > x$. This means that for a given heat flux, the equilibrium temperature drops more when condensing at $0.8 > x$ than at $0.8 < x$. This reduces the driving temperature difference in the condensation process and results in a lower heat transfer coefficient. This coincides well with the measurements in Figure 5.32.

The range where $\mathrm{d}T/\mathrm{d}e$ is steep for Ethane-27 goes down to $x \approx 0.6$. This coincides well with the reduction for $x > 0.5$ in the 7 bar series in Figure 5.39. The behaviour is however not seen for the case with lower mass flux in Figure 5.40.

The same phenomena is found also for higher pressure in Figure 5.34, however the effect is not that large at this pressure. The higher heat flux (≈ 26 kW/m^2) than in Figure 5.31 and 5.32 (≈ 13 kW/m^2) can explain the larger reduction in the heat transfer coefficient.

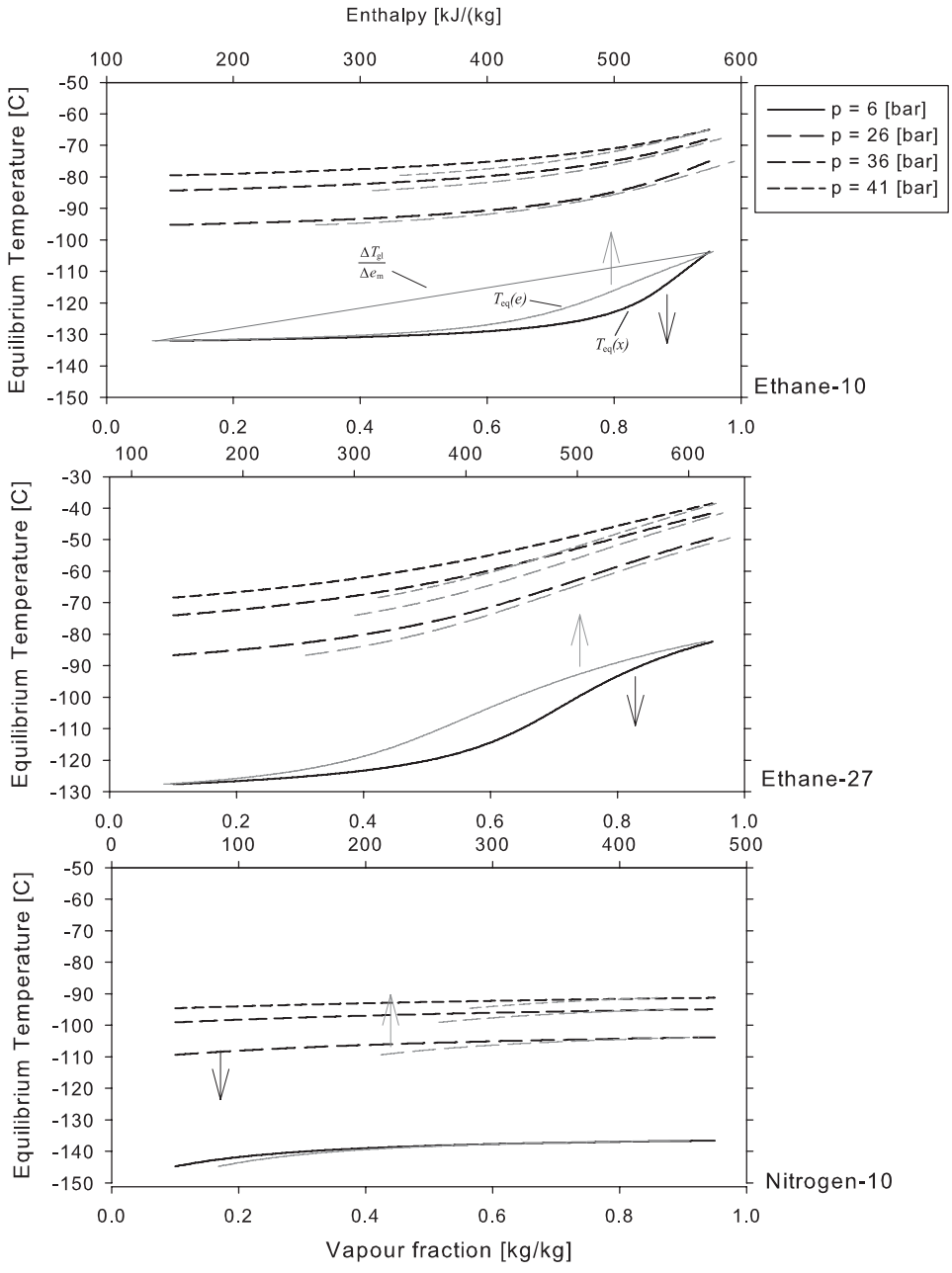

Figure 5.50: Equilibrium temperature for the binary fluids for different pressure.

Effect on model

The model R_{mc}, expressing the reduction in the heat transfer coefficient due to the temperature glide given in Equation 2.32, uses the approximation $dT/de \approx \Delta T/\Delta e$. From Figure 5.50, it is clear that the difference between the approximation and the actual glide can be considerable for low pressure. It holds much better for higher pressure. For Nitrogen-10, the approximation holds for all pressure levels and vapour fractions. This could explain why the agreement with the heat transfer model fits better for Nitrogen-10 than for Ethane-10 and Ethane-27 in Figure 5.54.

For a pure fluid it has been shown that increased vapour fraction generally gives a higher heat transfer coefficient. This is because of thinner liquid film and higher shear at the vapour/liquid interface. For a binary fluid, this effect is dampened or even overcome by the drop in T_{i}.

5.3.8 Comparison with models

The heat transfer model for condensation of mixtures presented in Equation 2.32 uses the Thome et al. [68] single component condensation model (denoted h_{sc}) as the basis for developing a multi component condensation model (denoted h_{sc}). Principally, any single component condensation heat transfer model can be used as h_{sc} in Equation 2.32. The results in Table 5.3 revealed that the Thome et al. [68] model did not fit that well with the 0.5 mm and 0.25 mm single component condensation measurements. Therefore, in the following comparison with a heat transfer model, the Cavallini et al. [11] single component condensation model presented on page 25 is used as h_{sc} in Equation 2.32. The binary mixture properties were found assuming equilibrium between the phases.

To take into account the actual diameter through which the vapour core flows, Equation 2.34 is changed to

$$h_{\mathrm{conv,v}} = 0.023 Re_{\mathrm{v}}^{0.8} Pr_{\mathrm{v}}^{0.33} \frac{k_{\mathrm{v}}}{d - 2\delta} f_{\mathrm{i}} \tag{5.4}$$

and the Reynolds number in Equation 2.35 is changed to

$$Re_{\mathrm{v}} = \frac{\rho_{\mathrm{v}} u_{\mathrm{v}} (d - 2\delta)}{\mu_{\mathrm{v}}} \tag{5.5}$$

A comparison between the experimental results and the original model using Thome et al. [68] as h_{sc} will also be presented.

The effect of the factor R_{mc} on the predicted heat transfer coefficient is illustrated in Figure 5.51 and 5.52.

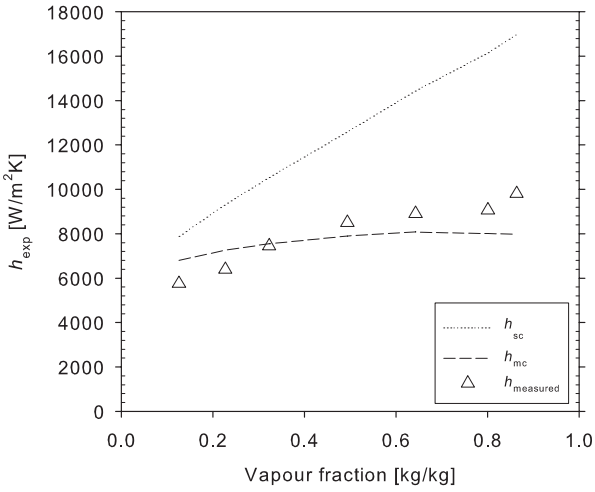

Figure 5.51: The effect of R_{mc} on the heat transfer coefficient in the 1 mm tube for Ethane-27. The measurement series is the G = 490 kg/m^{2}s series in Figure 5.38.

The measurement series in Figure 5.51 is the same as in Figure 5.38. It is shown together with the calculated heat transfer coefficient h_{mc} using Equation 5.4 and 5.5. The values of h_{sc} are also shown, which compared to h_{mc} shows the effect of R_{mc}.

The values of h_{sc} are far higher than h_{mc} showing the increasing effect of R_{mc} at increasing vapour fraction. The values of h_{mc} fit quite well with the experimental results. The temperature glide ΔT_{gl} for Ethane-27 at approx. 26 bar is around 41°C and the heat of evaporation Δe_m = 440 kJ/kg.

Figure 5.52 shows the same for the 0.5 mm tube for Ethane-10. Here the temperature glide and heat of evaporation is smaller ($\Delta T_{gl} = 20°C, \Delta e_m$ = 320 kJ/kg) as the pressure is higher and the concentration of the main component higher. The agreement between h_{mc} and the experimental data is good also here.

Del Col et al. (2005)

Figure 5.53 shows the experimental data for Ethane-10, Ethane-27 and Nitrogen-10 compared to h_{mc} as presented in Del Col et al. [23] in Chapter 2.4.3. Most of the measurements are under predicted, although the scatter for the Ethane-27 and Nitrogen-10 measurements is not large. For Ethane-

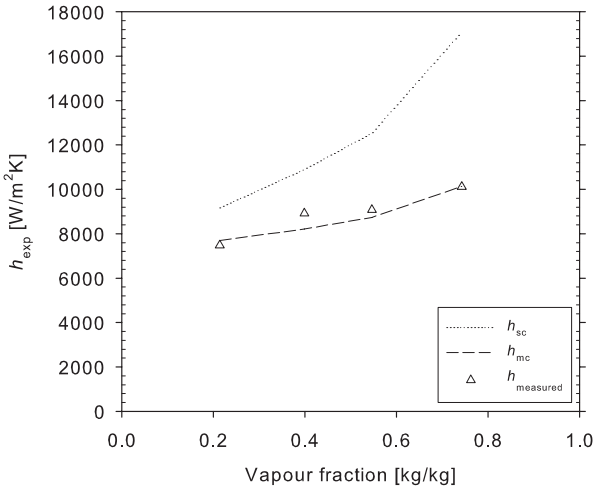

Figure 5.52: The effect of R_{mc} on the heat transfer coefficient in the 0.5 mm tube for Ethane-10. The measurement series is the $q'' = 12.3$ kW/m^2 series in Figure 5.35.

10, the model tends to predict high heat transfer coefficients better than lower.

For Ethane-27, the model seems to under predict the 0.5 and 0.25 mm tubes more than the 1 mm tube. For Nitrogen-10 there is low, but the model under predicts the results by 36 %.

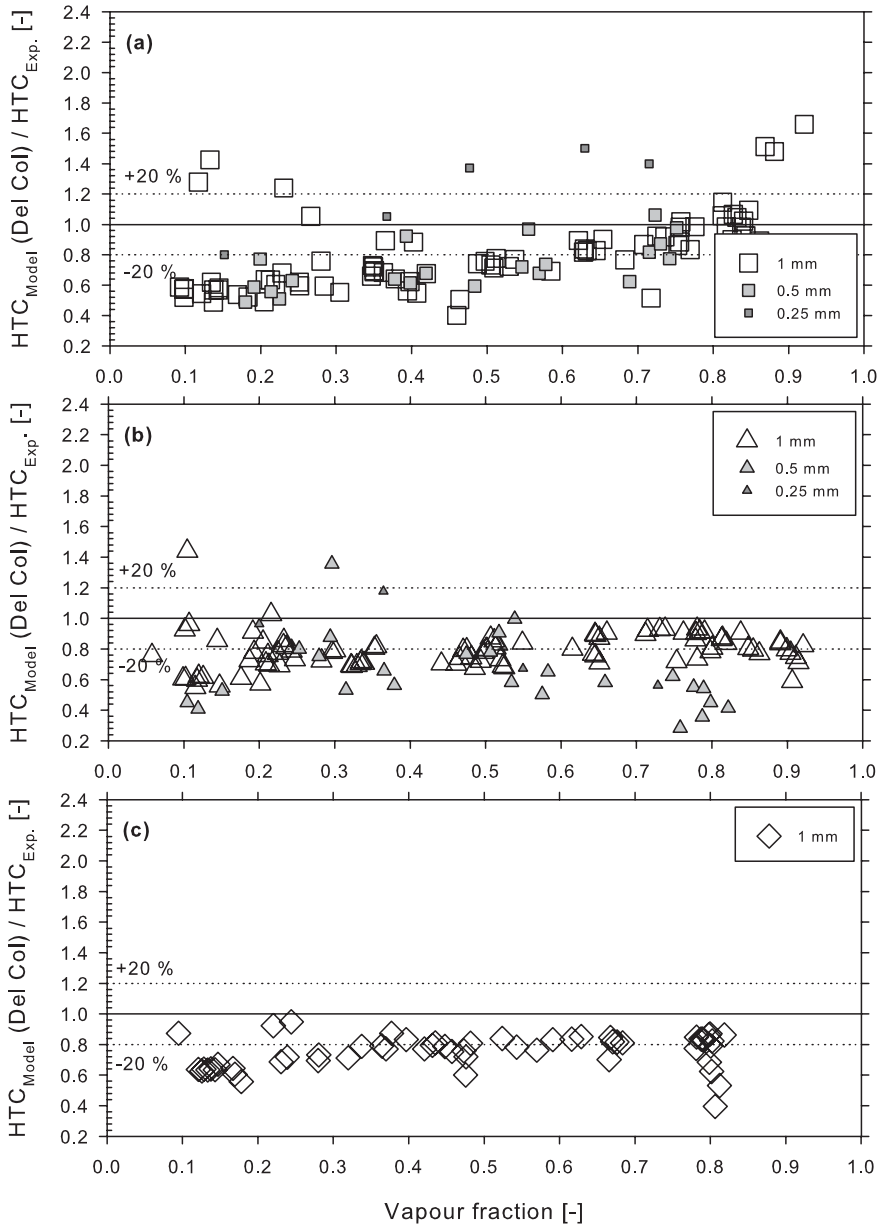

Figure 5.53: Comparison between experimental and calculated heat transfer coefficient for (a) Ethane-10, (b) Ethane-27 and (c) Nitrogen-10 as described in Del Col et al. [23].

Using Cavallini et al. (2006) as h_{sc}

For Ethane-10, some measurements at low and high vapour fraction are over predicted by approx. 100 %. This is the 4.8-6.8 bar measurement series shown in Figure 5.32, the 6.8-7.5 bar series in Figure 5.31 and a similar measurement series at $p = 16.5$ bar. The low heat transfer occurring for $0.3 > x > 0.6$ is implemented in the model for h_{mc}. The same series can also be identified in Figure 5.53 (a).

The agreement for Ethane-10 is otherwise very good both for the 1 mm and 0.5 mm tube, but not for the 0.25 mm tube. Also for Ethane-27 the agreement is very good for the 1 mm tube, while there is a scatter and a general under prediction for the 0.5 mm and 0.25 mm tubes. For the Nitrogen-10 measurements in the 1 mm tube, the agreement is very good with the Cavallini-based model as 87.7 % of the measurements are within $\pm$ 20 %.

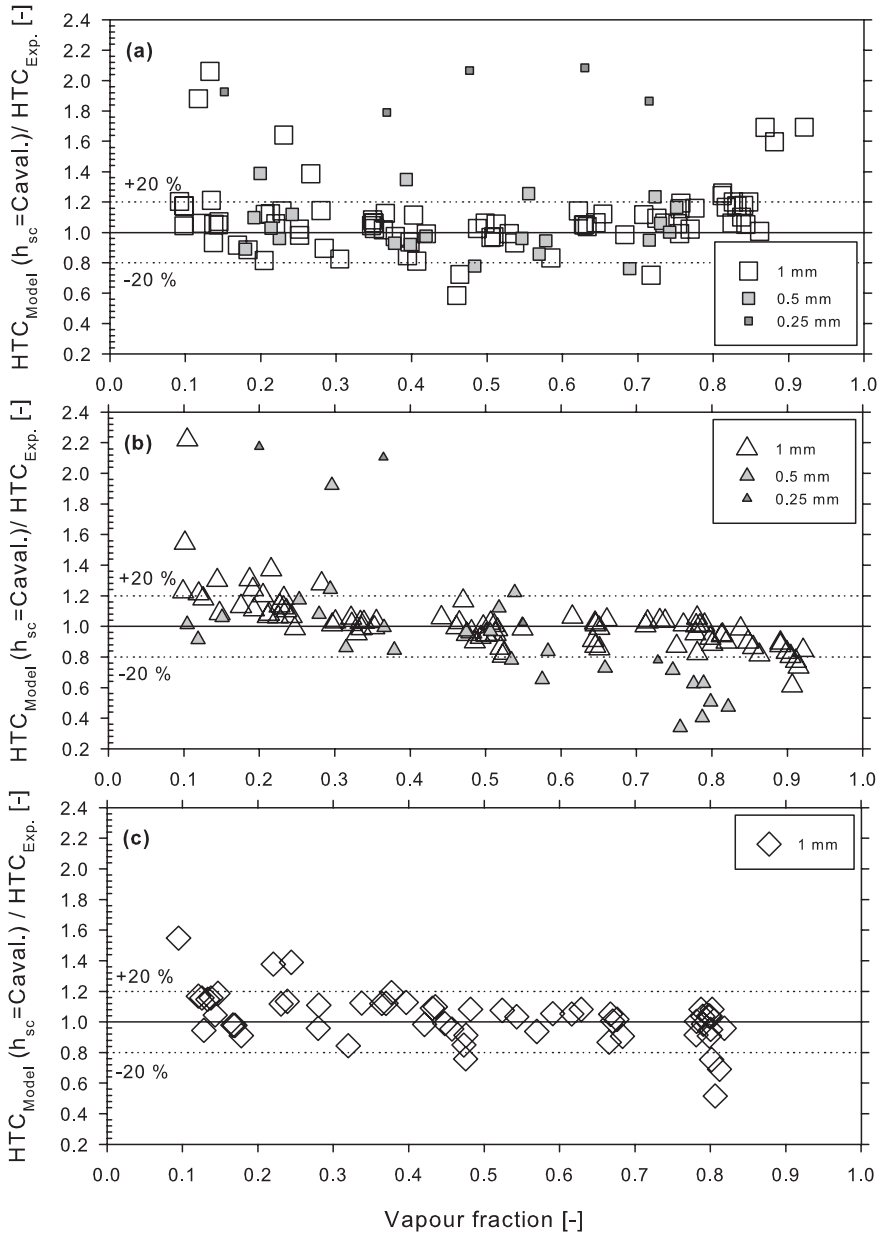

Figure 5.54: Comparison between experimental and calculated heat transfer coefficient for (a) Ethane-10, (b) Ethane-27 and (c) Nitrogen-10 using Cavallini et al. [11] as h_{sc}.

Summary

The results are summarised in Table 5.4. A positive average deviation means that the experimental results are greater than the predicted results.

In general, the zeotropic condensation model described in Del Col et al. [23] generally under predicts the heat transfer results. For the 1 mm tube, the Ethane-10 and Ethane-27 heat transfer coefficient is predicted 21 % lower than the experimental results. Around 30 % of the experimental results are within ±20 % of the predicted. The model fails even more to predict the 0.5 mm tube results, however the few 0.25 mm tube measurements are predicted satisfactory well.

If the single phase flow model by Thome et al. [68] is replaced by the model from Cavallini et al. [11] in Equation 2.32, the fit is much better. In fact, over 80 % of all the experimental values are within ± 20 % of the predicted values for the 1 mm tube. The model appears to over predict the results for low vapour fraction for Ethane-27, and under predicts them for high vapour fraction. The same is noted for the Nitrogen-10 measurements for the 1 mm tube.

The results from the 0.5 mm tube are predicted with slightly reduced precision than the 1 mm results. None of the models manages to predict the 0.25 mm results very well.

Correlation/Tube		Del Col et al.			h_{sc} = Cavallini et al.		
		Ethane-10	Ethane-27	Nitrogen-10	Ethane-10	Ethane-27	Nitrogen-10
1 mm	Av. dev.	0.79	0.79	0.75	1.08	0.94	1.03
	$0.8 \leq \kappa \leq 1.2$	33 %	31 %	25 %	81 %	83 %	88 %
0.5 mm	Av. dev.	0.73	0.64	-	1.03	0.88	-
	$0.8 \leq \kappa \leq 1.2$	24 %	12 %	-	76 %	56 %	-
0.25 mm	Av. dev.	1.22	0.84	-	1.94	1.52	-
	$0.8 \leq \kappa \leq 1.2$	20 %	50 %	-	0 %	25 %	-

Table 5.4: Results for binary component condensation. Av. dev. refers to the average value of $\kappa = \mathrm{HTC}_{\mathrm{Model}} / \mathrm{HTC}_{\mathrm{Exp.}}$.

5.3.9 Two phase pressure drop

The measured frictional pressure drop Δp_f was extracted as shown in Equation 3.7. As discussed there, $\Delta p_\mathrm{inlet/outlet}$ was set to zero.

The measured frictional pressure drop is an average quantity over a distance. It is measured as the pressure difference Δp between the inlet and outlet of the test tube, which has a length of $\Delta z = 20$ cm. Except for the adiabatic measurements, condensation takes place along a 5 cm long section in the middle of the tube, so the vapour fraction changes along the test section and is also different on both sides of the test section. As the change in vapour fraction Δx is small, the pressure drop can be approximated using $\overline{x} = x_\mathrm{in} - \Delta x/2$. Equation 5.6 gives a good approximation:

$$\left(\frac{\mathrm{d}p}{\mathrm{d}z}\right)_{\mathrm{f,x}} \approx \left(\frac{\mathrm{d}p}{\mathrm{d}z}\right)_{\mathrm{f},\overline{\mathrm{x}}} \approx \left(\frac{\Delta p}{\Delta z}\right)_{\mathrm{f},\overline{\mathrm{x}}} \tag{5.6}$$

Only a limited number of measurements for Methane-100 are presented in detail here. They are all diabatic measurements. Comparison of all results with two phase flow models is found in Chapter 5.3.10.

The points in Figure 5.55 are the same as for the heat transfer measurements presented in Figure 5.15. Included in Figure 5.55 are also three corresponding single phase flow measurements for comparison. As for the heat transfer coefficient, the pressure drop increases for increasing mass flux and increasing vapour fraction. The experimental data are also compared to a pressure drop model, in this case to the model from Friedel [25]. It appears that his model over predicts the pressure drop at the higher vapour fraction.

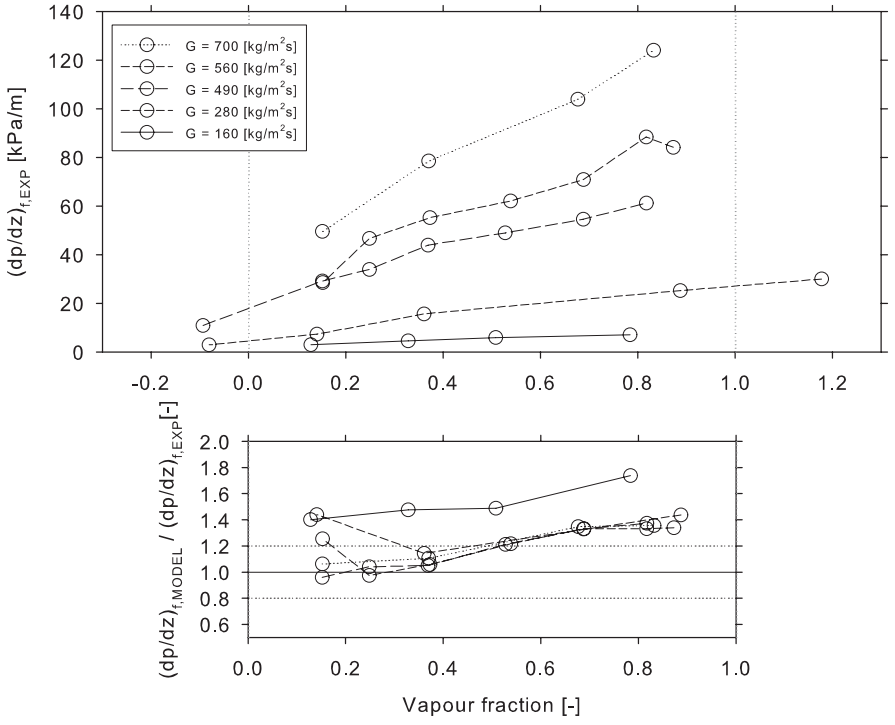

Figure 5.55: Frictional pressure drop for Methane-100 in the 1 mm tube with constant heat flux $q'' = 26.3$ kW/m^2 and pressure $p = 26$ bar.

More single phase flow pressure drop results are shown in Figure 5.56 which corresponds to the heat transfer data presented in Figure 5.17. It is evident that the frictional pressure drop increases for decreasing pressure and increasing vapour fraction. It appears that the agreement with the pressure drop model from Friedel depends on the pressure level. The relative deviation for $p = 41.6$ bar is large, however the absolute deviation is not large.

The transition from liquid into two phase pressure drop appears to be smooth. The transition from two phase flow into the gas phase also appears to be smooth, although most models shown in Figure 2.12 predict a peak at $x \approx 0.9$. This could not be demonstrated by the test setup as the two phase flow was unstable for $0.85 < x < 1.1$. Most models also predict that the two phase pressure drop for $0.4 < x < 0.6$ is the same as the gas phase pressure drop. This does not seem to be the case for the measurements presented in Figures 5.55 or 5.56.

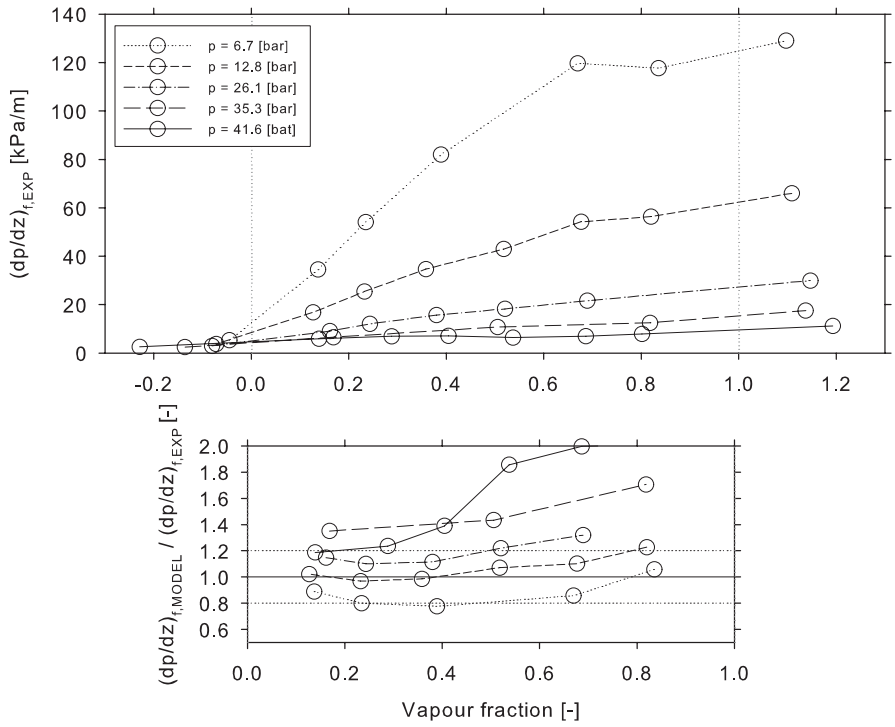

Figure 5.56: Frictional pressure drop for Methane-100 in the 1 mm tube with constant mass flux $G = 280$ kg/m^{2}s and $q'' = 12.9$ kW/m^2.

The figures 5.57 and 5.58 show the pressure drop characteristics for the 0.5 mm and 0.25 mm tubes respectively. The pressure drop increases for increasing vapour fraction and mass flux in the 0.5 mm tube, and the lower pressure gives a higher velocity and a higher pressure drop in the 0.25 mm tube. The deviation from the Friedel model shows the same characteristics for the 0.5 mm tube as for the 1 mm tube.

The predicted frictional pressure drop for the 0.25 mm tube is more than twice as large as predicted. The deviation between model and experimental results do not appear to be a function of neither the vapour fraction nor pressure in the 0.25 mm tube.

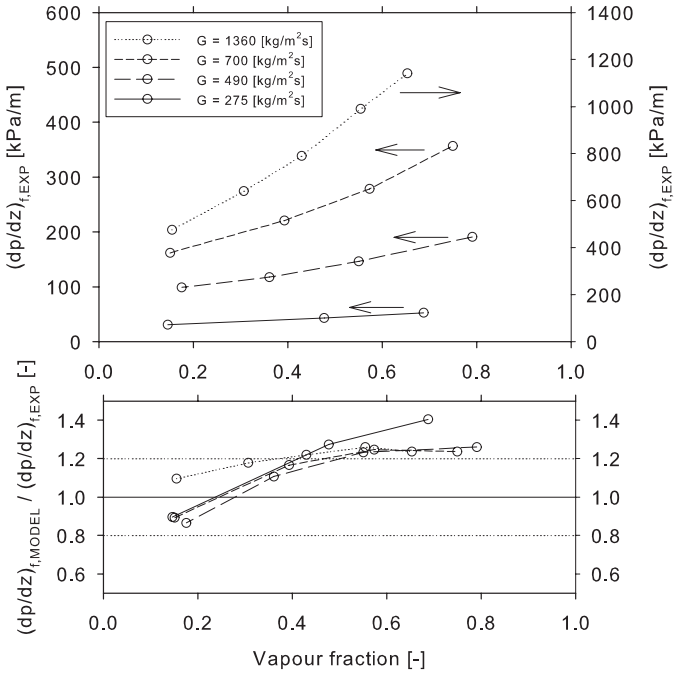

Figure 5.57: Frictional pressure drop for Methane-100 in the 0.5 mm tube with constant heat flux $12.2 < q'' < 38.7$ kW/m^2 and pressure $24.3 < p < 26.0$ bar.

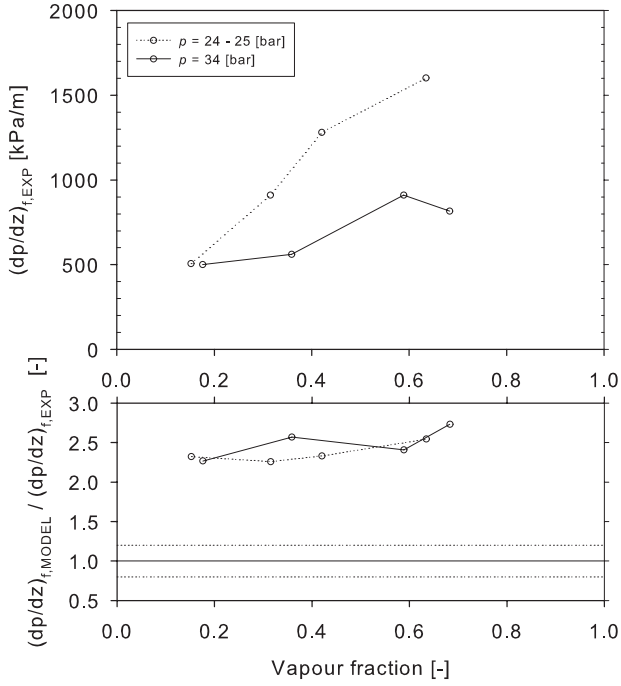

Figure 5.58: Frictional pressure drop for Methane-100 in the 0.25 mm tube with mass flux $1114 < G < 1325$ kg/m^{2}s and heat flux $19.3 < q'' < 36.8$ kW/m^2.

The fricional pressure drop $\Delta p_{\text{friction}}$ presented in the previous figures is calculated from Equation 3.7 where $\Delta p_{\Delta x} > 0$. For most measurement series, $\Delta p_{\Delta x} \ll \Delta p_{\text{friction}}$ but still $\Delta p_{\Delta x}$ is taken into account when calculating the friction pressure drop. Figure 5.59 shows two series where the frictional pressure drop at diabatic conditions when $\Delta p_{\Delta x}$ is taken into account and two corresponding adiabatic series.

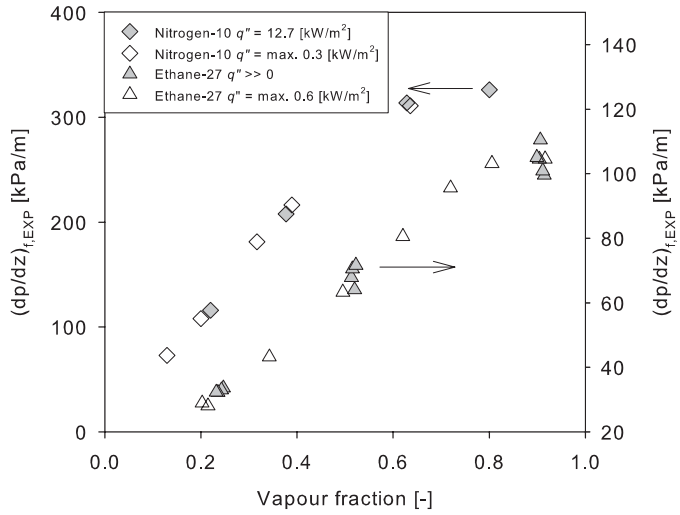

Figure 5.59: Frictional pressure drop for the 1 mm tube with adiabatic and diabatic flow. Pressure $6.8 < p < 7.3$ bar and mass flux $484 < G < 501$ kg/m^{2}s for Nitrogen-10, $274 < G < 282$ kg/m^{2}s and $3.4 < q'' < 26.0$ kW/m^2 for Ethane-27.

5.3.10 Comparison with models

The measurements compared with the different models are a mix of adiabatic and diabatic measurements, where the vast majority are diabatic measurements.

Two-phase pressure drop for binary fluids should be no different than from single component fluids. The fluid properties for the binary fluids are evaluated at equilibrium state, i.e. assuming different concentrations in the phases according to the dew- and bubble point lines in the equilibrium diagram. This gave a better agreement with the models than evaluating the properties at the total concentration.

All the pressure drop results are presented and compared with different correlations in Figure 5.60 to 5.65, and the same results can be found in Table 5.5. In the table, a positive average deviation means that the experimental results are greater than the predicted result, relative to the predicted result. Within ±20 % refers to the share of experimental result within ±20 % of the predicted.

Niño (2002)

The comparison with the correlation from Niño [55] in Figure 5.60 shows some scatter and the model systematically over predicts the pressure drop. Particularly for the 0.25 mm tube where the correlation predicts the pressure drop to be 74.4 % higher than measured. Only 33.9 % and 10.2 % of the results are within ±20 % of the predicted pressure drop for the 1 mm and 0.5 mm tube respectively.

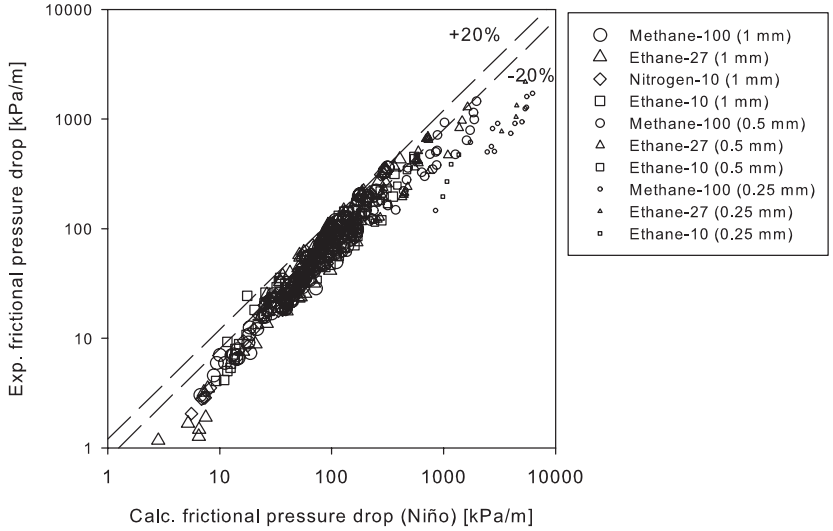

Figure 5.60: Experimentally obtained frictional pressure drop compared with the correlation from Niño [55] for all tubes and all fluids.

Garimella et al. (2005)

For the Garimella-correlation in Figure 5.61, the agreement between the experimental results and the predicted values is even worse. The average value deviation for the 1 mm tube is not far from zero, but the scatter is significant. Only 22.7 % of the experimental values for all the tubes are within ±20 % of the predicted. This correlation was developed using R-134a only, while the tubes used ranged from 0.5 mm to 4.91 mm. The way the Colebrook friction factor is implemented into the correlation by the current author may also be unfavourable.

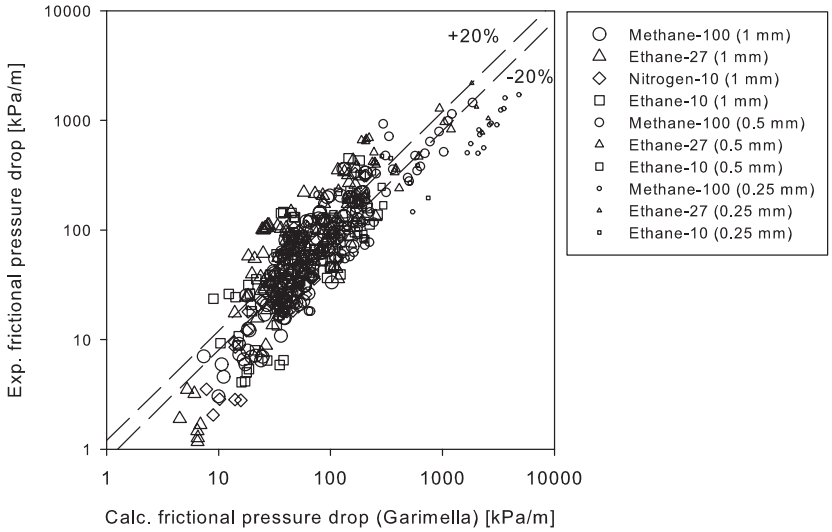

Figure 5.61: Experimentally obtained frictional pressure drop compared with the correlation from Garimella et al. [27] for all tubes and all fluids.

Friedel (1979)

The second best prediction is made by the Friedel-correlation, which over predicts the results by 13.0 % and where 63.2 % of the experimental results are within ±20 % of the predicted. As the other correlations, the prediction for the 0.25 mm tube is not good, as is visible in Figure 5.62. This correlation was developed using conventional tubes.

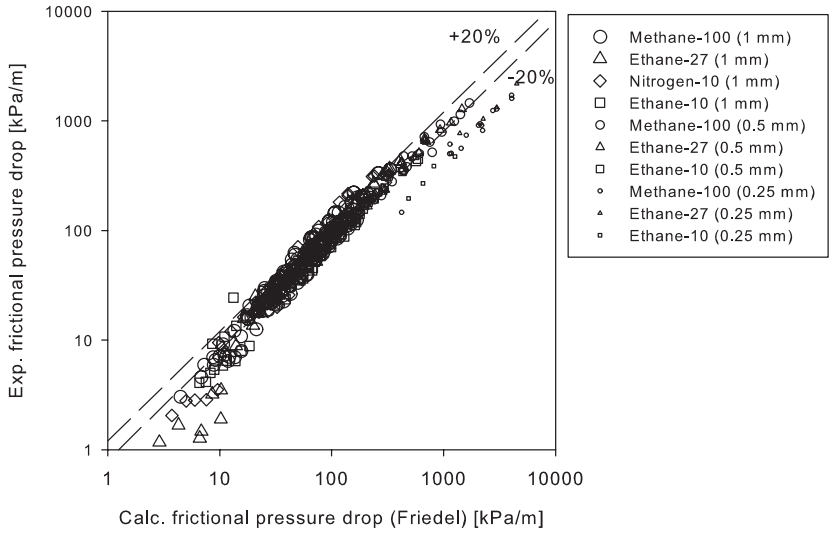

Figure 5.62: Experimentally obtained frictional pressure drop compared with the correlation from Friedel [25] for all tubes and all fluids.

Cavallini et al. (2006)

The pressure drop model taken from Cavallini et al. [11] under predicts the pressure drop by 12.1 % and 49.3 % of the predictions are within ±20 % of the experimental results. A under prediction can be seen for the 1 mm and the 0.5 mm tube. The precision for this correlation is improved if the entrainment ratio in Equation 2.26 is set to 0 and W in Equation B.3.19 is set to 1. Then, 66.4 % of the experimental results are within ±20 % of the predicted and the average deviation is -9.9 %.

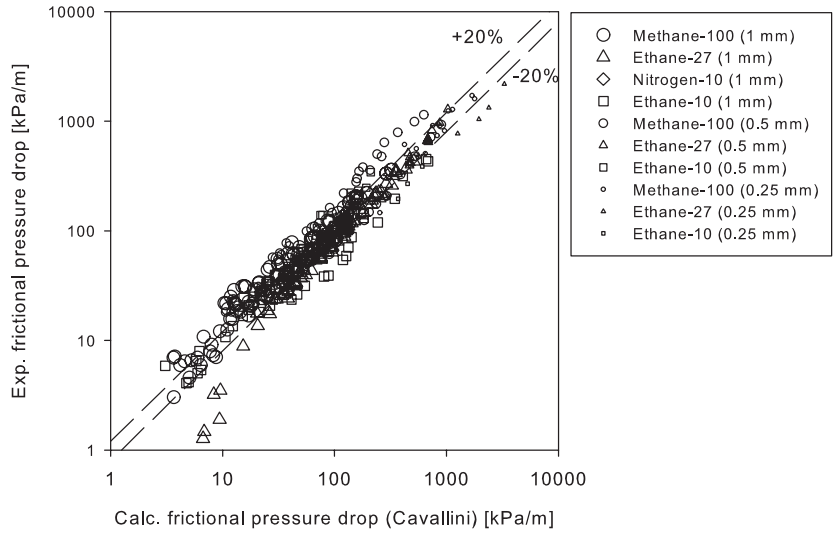

Figure 5.63: Experimentally obtained frictional pressure drop compared with the correlation from Cavallini et al. [11] for all tubes and all fluids.

Figure 5.64 shows that the deviations are pressure dependent, where pressure drop at low pressure is over predicted and pressure drop at high pressures are under predicted. The deviations are more extreme for the 0.5 mm tube, but not for the 0.25 mm tube.

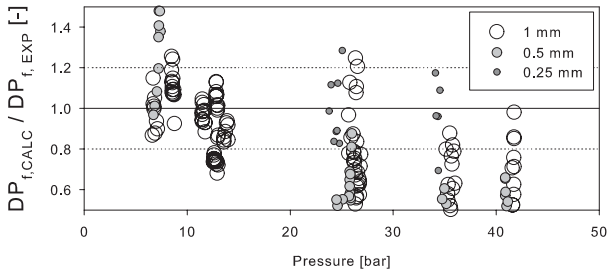

Figure 5.64: Deviations from the correlation from Cavallini et al. [11] as a function of pressure for Methane-100 in all tubes.

Müller-Steinhagen and Heck (1986)

The correlation from Müller-Steinhagen and Heck [53] is not presented in this thesis. As shown in Figure 5.65, it predicts the experimental results for the 1 mm tube well, where 60.6 % of the experimental values are within ±20 % of the predicted. For the 0.5 mm and particularly for the 0.25 mm tube, the deviation is larger.

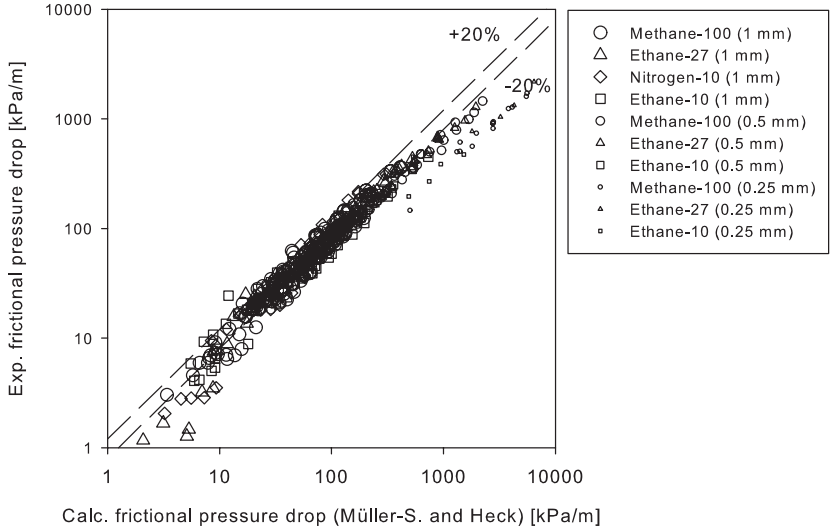

Figure 5.65: Experimentally obtained frictional pressure drop compared with the correlation from Müller-Steinhagen and Heck [53] for all tubes and all fluids.

CESNEF-2 by Lombardi et al. (2000)

Figure 5.66 shows the model from Lombardi et al. [45] which gives the best prediction for both the 1 mm and 0.5 mm tubes. The parameters for CESNEF-2 were used in the calculations along with the Colebrook-friction factor. The model introduces a dimensionless parameter *Lo* and weights the friction factor contribution from the liquid, vapour and mixed phase conditions respectively.

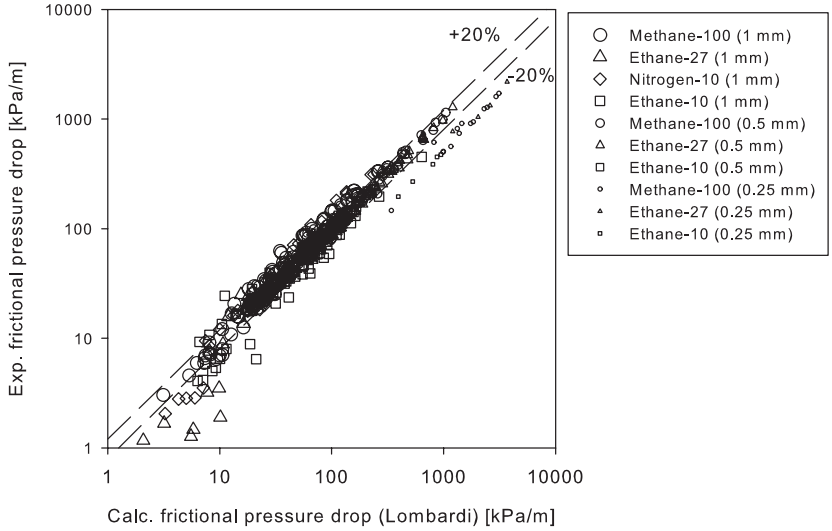

Figure 5.66: Experimentally obtained frictional pressure drop compared with the correlation from Lombardi et al. [45] for all tubes and all fluids.

Summary

The CESNEF-2 model from Lombardi et al.[45] correlation gives the best agreement for both the 1 mm and 0.5 mm tube.

As mentioned earlier, the Colebrook friction factor was used in the pressure drop correlations in Figures 5.60 to 5.65, which is based on the measured relative surface roughness listed in Table 3.2.

The relative roughness increases with smaller tube diameter, and it appears that except for the Cavallini-correlation, the over prediction increases for decreasing tube diameters. In Chapter 3.2.2 it was discussed if the relative roughness is a representative characteristic in a friction factor used to predict pressure drop for drawn tubes. As a comparison, Figure 5.67 shows the measured and predicted pressure drop using the Mũller-Steinhagen and Heck-correlation where the friction factor f for a smooth tube is used. The results are also shown in Table 5.5.

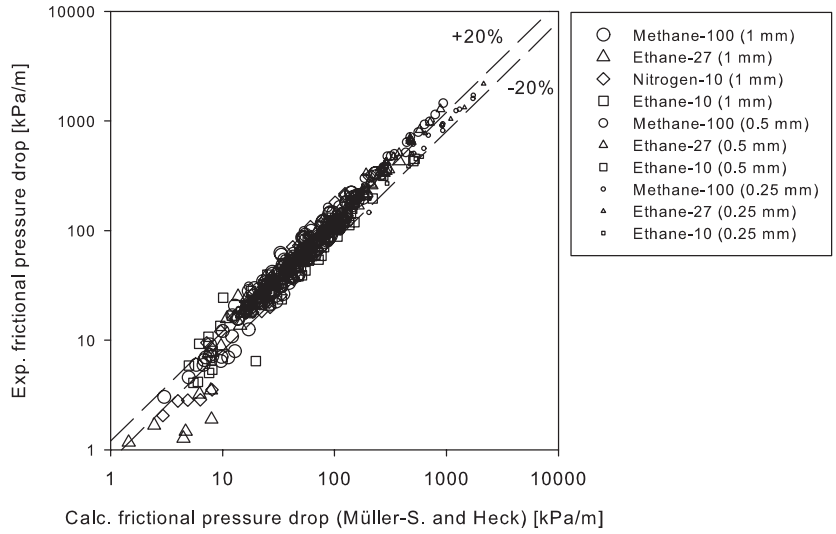

Figure 5.67: Experimentally obtained frictional pressure drop compared with the correlation from Müller-Steinhagen and Heck [53] for all tubes, using f for a smooth tube.

For the 1 mm tube, there is now a under prediction of the pressure drop of 12.7 %. For the 0.5 mm tube, the under prediction is greater; 34.5 %. However for the 0.25 mm tube, the average deviation is very small and 87.0 % of the predictions are with in ±20 % of the measured pressure drop

for the Mũller-Steinhagen and Heck-correlation. This can be caused by a faulty determination of d_c for the 0.25 mm tubes, or the relative roughness calculated does not reflect the physics.

An attempt was also made to use the single phase friction factors obtained from Figure 5.13 to predict the two-phase flow pressure drop in the 0.5 mm and 0.25 mm tubes. A fit was made from the single phase friction factor on the form:

$$f_{1ph} = a \cdot Re + b \qquad \text{for } Re < 5000 \tag{5.7}$$

$$f_{1ph} = c \qquad \text{for } Re > 5000 \tag{5.8}$$

where $a = 7 \cdot 10^{-6}$, $b = 0.023$ and $c = 0.058$ for the 0.5 mm tube and $a = 5 \cdot 10^{-6}$, $b = 0.02$ and $c = 0.045$ for the 0.25 mm tube. This fit was used to predict the friction factor for the two phase flow measurements using the Reynolds number as defined in the different pressure drop models. The agreement is presented in Table 5.5 and it is clear that the agreement is not that good.

Tube / Correlation	1 mm		0.5 mm		0.25 mm	
	Average dev.	within ±20 %	Average dev.	within ±20	Average dev.	within ±20%
Single Phase Eq. 2.37 and $f_{\text{Colebrook}}$	+21.1 %	62.6 %	+25.9 %	27.7 %	-44.7 %	0 %
Single Phase Eq. 2.37 and f_{smooth}	+41.5 %	48.2 %	+83.0 %	4.6 %	+19.8 %	33.3 %
Garimella et al. [27]*	-12.3 %	23.0 %	+6.9 %	26.1 %	-49.9 %	4.3 %
Niño [55]*	-26.7 %	33.9 %	-40.3 %	10.2 %	-74.4 %	0 %
Friedel [25]*	-9.9 %	64.8 %	-15.0 %	72.7 %	-57.0 %	0.0 %
Cavallini et al. [11]*	+9.5 %	51.9 %	+30.2 %	37.5 %	-12.9 %	52.2 %
Müller-Steinhagen and Heck [53]*	-13.5 %	60.6 %	-27.5 %	15.9 %	-66.1 %	0.0 %
Lombardi et al. [45]*	1.7 %	69.5 %	3.5 %	88.6 %	-46.2	0 %
Cavallini [11] f_{smooth}	+30.7 %	46.3 %	+99.7 %	15.6 %	+95.6 %	21.7 %
Müller-Steinhagen and Heck [53] f_{smooth}	+12.7 %	59.8 %	+34.5 %	20.0 %	-3.8 %	87.0 %
Cavallini [11] f_{1ph}**			+15.8 %	47.7 %	+46.6 %	26.1 %
Müller-Steinhagen and Heck [53] f_{1ph}**			-47.0 %	2.3 %	-49.2 %	0 %

Table 5.5: Pressure drop agreement with correlations. (*using $f_{\text{Colebrook}}$)

Chapter 6

Validity of results

This chapter presents and discusses different ways of verifying the experimental set-up.

6.1 Equilibrium between the phases

The assumption that the phases are in equilibrium is vital for the discussion of the results. This includes a uniform temperature between the phases and zero net exchange of mass. It is reasonable to assume equilibrium for several reasons; The phases are well mixed after the pre-heaters due to the high velocity and the relatively long distance and a bend between the pre-heaters and the test tube. This offers time for exchange of heat and mass between vapour and liquid. Also, the space where the fluid flow occurs is confined.

There might be concentration stratification in the liquid film during condensation as the mixing of this can be limited. However a meaningful quantification of this is regarded as very difficult.

6.2 Temperature differences in adiabatic and diabatic flow

A comparison of the expected drop in saturation temperature due to the measured pressure drop through the test section $T_{\text{sat}}(p_{\text{in}}) - T_{\text{sat}}(p_{\text{in}} - \Delta p)$ and the measured temperature difference $T_{\text{in}} - T_{\text{out}}$ were done. As seen in Figure 3.4, the pressure drop is measured over a tube length of 20 cm while the distance between T_{in} and T_{out} is 15 cm. The pressure drop used in these calculations is therefore adjusted to the distance between T_{in} and T_{out}.

An example for Methane-100 in the 1 mm tube of such a comparison is showed in Figure 6.1. For the adiabatic case (a and b), the calculated drop in saturation temperature due to pressure loss coincide very well. For the case of heat removal (c and d), the temperature difference is not the same. As the deviation from the expected temperature drop varies with vapour fraction, it is unlikely that the effect is connected to axial conduction in the test tube as this should be independent from what happens inside the tube. For other cases not shown here, the deviation at $x < 0.5$ are smaller.

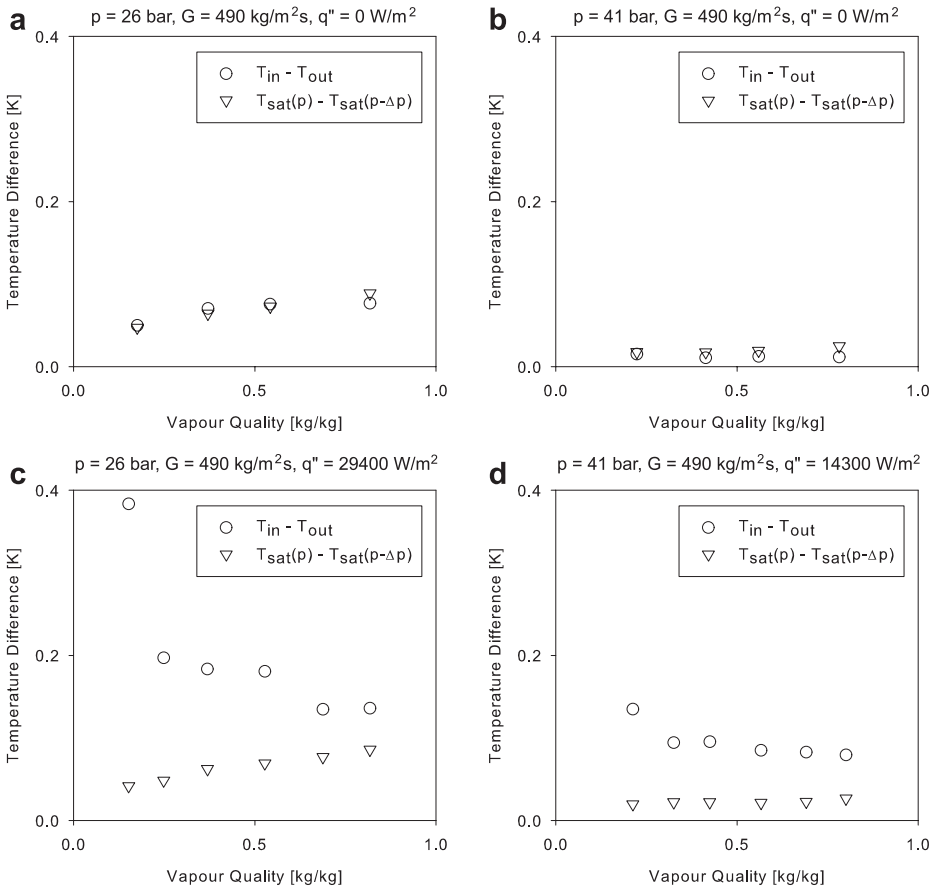

Figure 6.1: Comparison of measured temperature difference and calculated temperature difference for Methane-100 in the 1 mm tube.

No satisfactory explanation for this deviation was found, but it is assumed that only T_{out} is affected; T_{in} is measured upstream from the test section, and when tube wall conduction has been ruled out, T_{in} is oblivious

to what happens downstream. Assuming this, the deviation has limited effect on the temperature difference $\Delta T_{\mathrm{m,w}}$ in Equation 3.3. Using an estimated $T_{\mathrm{out,est}}$ based on drop in saturation temperature due to pressure drop instead of T_{out}, yields a maximum of 6 % increase in the heat transfer coefficient for Methane-100 for the 1 mm tube. T_{out} is therefore left uncorrected. The phenomenon illustrated in Figure 6.1 was also observed for some situations in the 0.5 mm tube and also for the 0.25 mm tube.

6.3 Verification of inlet conditions

The change of thermodynamic state of the fluid through the test tube/section is verified both through pressure drop and temperature measurements. It is just as important to verify the thermodynamic state at the inlet.

For two phase flow, the measured temperature T_{in} was compared to the predicted temperature $T_{\mathrm{in,pred}}$ based on the measured pressure, vapour fraction and fluid composition X at the inlet of the test tube. $T_{\mathrm{in,pred}}$ for binary fluids was found from REFPROP [43] as

$$T_{\mathrm{in,pred}} = \mathrm{Temperature}(X, x_{\mathrm{in}}, p_{\mathrm{in}}) \tag{6.1}$$

where X is the molar composition of the fluid and x_{in} is found by Equation 3.21 at inlet conditions. Equilibrium between the phases and hence the equilibrium temperature should be expected at the inlet of the test tube. The inlet pressure p_{in} is estimated by measured pressure at the pre-heater minus the estimated pressure drop from the pre-heater to the location of T_{in}. For a pure fluid like Methane-100, only the pressure is needed to determine the inlet condition as T_{in} should be equal to the saturation temperature at the given pressure.

After the pre-heater, there is 20 cm adiabatic 1/8" tubing before the entrance to the test tube. In this section, it is assumed that any radial temperature gradients from the pre heaters have vanished and that the phases are in equilibrium.

Deviations between T_{in} and $T_{\mathrm{in,pred}}$ were observed and two explanations are given:

6.3.1 Verification of fluid composition

The fluid circulated in the experimental setup was measured with a gas chromatograph. The gas was drawn off on the warm side of the circuit after the test section (see Figure 3.1). The gas chromatograph was calibrated using gas taken directly from the different bottles. The gas composition

from the manufacturer had an uncertainty of ±1 % and is given in Table 6.1 together with the measured composition at different flow rates and pressure.

There seems to be an enrichment of the heaviest component in the circulated fluid compared to the measured composition from the bottle. This can be explained by regarding an equilibrium diagram (an example is found in Figure 2.9). The liquid being condensed inside the thermal interface is much richer on the heaviest component and more of the lighter component will remain in the vapour phase. As only the liquid leaves the thermal interface, the gas with light components will be "trapped" and lead to a slightly heavier liquid being circulated.

The enrichment of the less volatile component seems stronger for higher pressure and higher mass flux. Some scatter in the concentration is seen for the same operating conditions, which can be expected. The table also gives which compositions were used for the fluid property calculations.

The deviation from the bottle composition is not large, but has an impact. For instance, for Ethane-27 at 8 bar and $x = 0.5$, the equilibrium temperature is -114.78 °C for the composition in the bottle and -112.95 °C for the circulated composition. Deviations of up to 3.1 °C could be found between the use of a ethane concentration of 25 % and 27 % respectively. For the other fluids, the difference is smaller.

Using the measured concentrations reduced the difference between T_{in} and $T_{\text{in,pred}}$ but there is still a difference.

Fluid	Bottle composition		p [bar]	G [kg/m^{2}s]	Circulated composition Measured	Composition used in calculations
	From certificate	Measured				
Ethane-27	24.82 %	24.9 %	8	280	26.9%	27% for all
			8	490	26.6% - 27.0%	
			35	490	27.2%	
			35	150	27.1%	
			41	490	27.2%	
Ethane-10	10.04 %	9.9 %	8	280	10.1% - 10.2%	10% for $p < 49$ bar, 13% for $p = 49$ bar
			8	490	10.3%	
			26	490	9.9%	
			49	280	13.3% - 13.7%	
			49	150	12.7%	
Nitrogen-10	9.93 %	9.9 %	8	280	9.5% - 9.9%	9.5% for $p < 42$ bar, 8.5% for $p = 42$ bar
			8	490	9.3%	
			26	490	9.7%	
			36	280	9.5%	
			42	490	8.5%	

Table 6.1: Circulated fluid molar concentrations for the 1.0 mm tube. The concentrations refer to the component not being methane.

6.3.2 T_{in} and ΔT_{gl}

Using the measured concentrations presented in Table 6.1, the difference between $T_{\text{in,pred}}$ and T_{in} is shown in Figure 6.2. The results for Methane-100 are also shown.

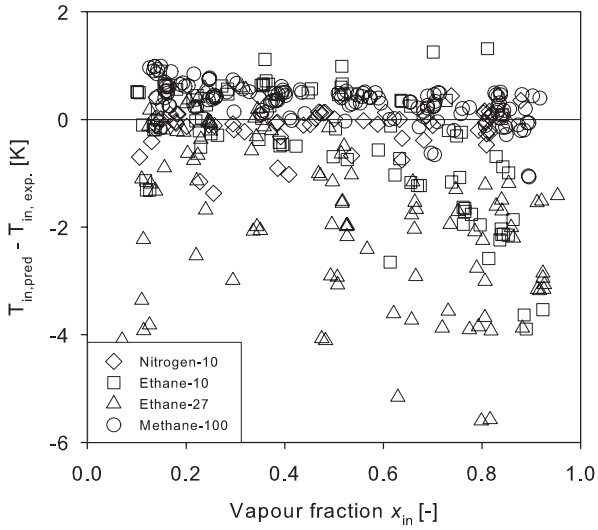

Figure 6.2: Difference between measured and calculated T_{in} for the 1 mm tube.

Clearly, there is a discrepancy up to 6 K for the predicted temperature and the measured temperature for Ethane-27 and up to 4 K for Ethane-10. For Nitrogen-10, the discrepancies are a lot smaller. The deviations are also small for Methane-100 where 71% of the measurements are within ± 0.5 K. The fact that most of the Methane-100 measurements are close to expected indicates that the pressure drop estimation or T_{in} are only slightly off. Also binary fluids change saturation temperature with changing pressure, but on the same order as for Methane-100. The cause for the larger deviations for the binary fluids is therefore not related to the pressure.

Figure 6.3 shows the same data relative to their temperature glide ΔT_{gl}. As seen from Figure 5.50, the temperature glide is largest for Ethane-27 and smallest for Nitrogen-10. Here, 92 % of the measurements are within ±10 %

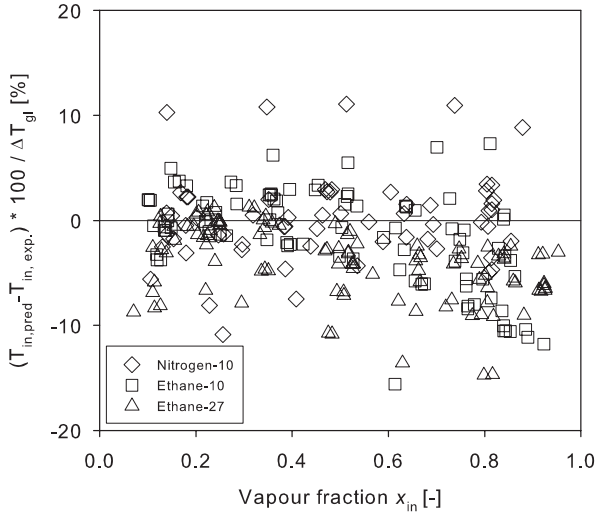

Figure 6.3: Relative difference between measured and calculated T_{in} for the 1 mm tube.

of the relative temperature glide and 73 % are with in ±5 %. Approx. 90 % of the Ethane-27 measurements are colder than expected, while 57 % of the Ethane-10 measurements are colder than expected. For Nitrogen-10, just as many measurements are colder as expected as warmer.

As the agreement for Methane-100 was good, the larger disagreement for the binary fluids is most probably caused by the uncertainty of the vapour fraction x, again most probably caused by the uncertainty in $\dot{m}$. Plotting the temperature difference versus the applied power to the pre heaters gives a distribution very similar to the one in Figure 6.2, which indicates that a heat leakage from the pre heater is not the cause of the temperature deviation.

A corresponding plot for the 0.5 mm tube shows larger deviations, which is not unexpected as the uncertainty of x is greater.

It is the authors opinion that the magnitude of the relative disagreement is to be expected. The fact that the deviation between $\dot{Q}_{\text{TS}}$ and $\dot{Q}_{\text{HB}}$ in Figure 5.1 is small, indicates that an eventual leakage from the pre-heater is small. Nevertheless, the uncertainty should be kept in mind when regarding the experimental results for both pressure drop and heat transfer.

Chapter 7

Conclusion

7.1 Uncertainty and validity for measurements

A number of calibration and verification techniques were employed to ensure the measurement set-up is reliable.

The uncertainty for the heat transfer coefficient in the 1 mm tube is mainly connected to the temperature readings. For the 0.5 mm tube and particularly for the 0.25 mm tube, the uncertainty caused by the flow meter is more important. The uncertainty of the tube diameter and roughness could not be fully quantified for either of the tubes but must be considered substantial for the 0.25 mm tube. In addition to this, the large scattering of the 0.25 mm results questions the quality of these measurements. Therefore, the following conclusions are made without the 0.25 mm tube results.

7.2 Single phase flow

Heat transfer measurements of liquid methane and binary methane mixtures show that the turbulent liquid phase Nusselt number in minichannels can be well predicted by using a conventional model. This includes the use of a friction factor which takes the tube roughness into account.

Knowledge of the exact diameter and friction factor is not that decisive for heat transfer as it is for pressure drop. The region where $2300 < Re < 10000$ is regarded as the transition region where the flow can be indeterminable or a combination of turbulent and laminar. This is in agreement with the heat transfer observations from both the 1 mm and 0.5 mm tubes.

For pressure drop in turbulent flow, the experimental results from the 1 mm tube fits well with the established models in the literature. For the

0.5 mm tube, the friction factor is higher than predicted. This can be related to the tube wall roughness.

7.3 Two phase flow

7.3.1 Pure methane

For pure fluids, the heat transfer coefficient increases with increasing mass flux, higher vapour fraction and it generally decreases for increasing pressure. These effects can be related to the shear at the vapour/liquid interface and to the thickness of the liquid layer. The heat transfer coefficient is also independent of heat flux.

It is important to notice that all the heat transfer models inherently predict a higher heat transfer coefficient for reduced tube diameter. This is also in line with the presented measurements. For the 0.5 mm tube, the measured heat transfer coefficient seems systematically higher than most of the models. As this was not seen for single phase flow, the increase could be related to the vapour/liquid interaction. However, the uncertainty of the 0.5 mm tube makes it difficult to make a final conclusion.

The condensation heat transfer models from Thome et al. [68], Akers [3] and Bandhauer et al. [4] can be used to predict the results for the 1 mm tube reasonably well. The model from Shah [62] appears to be the most precise model for the 0.5 mm tube, however it completely fails to predict the 1 mm results. No model can predict the results from both the 1 mm and 0.5 mm tubes with reasonable accuracy. The model from Cavallini et al. [11] is closest.

7.3.2 Binary fluids

In addition to the effects determining the heat transfer coefficient for pure fluid condensation, mass transfer effects causes a drop in the interface temperature for binary fluid condensation. This impairs the heat transfer coefficient.

This effect is strongest when the equilibrium temperature changes the most for a change in the vapour fraction. The change depends on the composition and the pressure. Also, a larger heat flux causes a larger change in vapour fraction, causing a larger temperature drop and hence a reduced temperature difference for heat transfer. For this reason, the heat transfer coefficient is dependent on the heat flux for binary fluid condensation.

A model of the Silver-Bell-Ghaly type can predict the heat transfer coefficient with reasonably good accuracy for the 1 mm and 0.5 mm tubes. The

single component model in this approach was based on the Cavallini-model [11]. The agreement between model and experimental results appears to be better for fluids with a small change in equilibrium temperature.

For Ethane-10 and Ethane-27, the 0.5 mm measurements deviate slightly more from the model than the 1 mm measurements. However, the deviation is much smaller than between the 1 mm and 0.5 mm tube measurements for Methane-100. For condensation in the 0.5 mm tube, the uncertainty is around 20 % for Methane-100 and 10 % for the binary fluids. This suggests that the much larger heat transfer coefficient measured in the 0.5 mm tube for Methane-100 can be linked to measurement uncertainty. *This leads to the conclusion that the heat transfer phenomena in 1 mm and 0.5 mm tubes are no different than in conventional tubes.*

7.3.3 Pressure drop

The two-phase frictional pressure drop for the 1 mm and 0.5 mm tube can be well predicted by conventional models. The CESNEF-2 model gives a good prediction for both the 1 mm and 0.5 mm tubes, whereas the Friedel [25] model gives the second best prediction.

Chapter 8

Suggestions to Future Work

Improve accuracy for smaller tubes The results for the smaller tubes are burdened with high uncertainties due to the mass flow meter. A more precise meter would improve the accuracy and quality of the measurements for $d < 0.5$ mm.

Tube smoothness It would be beneficial to investigate the effect of tube roughness on condensation more thoroughly, using a smooth test tube made of glass or similar.

Other tube diameters The threshold in behaviour between the 1 mm and 0.5 mm tube for two phase flow of pure methane is explained by measurement uncertainty in this thesis. It would be interesting to investigate this further by doing experiments in a 0.75 mm tube. As conventional behaviour was observed in the 1 mm tube, test on a 2 mm tube would be of secondary importance. The test rig is designed to do measurements on tube with diameter up to 2 mm at mass flux rates of $G = 800$ kg/m^{2}s.

Flow boiling measurements Only a small modification of the test facility is necessary to investigate flow boiling in mini- and microchannels. The copper block surrounding the test section must be removed from the copper rod and mounted where it is thermally insulated from the cryocooler. The heat sink heater yielding $\dot{Q}_{\mathrm{HSH}}$ can be inserted into the copper block to provide heating. The measurement concept would be the same, except that the parameter c in Equation 3.6 would have a negative value.

Bibliography

[1] T.M. Adams, S.I. Abdel-Khalik, S.M. Jeter, and Z.H. Qureshi. An experimental investigation of single-phase forced convection in microchannels. *International Journal of Heat and Mass Transfer*, 41:851–857, 1998.

[2] Bruno Agostini, Barbara Watel, Andre Bontemps, and Bernard Thonon. Liquid flow friction factor and heat transfer coefficient in small channels: an experimental investigation. *Experimental Thermal and Fluid Science*, 28:97–103, 2004.

[3] W.W. Akers, H.A. Deans, and O.K. Crosser. Condensation heat transfer within horizontal tubes. *Chem. Eng. Prog. Symp. Ser.*, 55(29):171–176, 1959.

[4] Todd M. Bandhauer, Akhil Agarwal, and Srinivas Garimella. Measurement and modeling of condensation heat transfer coefficients in circular microchannels. In *Proceedings of ICMM2005 3rd International Conference on Microchannels and Minichannels*, June 2005. Toronto, Canada.

[5] K.J. Bell and M.A. Ghaly. An approximate generalized design method for multicomponent/partial condenser. *AIChE Symp. Ser.*, 69:72–79, 1973.

[6] Neima Brauner and David Moalem Maron. Identification of the range of small diameters conduits, regarding two-phase flow pattern transitions. *International Communications of Heat and Mass Transfer*, 19:29–39, 1992.

[7] Van P. Carey. *Liquid-Vapor Phase-Change Phenomena*. Taylor & Francis, 1987.

[8] Alberto Cavallini, D. Del Col, L. Doretti, M. Matkovic, L. Rossetto, and C. Zillo. Two-phase frictional pressure gradient of r236ea, r134a and r410a inside multi-port mini-channels. In *3rd Int. Symposium on Two-Phase Flow Modelling and Experimentation*, Pisa, 22-24 September 2004.

[9] Alberto Cavallini, D. Del Col, L. Doretti, M. Matkovic, L. Rossetto, and C. Zillo. A model for frictional pressure drop inside minichannels. In *Proc. HT05 National Heat Transfer Conf., Paper HT2005-72528, ASME*, San Francisco, 2005.

[10] Alberto Cavallini, Davide Del Col, Luca Doretti, Marko Matkovic, Luisa Rossetto, and Claudio Zilio. A model for condensation inside minichannels. In *Proceedings of HT05 National Heat Transfer Conference July 2005, San Francisco*, 2005.

[11] Alberto Cavallini, Luca Doretti, Marko Matkovic, and Luisa Rossetto. Update on condensation heat transfer and pressure drop inside minichannels. *Heat Transfer Engineering*, 27(4):74–87, 2006.

[12] Alberto Cavallini, L. Rossetto, M. Matkovic, and D. Del Col. A model for frictional pressure drop during vapour-liquid flow in minichannels. In *IIR Int. Conf. Thermophysical Properties and Transfer Processes of Refrigerants*, Vincenza, August 31st-September 2nd 2005. Paper TP128.

[13] Gian Piero Celata. Single-phase laminar & turbulent heat transfer in smooth and rough microtubes. *XXIV Congresso Nazionale UIT sulla Trasmissione del Calore Napoli, 21-23 Giugno 2006*, 2006.

[14] Gian Piero Celata, Gian Luca Morini, V. Marconi, S.J. McPhail, and G. Zummo. Using viscous heating to determine the friction factor in microchannels an experimental validation. *Experimental Thermal And Fluid Science*, 30:725–731, 2006.

[15] S.L. Chen, F.M. Gerner, and C.L. Tien. General film condensation correlations. *Experimental Heat Transfer*, 1:93–107, 1987.

[16] Lixin Cheng, Gherhardt Ribatski, Leszek Wojtan, and John R. Thome. New flow boiling heat transfer model and flow pattern map for carbon dioxide evaporating inside horizontal tubes. *International Journal of Heat and Mass Transfer*, 49:4082–4094, 2006.

[17] J.P. Chiou. The advancement of compact heat exchanger theory considering the effects of longitudinal heat conduction and flow nonuniformity. *Symposium on Compact Heat Exchangers*, 1980.

[18] D. Chisholm. Pressure gradients due to friction during the flow of evaporating two-phase mixtures in smooth tubes and channels. *International Journal of Heat and Mass Transfer*, 16(2):347–358, 1973.

[19] A.D. Colburn and T.B. Drew. Design of cooler-condensers for mixture of vapours with a non-condensing gas. *Trans. Inst. Chem. Eng. AIChE*, 33:30–42, 1937.

[20] C.F. Colebrook. Turbulent flow in pipes, with particular reference on the transition between the smooth and rough pipe laws. *J. Inst. Civ. Eng. Lond.*, 11 (4):133–156, 1939.

[21] John W. Coleman. *Flow Visualization and Pressure Drop for Refrigerant Phase Change and Air-Water Flow in Small Hydraulic Diameter Geometries*. PhD thesis, Iowa State University, Ames, Iowa, 2000.

[22] John W. Coleman and Srinivas Garimella. Characterization of two-phase flow patterns in small diameter round and rectangular tubes. *International Journal of Heat and Mass Transfer*, 42(15):2869–2881, 1999.

[23] D. Del Col, Antonio Cavallini, and John R. Thome. Condensation of zeotropic mixtures in horizontal tubes: New simplified heat transfer model based on flow regimes. *Journal of Heat Transfer*, 127:221–230, 2005.

[24] J. El Hajal, John R. Thome, and A. Cavallini. Condensation in horizontal tubes part 1: two-phase flow pattern map. *International Journal of Heat and Mass Transfer*, 46:3349–3363, 2003.

[25] L. Friedel. Improved friction pressure drop correlations for horizontal and vertical two phase pipe flow. *Paper E2, European Two Phase Flow Group Meeting, Ispra, Italy, 1979*, 1979.

[26] L. Friedel. Pressure drop during gas/vapour-liquid flow in pipes. *Int. Chem. Eng.*, 20(3):352–367, 1980.

[27] Srinivas Garimella, Akhal Agarwal, and Jesse Killon. Condensation pressure drop in circular microchannels. *Heat Transfer Engineering*, 26(3):28–35, 2005.

[28] Srinivas Garimella, Jesse Killion, and John W. Coleman. An experimentally validated model for two-phase pressure drop in the intermittent flow regime for cirular microchannels. *Journal of Fluid Engineering*, 124(1):205–214, 2002.

[29] Volker Gnielinski. New equations for heat and mass transfer in turbulent pipe and channel flow. *Int. Chem. Eng.*, 16:359–368, 1976.

[30] Steffen Grohmann. Design and operation of the compact lng heat exchanger test stand. Technical report, SINTEF, 2004.

[31] H. Hausen. New equations for heat transfer in free or forced flow. *Allg. Wärmetechnik*, 9:75–79, 1959.

[32] G. Hetsroni, A Mosyak, E. Pogrebnyak, and L.P. Yarin. Heat transfer in micro-channels: Comparison of experiments with theory and numerical results. *International Journal of Heat and Mass Transfer*, 48:5580–5601, 2005.

[33] Frank Incopera and David DeWitt. *Fundamentals of Heat and Mass Transfer*. John Wiley & Sons, New York, 5th edition, 2002.

[34] J. Judy, D. Maynes, and B.W. Webb. Characterization of frictional pressure drop for liquid flows through microchannels. *International Journal of Heat and Mass Transfer*, 45:3477–3489, 2002.

[35] Satish Kandlikar, Srinivas Garimella, Dongqing Li, Stphane Colin, and Michael King. *Heat Transfer and Fluid Flow in Minichannels and Microchannels*. Elsevier Ltd., 2006.

[36] Satish Kandlikar and William Grande. Evolution of microchannel flow passages - thermohydraulic performance and fabrication technology. *Heat Transfer Engineering*, 24(1), January/February 2003.

[37] N. Kattan, John R. Thome, and D. Favrat. Flow boiling in horizontal tubes: Part 1-development of a diabatic two-phase flow mattern map. *International Journal of Heat Transfer*, 120:140–147, 1998.

[38] William M. Kays, Michael E. Crawford, and Bernhard Weigand. *Convective Heat and Mass Transfer*. McGraw-Hill, New York, 4th edition, 2005.

[39] Peter A. Kew and Keith Cornwell. Correlation for the prediction of boiling heat transfer in small-diameter channels. *Applied Thermal Engineering*, 17:705–715, 1997.

[40] M.H. Kim, J.S. Shin, C. Huh, T.J. Kim, and K.W. Seo. A study of condensation heat transfer in a single mini-tube and review of korean micro- and mini-channel studies. In *1st International Conference on Microchannels and Minichannels*, 2003.

[41] P.G Kosky and F.W. Staub. Local condensing heat transfer coefficients in the annular flow regime. *AIChE J*, 17:1037–1043, 1971.

[42] Dorin Lelea, Shigefumi Nishio, and Kiyoshi Takano. The experimental research on microtube heat transfer and fluid flow of distilled water. *International Journal of Heat and Mass Transfer*, 47:2817–2830, 2004.

[43] E.W. Lemmon, M.L. Huber, and M.O. McLinden. Nist standard reference database 23: Reference fluid thermodynamic and transport properties (refprop). 2007.

[44] R.W. Lockhart and R.C. Martinelli. Proposed correlation of data for isothermal two-phase, two-component flow in pipes. *Chem. Eng. Prog.*, 45(1):39–45, 1949.

[45] C. Lombardi, L. Maran, L. Oriani, and Ricotti M.E. Cesnef-3 pressure drop correlation for gasliquid mixtures flowing upflow in vertical ducts. In *XVIII congresso nazionale della trasmissione del calore*, Cernobbio, Italy, June 2000.

[46] Maranzana, Perry, and Maillet. Mini- and micro-channels: influence of axial conduction in the walls. *International Journal of Heat and Mass Transfer*, 47:3993–4004, 2004.

[47] W. H. McAdams. *Heat Transmission*. McGraw-Hill, New York, 2nd edition, 1942.

[48] L.F. Moody. *Trans. ASME*, 66:671, 1944.

[49] G. L. Morini. Single-phase convective heat transfer in laminar and transitional regime in microchannels. In *ECI International Conference on Heat Transfer and Fluid Flow in Microscale*, Whistler, Canada 21st - 26th September 2008.

[50] Gian Luca Morini. Single-phase convective heat transfer in microchannels: a review of experimental results. *International Journal of Thermal Science 43*, 2004.

[51] Gian Luca Morini. Scaling effects for liquid flows in microchannels. *Heat Transfer Engineering*, 27(4):64–73, 2006.

[52] K.W. Moser and R.L. Webb. A new equivalent reynolds number model for condensation in smooth tubes. *Journal of Heat Transfer*, 120:410–417, 1998.

[53] Müller-Steinhagen, H AND Heck, KS. A simple friction pressure drop correlation for two-phase flow in pipes. *Chem. Eng. Process*, 20:279–308, 1986.

[54] Bengt Olav Neeraas. *Condensation of Hydrocarbon Mixtures in Coil-Wound LNG Heat Exchanger*. PhD thesis, NTH, Universitetet i Trondheim, September 1993.

[55] V.G. Niño. *Characterization of two-phase flow in microchannels*. PhD thesis, University of Illinois, Urbana-Champaign, IL, 2002.

[56] Jostein Pettersen. *Flow Vapourization of CO_2 in Microchannel Tubes*. PhD thesis, NTNU, 2002.

[57] B.S. Petukhov. *Advances in Heat Transfer*, volume 6. Academic Press, 1970.

[58] S.L. Qi, P. Zhang, R.Z. Wang, and L.X. Xu. Single-phase pressure drop and heat transfer characteristics of turbulent liquid nitrogen flow in micro-tubes. *International Journal of Heat and Mass Transfer*, 50:1993 – 2001, 2007.

[59] Rémi Revellin. *Experimental Two-Phase Flow in Microchannels*. PhD thesis, École Polytechnique de Fédérale de Lausanne, 2005.

[60] Rémi Revellin and John R. Thome. Experimental investigation of R-134a and R-245fa two-phase flow in microchannels for different flow conditions. *International Journal of Heat and Fluid Flow*, 28:63–71, 2007.

[61] R.G. Sardesai, J.W. Palen, and J. Taborek. Modified restistance proration method for condensation of vapour mixtures. *AIChE Symp. Series*, 79:41–46, 1983.

[62] M.M. Shah. A general correlation for heat transfer during film condensation inside pipes. *International Journal of Heat and Mass Transfer*, 22:547–556, 1979.

[63] Jeong Seob Shin and Moo Hwan Kim. An experimental study of flow condensation heat transfer inside circular and rectangular mini-channels. *Heat Transfer Engineering*, 26(3):36–44, 2005.

[64] L. Silver. Gas cooling with aqueous condensation. *Trans.Inst.Chem.Eng*, 25:30–42, 1947.

[65] M. Soliman, J.R. Schuster, and P.J. Berenson. A general heat transfer correlation for annular flow condensation. *Journal of Heat Transfer*, 90:267–276, 1968.

[66] D. Steiner. *VDI Wärmeatlas*. Springer, 2002. chapter Hbb6.

[67] John R. Thome. Boiling in microchannels: a review of experiment and theory. *International Journal of Heat and Fluid Flow*, 25:128–139, 2004.

[68] John R. Thome, J. El-Hajal, and A. Cavallini. Condensation in horizontal tubes part 2: new heat transfer model based on flow regimes. *International Journal of Heat and Mass Transfer*, 46:3365–3387, 2003.

[69] D.P. Traviss, W.M. Rohsenov, and A.B. Baronm. Forced convection condensation in tubes: A heat transfer correlation for condenser design. *ASHRAE Trans.*, 79:157–165, 1973.

[70] K.A. Triplett, S.M. Ghiaasiaan, S.I. Abdel-Khalik, and D.L. Sadowski. Gas-liquid two-phase flow in microchannels part i: two-phase flow patterns. *International Journal of Multiphase Flow*, 25:377–394, 1999.

[71] Wei-Wen William Wang, Thomas D. Radcliff, and Richard N. Christensen. A condensation heat transfer correlation for millimeter-scale tubing with flow regime transition. *Experimental Thermal and Fluid Science*, 26:473–485, 2002.

[72] R.H.S. Winterton. Where did the dittus-boelter equation come from? *International Journal of Heat and Mass Transfer*, 41(4-5):809–810, 1997.

[73] C.-Y Yang and R.L. Webb. Condensation of R-12 in small hydraulic diameter extruded aluminium tubes with and without micro-fins. *International Journal of Heat and Mass Transfer*, 39(4):791–800, 1996.

[74] D. Yu, R. Warrington, R. Barron, and T. Ameel. An experimental investigation of fluid flow and heat transfer in microtubes. In *Proceedings of the ASME/JSME Thermal Engineering Confecence*, volume 1, pages 523–530. Americal Society of Mechanical Engineers, 1995.

[75] Rin Yun and Yongchan Kim. Flow regimes for horizontal two-phase flow of co_2 in a heated narrow rectangular channel. *International Journal of Multiphase Flow*, 30:1259–1270, 2004.

[76] M. Zhang. *A New Equivalent Reynolds Number Model for Vapour Shear-controlled Condensation inside Smooth and Micro-Fin Tubes*. PhD thesis, The Pennsylvania State University, 1998.

Appendix A

Experimental measurement values

In the following tables, δNu and δh refers to the uncertainty of the experimental Nusselt number and heat transfer coefficient respectively. Δx is the change in vapour fraction through the test section.

The subscript m means the medium value in the middle of the test section. For the two phase flow of binary fluids, the vapour fraction and pressure is given at the inlet of the test section.

Some values are omitted cause they were regarded as unreliable or non-physical, such as the heat transfer coefficients for adiabatic flow. These are marked "-". A horizontal line divides the measurement series.

A.1 Single phase flow

A.1.1 Methane-100

G [kg/m^{2}s]	p_m [bar]	$(dp/dz)_f$ [kPa/m]	q'' [kW/m^2]	T_{out} [°C]	T_{in} [°C]	T_b [°C]	T_w [°C]	Re [-]	$\overline{Nu}$ [-]	$\overline{\delta Nu}$ [-]
1.0 mm tube measurements										
391	8.7	7.2	11.8	-136.05	-134.52	-138.73	-138.43	5756	27.2	2.1
393	8.7	7.3	10.6	-135.99	-134.63	-138.38	-138.12	5792	27.3	2.4
386	8.7	7.0	9.1	-135.85	-134.65	-137.94	-137.71	5686	26.9	2.7
387	8.7	7.0	7.7	-135.62	-134.62	-137.34	-137.15	5728	27.5	3.3
381	8.7	6.8	6.5	-135.47	-134.62	-136.93	-136.76	5637	27.6	3.9
584	9.0	14.8	7.4	-134.74	-134.08	-135.97	-135.78	8741	39.3	6.6
591	9.0	15.0	9.4	-134.94	-134.11	-136.53	-136.29	8834	38.8	5.1
597	9.0	15.2	10.5	-135.04	-134.11	-136.80	-136.54	8916	38.7	4.5
604	9.0	15.5	12.3	-135.23	-134.16	-137.33	-137.01	8998	38.4	3.8
602	9.0	15.3	13.4	-135.37	-134.19	-137.65	-137.31	8948	38.4	3.5
782	9.8	25.3	14.5	-133.63	-132.63	-135.74	-135.37	11986	47.4	4.8
781	10.1	25.3	13.0	-132.92	-132.03	-134.80	-134.47	12110	48.4	5.5
352	8.6	6.5	10.9	-135.95	-134.27	-138.86	-138.58	5206	22.7	1.7
529	8.9	12.6	10.9	-135.35	-134.27	-137.30	-137.03	7860	35.7	3.8

Continued on next page

Continuation of Table A.1: Measurements of single phase flow Methane-100

G [kg/m^{2}s]	p_m [bar]	$(dp/dz)_f$ [kPa/m]	q'' [kW/m^2]	T_{out} [°C]	T_{in} [°C]	T_b [°C]	T_w [°C]	Re [-]	$\overline{Nu}$ [-]	$\delta\overline{Nu}$ [-]
669	9.1	19.2	10.9	-134.67	-133.78	-136.35	-136.08	10052	43.0	5.3
777	10.6	25.5	10.9	-131.54	-130.79	-133.02	-132.74	12347	51.9	7.4
859	13.9	30.6	10.9	-125.69	-125.03	-127.06	-126.78	15139	61.1	9.6
991	20.0	41.1	10.9	-116.76	-116.21	-117.95	-117.67	20445	80.6	15.0
462	13.5	9.6	7.4	-124.61	-123.91	-126.11	-125.92	8324	35.7	5.0
566	13.7	14.2	7.4	-124.36	-123.78	-125.65	-125.46	10228	43.0	7.0
688	14.0	20.8	7.4	-123.94	-123.46	-125.07	-124.89	12525	50.4	9.5
793	14.6	27.2	7.4	-123.01	-122.59	-124.00	-123.82	14658	59.0	12.8
890	16.1	33.9	7.4	-121.23	-120.86	-122.14	-121.95	16972	67.4	16.3
984	19.8	41.6	7.4	-116.02	-115.70	-116.86	-116.67	20551	80.1	21.4
1091	23.7	51.9	7.5	-111.02	-110.74	-111.80	-111.61	24884	94.7	28.1
477	11.9	10.2	13.3	-128.92	-127.56	-131.54	-131.21	7996	34.7	2.8
602	12.2	15.9	13.3	-128.36	-127.27	-130.57	-130.23	10158	42.6	4.1
744	12.5	23.7	13.3	-127.71	-126.83	-129.63	-129.29	12689	51.4	5.7
862	14.2	31.6	13.3	-124.75	-123.99	-126.50	-126.16	15488	59.6	7.4
970	18.8	40.0	13.1	-117.76	-117.13	-119.30	-118.96	19697	74.7	10.8
438	11.7	8.9	7.9	-129.66	-128.96	-131.44	-131.24	7198	30.8	3.8
570	12.0	14.6	7.8	-129.10	-128.57	-130.60	-130.40	9449	38.0	5.5
673	12.2	20.0	7.8	-128.68	-128.24	-130.04	-129.84	11223	43.0	7.0
818	12.7	28.8	7.8	-127.70	-127.34	-128.92	-128.72	13882	50.2	9.2
921	12.9	36.2	7.8	-127.23	-126.92	-128.38	-128.18	15741	54.6	10.8
997	14.0	42.1	7.9	-125.33	-125.05	-126.42	-126.23	17626	59.8	12.6
1058	16.0	47.2	7.8	-122.32	-122.06	-123.36	-123.16	19738	65.4	14.5
470	11.1	10.5	22.2	-136.02	-133.96	-141.05	-140.49	6938	29.0	1.3
563	11.4	14.8	22.2	-135.38	-133.69	-139.89	-139.32	8370	33.4	1.7
668	11.6	20.7	22.3	-134.74	-133.34	-138.84	-138.27	10035	38.1	2.1
766	11.9	26.8	22.3	-133.78	-132.60	-137.52	-136.96	11673	43.0	2.6
871	12.1	34.2	22.3	-133.17	-132.14	-136.68	-136.12	13414	47.1	3.1
988	12.4	44.1	22.3	-132.40	-131.52	-135.66	-135.10	15408	52.2	3.7
249	9.6	5.0	-0.4	-140.16	-140.26	-140.20	-140.21	3339	-	-
421	10.1	7.8	-0.5	-139.89	-139.92	-139.93	-139.94	5668	-	-
432	10.3	-	19.4	-141.84	-139.48	-146.77	-146.28	5726	23.5	1.1
427	10.3	-	16.6	-141.63	-139.58	-145.95	-145.53	5674	23.0	1.2
425	10.3	-	13.2	-141.21	-139.58	-144.65	-144.32	5659	23.0	1.5
423	10.3	-	10.5	-140.90	-139.60	-143.64	-143.38	5654	22.9	1.8
423	10.3	-	7.8	-140.53	-139.56	-142.56	-142.37	5671	23.1	2.5
420	10.2	-	4.3	-140.02	-139.50	-141.12	-141.01	5666	23.9	4.6
630	10.8	-	2.9	-138.86	-138.62	-139.38	-139.30	8657	36.0	14.6
635	10.9	-	8.0	-139.39	-138.72	-140.85	-140.64	8671	34.7	5.0
633	10.9	-	11.1	-139.71	-138.78	-141.74	-141.46	8618	34.7	3.6
632	10.9	-	15.4	-140.20	-138.91	-143.01	-142.62	8552	34.5	2.6
631	10.9	-	19.3	-140.63	-139.01	-144.17	-143.68	8499	34.3	2.1
632	10.9	-	22.4	-140.97	-139.09	-145.08	-144.52	8478	34.1	1.8
813	11.2	-	24.1	-139.88	-138.30	-143.52	-142.91	11085	43.6	2.6
813	11.2	-	20.9	-139.58	-138.21	-142.71	-142.18	11139	43.9	3.1
812	11.2	-	16.8	-139.22	-138.12	-141.73	-141.30	11167	44.1	3.8
815	11.2	-	12.2	-138.80	-137.99	-140.63	-140.32	11260	44.4	5.2
816	11.2	-	8.3	-138.45	-137.90	-139.68	-139.47	11333	44.9	7.8
820	11.2	-	5.1	-138.16	-137.81	-138.90	-138.77	11424	45.5	12.9
428	10.4	9.6	17.7	-135.34	-133.27	-139.16	-138.72	6412	29.2	1.6
426	10.4	9.5	15.3	-135.11	-133.31	-138.45	-138.06	6386	28.9	1.8
426	10.4	9.4	10.3	-134.45	-133.24	-136.67	-136.41	6430	29.3	2.7
426	10.4	9.4	6.6	-133.92	-133.16	-135.32	-135.15	6471	30.1	4.4
628	11.2	19.9	6.4	-132.32	-131.80	-133.34	-133.17	9804	42.9	8.8
635	11.2	20.2	12.1	-132.87	-131.91	-134.82	-134.52	9847	41.9	4.5
485	26.5	10.9	25.4	-105.85	-103.86	-110.17	-109.53	12441	55.1	2.8
487	26.5	10.9	13.0	-104.70	-103.70	-106.83	-106.50	12669	57.6	5.7
486	26.5	10.8	6.4	-104.11	-103.62	-105.07	-104.90	12732	63.5	13.7
285	25.9	2.9	23.9	-106.38	-103.22	-112.08	-111.47	7318	36.5	1.5
286	26.0	3.0	13.0	-104.58	-102.94	-107.59	-107.26	7523	38.3	2.7
283	26.0	2.9	6.8	-103.50	-102.67	-104.99	-104.82	7568	41.0	5.7
282	25.6	30.0	11.4	-89.28	-87.29	-92.03	-91.75	37820	138.4	10.6
279	25.6	30.0	26.1	-89.07	-83.70	-96.27	-95.61	37108	119.0	4.0
287	35.3	2.5	9.1	-94.49	-93.62	-96.31	-96.08	9193	53.8	6.2
278	9.0	90.6	28.6	-112.48	-104.75	-121.71	-120.98	44651	131.6	3.9
283	6.5	129.1	13.0	-114.91	-111.29	-119.12	-118.79	47038	137.2	7.3

Continued on next page

Continuation of Table A.1: Measurements of single phase flow Methane-100

G [kg/m^{2}s]	p_m [bar]	$(dp/dz)_f$ [kPa/m]	q'' [kW/m^2]	T_{out} [°C]	T_{in} [°C]	T_b [°C]	T_w [°C]	Re [-]	Nu [-]	δNu [-]
283	7.1	5.3	12.8	-137.19	-134.81	-141.41	-141.09	4130	18.0	1.0
281	12.9	3.7	13.4	-125.70	-123.30	-129.61	-129.27	5042	22.6	1.3
281	12.6	66.0	12.6	-103.32	-99.92	-107.49	-107.17	42821	119.1	6.5
279	35.3	17.6	12.7	-87.25	-85.57	-89.99	-89.67	34117	127.9	9.9
487	35.2	55.0	13.0	-86.48	-85.25	-88.41	-88.08	59627	196.5	21.0
483	35.7	10.7	12.4	-93.56	-92.85	-95.35	-95.03	15825	82.3	10.1
494	41.5	11.3	14.4	-88.68	-88.04	-90.61	-90.25	18139	99.2	11.6
487	40.8	42.7	12.0	-83.09	-82.31	-84.76	-84.45	54556	180.6	23.2
277	41.6	11.2	10.9	-84.36	-83.31	-86.06	-85.79	30060	133.8	16.0
278	41.5	2.6	12.7	-88.28	-87.41	-90.97	-90.64	10434	59.6	5.0
275	47.6	1.3	9.8	-88.99	-88.03	-91.32	-91.07	9456	47.3	4.4
277	47.5	1.3	16.1	-89.93	-88.29	-93.75	-93.35	9364	46.9	2.7
276	47.6	3.3	27.4	-82.12	-82.07	-85.27	-84.58	13467	143.4	12.5
292	47.4	8.7	31.3	-81.72	-80.95	-84.12	-83.32	23525	179.9	20.0
285	51.9	11.5	36.8	-70.12	-65.72	-77.01	-76.08	28148	127.2	4.9
282	52.1	11.2	22.7	-67.53	-64.63	-72.37	-71.79	28077	114.5	5.2
274	52.2	10.9	12.7	-64.84	-62.96	-67.92	-67.60	27395	101.7	7.2
270	52.2	10.9	7.0	-62.82	-61.61	-64.77	-64.59	27131	89.0	9.8
500	51.5	12.9	23.6	-88.76	-87.39	-92.79	-92.20	16923	70.0	4.0
483	51.5	12.0	12.9	-87.98	-87.23	-90.21	-89.88	16577	69.8	6.9
502	51.7	16.9	20.9	-81.69	-81.15	-84.25	-83.72	22034	124.6	11.8
487	51.7	21.1	24.5	-79.62	-79.43	-81.60	-80.98	25965	227.7	33.0
485	51.7	27.7	25.8	-78.77	-78.47	-80.57	-79.92	31725	258.8	42.6
486	51.8	33.0	26.7	-77.77	-77.20	-79.88	-79.21	38695	248.5	31.9
493	51.8	42.2	29.4	-74.84	-73.55	-77.83	-77.09	45603	232.0	18.4
0.5 mm tube measurements										
1535	8.3	337.8	26.9	-137.98	-136.26	-139.78	-138.86	11690	63.0	8.8
1480	8.3	315.7	21.2	-137.74	-136.34	-139.19	-138.47	11295	60.6	10.3
1365	8.3	268.7	17.2	-137.68	-136.45	-138.91	-138.32	10411	55.7	10.8
1350	8.3	263.1	14.2	-137.50	-136.49	-138.53	-138.05	10310	54.4	12.5
1081	8.3	165.5	13.5	-137.91	-136.70	-139.00	-138.54	8204	44.4	9.0
855	8.2	103.5	9.4	-137.86	-136.79	-138.76	-138.45	6490	33.8	7.7
755	8.1	79.1	7.3	-137.74	-136.80	-138.54	-138.29	5737	28.7	7.3
615	8.0	51.5	5.3	-137.58	-136.77	-138.28	-138.10	4679	22.9	6.6
463	8.0	27.1	4.8	-137.67	-136.66	-138.51	-138.35	3529	16.1	4.0
363	7.9	15.7	3.1	-137.28	-136.46	-138.08	-137.97	2779	10.9	3.5
276	7.8	8.7	2.8	-137.15	-136.19	-138.19	-138.09	2123	7.6	2.3
162	7.5	3.0	3.8	-137.84	-135.76	-140.16	-140.04	1246	4.5	0.9
92	7.4	0.6	2.9	-137.82	-135.21	-140.51	-140.41	714	2.9	0.8
436	8.0	21.1	0.4	-136.50	-136.52	-136.72	-136.71	3364	-	-
1101	26.8	182.7	31.5	-111.22	-108.94	-113.64	-112.57	13527	67.3	6.6
970	26.6	142.2	25.3	-111.12	-109.05	-113.19	-112.33	11920	60.0	6.6
679	26.2	66.9	23.2	-112.03	-109.25	-114.28	-113.49	8255	43.5	4.0
560	26.0	46.4	19.0	-112.05	-109.33	-114.05	-113.41	6810	37.5	3.7
358	25.5	16.6	15.0	-112.48	-109.07	-114.86	-114.35	4355	22.4	1.9
237	25.0	5.8	11.9	-112.99	-108.67	-116.08	-115.68	2888	12.9	1.0
2702	11.7	986.4	32.0	-128.54	-127.46	-130.02	-128.94	24348	158.2	41.3
2177	11.9	636.4	26.9	-128.98	-127.84	-130.30	-129.38	19458	128.3	32.8
1792	12.4	425.3	24.2	-128.59	-127.32	-129.84	-129.01	16134	107.7	25.8
1205	12.5	188.5	13.2	-128.29	-127.25	-129.12	-128.67	10885	67.8	19.2
977	12.3	121.0	7.0	-128.65	-128.00	-129.18	-128.94	8734	51.2	21.1
913	12.3	104.9	1.9	-128.22	-128.06	-128.46	-128.39	8197	31.4	30.1
0.25 mm tube measurements										
1581	26.2	546.8	40.9	-110.21	-105.96	-111.25	-110.46	10009	70.1	4.2
1301	25.8	330.4	33.7	-110.93	-106.54	-111.80	-111.15	8138	58.1	4.1
1085	25.6	206.2	25.3	-110.57	-106.50	-111.30	-110.81	6820	44.9	4.2
791	25.4	92.4	16.8	-109.73	-105.98	-110.38	-110.05	5047	28.4	3.6
784	25.4	85.3	14.2	-108.94	-105.87	-109.49	-109.22	5050	29.1	4.4
553	25.1	33.7	10.0	-108.19	-105.02	-108.93	-108.73	3625	15.6	2.8
1473	34.8	452.1	64.9	-104.14	-97.33	-105.94	-104.68	10561	67.8	2.6
1019	35.0	178.2	47.1	-104.28	-96.67	-105.75	-104.84	7343	45.7	2.3
963	35.0	162.5	32.2	-101.76	-96.42	-102.82	-102.20	7164	43.9	3.2
961	35.0	163.6	24.7	-100.03	-96.39	-100.80	-100.32	7299	50.4	4.8
749	34.8	75.4	16.3	-99.10	-95.99	-99.73	-99.41	5789	36.5	4.9

Table A.1: Measurement of Methane-100

A.1.2 Ethane-10

G [kg/m^{2}s]	p_m [bar]	$(dp/dz)_f$ [kPa/m]	q'' [kW/m^2]	T_{out} [°C]	T_{in} [°C]	T_b [°C]	T_w [°C]	Re [-]	$\overline{Nu}$ [-]	$\delta\overline{Nu}$ [-]
0.25 mm tube measurements										
3079	9.8	2046	0.5	-124.44	-124.38	-124.56	-124.56	11640	6.5	20.2
3080	9.8	2031	0.9	-124.56	-124.50	-124.68	-124.66	11618	12.5	24.3
3084	9.8	2026	13.0	-125.70	-124.87	-126.11	-125.86	11480	53.8	12.4
3074	9.7	2006	29.8	-127.83	-125.89	-128.68	-128.10	11123	60.5	6.6
3076	9.6	2006	40.7	-128.70	-126.04	-129.83	-129.04	11031	62.4	5.1
2372	10.4	1156	38.3	-129.33	-126.04	-130.40	-129.66	8446	51.8	4.5
2065	10.7	891	37.0	-129.64	-125.98	-130.69	-129.98	7333	46.4	4.1
1920	10.9	761	41.1	-130.44	-125.98	-131.62	-130.82	6767	43.0	3.4
1581	10.9	499	37.9	-130.94	-125.83	-132.09	-131.36	5556	35.0	2.9
1421	10.9	397	36.1	-131.17	-125.70	-132.33	-131.63	4990	31.1	2.6
1235	10.9	291	33.8	-131.50	-125.50	-132.67	-132.02	4331	26.2	2.2
1020	10.9	190	30.6	-131.96	-125.23	-133.17	-132.58	3571	20.6	1.7
800	10.8	100	25.8	-132.37	-124.78	-133.94	-133.44	2801	13.0	1.0
626	10.8	60	20.7	-132.69	-124.02	-136.04	-135.64	2201	6.0	0.5
347	10.9	16	13.5	-135.97	-121.15	-137.92	-137.66	1215	3.8	0.4
258	10.8	0	8.7	-137.52	-119.29	-138.72	-138.55	905	2.6	0.4
4170	20.0	3846	76.2	-110.10	-106.85	-111.79	-110.31	20572	146.8	7.5
4192	20.1	3911	36.3	-108.12	-106.64	-108.89	-108.18	21101	178.7	21.0
3660	21.0	3021	36.0	-108.38	-106.69	-109.14	-108.44	18327	162.0	20.1
3029	21.9	2076	36.2	-108.69	-106.67	-109.43	-108.73	15096	152.2	21.4
2812	22.2	1736	36.4	-108.79	-106.58	-109.54	-108.84	13998	139.6	19.6
2372	22.5	1246	36.1	-109.24	-106.67	-109.99	-109.29	11741	122.5	18.2
2025	22.6	906	36.2	-109.70	-106.68	-110.47	-109.76	9982	103.0	14.9
1611	22.7	576	36.1	-110.46	-106.54	-111.27	-110.56	7891	73.4	9.4
1234	22.4	318	36.0	-111.87	-106.62	-112.78	-112.08	5969	49.5	5.3
1040	21.5	209	36.2	-113.98	-107.34	-114.99	-114.29	4912	36.4	3.4

Table A.2: Measurement of Ethane-10

A.1.3 Ethane-27

G [kg/m^{2}s]	p_m [bar]	$(dp/dz)_f$ [kPa/m]	q'' [kW/m^2]	T_{out} [°C]	T_{in} [°C]	T_b [°C]	T_w [°C]	Re [-]	$\overline{Nu}$ [-]	$\delta\overline{Nu}$ [-]
1.0 mm tube measurements										
316	8.9	16.3	5.26	-133.31	-132.27	-136.01	-135.88	2800	10.45	1.1
399	9.1	27.2	6.93	-133.31	-132.22	-135.96	-135.79	3537	14.10	1.3
492	9.0	74.0	8.56	-134.06	-132.97	-136.66	-136.44	4309	17.93	1.6
584	9.2	28.5	7.98	-132.53	-131.67	-134.69	-134.49	5235	20.65	2.2
707	8.8	64.6	8.99	-133.33	-132.53	-135.35	-135.12	6256	25.21	2.7
886	8.6	64.9	12.43	-133.58	-132.70	-135.62	-135.31	7815	35.27	3.7
983	7.8	60.5	13.72	-135.94	-135.07	-138.03	-137.68	8329	38.15	3.9
1062	7.6	60.1	13.76	-136.57	-135.75	-138.50	-138.15	8904	41.53	4.6
617	11.6	19.1	0.38	-121.99	-121.95	-121.88	-121.87	6521	-	-
616	11.6	20.0	4.38	-122.72	-122.28	-123.47	-123.35	6458	34.48	9.3
604	11.4	20.5	7.32	-124.20	-123.45	-125.66	-125.48	6196	29.25	4.1
604	11.4	20.4	9.21	-124.63	-123.69	-126.55	-126.32	6161	28.07	3.1
796	11.7	25.8	11.87	-123.91	-122.99	-125.75	-125.45	8212	39.26	4.4
798	11.7	27.2	9.63	-123.63	-122.89	-125.07	-124.82	8256	41.02	5.9
795	11.7	26.0	6.64	-123.30	-122.78	-124.20	-124.03	8256	44.61	10.1
796	11.7	25.7	4.15	-123.01	-122.69	-123.47	-123.37	8291	54.02	23.4
425	10.9	14.2	2.80	-124.37	-123.96	-125.05	-124.98	4338	22.63	6.8
423	10.9	13.9	5.49	-125.08	-124.28	-126.63	-126.49	4282	19.96	2.8
424	10.9	13.7	7.29	-125.57	-124.51	-127.69	-127.51	4265	19.30	2.0
271	10.3	6.9	5.54	-126.45	-125.19	-128.87	-128.73	2695	12.40	1.3
271	10.3	6.5	3.51	-125.56	-124.76	-127.04	-126.95	2726	12.80	2.1
341	26.1	4.0	14.75	-97.79	-95.37	-101.91	-101.54	5287	24.58	1.3
322	26.1	2.9	9.47	-96.80	-95.16	-99.52	-99.29	5040	23.80	1.9
392	26.7	6.0	9.28	-96.27	-94.95	-98.50	-98.27	6169	29.12	2.7
0.5 mm tube measurements										
1941	10.4	474	31.5	-126.63	-124.71	-128.44	-127.37	10345	72.0	11.7
1942	10.5	473	18.6	-125.83	-124.70	-126.93	-126.29	10419	70.2	18.5
1741	10.4	377	18.5	-126.16	-124.92	-127.28	-126.65	9296	64.4	15.9

Continued on next page

Continuation of Table A.3: Measurements of single phase flow Ethane-27

G [kg/m^{2}s]	p_m [bar]	$(dp/dz)_f$ [kPa/m]	q'' [kW/m^2]	T_{out} [°C]	T_{in} [°C]	T_b [°C]	T_w [°C]	Re [-]	$\overline{Nu}$ [-]	$\delta\overline{Nu}$ [-]
1587	10.4	309	18.3	-126.47	-125.12	-127.62	-126.99	8442	59.2	13.7
1313	10.4	216	15.1	-126.27	-124.93	-127.31	-126.80	7003	48.9	11.3
1171	10.3	164	11.9	-126.18	-125.00	-127.07	-126.66	6251	42.8	11.0
1013	10.2	117	8.4	-126.01	-125.05	-126.72	-126.44	5410	35.6	10.8
890	10.1	91	7.2	-126.00	-125.08	-126.66	-126.42	4757	31.0	9.7
789	10.1	67	6.8	-126.06	-125.09	-126.77	-126.54	4212	26.6	7.7
641	9.9	41.7	4.6	-125.79	-125.01	-126.41	-126.25	3431	20.2	6.6
444	9.7	17.9	4.2	-125.81	-124.77	-127.05	-126.91	2386	9.3	2.1
289	9.5	5.7	5.7	-126.48	-124.27	-129.43	-129.23	1547	5.2	0.7
937	10.2	103	0.3	-124.93	-124.95	-125.02	-125.01	5054	-	-
1432	25.9	269	26.6	-100.97	-99.06	-102.37	-101.46	11256	92.9	20.2
1868	26.4	466	28.1	-100.01	-98.47	-101.34	-100.38	14850	125.6	34.9
2217	26.4	671	28.9	-99.79	-98.46	-101.09	-100.11	17659	150.8	48.8
1044	25.4	138	20.4	-101.10	-99.10	-102.35	-101.66	8201	64.9	12.7
684	24.8	54	17.7	-101.92	-99.23	-103.40	-102.79	5337	38.5	5.2

Table A.3: Measurement of Ethane-27

A.1.4 Nitrogen-100

G [kg/m^{2}s]	p_m [bar]	$(dp/dz)_f$ [kPa/m]	q'' [kW/m^2]	T_{out} [°C]	T_{in} [°C]	T_b [°C]	T_w [°C]	Re [-]	$\overline{Nu}$ [-]	$\delta\overline{Nu}$ [-]
1.0 mm tube measurements										
144	58.63	2.0	11.1	-132.99	-129.89	-138.16	-137.88	8040	49.1	3.98
136	58.75	1.7	8.1	-132.34	-129.89	-136.60	-136.40	7669	44.1	3.91
157	58.87	3.0	9.9	-106.01	-98.98	-112.54	-112.29	11298	46.2	1.45
171	58.97	3.5	3.6	-104.36	-102.04	-106.81	-106.71	12305	46.2	3.81
326	59.25	13.8	4.8	-104.34	-102.74	-106.17	-106.05	23472	86.0	9.85
316	58.47	6.5	9.1	-132.47	-131.35	-134.85	-134.62	17410	93.4	13.16
637	59.05	28.3	10.4	-131.50	-130.84	-133.01	-132.75	35579	186.4	42.02
623	59.58	54.1	11.7	-101.51	-99.39	-104.09	-103.80	44723	157.5	13.67
359	13.85	13.1	5.2	-188.93	-187.57	-191.22	-191.09	2993	14.9	1.68
475	13.78	18.1	5.9	-189.04	-187.90	-191.10	-190.95	3934	18.9	2.49
586	13.78	22.9	6.3	-188.96	-187.96	-190.84	-190.68	4857	22.8	3.40
748	13.91	29.9	6.9	-188.76	-187.90	-190.42	-190.24	6223	29.1	5.03
668	63.23	20.2	14.3	-164.33	-162.49	-167.42	-167.06	10280	44.6	3.84
627	63.23	17.6	10.3	-163.75	-162.33	-166.13	-165.87	9742	42.0	4.67
287	63.05	2.7	10.3	-160.93	-157.97	-165.50	-165.24	4908	21.9	1.22
297	62.92	2.9	12.7	-161.60	-158.04	-167.07	-166.75	5023	22.5	1.07
148	62.46		8.7	-163.52	-158.60	-170.02	-169.80	2435	12.0	0.46
329	62.78	3.7	-	-161.69	-161.72	-161.72	-161.72	5304	-	-
0.5 mm tube measurements										
597	63.19	41.4	12.1	-168.05	-164.73	-170.09	-169.68	4549	22.8	1.90
591	62.73	44.3	22.4	-164.72	-158.71	-167.97	-167.20	5092	28.3	1.47
282	57.00	12.5	12.5	-165.37	-158.44	-167.75	-167.32	2465	17.1	0.98
289	58.67	22.8	12.8	-132.05	-128.48	-133.47	-133.03	9015	85.5	10.72
141	58.57	5.5	15.7	-133.07	-122.45	-134.96	-134.43	4722	55.1	4.76
590	57.86	102.6	16.0	-133.05	-131.08	-134.31	-133.76	17571	158.1	27.34
601	57.45	178.1	10.3	-99.90	-96.10	-100.58	-100.23	23329	162.6	30.76
308	57.73	38.6	9.1	-105.76	-99.54	-106.74	-106.43	11955	80.3	9.01
166	57.70	10.4	11.6	-112.02	-97.75	-113.85	-113.46	6447	45.7	3.09

Table A.4: Measurement of Nitrogen-100

A.1.5 Nitrogen-10

G [kg/m^{2}s]	p_m [bar]	$(dp/dz)_f$ [kPa/m]	q'' [kW/m^2]	T_{out} [°C]	T_{in} [°C]	T_b [°C]	T_w [°C]	Re [-]	$\overline{Nu}$ [-]	$\delta\overline{Nu}$ [-]
1.0 mm tube measurements										
200	41.24	1.25	6.53	-101.22	-100.13	-103.17	-103.00	5940	32.7	3.7
208	41.18	1.43	12.35	-102.44	-100.36	-106.11	-105.80	6084	32.4	2.2
218	41.16	1.69	16.53	-103.28	-100.53	-108.10	-107.68	6288	32.6	2.1
897	28.12	37.3	19.98	-115.48	-114.44	-117.97	-117.47	20384	76.4	6.8
940	28.34	40.9	9.87	-114.60	-114.09	-115.75	-115.50	21624	83.0	15.8

Continued on next page

Continuation of Table A.5: Measurements of single phase flow Nitrogen-10

G [kg/m^{2}s]	p_m [bar]	$(dp/dz)_f$ [kPa/m]	q'' [kW/m^2]	T_{out} [°C]	T_{in} [°C]	T_b [°C]	T_w [°C]	Re [-]	$\overline{Nu}$ [-]	$\delta\overline{Nu}$ [-]
570	26.77	15.8	8.35	-116.34	-115.65	-117.66	-117.45	12741	54.4	8.4
580	26.71	16.3	18.10	-117.39	-115.93	-120.36	-119.90	12787	52.6	3.8
416	25.94	8.96	16.75	-118.47	-116.60	-121.84	-121.42	9025	40.3	2.6
425	25.81	9.31	13.57	-118.58	-117.08	-121.28	-120.94	9176	40.6	3.2
420	25.84	9.10	6.44	-117.65	-116.93	-118.89	-118.73	9150	42.2	6.9

Table A.5: Measurement of Nitrogen-10

A.2 Two phase flow

A.2.1 Methane-100

G [kg/m^{2}s]	p_m [bar]	$(dp/dz)_f$ [kPa/m]	q'' [kW/m^2]	T_{out} [°C]	T_{in} [°C]	T_w [°C]	x_m [-]	Δx [-]	$\overline{h}$ [W/m^{2}K]	$\delta\overline{h}$ [W/m^{2}K]
1.0 mm tube measurements										
395	11.7	42.0	23.2	-120.88	-120.67	-123.83	0.15	0.03	7580	489
392	11.7	48.5	23.8	-120.87	-120.70	-123.56	0.20	0.03	8586	605
396	11.6	66.4	24.7	-120.86	-120.71	-123.00	0.34	0.03	11123	962
400	11.6	80.0	25.1	-120.89	-120.73	-122.83	0.42	0.03	12428	1176
386	11.5	104.9	25.3	-121.03	-120.83	-122.73	0.60	0.03	14080	1488
397	11.4	119.3	25.5	-121.01	-120.79	-122.56	0.69	0.03	15421	1775
395	11.4	125.5	25.7	-120.98	-120.75	-122.39	0.79	0.03	16828	2085
397	11.4	127.3	25.9	-120.95	-120.71	-122.30	0.82	0.03	17594	2268
396	11.4	123.0	26.0	-120.92	-120.66	-122.17	0.87	0.03	18941	2601
391	11.5	118.5	17.2	-120.91	-120.65	-121.72	0.87	0.02	18284	3658
392	11.5	105.8	16.7	-120.99	-120.80	-122.09	0.60	0.02	13933	2196
393	11.6	65.5	16.5	-120.86	-120.72	-122.23	0.35	0.02	11460	1512
392	11.7	40.4	15.7	-120.84	-120.67	-122.79	0.16	0.02	7742	740
495	12.9	62.4	39.6	-119.69	-119.19	-125.48	0.11	0.04	6552	231
487	12.8	86.3	41.7	-119.45	-119.09	-124.45	0.22	0.04	8047	320
493	12.8	99.1	42.7	-119.38	-119.02	-124.05	0.28	0.04	8822	370
490	12.7	119.6	43.5	-119.36	-119.00	-123.61	0.37	0.04	9820	444
488	12.6	145.6	44.2	-119.35	-118.95	-123.20	0.49	0.04	10914	534
487	12.6	163.9	44.6	-119.35	-118.92	-122.97	0.57	0.04	11634	598
491	12.5	182.7	45.0	-119.33	-118.87	-122.71	0.65	0.04	12436	673
491	12.5	199.5	45.2	-119.25	-118.75	-122.45	0.73	0.04	13096	740
487	12.6	204.7	45.2	-119.14	-118.62	-122.18	0.81	0.04	13677	804
486	12.6	205.8	45.2	-119.10	-118.54	-122.02	0.87	0.05	14151	859
565	14.0	61.4	26.5	-116.99	-116.61	-119.83	0.14	0.02	8756	567
554	13.9	68.7	26.9	-116.89	-116.58	-119.48	0.20	0.02	9813	697
556	13.9	83.4	27.0	-116.88	-116.59	-119.06	0.28	0.02	11617	965
554	13.8	94.5	26.7	-116.90	-116.62	-118.85	0.34	0.02	12761	1164
557	13.7	134.5	26.5	-116.97	-116.65	-118.58	0.51	0.02	14946	1600
548	13.5	169.2	26.5	-117.11	-116.74	-118.53	0.66	0.02	16544	1953
556	13.5	188.1	26.6	-117.06	-116.66	-118.38	0.73	0.02	17500	2272
554	13.5	199.0	26.4	-117.01	-116.59	-118.19	0.84	0.02	19020	2588
285	8.8	28.1	33.8	-128.30	-127.79	-133.55	0.12	0.05	6144	235
284	8.7	33.7	35.2	-128.13	-127.78	-132.98	0.19	0.06	7007	288
283	8.7	42.5	37.2	-128.01	-127.71	-132.31	0.26	0.06	8371	380
282	8.6	55.0	38.3	-127.98	-127.69	-131.77	0.36	0.06	9730	491
278	8.6	66.4	39.1	-127.96	-127.67	-131.35	0.47	0.06	11072	614
276	8.5	73.6	39.6	-127.96	-127.65	-131.11	0.56	0.06	12000	708
283	8.5	81.4	40.2	-127.86	-127.54	-130.78	0.62	0.06	13056	822
279	8.5	86.1	40.6	-127.86	-127.54	-130.48	0.74	0.07	14636	1013
277	8.5	80.7	41.2	-127.87	-127.31	-130.08	0.84	0.07	16578	1275
283	8.5	86.9	41.0	-127.86	-127.51	-130.25	0.80	0.07	15967	1191
283	8.6	83.3	24.0	-127.59	-127.23	-128.81	0.82	0.04	17128	2305
285	8.6	86.5	23.7	-127.62	-127.31	-129.03	0.74	0.04	15155	1837
277	8.6	77.2	22.9	-127.80	-127.52	-129.40	0.63	0.04	13197	1445
276	8.5	71.3	22.5	-127.89	-127.63	-129.64	0.55	0.04	11963	1215
481	12.6	198.9	26.4	-119.01	-118.49	-120.62	0.88	0.03	14063	1427
487	12.6	179.9	26.4	-119.16	-118.70	-121.00	0.67	0.03	12741	1174

Continued on next page

Continuation of Table A.6: Two phase flow measurement of Methane-100

G [kg/m^{2}s]	p_m [bar]	$(dp/dz)_f$ [kPa/m]	q'' [kW/m^2]	T_{out} [°C]	T_{in} [°C]	T_w [°C]	x_m [-]	Δx [-]	$\bar{h}$ [W/m^{2}K]	$\delta\bar{h}$ [W/m^{2}K]
491	12.8	122.8	26.4	-119.16	-118.82	-121.52	0.39	0.03	10430	796
491	12.9	86.9	26.4	-119.23	-118.92	-122.10	0.23	0.03	8740	567
492	13.0	60.0	26.4	-119.46	-119.07	-122.98	0.12	0.03	7101	383
491	7.0	84.8	26.4	-131.81	-131.31	-134.14	0.13	0.02	10196	762
487	7.1	143.0	26.4	-131.85	-131.23	-133.50	0.24	0.02	13475	1310
493	6.9	221.9	26.4	-132.03	-131.16	-133.13	0.39	0.02	17162	2108
486	6.6	332.8	26.4	-132.24	-130.99	-132.75	0.68	0.02	23179	3846
485	6.6	359.6	26.4	-132.14	-130.76	-132.31	0.88	0.02	-	-
486	6.6	359.5	12.9	-132.08	-130.70	-131.76	0.88	0.01	-	-
487	6.6	332.7	13.0	-132.16	-130.90	-132.05	0.69	0.01	-	-
485	6.9	220.8	13.0	-131.99	-131.13	-132.29	0.40	0.01	-	-
490	7.1	146.8	13.0	-131.78	-131.17	-132.40	0.24	0.01	-	-
489	7.3	91.6	12.9	-131.74	-131.29	-132.72	0.13	0.01	-	-
281	6.8	34.5	13.0	-133.22	-132.90	-134.77	0.14	0.02	7580	858
280	6.8	54.2	13.0	-133.06	-132.74	-134.24	0.23	0.02	9674	1375
283	6.8	82.0	12.9	-132.77	-132.37	-133.63	0.39	0.02	12201	2179
283	6.7	119.7	12.9	-132.61	-132.09	-133.15	0.67	0.02	16142	3789
282	6.7	117.7	12.9	-132.47	-131.95	-132.81	0.84	0.02	21608	6768
279	13.0	20.6	26.4	-118.85	-118.49	-123.24	0.13	0.05	5777	262
279	13.0	29.9	26.4	-118.70	-118.50	-122.33	0.23	0.05	7076	382
274	12.9	33.5	26.4	-118.70	-118.56	-121.66	0.35	0.05	8692	562
279	12.9	42.5	26.4	-118.66	-118.54	-120.99	0.51	0.05	11059	890
281	12.8	53.3	26.4	-118.75	-118.62	-120.80	0.68	0.05	12498	1129
281	12.8	53.3	26.4	-118.75	-118.62	-120.80	0.68	0.05	12498	1129
277	12.8	54.6	26.4	-118.70	-118.55	-120.39	0.83	0.05	14889	1595
283	12.8	56.3	12.9	-118.65	-118.51	-119.45	0.82	0.02	14931	3256
286	12.8	54.2	13.0	-118.73	-118.60	-119.71	0.68	0.02	12423	2246
281	12.8	43.0	13.0	-118.74	-118.63	-119.82	0.52	0.02	11460	1920
280	12.9	34.7	12.9	-118.73	-118.61	-120.09	0.36	0.02	9099	1231
275	12.9	25.4	12.9	-118.67	-118.52	-120.39	0.23	0.02	7236	792
276	13.0	16.8	13.0	-118.74	-118.53	-120.90	0.13	0.02	5719	504
270	26.1	9.1	12.0	-100.75	-100.48	-103.01	0.15	0.03	5025	424
275	26.1	12.1	12.7	-100.54	-100.39	-102.72	0.23	0.03	5660	501
277	26.2	15.7	13.1	-100.41	-100.35	-102.30	0.36	0.03	6812	695
279	26.2	18.2	13.0	-100.37	-100.33	-101.97	0.51	0.03	8046	958
281	25.9	21.7	13.1	-100.64	-100.60	-102.05	0.67	0.03	9198	1236
284	25.7	25.2	26.4	-100.87	-100.83	-103.26	0.89	0.06	10964	875
279	25.7	15.6	26.4	-101.01	-100.88	-104.92	0.36	0.06	6633	338
278	25.8	7.3	26.3	-101.64	-100.97	-106.56	0.13	0.06	5007	203
489	26.6	29.2	26.4	-100.33	-99.95	-103.66	0.14	0.03	7486	423
485	26.7	33.9	26.3	-99.93	-99.73	-102.90	0.24	0.03	8558	545
493	26.7	43.9	26.4	-99.81	-99.63	-102.30	0.37	0.03	10244	769
490	26.7	49.0	26.3	-99.76	-99.58	-101.85	0.53	0.03	12089	1062
484	26.8	54.5	26.3	-99.66	-99.53	-101.55	0.69	0.04	13458	1312
484	26.8	61.2	26.3	-99.57	-99.43	-101.26	0.82	0.04	15034	1626
560	26.2	84.1	26.3	-100.22	-100.06	-101.73	0.82	0.03	16624	1987
559	26.3	88.4	26.3	-100.17	-99.95	-101.47	0.87	0.03	18697	2532
558	26.5	70.8	26.5	-99.88	-99.73	-101.59	0.69	0.03	14849	1578
552	26.4	62.1	26.4	-100.06	-99.88	-101.95	0.54	0.03	13325	1281
559	26.4	55.2	26.3	-100.12	-99.94	-102.34	0.37	0.03	11374	943
558	26.4	46.7	26.3	-100.17	-99.98	-102.80	0.24	0.03	9645	686
560	26.4	28.5	26.4	-100.55	-100.20	-103.52	0.14	0.03	8404	525
697	26.3	49.5	26.4	-100.49	-100.21	-103.04	0.14	0.02	9835	709
701	26.3	78.5	26.4	-100.20	-100.04	-102.19	0.37	0.02	12765	1177
701	26.5	103.9	26.3	-99.83	-99.69	-101.36	0.68	0.02	16493	1952
695	26.3	124.1	26.3	-100.09	-99.90	-101.32	0.83	0.02	19792	2808
494	35.8	21.5	26.4	-91.68	-91.43	-95.19	0.15	0.04	7273	400
493	35.7	18.5	26.4	-91.87	-91.56	-95.48	0.10	0.04	7020	374
488	35.8	25.0	26.4	-91.09	-91.00	-94.34	0.26	0.05	8011	479
497	35.7	28.9	26.4	-91.14	-91.09	-94.09	0.37	0.04	8856	581
492	35.8	31.0	26.4	-91.00	-90.94	-93.65	0.52	0.05	9851	713
491	36.0	33.2	26.3	-90.86	-90.84	-93.24	0.68	0.05	11020	886
486	35.9	38.9	26.3	-90.92	-90.92	-92.99	0.86	0.05	12676	1167
480	35.8	39.3	12.8	-91.00	-91.00	-91.97	0.89	0.02	13226	2572
490	35.6	31.2	13.0	-91.19	-91.15	-92.43	0.54	0.02	10297	1550
491	35.3	21.9	12.9	-91.72	-91.65	-93.38	0.18	0.02	7614	872

Continued on next page

Continuation of Table A.6: Two phase flow measurement of Methane-100

G [kg/m^{2}s]	p_m [bar]	$(dp/dz)_f$ [kPa/m]	q'' [kW/m^2]	T_{out} [°C]	T_{in} [°C]	T_w [°C]	x_m [-]	Δx [-]	$\bar{h}$ [W/m^{2}K]	$\delta\bar{h}$ [W/m^{2}K]
489	35.3	22.8	6.5	-91.56	-91.57	-92.40	0.19	0.01	7729	1776
482	35.5	30.7	6.5	-91.24	-91.19	-91.83	0.57	0.01	10503	3223
499	35.6	39.6	6.4	-91.09	-91.09	-91.59	0.83	0.01	12666	4743
276	35.1	6.6	12.9	-91.99	-91.76	-94.52	0.17	0.04	4860	373
281	35.3	10.8	12.9	-91.45	-91.46	-93.45	0.51	0.04	6487	637
277	35.5	12.5	13.0	-91.28	-91.30	-92.95	0.82	0.04	7843	916
496	41.7	19.3	13.1	-86.49	-86.36	-87.64	0.19	0.03	10735	1677
494	41.7	21.8	12.8	-86.34	-86.24	-87.37	0.31	0.03	11892	2088
491	41.7	21.8	12.8	-86.33	-86.24	-87.30	0.42	0.03	12680	2372
487	41.7	21.0	12.8	-86.31	-86.23	-87.20	0.57	0.03	13749	2795
487	41.7	22.5	12.7	-86.30	-86.21	-87.08	0.70	0.03	15552	3909
495	41.7	26.3	13.1	-86.25	-86.17	-86.92	0.82	0.03	18529	4991
282	41.7	7.9	12.3	-86.25	-86.19	-87.56	0.80	0.05	9151	1309
280	41.7	6.9	12.2	-86.28	-86.21	-87.77	0.69	0.05	7988	1012
283	41.7	6.4	12.2	-86.28	-86.21	-87.92	0.54	0.05	7299	846
277	41.6	7.1	12.7	-86.36	-86.35	-88.32	0.40	0.05	6446	644
277	41.6	6.9	12.6	-86.41	-86.38	-88.47	0.29	0.05	6060	577
275	41.5	5.9	12.3	-86.57	-86.45	-88.79	0.14	0.05	5407	474
168	26.5	3.0	25.7	-101.10	-99.97	-107.71	0.11	0.10	3582	118
164	26.4	4.6	26.8	-100.42	-100.07	-106.32	0.32	0.10	4406	161
162	26.4	5.9	27.2	-100.20	-100.11	-105.46	0.51	0.11	5121	206
162	26.3	7.0	27.0	-100.18	-100.15	-104.03	0.78	0.11	6977	363
0.5 mm tube measurements										
493	7.4	147.9	29.2	-130.67	-129.93	-132.74	0.13	0.05	12016	934
492	7.2	326.1	28.8	-131.40	-130.27	-132.32	0.30	0.05	19406	2381
494	7.1	477.6	28.1	-132.08	-130.43	-132.38	0.41	0.05	25047	4027
489	6.8	715.4	27.5	-133.16	-130.58	-132.63	0.62	0.05	36190	8511
502	6.7	930.7	27.6	-133.96	-130.63	-132.86	0.79	0.04	48858	15406
275	7.2	208.3	12.4	-131.16	-130.33	-131.27	0.76	0.04	23699	8117
274	7.2	175.0	12.6	-131.14	-130.53	-131.51	0.55	0.04	18743	5054
275	7.3	124.3	12.6	-130.95	-130.51	-131.52	0.40	0.04	15991	3692
274	7.3	60.9	12.4	-130.67	-130.37	-131.68	0.16	0.04	10733	1745
688	25.8	162.0	26.0	-100.42	-100.01	-101.89	0.15	0.05	15585	1717
702	25.9	220.7	25.6	-100.35	-100.02	-101.33	0.39	0.04	22345	3524
699	25.9	278.4	25.7	-100.39	-100.01	-101.15	0.57	0.04	27020	5102
694	25.8	356.8	25.6	-100.50	-100.01	-101.04	0.75	0.04	32703	7480
487	25.8	190.9	25.7	-100.44	-100.16	-101.34	0.79	0.06	24677	4270
498	25.8	146.4	25.8	-100.40	-100.18	-101.63	0.55	0.06	19215	2602
497	25.8	117.6	25.5	-100.44	-100.19	-101.95	0.36	0.06	15619	1760
494	25.7	99.0	25.4	-100.55	-100.20	-102.47	0.18	0.06	12129	1087
274	25.8	30.9	13.6	-100.38	-100.07	-101.92	0.15	0.06	8029	929
275	26.0	43.3	12.7	-100.13	-100.06	-101.10	0.48	0.06	12682	2340
275	26.0	52.8	12.3	-100.10	-100.01	-100.76	0.69	0.05	17521	4544
1359	25.1	476.0	38.4	-101.40	-100.72	-102.56	0.15	0.03	25610	3087
1357	24.9	640.4	38.6	-101.70	-100.87	-102.35	0.31	0.03	36093	6051
1352	24.7	790.5	38.7	-101.94	-100.95	-102.28	0.43	0.03	46350	9901
1372	24.6	990.7	38.6	-102.28	-100.99	-102.26	0.55	0.03	61423	17424
1342	24.5	1140.8	38.4	-102.49	-100.98	-102.24	0.65	0.03	75535	26421
1365	24.3	1451.0	38.1	-102.89	-100.96	-102.27	0.76	0.03	-	-
1173	35.2	299.9	36.3	-91.27	-90.87	-92.14	0.17	0.05	34058	5724
1166	35.2	347.6	36.4	-91.23	-90.89	-91.86	0.36	0.05	45144	10011
1164	35.1	500.3	36.6	-91.38	-90.89	-91.62	0.57	0.05	75353	27639
1160	35.0	515.8	36.4	-91.54	-90.85	-91.45	0.76	0.05	-	-
1221	35.3	380.6	0.1	-91.12	-90.75	-90.81	0.35	0.00	-	-
484	34.7	60.4	26.3	-91.58	-91.30	-93.37	0.20	0.09	13623	1311
486	34.9	77.1	26.1	-91.39	-91.29	-92.76	0.45	0.08	18381	2362
491	35.0	109.8	25.8	-91.31	-91.18	-92.12	0.73	0.08	29431	6029
491	40.9	54.8	14.0	-86.43	-86.27	-87.04	0.16	0.06	20283	5300
486	41.0	57.1	13.8	-86.29	-86.22	-86.76	0.35	0.06	27730	9974
487	41.0	62.4	13.7	-86.28	-86.22	-86.60	0.50	0.06	39000	19876
509	41.1	72.6	13.6	-86.21	-86.13	-86.38	0.57	0.06	65041	55467
482	41.1	91.1	13.4	-86.25	-86.15	-86.27	0.77	0.06	-	-
280	40.9	20.9	11.8	-86.36	-86.34	-87.02	0.60	0.09	17615	4753
289	40.9	18.1	11.8	-86.34	-86.32	-87.27	0.39	0.09	12574	2479
298	40.9	18.1	11.8	-86.39	-86.32	-87.45	0.19	0.09	10806	1859
0.25 mm tube measurements										

Continued on next page

Continuation of Table A.6: Two phase flow measurement of Methane-100

G [kg/m^{2}s]	p_m [bar]	$(dp/dz)_f$ [kPa/m]	q'' [kW/m^2]	T_{out} [°C]	T_{in} [°C]	T_w [°C]	x_m [-]	Δx [-]	$\overline{h}$ [W/m^{2}K]	$\delta\overline{h}$ [W/m^{2}K]
549	24.7	146	22.1	-101.61	-101.34	-102.27	0.27	0.09	27681	5530
1125	25.0	505	20.5	-101.56	-100.65	-101.74	0.15	0.04	32122	7960
1225	24.8	910	19.6	-102.09	-100.73	-101.79	0.32	0.04	52042	21545
1325	24.5	1281	19.4	-102.74	-100.82	-102.08	0.42	0.03	65715	34601
1265	24.0	1601	20.0	-103.62	-101.09	-102.54	0.63	0.04	-	-
1353	23.8	1714	59.2	-103.87	-101.27	-103.43	0.55	0.10	69451	12693
1312	24.2	1238	59.9	-102.93	-101.10	-103.24	0.39	0.11	49099	6317
1367	24.5	942	60.0	-102.47	-100.91	-103.26	0.23	0.10	38183	3851
1310	24.6	737	62.1	-102.38	-100.81	-103.64	0.16	0.11	30457	2404
1211	34.5	500	36.4	-91.97	-91.26	-92.76	0.18	0.09	31783	4407
1158	34.4	561	36.1	-92.16	-91.41	-92.59	0.36	0.10	44620	8653
1188	34.1	911	35.8	-92.50	-91.44	-92.50	0.59	0.09	67207	19602
1114	34.1	816	36.2	-92.59	-91.43	-92.53	0.68	0.10	69796	20892
908	34.4	610	8.1	-92.06	-91.47	-91.75	0.50	0.03	-	-

Table A.6: Two phase flow measurement of Methane-100

A.2.2 Ethane-10

G [kg/m^{2}s]	p_m [bar]	$(dp/dz)_f$ [kPa/m]	q'' [kW/m^2]	T_{out} [°C]	T_{in} [°C]	T_w [°C]	x_{in} [-]	Δx [-]	$\overline{h}$ [W/m^{2}K]	$\delta\overline{h}$ [W/m^{2}K]
1.0 mm tube measurements										
277	7.5	26	13.0	-127.25	-125.00	-129.33	0.13	0.02	4051	275
279	7.3	38	13.0	-126.75	-125.32	-128.44	0.24	0.02	5406	612
281	7.2	54	12.8	-126.15	-125.62	-127.39	0.37	0.02	8517	1098
282	7.1	88	13.0	-124.24	-123.61	-125.18	0.55	0.02	10339	1571
283	6.8	131	12.7	-119.22	-117.79	-119.93	0.76	0.02	8926	1204
285	7.0	143	12.1	-114.39	-112.60	-115.17	0.82	0.02	7234	839
282	7.3	146	12.8	-104.94	-103.19	-106.25	0.89	0.02	5893	536
281	7.4	142	-0.1	-102.72	-102.31	-102.58	0.90	0.00	-	-
281	6.8	131	-0.2	-117.34	-116.86	-117.15	0.77	0.00	-	-
278	6.8	59	-0.3	-126.54	-126.30	-126.43	0.38	0.00	-	-
278	7.1	39	-0.4	-127.03	-126.38	-126.89	0.24	0.00	-	-
280	7.2	31	-0.2	-127.43	-125.54	-127.28	0.13	0.00	-	-
495	25.8	28	26.1	-96.09	-95.39	-100.13	0.11	0.03	5943	278
491	25.7	39	26.4	-94.95	-94.62	-98.60	0.22	0.03	6920	364
488	25.8	53	26.3	-93.80	-93.67	-96.93	0.36	0.03	8234	507
489	25.8	64	26.2	-92.41	-91.71	-94.81	0.52	0.03	9495	669
495	25.7	77	26.2	-90.06	-89.35	-92.48	0.64	0.03	9436	662
488	25.6	87	26.5	-87.19	-86.15	-89.53	0.74	0.03	9249	630
491	25.8	101	26.2	-80.40	-79.31	-82.97	0.86	0.03	8417	532
557	25.4	130	26.3	-81.73	-80.50	-83.79	0.85	0.03	9821	711
558	25.3	96	26.6	-90.55	-89.73	-92.63	0.65	0.02	10681	828
559	25.5	66	26.3	-94.36	-94.03	-96.88	0.36	0.02	9779	706
560	25.6	32	26.5	-96.11	-95.59	-99.76	0.11	0.02	6772	349
695	25.7	45	26.3	-95.90	-95.47	-98.97	0.11	0.02	7985	479
697	25.6	67	26.2	-95.04	-94.67	-97.52	0.23	0.02	9819	714
690	25.4	91	26.1	-94.25	-93.99	-96.49	0.36	0.02	11028	894
685	25.3	109	26.3	-92.60	-92.15	-94.67	0.52	0.02	11462	958
691	25.2	138	26.3	-89.82	-89.17	-91.77	0.66	0.02	11542	972
685	25.4	158	26.5	-86.16	-85.21	-88.04	0.77	0.02	11250	917
683	25.3	180	26.1	-82.43	-81.45	-84.36	0.84	0.02	10784	859
488	6.8	70	12.4	-127.35	-125.53	-128.50	0.14	0.01	6018	603
485	6.2	119	12.4	-127.01	-126.55	-127.97	0.27	0.01	10478	1699
496	5.6	196	12.3	-126.54	-125.86	-127.09	0.41	0.01	13853	2947
491	4.9	316	12.4	-125.18	-123.83	-125.19	0.59	0.01	18155	4975
491	5.3	429	12.3	-118.44	-116.38	-118.33	0.82	0.01	13349	2740
489	6.0	452	12.6	-111.53	-109.56	-111.92	0.87	0.01	9204	1287
193	16.5	24	6.3	-82.79	-82.06	-84.25	0.93	0.02	3439	403
192	16.5	26	6.1	-98.63	-98.15	-99.52	0.74	0.02	5380	952
189	16.5	18.1	6.2	-105.44	-105.31	-106.52	0.51	0.01	5391	930
190	16.5	24.3	6.3	-107.86	-107.52	-109.13	0.29	0.01	4337	613
190	16.5	9.2	6.3	-108.55	-108.05	-110.08	0.14	0.01	3533	424
277	25.7	11	12.7	-95.32	-94.88	-98.28	0.15	0.02	4002	266

Continued on next page

Continuation of Table A.7: Two phase flow measurement of Ethane-10

G [kg/m^{2}s]	p_m [bar]	$(dp/dz)_f$ [kPa/m]	q'' [kW/m^2]	T_{out} [°C]	T_{in} [°C]	T_w [°C]	x_{in} [-]	Δx [-]	$\bar{h}$ [W/m^{2}K]	$\delta\bar{h}$ [W/m^{2}K]
280	25.8	14	13.0	-94.82	-94.25	-97.40	0.22	0.02	4554	327
278	25.9	17	13.1	-93.45	-93.14	-95.85	0.36	0.02	5114	404
284	26.0	23	12.8	-91.24	-91.03	-93.40	0.51	0.02	5629	495
285	25.9	29	12.7	-88.78	-88.32	-90.65	0.64	0.02	6057	569
280	25.8	33	13.0	-84.18	-83.46	-86.16	0.77	0.03	5582	478
279	25.8	35	13.0	-80.19	-79.17	-82.03	0.85	0.03	5525	470
286	36.0	21	12.7	-70.11	-69.36	-72.20	0.86	0.03	5144	422
498	36.5	26	12.7	-82.14	-82.20	-84.18	0.24	0.01	6306	618
503	36.5	33	12.5	-80.92	-80.99	-82.75	0.36	0.01	6956	754
488	36.1	22	12.4	-83.52	-83.15	-85.22	0.15	0.01	6601	685
497	36.2	30	12.9	-82.50	-82.24	-84.10	0.26	0.01	7456	833
485	36.2	34	12.7	-81.09	-80.76	-82.55	0.41	0.02	7814	929
490	36.0	39	12.7	-79.45	-79.02	-80.80	0.54	0.02	8109	995
488	36.0	46	12.6	-76.50	-75.97	-77.74	0.68	0.02	8360	1069
491	36.0	53	12.3	-73.43	-72.85	-74.60	0.78	0.02	8446	1111
492	36.0	60	12.5	-70.15	-69.54	-71.28	0.85	0.02	8748	1173
483	36.0	58	6.0	-69.29	-68.94	-69.79	0.87	0.01	8899	2519
487	35.9	45	6.1	-76.23	-75.91	-76.79	0.69	0.01	8559	2281
491	35.9	34	6.1	-81.41	-81.20	-81.99	0.40	0.01	8832	2453
494	36.0	20	6.1	-83.65	-83.42	-84.38	0.14	0.01	7154	1628
501	35.9	19	37.2	-84.96	-83.68	-90.02	0.12	0.04	6537	242
493	36.1	21	35.6	-84.37	-83.26	-89.44	0.14	0.04	6332	237
482	36.1	28	35.7	-82.88	-82.26	-87.64	0.27	0.04	7035	287
485	35.8	35	35.7	-81.91	-81.15	-86.22	0.40	0.04	7612	331
503	35.6	41	36.0	-80.91	-79.95	-84.83	0.51	0.04	8173	374
489	35.6	46	35.9	-78.05	-76.73	-81.80	0.67	0.05	8142	373
490	36.0	52	35.8	-74.28	-72.78	-77.91	0.78	0.05	8172	377
491	36.0	59	36.0	-71.24	-69.64	-74.83	0.85	0.05	8209	378
758	36.3	112	35.3	-73.05	-72.01	-75.86	0.79	0.03	10612	624
768	36.2	88	35.3	-77.75	-76.86	-80.76	0.64	0.03	10243	582
757	36.0	68	35.8	-81.20	-80.51	-84.38	0.43	0.03	10163	566
760	36.0	47	35.4	-83.63	-83.18	-87.21	0.16	0.03	9274	482
490	41.1	17.8	12.8	-78.67	-78.33	-80.60	0.15	0.02	6109	574
480	41.2	25.0	12.7	-76.75	-76.44	-78.48	0.37	0.02	6723	696
491	41.2	-	12.8	-74.80	-74.38	-76.43	0.53	0.02	6919	732
493	41.2	36.6	12.4	-71.05	-70.53	-72.57	0.72	0.02	6976	765
499	41.3	43.3	12.9	-67.53	-66.97	-69.01	0.83	0.02	7325	807
278	49.4	4.1	13.0	-70.89	-70.24	-73.51	0.19	0.03	4401	309
279	49.4	5.0	12.3	-69.76	-69.31	-72.15	0.30	0.03	4716	369
277	49.5	5.8	12.5	-67.99	-67.48	-70.24	0.48	0.04	4987	403
285	49.5	-	13.0	-65.91	-65.24	-68.17	0.63	0.04	4988	390
276	49.4	8.0	13.1	-63.73	-62.94	-65.99	0.75	0.06	4922	378
274	49.4	-	13.1	-60.59	-59.70	-62.75	0.86	-	5016	391
276	49.0	-	6.0	-60.19	-59.78	-61.08	0.85	-	5478	991
280	49.0	6.4	6.2	-65.38	-65.06	-66.34	0.64	0.02	5554	981
285	49.0	6.5	6.2	-68.18	-67.92	-69.19	0.47	0.02	5384	932
284	49.1	5.4	6.2	-69.74	-69.50	-70.83	0.31	0.02	5179	857
288	49.0	4.2	6.5	-70.64	-70.34	-71.79	0.21	0.02	4987	766
154	48.6	-0.2	6.1	-71.50	-70.84	-73.11	0.20	0.03	3141	354
142	49.0	-0.3	6.1	-69.04	-68.49	-70.73	0.42	0.03	3097	346
146	49.1	-0.1	6.4	-65.72	-65.09	-67.37	0.64	0.04	3260	361
144	49.2	-0.4	6.0	-62.63	-61.95	-64.03	0.77	0.06	3456	425
0.5 mm tube measurements										
482	26.1	84	28.0	-95.60	-93.84	-97.63	0.25	0.05	9604	649
486	26.2	121	26.4	-93.88	-92.19	-95.42	0.40	0.05	11072	890
492	26.3	180	26.6	-90.47	-88.65	-91.64	0.60	0.05	12808	1161
500	26.4	232	25.8	-84.82	-82.30	-85.62	0.74	0.05	12526	1151
483	26.2	92	11.3	-94.62	-93.67	-95.53	0.25	0.02	8175	1160
485	26.4	223	11.7	-82.65	-81.06	-83.05	0.76	0.03	9780	1563
275	25.8	61	12.8	-82.42	-79.51	-83.24	0.75	0.05	5620	538
269	26.2	44.5	12.3	-89.80	-87.59	-90.98	0.58	0.04	5368	512
275	26.1	34.2	12.7	-93.32	-91.27	-94.91	0.41	0.04	4875	423
271	26.1	23.0	13.1	-95.71	-93.80	-97.86	0.22	0.04	4224	327
616	26.5	343	21.6	-84.36	-82.45	-84.98	0.75	0.04	13713	1619
592	26.3	247	21.2	-89.80	-88.40	-90.69	0.60	0.03	13347	1565
565	26.1	168	22.1	-92.99	-91.73	-94.22	0.44	0.04	11844	1199

Continued on next page

Continuation of Table A.7: Two phase flow measurement of Ethane-10

G [kg/m^{2}s]	p_m [bar]	$(dp/dz)_f$ [kPa/m]	q'' [kW/m^2]	T_{out} [°C]	T_{in} [°C]	T_w [°C]	x_{in} [-]	Δx [-]	$\overline{h}$ [W/m^{2}K]	$\delta\overline{h}$ [W/m^{2}K]
589	26.1	113	22.2	-95.34	-94.11	-96.99	0.21	0.03	9794	836
470	36.5	55.7	12.3	-83.66	-82.63	-84.79	0.23	0.03	7482	906
494	36.6	82	12.2	-81.38	-80.50	-82.30	0.41	0.03	8922	1261
501	36.7	106	12.5	-78.90	-78.02	-79.84	0.56	0.03	9084	1270
493	36.8	139	11.9	-73.55	-72.38	-74.14	0.76	0.03	10120	1633
508	36.7	139	35.9	-76.20	-73.55	-77.83	0.73	0.09	12141	791
474	36.5	90	36.2	-80.82	-78.85	-83.07	0.53	0.08	11165	673
479	36.4	55.0	35.5	-85.36	-82.85	-87.98	0.22	0.08	9181	481
0.25 mm tube measurements										
675	25.8	196	21.8	-97.48	-94.07	-98.31	0.18	0.06	8574	690
586	25.7	269	22.6	-94.68	-90.54	-95.19	0.40	0.07	8792	690
635	25.7	387	22.3	-92.33	-87.77	-92.65	0.51	0.07	8557	672
581	25.7	452	21.7	-83.13	-78.09	-83.14	0.67	0.08	8574	689
568	25.9	474	21.8	-76.12	-71.29	-75.90	0.76	0.10	9939	870

Table A.7: Two phase flow measurement of Ethane-10

A.2.3 Ethane-27

G [kg/m^{2}s]	p_m [bar]	$(dp/dz)_f$ [kPa/m]	q'' [kW/m^2]	T_{out} [°C]	T_{in} [°C]	T_w [°C]	x_{in} [-]	Δx [-]	$\overline{h}$ [W/m^{2}K]	$\delta\overline{h}$ [W/m^{2}K]
1.0 mm tube measurements										
502	10.0	68	28.8	-116.18	-114.02	-119.19	0.16	0.02	7045	388.1
487	10.0	80	29.5	-115.83	-114.67	-118.69	0.21	0.02	8594	496.1
488	10.0	92	30.2	-115.49	-114.41	-118.21	0.24	0.03	9246	555.7
494	9.8	118	33.0	-114.70	-113.48	-117.26	0.31	0.03	10421	641.4
490	9.7	190	33.0	-109.50	-107.76	-111.48	0.49	0.03	11574	784.8
486	9.4	269	33.0	-98.43	-95.96	-100.24	0.66	0.03	10839	692.3
493	9.2	318	35.0	-89.88	-87.41	-91.90	0.75	0.03	10788	648.4
495	9.2	338	34.9	-84.14	-81.89	-86.17	0.81	0.03	11051	681.2
490	9.1	352	33.2	-80.13	-78.06	-82.05	0.85	0.03	11251	739.9
279	10.4	25.0	25.5	-116.86	-110.59	-121.12	0.13	0.04	3443	111.1
281	10.2	30.4	25.9	-115.29	-112.76	-118.98	0.22	0.04	5228	229.8
278	10.3	40	26.9	-113.86	-112.25	-117.25	0.32	0.04	6416	312.1
278	10.1	67	25.6	-107.21	-105.10	-109.65	0.52	0.04	7351	419.7
282	9.9	93	26.8	-96.62	-93.81	-99.01	0.67	0.04	7061	373.5
281	9.9	104	24.8	-89.32	-86.85	-91.69	0.74	0.04	6879	383.3
276	9.9	108	29.3	-79.92	-77.61	-82.79	0.84	0.05	7280	365.4
281	9.9	110	32.9	-73.91	-71.83	-77.04	0.92	0.06	7903	381.5
280	9.9	101	34.6	-72.08	-70.04	-75.31	0.95	0.06	8155	386.5
386	10.3	23.9	23.4	-115.96	-111.08	-118.96	0.07	0.02	4309	173.0
392	10.2	37.8	23.8	-116.10	-111.07	-118.77	0.11	0.02	4579	192.4
387	10.0	54	23.6	-115.25	-114.34	-117.88	0.22	0.02	7656	491.2
389	9.9	122	23.6	-107.30	-105.70	-108.93	0.51	0.03	9698	771.4
388	9.7	174	23.1	-96.53	-94.52	-98.01	0.66	0.03	9298	726.8
395	9.5	206	23.7	-88.04	-86.08	-89.70	0.75	0.03	8995	664.8
388	9.4	214	25.8	-81.07	-79.25	-82.82	0.83	0.03	9692	704.6
389	9.4	219	32.5	-75.17	-73.31	-77.44	0.91	0.04	10154	619.3
286	16.6	15.7	12.0	-102.21	-101.29	-104.30	0.13	0.02	4699	376.6
282	16.8	18.7	11.8	-100.44	-99.58	-102.33	0.22	0.02	5074	439.8
280	16.9	26.9	12.2	-97.54	-96.67	-99.18	0.34	0.02	5894	563.3
280	16.6	26.3	13.0	-98.15	-97.21	-99.79	0.34	0.02	6140	574.4
281	16.5	44	12.9	-90.27	-89.20	-91.48	0.54	0.02	7404	825.4
281	16.5	56	13.3	-81.73	-80.45	-82.98	0.66	0.02	7040	731.5
272	16.3	61	21.4	-67.76	-66.07	-70.18	0.84	0.04	6571	404.0
278	26.5	7.6	11.5	-86.48	-85.54	-88.83	0.12	0.02	4069	302.2
275	26.5	8.8	10.1	-85.01	-84.16	-87.37	0.20	0.02	3631	279.0
277	26.7	13.6	13.1	-81.56	-80.48	-83.77	0.33	0.02	4747	352.2
284	26.6	23.8	12.5	-75.43	-74.42	-77.05	0.50	0.02	5871	548.8
285	26.6	32.7	12.3	-65.79	-64.73	-67.23	0.66	0.02	6259	625.6
283	26.5	37.4	19.0	-57.07	-55.64	-59.30	0.80	0.04	6437	437.4
206	10.1	24.2	17.8	-112.48	-110.86	-115.08	0.37	0.04	5221	313.7
206	9.9	17.5	17.0	-115.72	-113.73	-118.68	0.25	0.03	4295	232.4

Continued on next page

Continuation of Table A.7: Two phase flow measurement of Ethane-27

G [kg/m^{2}s]	p_m [bar]	$(dp/dz)_f$ [kPa/m]	q'' [kW/m^2]	T_{out} [°C]	T_{in} [°C]	T_w [°C]	x_{in} [-]	Δx [-]	$\bar{h}$ [W/m^{2}K]	$\delta\bar{h}$ [W/m^{2}K]
203	10.2	40	17.2	-102.64	-100.35	-104.60	0.57	0.04	5538	361.6
209	9.9	55	17.3	-87.81	-85.56	-89.82	0.73	0.04	5526	357.7
203	9.9	58	18.2	-81.25	-79.15	-83.60	0.81	0.04	5367	324.1
280	10.3	28.9	0.4	-113.75	-113.08	-113.42	0.20	0.00	-	-
268	10.2	28.0	0.2	-113.55	-112.81	-113.18	0.22	0.00	-	-
282	10.0	43	0.1	-111.60	-111.48	-111.45	0.34	0.00	-	-
274	9.9	63	0.1	-105.66	-105.44	-105.46	0.50	0.00	-	-
275	9.9	81	0.2	-96.32	-96.07	-96.06	0.62	0.00	-	-
280	9.9	96	-0.2	-86.78	-86.49	-86.49	0.72	0.00	-	-
282	10.0	103	0.1	-78.44	-78.15	-78.07	0.81	0.00	-	-
282	9.6	105	0.7	-71.52	-71.17	-71.18	0.92	0.00	-	-
283	9.6	110	6.6	-72.17	-71.51	-72.43	0.91	0.01	11291	3632.8
278	9.8	100	11.4	-71.08	-70.19	-71.87	0.93	0.02	9205	1425.9
278	9.8	101	15.9	-71.44	-70.31	-72.69	0.93	0.03	8749	929.6
279	9.7	104	20.6	-72.12	-70.73	-73.85	0.92	0.04	8449	674.8
278	9.7	105	26.0	-72.55	-70.86	-74.89	0.92	0.05	8169	505.9
279	9.6	68	18.5	-106.33	-104.56	-107.95	0.53	0.03	7404	579.7
280	9.7	70	13.0	-105.93	-104.56	-107.06	0.53	0.02	7209	774.8
279	9.6	64	8.4	-105.48	-104.55	-106.03	0.53	0.01	8227	1550.3
281	9.7	72	3.4	-105.00	-104.46	-105.11	0.53	0.01	8792	4350.6
278	9.8	33.6	4.4	-114.52	-114.09	-114.98	0.25	0.01	6569	1908.5
279	9.8	33.0	8.3	-114.86	-114.24	-115.91	0.25	0.01	6077	876.5
281	9.7	32.2	13.5	-115.30	-114.40	-117.16	0.25	0.02	5870	505.7
281	9.7	32.3	17.0	-115.56	-114.47	-117.97	0.24	0.02	5767	391.9
491	26.1	23.8	26.2	-86.03	-84.64	-89.90	0.14	0.03	5757	261.5
486	26.2	31.8	26.0	-83.55	-82.28	-86.98	0.24	0.03	6394	319.4
487	26.3	47	26.3	-80.68	-79.51	-83.63	0.34	0.03	7454	420.2
488	26.1	73	26.1	-74.11	-72.79	-76.52	0.51	0.03	8505	543.5
493	25.9	92	26.6	-65.66	-64.23	-67.93	0.66	0.03	8909	582.8
487	25.8	100	26.5	-54.81	-53.55	-57.11	0.82	0.03	9068	604.6
486	25.7	103	26.1	-50.74	-49.62	-52.84	0.88	0.04	9809	717.5
558	25.8	126	26.1	-56.34	-55.20	-58.55	0.79	0.03	9375	656.5
557	26.1	88	26.4	-74.75	-73.57	-77.09	0.49	0.02	9011	601.7
553	26.2	63	26.8	-80.12	-79.14	-82.91	0.35	0.02	8166	490.1
557	26.2	25.6	26.8	-86.48	-85.12	-90.32	0.11	0.02	5925	270.6
680	26.2	42	26.1	-85.70	-84.79	-88.90	0.13	0.02	7152	391.4
683	26.1	95	26.0	-80.44	-79.63	-82.75	0.34	0.02	9592	685.9
686	25.9	132	26.4	-74.26	-73.18	-76.28	0.51	0.02	10315	778.3
675	25.7	170	26.9	-57.56	-56.48	-59.63	0.77	0.02	10284	760.3
144	35.7	1.2	6.5	-73.21	-71.92	-75.92	0.11	0.02	1927	151.6
140	36.1	0.3	6.2	-70.42	-69.29	-73.02	0.22	0.02	1970	162.3
143	36.2	0.0	6.6	-68.20	-67.06	-70.68	0.29	0.02	2153	177.4
144	36.1	1.5	6.3	-61.73	-60.44	-63.71	0.48	0.03	2396	218.7
145	35.8	3.2	6.4	-54.50	-53.41	-56.35	0.63	0.03	2659	255.7
145	35.6	1.9	6.4	-44.06	-43.09	-45.71	0.82	0.04	2996	311.6
148	35.6	3.5	17.0	-46.61	-44.17	-50.63	0.80	0.09	3251	142.3
144	35.6	1.3	17.1	-64.37	-61.30	-69.25	0.48	0.07	2666	102.4
149	34.9	1.7	16.9	-74.89	-72.67	-80.34	0.23	0.06	2581	98.3
495	35.0	23.7	12.2	-74.06	-73.57	-75.92	0.18	0.01	5789	544.0
489	35.3	44	12.2	-65.30	-64.74	-66.80	0.47	0.01	6817	745.6
498	33.9	74	11.5	-45.76	-45.24	-46.84	0.86	0.02	8561	1229.2
490	41.1	17.7	12.7	-67.80	-67.24	-69.77	0.15	0.01	5647	499.4
496	41.2	35.7	11.8	-59.08	-58.58	-60.63	0.47	0.01	6544	710.7
487	41.0	52	11.7	-41.23	-40.69	-42.56	0.86	0.02	7294	883.0
491	7.7	56	13.0	-122.72	-118.58	-123.82	0.11	0.01	4077	270.7
484	7.9	100	13.3	-120.53	-118.71	-121.38	0.22	0.01	7529	841.3
495	7.4	174	13.0	-119.84	-118.87	-120.47	0.36	0.01	11665	1984.4
494	7.1	260	12.8	-114.44	-113.02	-114.81	0.52	0.01	11837	2083.1
489	6.7	366	12.6	-103.64	-101.83	-103.83	0.67	0.01	11454	1974.4
493	6.5	431	13.0	-91.58	-89.72	-91.79	0.79	0.01	11330	1879.8
281	7.1	147	12.4	-89.15	-87.71	-90.11	0.79	0.02	7382	850.2
280	7.2	89	13.1	-114.71	-113.29	-115.77	0.52	0.02	7426	814.3
281	7.4	37.1	12.8	-122.91	-122.03	-124.80	0.20	0.02	5482	475.3
0.5 mm tube measurements										
522	12.9	193	51.9	-109.95	-103.80	-112.32	0.29	0.08	9531	303
517	13.0	203	24.0	-107.83	-105.40	-108.93	0.30	0.04	10384	862

Continued on next page

Continuation of Table A.7: Two phase flow measurement of Ethane-27

G [kg/m^{2}s]	p_m [bar]	$(dp/dz)_f$ [kPa/m]	q'' [kW/m^2]	T_{out} [°C]	T_{in} [°C]	T_w [°C]	x_{in} [-]	Δx [-]	$\overline{h}$ [W/m^{2}K]	$\delta\overline{h}$ [W/m^{2}K]
512	13.1	205	9.8	-106.58	-105.19	-106.97	0.30	0.02	8984	1587
517	13.1	213	2.5	-105.98	-105.15	-105.99	0.30	0.00	5855	2861
536	12.8	394	51.0	-102.69	-97.01	-103.91	0.51	0.08	12561	609
526	12.9	414	23.6	-98.97	-95.75	-99.27	0.52	0.04	12336	1213
526	12.9	416	9.6	-97.48	-95.55	-97.42	0.53	0.02	10690	2230
514	13.1	416	2.6	-95.45	-94.28	-95.14	0.54	0.00	9619	6684
529	12.7	691	50.7	-76.68	-71.41	-76.88	0.79	0.09	17866	1186
526	12.8	675	24.1	-74.10	-70.99	-73.74	0.80	0.04	20275	3112
513	12.8	660	13.8	-72.05	-69.86	-71.52	0.81	0.03	24606	7909
528	12.8	644	9.8	-72.78	-70.77	-72.09	0.80	0.02	31599	18378
1116	26.6	336	28.0	-86.59	-85.39	-87.63	0.13	0.02	17153	1926
1088	26.7	468	28.1	-82.39	-80.67	-83.01	0.33	0.02	19010	2343
1094	25.6	830	27.6	-74.62	-72.53	-74.79	0.55	0.02	22706	3396
1089	25.5	965	28.1	-66.97	-64.64	-66.93	0.67	0.03	25023	1240
1132	25.3	1285	25.5	-59.94	-57.71	-59.27	0.77	0.03	56724	23938
477	26.2	236	19.5	-55.19	-53.22	-55.51	0.81	0.05	14962	2195
492	26.1	195	19.2	-70.22	-67.94	-70.80	0.60	0.04	11197	1245
499	25.9	121	20.9	-81.85	-79.35	-82.87	0.38	0.04	9221	788
496	25.9	74	20.2	-87.27	-85.53	-88.94	0.17	0.04	7956	624
693	26.3	126	22.4	-87.47	-86.06	-88.91	0.12	0.03	10443	930
691	26.6	240	22.8	-80.33	-78.44	-81.04	0.39	0.03	13748	1540
694	26.8	363	22.2	-69.74	-67.92	-70.03	0.59	0.03	18546	2822
689	26.5	513	23.1	-53.03	-51.21	-52.99	0.84	0.04	26645	5524
0.25 mm tube measurements										
1131	26.00	770	35.2	-87.36	-82.19	-88.00	0.23	0.055	10931	641.2
1164	25.57	1040	28.1	-81.90	-77.57	-81.95	0.39	0.044	12715	1031.9
1093	25.62	1326	29.3	-70.18	-66.40	-69.39	0.58	0.054	26753	3927.4
1153	25.10	2187	28.4	-57.05	-52.70	-55.59	0.76	0.059	40004	8865.9

Table A.8: Two phase flow measurement of Ethane-27

A.2.4 Nitrogen-10

G [kg/m^{2}s]	p_m [bar]	$(dp/dz)_f$ [kPa/m]	q'' [kW/m^2]	T_{out} [°C]	T_{in} [°C]	T_w [°C]	x_{in} [-]	Δx [-]	$\overline{h}$ [W/m^{2}K]	$\delta\overline{h}$ [W/m^{2}K]
1.0 mm tube measurements										
485	7.3	108	-0.1	-138.15	-137.73	-137.94	0.20	0.00	-	-
497	7.2	181	-0.2	-136.88	-136.21	-136.52	0.32	0.00	-	-
496	7.2	216	-0.3	-136.30	-135.52	-135.88	0.39	0.00	-	-
501	7.2	311	-0.1	-135.38	-134.27	-134.81	0.64	0.00	-	-
495	7.0	73	0.0	-140.15	-139.84	-140.00	0.13	0.00	-	-
283	7.1	18	13.0	-141.22	-140.16	-143.69	0.11	0.02	4339	250
275	6.7	40	12.8	-137.52	-136.95	-139.17	0.26	0.02	6594	499
282	6.9	71	12.7	-135.73	-135.24	-136.86	0.41	0.02	9282	861
280	7.0	88	12.4	-134.92	-134.43	-135.80	0.53	0.02	11070	1155
278	7.1	98	12.4	-134.31	-133.82	-135.05	0.68	0.02	12678	1416
281	7.2	104	12.6	-133.99	-133.49	-134.60	0.79	0.02	14640	1722
494	6.9	326	12.8	-135.38	-134.18	-135.34	0.81	0.01	22904	3086
499	6.8	314	12.6	-136.03	-134.84	-136.10	0.63	0.01	18962	2456
490	6.8	208	12.6	-136.78	-135.92	-137.23	0.38	0.01	14315	1663
484	6.8	116	12.8	-138.13	-137.47	-139.04	0.23	0.01	10336	1008
484	26.3	27	26.4	-108.81	-107.97	-112.60	0.14	0.04	6256	232
494	26.0	38	26.4	-107.44	-106.95	-110.81	0.26	0.04	7293	294
487	26.1	44	26.3	-106.30	-105.91	-109.36	0.38	0.04	8085	346
487	26.2	48	26.0	-105.52	-105.19	-108.26	0.50	0.04	8961	409
483	26.3	55	26.2	-104.58	-104.30	-106.89	0.69	0.04	10728	533
493	26.3	66	26.5	-104.06	-103.79	-106.07	0.82	0.04	12332	649
563	26.4	83	26.4	-104.01	-103.73	-105.80	0.81	0.03	13668	755
567	26.2	68	25.8	-104.79	-104.51	-106.86	0.63	0.03	11653	613
559	26.0	56	25.8	-105.85	-105.51	-108.37	0.45	0.03	9588	456
558	25.9	47	25.7	-107.11	-106.70	-109.95	0.30	0.03	8439	377
562	26.2	34	26.1	-108.78	-108.11	-112.09	0.15	0.03	7162	289
689	26.3	48	26.5	-108.68	-108.13	-111.63	0.14	0.03	8229	353
681	26.4	69	26.1	-106.35	-105.99	-108.77	0.35	0.03	10010	483
682	26.4	90	25.7	-104.90	-104.61	-106.71	0.60	0.03	13126	732

Continued on next page

Continuation of Table A.9: Two phase flow measurement of Nitrogen-10

G [kg/m^{2}s]	p_m [bar]	$(dp/dz)_f$ [kPa/m]	q'' [kW/m^2]	T_{out} [°C]	T_{in} [°C]	T_w [°C]	x_{in} [-]	Δx [-]	$\bar{h}$ [W/m^{2}K]	$\delta\bar{h}$ [W/m^{2}K]
688	26.2	119	25.9	-104.34	-104.04	-105.80	0.80	0.03	16151	973
280	26.4	22.2	25.7	-103.99	-103.69	-107.01	0.81	0.07	8088	354
284	26.3	17.9	25.5	-105.74	-105.28	-109.76	0.46	0.06	6000	224
277	26.1	8.5	26.5	-109.14	-107.72	-114.72	0.18	0.06	4203	126
276	26.4	9.5	12.9	-108.42	-107.66	-111.12	0.15	0.03	4177	238
279	26.4	12.0	13.0	-107.14	-106.63	-109.61	0.25	0.03	4768	291
275	26.2	16.1	12.0	-106.07	-105.77	-108.19	0.39	0.03	5284	370
280	26.4	20.0	12.8	-104.86	-104.63	-106.70	0.56	0.03	6555	492
277	26.3	21.4	12.9	-104.34	-104.14	-106.00	0.69	0.03	7280	580
280	26.2	22.5	12.6	-103.95	-103.76	-105.40	0.81	0.03	8170	709
493	36.2	22.0	5.9	-98.04	-97.87	-98.75	0.18	0.01	7503	1302
494	36.2	21.9	12.6	-98.20	-97.93	-99.82	0.18	0.02	7151	577
493	36.3	21.1	26.3	-98.56	-98.03	-102.20	0.17	0.05	6740	261
487	36.3	26.7	25.8	-96.46	-96.16	-99.55	0.47	0.05	7963	344
494	36.4	27.0	12.6	-96.26	-96.08	-97.68	0.47	0.02	8326	734
487	36.4	26.6	6.4	-96.13	-96.00	-96.80	0.48	0.01	8656	1529
491	36.5	26.7	3.2	-96.07	-95.97	-96.33	0.48	0.01	10358	4060
493	36.5	36.6	3.3	-94.56	-94.49	-94.68	0.81	0.01	21086	10652
490	36.5	37.4	2.9	-94.92	-94.81	-95.05	0.81	0.01	15909	8398
495	36.5	37.5	6.4	-94.98	-94.85	-95.44	0.81	0.01	12350	2611
492	36.3	36.9	12.7	-94.70	-94.55	-95.86	0.82	0.03	10313	1016
484	36.2	35.7	25.9	-94.92	-94.70	-97.34	0.81	0.05	10199	500
485	42.6	25.7	13.8	-90.23	-90.11	-91.21	0.86	0.11	13264	1365
497	42.5	22.4	14.0	-90.62	-90.50	-91.86	0.70	0.07	10838	989
493	42.4	19.9	13.7	-91.01	-90.88	-92.40	0.59	0.04	9376	813
490	42.2	18.3	13.6	-91.66	-91.51	-93.24	0.44	0.03	8239	667
488	42.1	17.9	13.6	-92.27	-92.10	-93.88	0.30	0.03	8059	641
494	42.1	17.7	13.7	-92.83	-92.64	-94.45	0.18	0.03	7966	628
203	41.6	3.5	14.0	-90.93	-90.72	-93.57	0.87	0.09	5093	300
192	41.5	2.9	13.6	-91.38	-91.15	-94.21	0.73	0.09	4630	263
191	41.4	2.8	13.6	-92.10	-91.81	-95.14	0.52	0.09	4273	232
192	41.3	2.8	13.6	-92.78	-92.40	-95.88	0.36	0.08	4111	219
196	41.3	2.0	13.6	-94.13	-93.33	-97.41	0.17	0.07	3688	184

Table A.9: Two phase flow measurement of Nitrogen-10

Appendix B

Models for heat transfer and pressure drop

B.1 Condensation heat transfer models

B.1.1 The correlation from Traviss (1973)

Traviss et al. [69] developed the following relation for the local heat transfer coefficient for annular-flow convective condensation:

$$Nu = \frac{0.15 Pr_{\mathrm{l}} Re_{\mathrm{l}}^{0.9}}{F_T} \left[\frac{1}{X_{tt}} + \frac{2.85}{X_{tt}^{0.476}} \right] \tag{B.1.1}$$

where the Martinelli-parameter X_{tt} is given by

$$X_{tt} = \left(\frac{1-x}{x} \right)^{0.9} \left(\frac{\rho_{\mathrm{v}}}{\rho_{\mathrm{l}}} \right)^{0.5} \left(\frac{\mu_{\mathrm{l}}}{\mu_{\mathrm{v}}} \right)^{0.1} \tag{B.1.2}$$

$$F_T = 5 Pr_{\mathrm{l}} + 5 ln\left(1 + 5 Pr_{\mathrm{l}}\right) + 2.5 ln\left(0.0031 Re_{\mathrm{l}}^{0.812}\right) \tag{B.1.3}$$

for $Re_{\mathrm{l}} > 1125$. Other expressions for F_T are available for lower Reynold numbers. The Reynolds number for the liquid part of a two-phase flow is given by

$$Re_{\mathrm{l}} = \frac{G\left(1-x\right) d_{\mathrm{h}}}{\mu_{\mathrm{l}}} \tag{B.1.4}$$

B.1.2 The work of Moser and Webb (1998)

Moser and Webb [52] improved the correlation by Akers el at. [3] by finding a new equivalent Reynolds number based on the heat-momentum analogy. Akers' correlation is based on annular flow with a vapour core at higher velocities. It is assumed that the vapour core will produce the same liquid-vapour interface shear stress as if the vapour core would have been liquid, expressed by an equivalent Reynolds number Re_{eq}. Moser and Webb believed that the Akers' correlation is inaccurate for two reasons:

- The driving temperature difference of single phase $(T_b - T_{\mathrm{w}})$ and two-phase flow $(T_{\mathrm{sat}} - T_{\mathrm{w}})$ are different.
- The friction factors f_{v} and f_{l} are not equal.

They came to the following correlation:

$$Nu = \frac{hd_{\mathrm{h}}}{k_{\mathrm{l}}} = \frac{0.0994^{C_1} Re_{\mathrm{l}}^{C_2} Re_{\mathrm{eq}}^{1+0.875C_1} Pr_{\mathrm{l}}^{0.815}}{(1.58 ln Re_{\mathrm{eq}} - 3.28)\left(2.58 ln Re_{\mathrm{eq}} + 13.7 Pr_{\mathrm{l}}^{2/3} - 19.1\right)} \tag{B.1.5}$$

where $C_1 = 0.126 Pr_{\mathrm{l}}^{-0.448}$ and $C_2 = -0.113 Pr_{\mathrm{l}}^{-0.563}$. The equivalent Reynolds number is expressed by

$$Re_{\mathrm{eq}} = \Phi_{lo}^{8/7} Re_{lo} \tag{B.1.6}$$

where Φ_{lo} is the two-phase multiplier developed by Friedel [25] and the subscript lo denotes the flow as if it would have been in liquid form.

Using this model, Moser and Webb predicted the Nusselt number for 1197 data points from 18 sources, and found that the mean absolute deviation was (13.6%), which is slightly better than the correlation from Shah [62] (14.3%) and more accurate than the correlation from Traviss [69] (20.0%). The tube diameters tested ranged from 3.14 to 20 mm. Fluids used were mostly R-22, but also R-12, R-113, R-134a and R-410a.

B.1.3 Thome et al. (2003)

The roughness factor is found by

$$f_i = 1 + \left(\frac{u_{\mathrm{v}}}{u_{\mathrm{l}}}\right)^{1/2} \left[\frac{(\rho_{\mathrm{l}} - \rho_{\mathrm{v}})\, g\delta^2}{\sigma}\right]^{1/4} \tag{B.1.7}$$

Here u_v and u_l are the phase velocities for vapour and liquid respectively which are found from Equation B.1.8. σ denotes the surface tension and ε the void fraction.

$$u_\mathrm{l} = \frac{G\,(1-x)}{\rho_\mathrm{l}\,(1-\varepsilon)}, u_\mathrm{v} = \frac{Gx}{\rho_\mathrm{v}\varepsilon} \tag{B.1.8}$$

The Reynolds number Re_l is based on the film thickness δ and is defined as

$$Re_\mathrm{l} = \frac{4G\,(1-x)\,\delta}{(1-\varepsilon)\,\mu_\mathrm{l}} \tag{B.1.9}$$

In order to find the film thickness δ, Equation B.1.10 needs to be solved for δ:

$$A_\mathrm{l} = \frac{\pi}{4}\left[d^2 - (d-2\delta)^2\right] \tag{B.1.10}$$

where A_l is the cross-sectional area covered by liquid and A is the tube cross-sectional area. This can be found by solving Equation B.1.11:

$$A_\mathrm{l} = (1-\varepsilon)\,A \tag{B.1.11}$$

which results in

$$\delta = \frac{d}{2} - \frac{\sqrt{\varepsilon d^2}}{2} \tag{B.1.12}$$

The void fraction ε is the ratio of the cross-sectional area occupied by vapour to the total cross-section in a tube. The void fraction is the foremost parameter in determining two-phase flow pattern transitions, two-phase heat transfer coefficients and two-phase pressure drop. Hence, knowing this parameter is vital.

El Hajal and coworkers [24] worked together with Thome et al. [68] and introduced a new way to find the void fraction ε.

The homogeneous void fraction model in Equation B.1.13 assumes that the vapour and liquid phases travel at the same velocity. This approach is applicable at high reduced pressure, where the densities of the two phases are not that different, and at mist/dispersed flow where the phases are well mixed.

$$\varepsilon_\mathrm{h} = \left[1 + \left(\frac{1-x}{x}\right)\left(\frac{\rho_\mathrm{v}}{\rho_\mathrm{l}}\right)\right]^{-1} \tag{B.1.13}$$

For non-homogeneous flow, where $u_\mathrm{v} \gg u_\mathrm{l}$, El Hajal et al. chose the drift flux model for horizontal tubes from Steiner [66]. His model is originally

based on a vertical model from Rouhani and Axelsson:

$$\varepsilon_{\mathrm{ra}} = \frac{x}{\rho_{\mathrm{v}}}\left(\left[1+0.12\,(1-x)\right]\left[\frac{x}{\rho_{\mathrm{v}}}+\frac{1-x}{\rho_{\mathrm{l}}}\right]+\frac{1.18\,(1-x)\left[g\sigma\,(\rho_{\mathrm{l}}-\rho_{\mathrm{v}})\right]^{0.25}}{G\rho_{\mathrm{l}}^{0.5}}\right)^{-1} \tag{B.1.14}$$

In order to make a void fraction model that is valid both for pressures near the critical pressure (where $\rho_{\mathrm{v}} \rightarrow \rho_{\mathrm{l}}$) and for low pressure (where $\rho_{\mathrm{l}} >> \rho_{\mathrm{v}}$), El Hajal et al. combined these two void fraction models in the following way:

$$\varepsilon = \frac{\varepsilon_{\mathrm{h}} - \varepsilon_{\mathrm{ra}}}{ln\,(\varepsilon_{\mathrm{h}}/\varepsilon_{\mathrm{ra}})} \tag{B.1.15}$$

which they called the logarithmic mean void fraction LMε. This new value of ε improved the heat transfer correlation given in Equation 2.13.

B.2 Basis for binary condensation heat transfer

Referring to Figure 2.10, the heat flux from the cooling of the mixture vapour down to interface temperature can be expressed as

$$q''_{\mathrm{v}} = h_{\mathrm{v}}(T_{\mathrm{v,bulk}} - T_{\mathrm{i}}) \tag{B.2.1}$$

The total heat flux through the film, which is assumed to behave as single component condensation, can be expressed as

$$q''_{\mathrm{mc}} = h_{\mathrm{sc}}(T_{\mathrm{i}} - T_{\mathrm{w}}) \tag{B.2.2}$$

Equations B.2.1 and B.2.2 can be solved for q''_{mc}:

$$q''_{\mathrm{mc}} = \left[\frac{1}{h_{\mathrm{sc}}} + \left(\frac{q''_{\mathrm{v}}}{q''_{\mathrm{mc}}}\right)\frac{1}{h_{\mathrm{v}}}\right]^{-1}(T_{\mathrm{v,bulk}} - T_{\mathrm{w}}) \tag{B.2.3}$$

Further, if the total heat flux is expressed across the total temperature span as

$$q''_{\mathrm{mc}} = h_{\mathrm{mc}}(T_{\mathrm{v,bulk}} - T_{\mathrm{w}}) \tag{B.2.4}$$

$q''_{\mathrm{mc}}/(T_{\mathrm{v,bulk}} - T_{\mathrm{w}})$ can be eliminated from Equations B.2.3 and B.2.4 which yields

$$\frac{1}{h_{\mathrm{mc}}} = \frac{1}{h_{\mathrm{sc}}} + \left(\frac{q''_{\mathrm{v}}}{q''_{\mathrm{mc}}}\right)\frac{1}{h_{\mathrm{v}}} \tag{B.2.5}$$

B.3 Pressure drop models

B.3.1 Conventional channels

The correlation from Friedel (1979/1980)

The correlation from Friedel [26] use a two-phase multiplier based on the total flow occurring as a liquid only, and is given as follows:

$$\Phi_{\mathrm{lo}}^2 = E + \frac{3.24 \cdot F \cdot H}{Fr^{0.045} We^{0.035}} \tag{B.3.1}$$

It takes into account the dimensionless Weber-number We and the Froude number Fr. They express the momentum forces in relation to surface tension forces and gravitational forces respectively:

$$We = \frac{G^2 d}{\rho_{2\mathrm{ph}} \sigma} \tag{B.3.2}$$

$$Fr = \frac{G^2}{\rho_{2\mathrm{ph}}^2 g d} \tag{B.3.3}$$

The two-phase mixture density $\rho_{2\mathrm{ph}}$ found by Equation B.3.4:

$$\rho_{2ph} = \left(\frac{x}{\rho_{\mathrm{v}}} + \frac{1-x}{\rho_{\mathrm{l}}} \right)^{-1} \tag{B.3.4}$$

E is found by the following expression:

$$E = (1-x)^2 + x^2 \frac{\rho_{\mathrm{l}} f_{\mathrm{vo}}}{\rho_{\mathrm{v}} f_{\mathrm{lo}}} \tag{B.3.5}$$

where f_{vo} and f_{lo} are the friction factors for the flow occurring as vapour only and liquid only. These can be found from the Moody-diagram or from various correlations.

F is given by

$$F = x^{0.78} (1-x)^{0.24} \tag{B.3.6}$$

and H is given by

$$H = \left(\frac{\rho_{\mathrm{l}}}{\rho_{\mathrm{v}}} \right)^{0.91} \left(\frac{\mu_{\mathrm{v}}}{\mu_{\mathrm{l}}} \right)^{0.19} \left(1 - \frac{\mu_{\mathrm{v}}}{\mu_{\mathrm{l}}} \right)^{0.7} \tag{B.3.7}$$

B.3.2 Work on pressure drop in mini- and microchannels

Kandlikar et al. [35] give a good review of flow, heat transfer and pressure drop models for adiabatic and condensation flow in channels.

The work of Garimella (2005)

Garimella et al. [27] have in a series of articles developed experimentally validated models for pressure drop during condensation of R-134a for several flow regimes in circular and non-circular minichannels. Their comprehensive model covers the annular, disperes wave, mist, discrete wave and intermittent flow regimes. It is reported valid for $150 < G < 750$ kg/m^{2}s and for diameters in the range $0.5 < d < 4.9$ mm.

It is based on Equation 2.37 where the friction factor f is modified to take two-phase flow effects into account. For the vapour core flowing through the liquid annulus, the pressure drop is given as:

$$\left(\frac{\mathrm{d}p}{\mathrm{d}z}\right)_{\mathrm{f,2ph}} = \frac{1}{2} \cdot f_{\mathrm{i}} \frac{G^2 x^2}{\rho_{\mathrm{v}} \varepsilon^{2.5}} \frac{1}{d} \tag{B.3.8}$$

where ε takes into account the liquid layer thickness. The interface friction factor f_{i} takes into the interfacial friction at the liquid/vapour interface as well as the friction between the liquid and tube wall:

$$f_{\mathrm{i}} = f_{\mathrm{l}} \cdot A X^a {Re_{\mathrm{l}}}^b \psi^c \tag{B.3.9}$$

Here, X is the Martinelli parameter defined in Equation B.3.10, ψ takes surface tension effects into account in Equation B.3.11 and the liquid Re-number is found from Equation B.3.12.

$$X = \left[\frac{(\mathrm{d}p/\mathrm{d}z)_{\mathrm{l}}}{(\mathrm{d}p/\mathrm{d}z)_{\mathrm{v}}}\right]^{1/2} \tag{B.3.10}$$

To take surface tension effects into account, a dimensionless parameter was used:

$$\psi = \frac{j_{\mathrm{l}} \mu_{\mathrm{l}}}{\sigma} \tag{B.3.11}$$

where $j_{\mathrm{l}} = \frac{G(1-x)}{\rho_{\mathrm{l}}(1-\varepsilon)}$ is the superficial velocity of the liquid. For calculating the single phase liquid and vapour phase pressure drop, the following Re-numbers are used:

$$Re_{\mathrm{l}} = \frac{Gd(1-x)}{\mu_{\mathrm{l}}(1+\sqrt{\varepsilon})} \tag{B.3.12}$$

$$Re_{\mathrm{v}} = \frac{Gdx}{\mu_{\mathrm{v}}\sqrt{\varepsilon}} \tag{B.3.13}$$

The parameters A, a, b and c in Equation B.3.9 were found by regression. This model predicted 87% of the measurements by Garimella et al. within ±20%. All though smaller than the liquid/vapour interface shear, the liquid/surface shear caused by tube roughness wall must be accounted for also in two-phase flow. This is done in Garimella et al.'s correlation as the friction factor f_{l} for liquid is included.

Nino (2002)

Niño [55] developed a frictional pressure drop correlation for annular flow that he implemented in his probabilistic flow mapping pressure drop correlation. It employs an two-phase multiplier approach which is multiplied with the vapour only pressure drop correlation where Φ^2_{vo} is experimentally determined and given as

$$\Phi^2_{\mathrm{vo}} = e^{-0.046X_{\mathrm{ann}}} + 0.22(e^{-0.02X_{\mathrm{ann}}} - e^{-7X_{\mathrm{ann}}}) \tag{B.3.14}$$

and

$$X_{\mathrm{ann}} = \left(X_{tt} + \frac{1}{We_{\mathrm{v}}^{1.3}}\right)\left(\frac{\rho_{\mathrm{l}}}{\rho_{\mathrm{v}}}\right)^{0.9} \tag{B.3.15}$$

and the Weber number of the vapour part of the two-phase flow:

$$We_{\mathrm{v}} = \frac{(xG)^2 d}{\rho_v \sigma} \tag{B.3.16}$$

where

$$X_{tt} = \left(\frac{1-x}{x}\right)^{0.875}\left(\frac{\rho_{\mathrm{v}}}{\rho_{\mathrm{l}}}\right)^{0.5}\left(\frac{\mu_{\mathrm{l}}}{\mu_{\mathrm{v}}}\right)^{0.125} \tag{B.3.17}$$

which is the Martinelli-parameter in Equation B.1.2. For the single phase vapour pressure drop multiplied with Equation B.3.14, Niño used the single phase pressure drop given in Equation 2.37.

Cavallini et al. (2006)

Cavallini et al. [11] interpolated the pressure drop measurements from Zhang [76], Coleman [21] and Cavallini et al. [8] and obtained an equation for this presented in Cavallini et al. [9] and [12]:

$$\left(\frac{\mathrm{d}p}{\mathrm{d}z}\right)_{\mathrm{f,2ph}} = \Phi^2_{\mathrm{lo}}\left(\frac{\mathrm{d}p}{\mathrm{d}z}\right)_{\mathrm{f,lo}} = \Phi^2_{\mathrm{lo}} f_{\mathrm{lo}} \frac{2G^2}{\rho_{\mathrm{l}} d_{\mathrm{h}}} \tag{B.3.18}$$

The two phase flow multiplier is defined as

$$\Phi_{\mathrm{lo}}^2 = Z + 3.595FH(1-E)^W \qquad \text{where } W = 1.398p_{\mathrm{r}} \tag{B.3.19}$$

and

$$Z = (1-x)^2 + x^2(\rho_{\mathrm{l}}/\rho_{\mathrm{v}})(\mu_{\mathrm{v}}/\mu_{\mathrm{l}})^{0.2} \tag{B.3.20}$$

$$F = x^{0.9525}(1-x)^{0.414} \tag{B.3.21}$$

$$H = \left(\frac{\rho_{\mathrm{l}}}{\rho_{\mathrm{v}}}\right)^{1.132}\left(\frac{\mu_{\mathrm{v}}}{\mu_{\mathrm{l}}}\right)^{0.44}\left(1-\frac{\mu_{\mathrm{v}}}{\mu_{\mathrm{l}}}\right)^{3.542} \tag{B.3.22}$$

The entrainment factor is defined in Equation 2.26 and 2.27.

B.3.3 Pressure drop due to geometry changes

Kandlikar et al. [35] reports that the following equation can be used when calculating the pressure loss for two-phase flow due to a contraction:

$$\Delta p_{\mathrm{inlet}} = \frac{G^2}{2\rho_{\mathrm{l}}}\left[\left(\frac{1}{C_0}-1\right)^2 + 1 - \frac{1}{\sigma_c^2}\right]\Psi_{\mathrm{h}} \tag{B.3.23}$$

where σ_{c} is the contraction area ratio ($\sigma_c > 1$) and C_0 a contraction coefficient given by:

$$C_0 = \frac{1}{0.639(1-1/\sigma_{\mathrm{c}})^{0.5}+1} \tag{B.3.24}$$

and Ψ_{h} a two-phase flow multiplier:

$$\Psi_{\mathrm{h}} = [1 + x(\rho_l/\rho_v - 1)] \tag{B.3.25}$$

The pressure loss for a sudden expansion is reported by Kandlikar et al. [35]:

$$\Delta p_{\mathrm{outlet}} = G^2\sigma_e(1-\sigma_e)\Psi_s \tag{B.3.26}$$

where σ_{e} is the contraction area ratio ($\sigma_e < 1$) and Ψ_{s} a flow ultiplier:

$$\Psi_{\mathrm{s}} = 1 + \left(\frac{\rho_l}{\rho_v} - 1\right)[0.25x(1-x) + x^2] \tag{B.3.27}$$

Appendix C

Overview over measurements

C.1 Overview over measurements

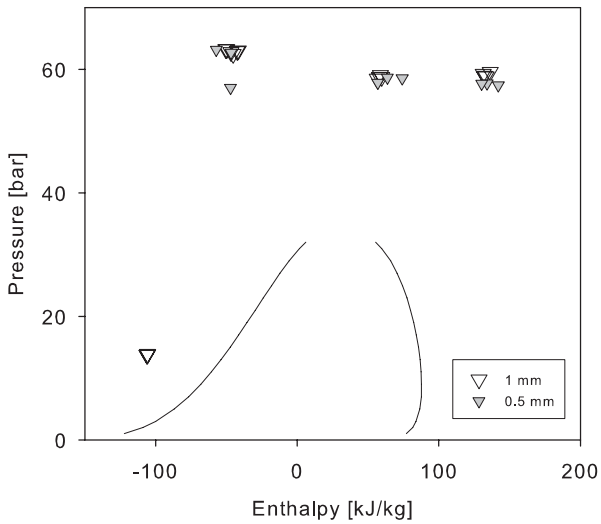

Figure C.1: Overview over two-phase flow measurements for Nitrogen-100, pressure p versus enthalpy e.

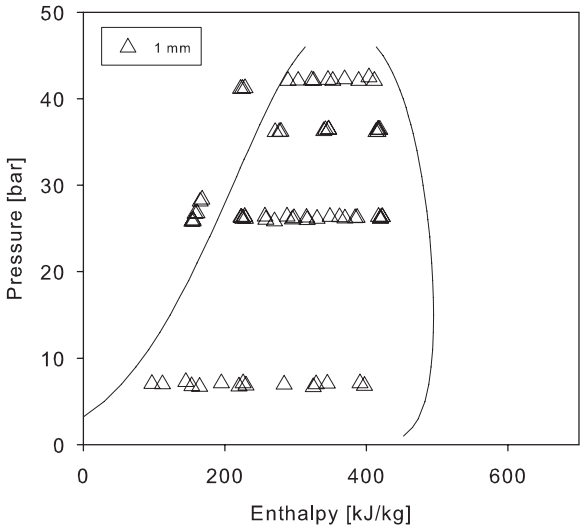

Figure C.2: Overview over two-phase flow measurements for Nitrogen-10, pressure p versus enthalpy e.

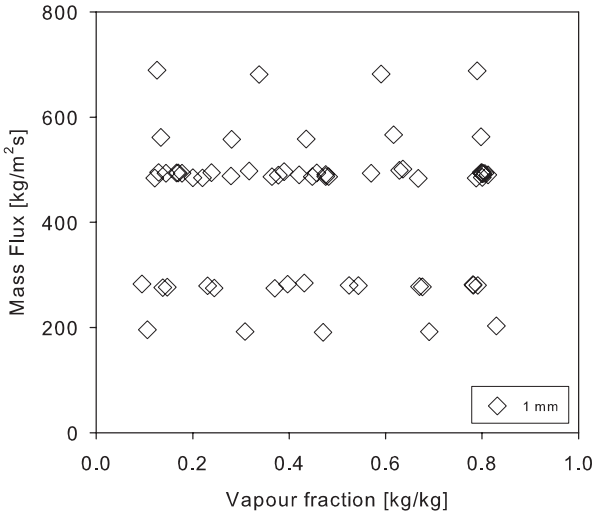

Figure C.3: Overview over measurements for Nitrogen-10, mass flux G versus vapour fraction x.

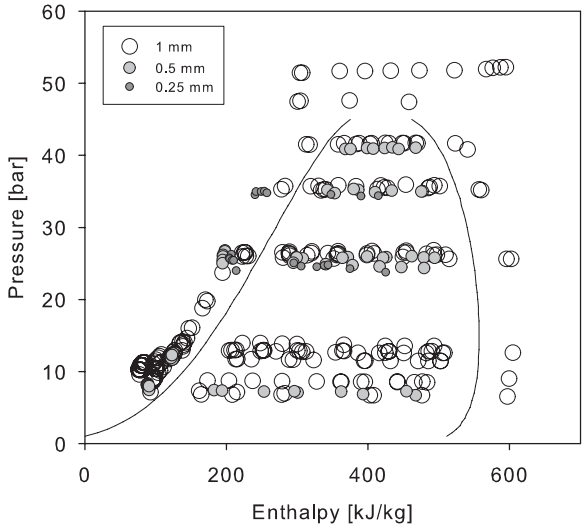

Figure C.4: Overview over two-phase flow measurements for Methane-100, pressure p versus enthalpy e.

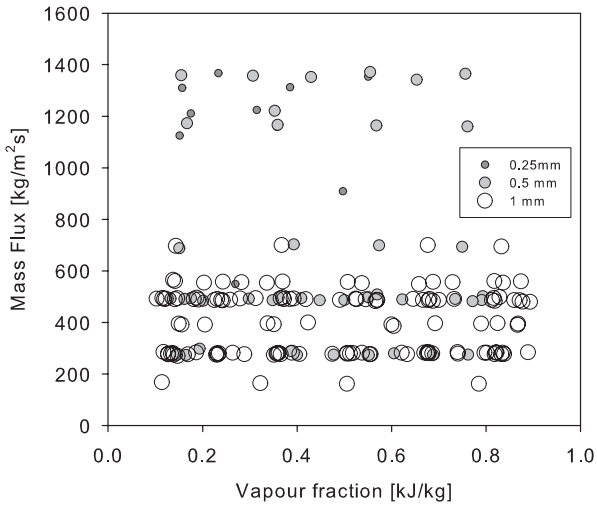

Figure C.5: Overview over measurements for Methane-100, mass flux G versus vapour fraction x.

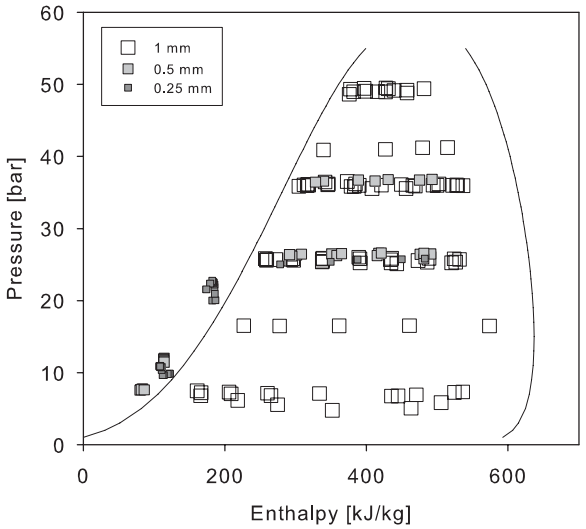

Figure C.6: Overview over two-phase flow measurements for Ethane-10, pressure p versus enthalpy e.

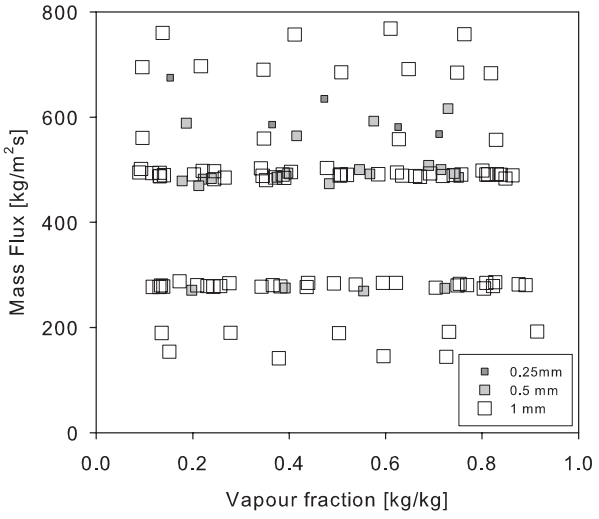

Figure C.7: Overview over measurements for Ethane-10, mass flux G versus vapour fraction x.

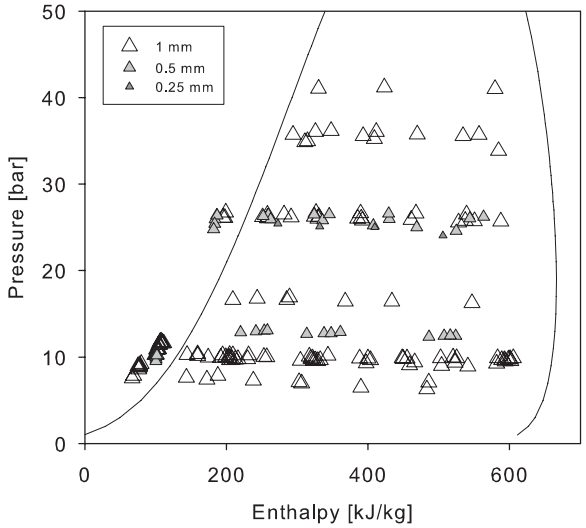

Figure C.8: Overview over two-phase flow measurements for Ethane-27, pressure p versus enthalpy e.

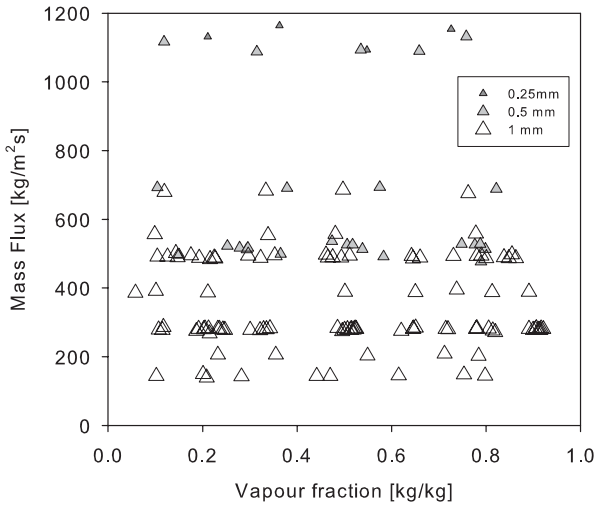

Figure C.9: Overview over measurements for Ethane-27, mass flux G versus vapour fraction x.